

MALAYSIAN JOURNAL OF SCIENCE

Vol. 43 • No 4 • December 2024

MALAYSIAN JOURNAL OF SCIENCE

M J S

ISSN 1394-3065

MJS is indexed in Scopus, Google Scholar, Chemical Abstracts Service Database, ASEAN Citation Index (ACI), and MYCite.

Physicochemical, Microbiological Characteristics of Meatballs from a Mixture of IPB D1 Chicken and Local Indonesian Rabbit Meats

Syafira Amalia Madjid^{1a}, Irma Isnafia Arief^{2a*}, Zakiah Wulandari^{3a}, Cece Sumantri^{4a}

Abstract: IPB D1 chicken meat originates from a novel hybrid domestic chicken lineage, possessing nutritional attributes comparable to those found in rabbits. IPB D1 chicken and rabbit meat are rich in protein and minerals and can be used as the main ingredients for nutrient-rich food products, such as meatballs. This study aims to analyze the physicochemical, microbiological, and organoleptic characteristics of meatballs made with 100% chicken meat from IPB D1, 100% rabbit meat, and a combination of 50% chicken meat from IPB D1 and 50% rabbit meat. The meatballs were tested for their physical characteristics, such as pH, water activity, cooking loss, and texture profile, alongside chemical, microbiological, and sensory test characteristics to identify which formulation produced a meatball with optimal results. The study employed a completely randomized design. Results showed that meatballs with a composition of 50% IPB D1 chicken meat and 50% rabbit meat exhibited superior physical, chemical, microbiological, and sensory test outcomes. Results obtained from this study are promising for development into functional and diverse food products, as they have potential for commercial advancement.

Keywords: IPB D1 chicken meatball, rabbit meatball, physicochemical

1. Introduction

Many Indonesians still suffer from malnutrition and various diseases due to inadequate animal protein consumption. According to BPS, meat consumption in Indonesia remains relatively low and declined in March 2021. The Central Statistics Agency in 2021 stated that purebred or free-range chicken consumption was recorded at 0.538 kg/capita/month, which decreased by 3.4% from the previous year at 0.557 kg/capita/month, whereas rabbit meat consumption only reached 0.27 kg/capita/year. A lack of animal protein can cause diseases such as iron deficiency anemia and toddler stunting. Therefore, animal protein consumption is significant for the sustainability of community nutrition. This problem can be addressed through food diversification, a strategy aimed at reducing malnutrition risk by consuming various types of food with different nutritional content.

Food diversification can aid in preventing micronutrient deficiencies that cause health issues such as anemia and vitamin deficiency. Moreover, food diversification can enhance food security in an area by boosting local food production and lessening dependence on limited food sources (Setyawardani et al., 2020). This approach can be a solution to improve the nutritional quality of Indonesian people, who are still fixated on consuming imported broiler chicken and red meat.

The IPB-D1 chicken is a new family of composite local chickens developed through a crossbreeding program between the F1 PS male (Pelung × Sentul) and the F1 KM female (Kampung × Cobb parent stock) (Habib et al., 2020). The establishment of IPB-D1 chickens aims to increase the participation of local chickens, which can utilize local feed, grow fast, and reach slaughter weight at 10-12 weeks. Their adaptability to the environment is quite good, with strong body resistance to New Castle Disease (ND) or Tetelo and Salmonella. IPB-D1 chicken meat is rich in protein content at 18.35% and minerals, especially Fe, Zn, Mn, and Se, which can prevent diseases such as anemia and stunting in children. Using IPB-D1 chicken can also increase protein diversification and reduce the consumption of imported broiler chickens, thus promoting food self-sufficiency and meeting food needs. A livestock commodity with good carcass potential, aside from chicken, is rabbit, which has high nutritional value and potential as a consumable meat for the Indonesian population.

Rabbit meat is less desirable than other animal meat. Rabbit meat exhibits a 20-21% protein content, with easily digestible amino acids and a relatively low fat content. Additionally, rabbit meat has a reasonably high mineral content, specifically Fe at 6 mg/kg and Zn at 13.23 mg/kg (Weller et al., 2014). Although using rabbit meat as a food ingredient is still relatively low and standard for the community, it can be improved through processing technology. One of the processed products that can compete in the market is meatballs. Considering that meatball products are trending among Indonesians, with the consumption rate reaching 31.4 portions per capita per year and increasing annually by 17.6% (Secretary General of Agriculture of the Republic of Indonesia,

Authors information:

^aJl. Raya Dramaga, Babakan, Departement of Animal Production and Technology, Faculty of Animal Science, IPB University, Bogor, INDONESIA.

E-mail: syafiramadjid@gmail.com¹; isnafia@apps.ipb.ac.id²; zakiahwu@apps.ipb.ac.id³; ceces@apps.ipb.ac.id⁴;

*Corresponding Author: isnafia@apps.ipb.ac.id

Received: March 17, 2023

Accepted: December 12, 2023

Published: December 31, 2024

2018). The use of rabbit meat still needs to be promoted, so innovation efforts are underway to combine chicken and rabbit meatballs to increase public consumption of rabbit meat in Indonesia. With the high nutritional value of IPB-D1 chickens and local rabbits, product diversification can be developed, enhancing food quality, preventing disease, and curtailing the increase of import trade by prioritizing local meat. This can be developed in underdeveloped villages to stimulate the regional economy.

Meatballs combining IPB-D1 chicken and rabbit, rich in protein and minerals, can mitigate the risk of stunting and anemia. Consequently, further research is necessary to assess the physicochemical, microbiological, and organoleptic qualities of meatballs incorporating IPB-D1 chicken and rabbit meat.

2. Materials and Methods

Time and Location

This research was conducted from June to August 2022 at the Integrated Laboratory of the Department of Animal Production Science and Technology, Faculty of Animal Science, IPB University, Indonesia.

Materials

The tools used were a meat pH meter, biuret, pipette, freezer (-18°C), petri dish, hot plate stirrer, test tube, Erlenmeyer tube, digital scale, measuring cup, micropipette, Bunsen heater, incubators, refrigerators, autoclaves, vortexes. Tools in the organoleptic test include paper plates, knives, forks, questionnaire paper, and stationery. The raw meatball materials utilized were IPB D1 chicken, rabbit meat, salt, pepper, tapioca flour, ice cubes, garlic powder, and Sodium tripolyphosphate (STPP).

Methods

Preparation of meatballs

The procedure for meatball production referred to Kia et al. (2016). Five hundred grams of cleaned and deboned meat was cut into small pieces and then ground using a food processor. The seasonings containing 3% salt, 0.3% sodium tripolyphosphate, 10% tapioca, 35% ice, 0.5% pepper, 0.3% garlic powder, and other ingredients were added to the food processor and mixed thoroughly. The dough was molded into rounds and placed in hot water at 80°C for 7–10 minutes. After that, each meatball sample was separated according to the needs of the analysis.

Physical Analysis

The physical analysis includes pH, cooking loss, water absorption, and texture profile. The pH meter was first calibrated with buffer solutions at pH 4 and 7 according to SNI (1995) guidelines. The electrodes were rinsed with distilled water and dried, and the pH meter was inserted into the meat sample approximately 2–4 cm. The pH value was obtained by reading the scale. Cooking loss is calculated according to Bouton (1971), where cooking loss is measured as the difference in the amount of water after centrifugation and the initial amount of water

before boiling. The value obtained was calculated using the formula from Fardiaz (1992). The texture profile of the meatball was measured using a Texture Analyzer Perten Instrument TVT6700 with a cylindrical probe of 20 mm, a compression rate of 80%, and a probe speed of 1 mm/s.

Chemical Analysis

Chemical analysis (water content, ash content, protein content, fat content, and carbohydrate content) was performed using the modified AOAC (2005) method. Mineral analysis employed the wet ashing method by Reitz (1960). Cholesterol analysis used the Chromatography Flame Ionization Detector according to the ASEAN Manual of Nutrient Analysis (2011) method.

Microbiological Analysis

Total Plate Count Analysis or total microbes was measured by the BAM (2001) method using Plate Count Agar as the medium, and the dilutions used were 10⁻², 10⁻³, and 10⁻⁴ for meatball products. The calculation was performed using the pour plate method when visible colonies were at 25–250. Total *Escherichia coli* analysis was performed by the BAM (2001) method using Eosin Methylene Blue Agar (EMBA) media, and the dilutions used were 10⁻¹, 10⁻², and 10⁻³ for meatball products.

Sensory Test

Sensory quality was assessed by 40 semi-trained panelists based on the modified Setyaningsih (2010) method. The method used for the sensory test was the hedonic test (preference test) and the hedonic quality test, which evaluated the meatballs' color, aroma, taste, texture, and general appearance. The hedonic and hedonic quality tests used a scale of 1 to 5. The hedonic quality scale was applied to color, aroma, taste, and texture.

Data Analysis Method

The experiment was conducted in a completely randomized design with three treatments, namely P1 (100% chicken meat from IPB D1), P2 (100% rabbit meat), and P3 (a combination of 50% chicken meat from IPB D1 and 50% rabbit meat). Each treatment was replicated four times, and the obtained data were subjected to an analysis of variance (ANOVA) in a Randomized Block Design, followed by Tukey's test to determine significant differences.

3. Result and Discussion

Meatballs Physical Characteristic

The results of the physical properties (pH, water absorption, cooking loss, and profile texture) are shown in Table 1. The pH value showed a significant difference at varying meatball formulations.

Table 1. Result of physical characteristic test

Parameter	Treatments		
	P1	P2	P3
pH	6.03±0.01 ^a	6.20±0.02 ^c	6.10±0.01 ^b
Cooking Loss (%)	2.21±0.02 ^b	2.55±0.14 ^c	1.79±0.09 ^a
WA (%)	4.5±0.41 ^a	4.25±0.35 ^a	5.25±0.25 ^b
Profile Texture <i>Cohesiveness</i>	0.19±0.03 ^a	0.19±0.01 ^a	0.20±0.02 ^b
<i>Springiness</i>	0.70±0.03 ^a	0.78 ±0.15 ^b	0.84±0.05 ^c

(P1; 100% IPB D1 chicken meat, P2; 100% rabbit meat, P3; 50% IPB D1 chicken meat+50% rabbit meat, F4)

^a means with different superscript are significantly different (P<0.05)

The highest pH was found in P2, with a value of 6.20. Widati et al. (2022) state that the pH of rabbit meatballs ranges from 6.59 to 6.64, indicating that the pH value is consistent with this study. According to Islam et al. (2018), the pH of chicken meatballs is 6.04. The pH can be affected by glycogen levels in different types of meat, thereby influencing the rate of glycolysis. Muscle glycogen levels impact the production of lactic acid and the pH of the meat. Low glycogen levels result in a high pH and slow down glycolysis. In addition, to decrease the pH, glycogen converts into lactic acid in the meat post-slaughter due to an extensive biochemical process. This causes acidification in the meat, leading to a decrease in the pH value. The high pH is also influenced by dietary fiber, which affects meatball pH. Several factors, such as muscle metabolism type and fiber, influence glycogen concentration, impacting the pH of meatballs. The cooking process can increase the pH value of meatballs because cooking can release bonds containing sulfhydryl, imidazole, and hydroxyl groups in the meat (Uzun and Oz., 2021).

Measurements of cooking losses showed significant differences in meatball samples with varying types of meat composition. The range of cooking losses in this study was 1.79-2.55%, with the lowest value being the combination treatment of rabbit meat and chicken IPB D1, at 1.79%. Cooking loss is an assessment of the nutritional value of meat related to its water content. During cooking, meat loses volume and weight due to the release of fluids; water is lost and melted fat drips from the product due to protein denaturation caused by heat (Mena et al., 2019). The decrease in the percentage of cooking loss in the meatballs could be due to the addition of specific types of meat, which resulted in reduced cooking loss; this could be attributed to the combination of a mixture of IPB D1 rabbit meat and chicken, which may increase the protein content more than other treatments. Jia et al. (2020) stated that protein could bind water, forming more hydrogen bonds, and high protein content will increase water-holding capacity, which can affect cooking shrinkage. According to research by Frunza et al. (2023), the protein content of rabbit meat in the Longissimus dorsi section is 21.6%, and the protein content

of IPB D1 chicken is 17-18%. Water absorption capacity is inversely proportional to cooking losses, so the higher the water-holding capacity, the lower the cooking losses.

Furthermore, the higher the cooking losses, the more nutrients will be lost from the meatballs during the cooking process. Meatballs of good quality have a lower cooking loss value (Patriani and Apsari, 2022; Malini et al., 2016). This is consistent with the results of the highest protein content in P3, which showed the lowest cooking loss value. The measurement of water absorption capacity showed a significant difference between the samples. The range of water absorption observed was 4.25-5.25%, with the highest yield obtained by P3.

In contrast, the lowest result was obtained by P2. Apriantini et al. (2021) stated that a high water absorption capacity in meat products results in minimal water loss, leading to a better meat structure. Increased water absorption enhances the texture value. Therefore, the highest value in P3 is the meat combination of chicken and rabbit. The decrease in water absorption is likely due to the denaturation of some proteins. This is supported by Hutabarat et al. (2021), who stated that water absorption affects the cooking shrinkage value. The cooking process causes changes in water absorption due to protein solubility in meat. High temperatures increase protein denaturation and reduce water absorption. All parameters of the physicochemical qualities of meatballs fitted the quality of animal products such as sausage and yogurt (Sulaiman et al., 2016; Astawan et al., 2012).

Furthermore, the higher the cooking losses, the more nutrients will leach from the meatballs during the cooking process. Meatballs of good quality have a lower cooking loss value (Patriani and Apsari, 2022). This is consistent with the results demonstrating that the highest protein content in P3 corresponds to the lowest cooking loss value.

Measurement of water absorption capacity demonstrated a significant difference between the samples. The range of water absorption obtained was 4.25-5.25%, with the highest yield found in P3. In contrast, the lowest result was obtained by P2. Apriantini et al. (2021) stated that high water absorption capacity of meat products results in minimal water loss, leading to better meat structure. Increased water absorption enhances the texture value. Therefore, the highest value in P3 reflects a meat combination of chicken and rabbit. The decrease in water absorption is likely due to the denaturation of some proteins. This is reinforced by Hutabarat et al. (2021), who stated that water absorption influences the cooking shrinkage value. The cooking process causes changes in water absorption due to the protein solubility in meat. High temperatures increase protein denaturation and reduce water absorption. All parameters of physicochemical qualities of meatballs fit the quality seen in animal products such as sausage and yoghurt (Sulaiman et al., 2016; Astawan et al., 2012).

3.1 Input Point Cloud Datasets

This study uses three different datasets for experimental verification purposes: (i) box, (ii) cup, and (iii) Stanford bunny obtained from the PointCleanNet database.

Meatballs Chemical Analysis

Based on the results of the research, chemical analysis such as fat, protein, carbohydrate, mineral and cholesterol that was significantly different.

Table 2. Chemical Analysis test results

Parameter	Treatments		
	P1	P2	P3
Water Content (%)	73.92±0.08	72.51±0.01	74.38±0.05
Ash (%)	2.68±0.01	2.34±0.07	2.35±0.02
Fat (%)	1.13±0.06 ^b	2.34±0.03 ^c	1.06±0.02 ^a
Protein (%)	15.41±0.05 ^a	15.17±0.35 ^a	16.71±0.20 ^b
Carbohydrate (%)	6.86±0.08 ^b	7.65±0.43 ^c	5.50±0.26 ^a
Mineral			
Fe (ppm)	12.25±0.10 ^a	13.15±0.13 ^b	15.76±0.10 ^c
Zn (ppm)	7.36±0.02 ^a	8.23±0.02 ^b	10.15±0.02 ^c
Mn (ppm)	0.23±0.03 ^a	0.39±0.03 ^b	0.46±0.03 ^c
Cholesterol (mg/100g)	33.33±0.01 ^a	37.55±0.16 ^c	36.30±0.13 ^b

(P1; 100% IPB D1 chicken meat, P2; 100% rabbit meat, P3; 50% IPB D1 chicken meat+50% rabbit meat)

^a means with different superscript are significantly different (P<0.05)

The water content in meatballs made from three different types of meat showed no significant difference. The highest water content was obtained in P3, with 74.38%. According to the Indonesian National Standard, the maximum water content is 70%, meaning that all three treatments did not meet the standard. The water content of food ingredients determines the acceptability and durability of these materials. Most changes in food ingredients occur in water media added or derived from the ingredients themselves (Persson et al., 2003). The heating time and the fillers affect the water content in the meatballs. Prolonged heating increases water absorption because water can diffuse into the food and bind starch and protein (Pramuditya & Yuwono, 2014).

The ash content of the meatballs in this study ranged from 2.34% to 2.68% and showed no significant differences between treatments. According to SNI, the maximum ash content in meatballs is 3%. Salazar et al. (2018) stated that the ash content of rabbit meatballs soaked in tamarillo juice was 1.16% to 2.66%. Thus, the ash content of the meatballs in this study did not exceed the SNI limits.

The average fat content of the meatballs using three different treatments ranged from 1.06% to 2.34% and showed a significant difference between the meatballs (Table 2). The combination of IPB D1 rabbit and chicken meatballs had the lowest fat content (1.06%). This is presumably due to the relatively low-fat content of IPB-D1 chicken meat. The average fat content of IPB-D1 chicken breast ranged from 0.15% to 0.32%. Nistor et al. (2013) stated that the fat content of rabbit meat was around 9.2 g/100 g sample. According to SNI, meatball products have a maximum fat content value of 10%. Thus, the fat content of meatball products in this study is still within the safe range of the Indonesian

National Standard. The fat content of meat is closely related to its water content; the greater the fat content, the lower the water content (Berutu et al., 2010). This is consistent with the results of this study, where the water content of the three treatments has a negative correlation with the fat content value.

The protein content of the meatballs with the three different meat compositions ranged from 15.27% to 16.71%, indicating that the protein content of the meatballs had a significant difference (Table 2). According to SNI 01-3818-1995, the minimum protein content of meatballs is 11%. Thus, the protein content of P1 and P2 fulfills the SNI requirements. Meanwhile, according to SNI, the minimum protein content of combined meatballs is 8%, indicating that P3 has fulfilled the SNI requirements. The highest protein content was found in meatballs P3, with 16.71%. This can be influenced by the high or low protein content of the raw meat used in the dough. Rabbit meat has a protein content of 20-21% (Sutaryo et al., 2021). Nusi (2010) states that high and low levels of meat protein are related to water and fat content. Protein content will increase if the intramuscular fat content is low and the water content is high. Protein content was effected by physical treatment and proteolytic enzyme during processing (Afiyah et al., 2015). The longer the boiling, the more proteins are damaged, and boiling at high temperatures will cause denaturation, causing the protein content to drop.

The carbohydrate composition of the raw materials impacted the carbohydrate content of the meatball samples. Carbohydrate levels in IPB D1 chicken meatballs, rabbit meat, and their combinations showed significant differences. The value of carbohydrate content in this study was 5.50% to 7.65%. Meatballs with 100% rabbit meat treatment have the highest carbohydrate content value. Water and protein content are related to the carbohydrate content of meatballs; the higher the water content and protein content, the lower the carbohydrate content of meatballs (Rahmah and Nurul, 2021). The average carbohydrate value of IPB-D1 chicken breast meat in this study ranged from 3.81% to 5.45%. According to Grace and Henry (2020), ingredients containing carbohydrates are present in tapioca flour, which has 89.04%.

The mineral content of the meatballs shown in Table 2 reveals a significant difference. Meatball Fe values in this study ranged from 12.25 ppm to 15.76 ppm. The Zn content was 7.36 ppm to 10.15 ppm, and the Mn level was 0.23 ppm to 0.46 ppm. P3 obtained the highest Fe, Zn, and Mn values. This is due to the high Fe mineral content in IPB D1 chicken meat, 16 mg/kg, and the mineral content in rabbit meat, 6 mg/kg Fe and 13.23 mg/kg Zn (Weller et al., 2014). Martinez et al. (2018) reported the content of control chicken meat without treatment had an Fe content of 10.65 mg/kg and Zn of 1.49 mg/kg. The high mineral content of IPB D1 chicken can be considered a functional food that can be beneficial for sufferers of iron diversification anemia and stunting in children.

The meatball cholesterol levels for the three treatments are presented in Table 2. The results showed that the highest cholesterol level was found in P2 (100% rabbit meat) with a score

of 37.55 mg/100g, while the lowest score was recorded by P1 (chicken meatballs with 100% IPB D1) of 33.33 mg/100g. It is suspected that IPB D1 chicken meat has low cholesterol content. The cholesterol content of rabbit meat in the study by Puspani et al. (2019) of 48.07 mg/dg also explained that a decrease in the activity of lipogenic enzymes and an increase in the excretion of bile acids in the feces partly caused the reduction in cholesterol.

Meatballs Microbiological Analysis

Measurement of microbiological analysis was performed to detect the presence of microorganisms in a food product. The results of the three different treatments of meatballs are presented in Table 3 below.

Table 3. Microbiological Analysis test results

Parameter	Treatments		
	P1	P2	P3
Total Microbes (log cfu/g)	3.01±0.24 ^b	3.03±0.13 ^b	2.68±0.13 ^a
Total <i>E. coli</i>	Negative	Negative	Negative

(P1; 100% IPB D1 chicken meat, P2; 100% rabbit meat, P3; 50% IPB D1 chicken meat+50% rabbit meat)

^a means with different superscript are significantly different (P<0.05)

The results of microbial analysis for the three treatments showed a significant difference. Using rabbit meat in meatball

products resulted in the highest number of microbes, namely 3.03 log cfu/g. In comparison, meatballs with a combination of IPB D1 chicken and rabbit meat had the lowest microbial count, at 2.68 log cfu/g. According to SNI 01-3818-2014 regarding microbial contamination, the allowable plate numbers for meatball products and combined meatballs are a maximum of 1 x 10⁵ colonies/g (5.0 log cfu/g). Therefore, the three meatball treatments met the quality requirements for total microbial content. *Escherichia coli* is a foodborne pathogen that causes diarrhea in humans, especially children and the elderly, and is characterized by acute kidney failure, hemolytic anemia, and thrombocytopenia (Sallam et al., 2021). Numerous materials are used as preservative agents in animal products, such as bacteriocin (Hanifah et al., 2016; Sihombing et al., 2015), teak leaf extract (Arief et al., 2014) and lactic acid bacteria which have antimicrobial properties (Adiyoga et al., 2022). Quantitative data from the study demonstrated that *Escherichia coli* levels in this study were negative (Table 3). The three meatball treatments met the requirements for being free from *E. coli* contamination. This is due to the entire process of making meatballs being conducted hygienically.

Sensory Test

Sensory tests include hedonic and hedonic quality tests. The color, taste, texture, and general appearance in the hedonic test showed that the results were significant. The average value of the hedonic quality test for meatball texture demonstrated a significant difference.

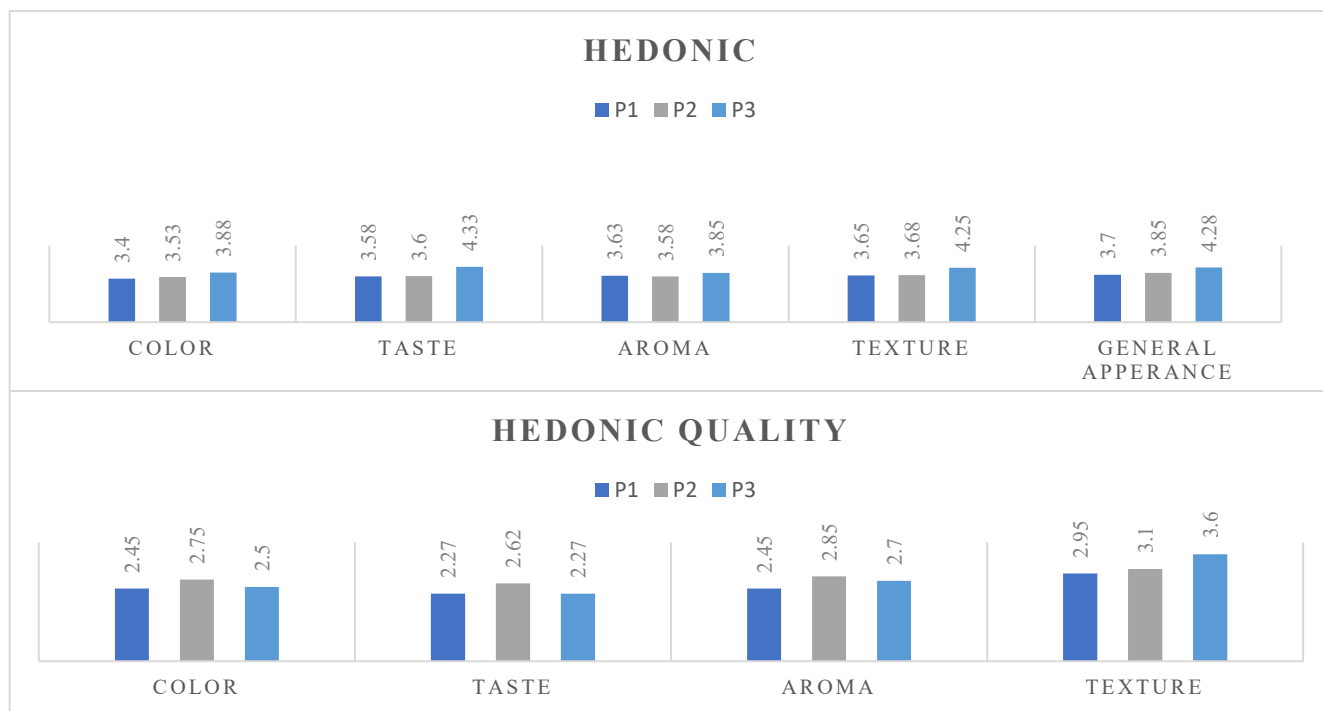


Figure 1. Sensory Test. P1 = 100% chicken meat from IPB D1, P2 = 100% rabbit meat, P3 50% chicken meat from IPB D1 + 50% rabbit meat. Hedonic scale 1 (dislike very much), 2 (dislike), 3 (kinda like or quite like), 4 (like), 5 (like very much). Color hedonic quality: scale 1 (very white), 2 (white), 3 (slightly gray), 4 (gray), 5 (very gray). Flavor: 1 (very meaty), 2 (meaty), 3 (slightly meaty), 4 (no meaty taste), 5 (very no meaty taste). Aroma: 1 (very meaty), 2 (meat-scented), 3 (slightly meaty), 4 (unscented meat), 5 (very unflavored meat). Texture: 1 (very not chewy), 2 (not chewy), 3 (slightly chewy), 4 (chewy), 5 (very chewy).

The panelists preferred the taste, texture, and general appearance of P3 meatballs (comprising 50% rejected IPB D1 chicken meat and 50% rabbit meat), compared to the other two treatments. Panelists showed quite favorable results for meatballs in the three different treatments regarding aroma and color. The release of cell fluids during cooking will reduce the intensity of the color along with the release of pigments. The panelists preferred the taste of meatballs with a mixture of IPB D1 chicken meat and rabbit meat (P3) compared to other meat compositions.

The score obtained for the "taste" of IPB D1 chicken and rabbit combination meatballs reached a value of 4.33 (the highest score), indicating that the IPB D1 chicken and rabbit combination meatballs were acceptable to consumers. The formulation between meat and the primary raw material, combined with flour and other supporting ingredients, significantly affects the taste of the meatballs, and this is reinforced by Gedrovica and Karklina et al. (2013). The added formulation between meat and raw materials will significantly influence the taste of the meatballs because it will impact the taste of the product, and this means that sensory evaluation of products is critical, especially for new products like this one. The mean values of the hedonic quality test for color, aroma, and taste also showed insignificant differences. In the color assessment, the three treatments showed that the meatballs were white. In the aroma assessment, the three meatballs could be interpreted as smelling of meat, while in the taste assessment, the three treatments had the result that the meatballs had a distinctive taste of meat. The texture value of the meatballs showed a significant difference; P3 had a slightly chewier texture than other treatments. High connective tissue content in meat can cause the rough texture of processed products. High connective tissue makes it difficult for the meat to be ground smoothly, resulting in a less chewy or rough texture.

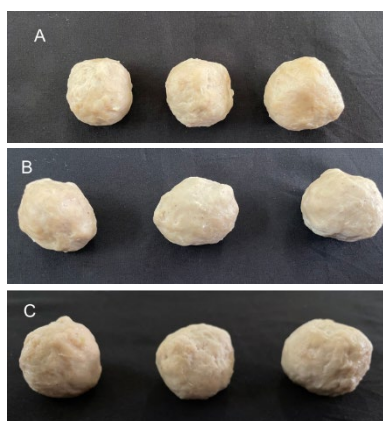


Figure 2. Sensory Test. A = 100% chicken meat from IPB D1, B = 100% rabbit meat, C = 50% chicken meat from IPB D1 + 50% rabbit meat.

4. Conclusion

The use of 50% IPB D1 chicken meat and 50% rabbit meat for meatball composition showed more effective results than the other treatments based on parameters of physical characteristics, chemical, microbiological, and sensory tests. Meatballs mixed with IPB D1 chicken and rabbit meat can be used for food diversification and as a food approach in society.

5. Acknowledgement

This research was supported by Riset Inovatif Produktif (RISPRO) Lembaga Pengelola Dana Pendidikan (LPDP) Kementerian Keuangan RI based ID PRJ-28/LPDP/2019 and continued to 2024 with No S-459/LPDP.4/2024 and IPB contract No : /IT3.L1/PT.01.01/M/M/2024. Thank to colleagues from the Department of Animal Product and Technology, Faculty of Animal Science IPB University, who provided assistant this research.

6. References

- Adiyoga R, Arief II, Budiman C, Abidin Z. 2022. In vitro anticancer potentials of *Lactobacillus plantarum* IIA-1A5 and *Lactobacillus acidophilus* IIA-2B4 extracts against WiDr human colon cancer cell line. *Food Science and Technology*. 42: Article number e87221
- Afiyah DN., Arief II, Budiman C. 2105. Proteolytic characterization of trimmed beef fermented sausages inoculated by Indonesian probiotics: *Lactobacillus plantarum* IIA-2C12 and *Lactobacillus acidophilus* IIA-2B4. *Advance Journal of Food Science and Technology* 8 (1) : 27-35.
- AOAC (Association of Official Analytical Chemistry). (2005) Official method of analysis. 18th Ed. Maryland (US): AOAC International.
- Apriantini A., Afriadi D., Febriyani N., Arief II. (2021) Fisikokimia, mikrobiologi dan organoleptik sosis daging sapi dengan penambahan tepung biji durian (*Durio zibethinus* Murr). *Jurnal Ilmu Produksi dan Teknologi Hasil Peternakan* 9(2):79–88.
- Arief, II., Suryati, T., Afiyah DN., Wardhani DP. 2014. Physicochemical and organoleptic of beef sausages with teak leaf extract (*Tectona grandis*) addition as preservative and natural dye. *International Food Research Journal* 21 (5) : 2033-2042.
- Astawan. M., Wresdiyati. T, Suliantari., Arief II, Septiawan R. 2012. Production of synbiotic yogurt-like using indigenous lactic acid bacteria as functional food. *Media Peternakan* . 35 (1): 9-14.
- Berutu, KM., Suryanto E., Utomo Ristiano. (2010) Kualitas bakso daging sapi peranakan ongole yang diberi pakan basal tongkol jagung dan undegraded protein dalam complete feed. *Buletin Peternakan* 34(2):103-113
- Fardiaz, S. (1992) Mikrobiologi pangan I. Jakarta (ID): Gramedia Pustaka Utama.
- Fitriyani E., Nueaenah N., Nofreena A. (2017) Tepung ubi jalar sebagai bahan filler pembentuk tekstur bakso ikan. *Jurnal Galung Tropika* 6(1): 19-32
- Frunză, G., Murariu OC., Ciobanu MM., Radu-Rusu RM., Simeanu D., Boișteanu PC. (2003) Meat quality in rabbit (*Oryctolagus cuniculus*) and hare (*Lepus europaeus Pallas*)-a nutritional and technological perspective. *Agriculture* 13(1):126.
- Gedrovica, I., Karlina D. (2013) Sensory evaluation of meatballs with jerusalem artichoke (*Helianthus tuberosus* L.). *International Journal of Nutrition and Food Engineering* 7(3):752-754
- Grace, NCF., Henry CJ. (2020) The physicochemical characterization of unconventional starches and flours used in Asia. *Foods* 9:182.
- Habib, MFA., Murtin S., Cyrilla L., Arief II., Mutia R., Sumantri C. 2020. Tepung ubi jalar sebagai bahan filler pembentuk tekstur bakso ikan. *Jurnal Agripet* 20(2):177-186.
- Hutabarat, R., Suardana IW., Swacita IBN. (2021) The comparison of the quality of balinese and landrace porks in terms of water holding capacity and cooking loss. *Journal of Veterinary and Animal Sciences* 4(1):26-31
- Indiarto, R., Nurhadi B., Tensiska., Subroto E., Istiqamah YJ. (2020) Effect of liquid smoke on microbiological and physico-chemical properties of beef meatballs during storage. *Food Research* 4(2):522-531.
- Islam, MA., Haque MA., Ferdwsi MJ., Ali MY., Hashem MA. (2018) Formulation of value added chicken meatball with different level of wheat flour. *SAARC J. Agri* 16(1):205-213
- Jia, F., Jing Y., Dai R., Li X., Xu B. (2020) High-Pressure thawing of pork: water holding capacity, protein denaturation and ultrastructure. *Food Bioscience*:100688.
- Kia KW , Arief, I.I, Sumantri C, Budiman C. 2016. Plantaricin IIA-1A5 from *Lactobacillus plantarum* IIA-1A5 retards pathogenic bacteria in beef meatball stored at room temperature. *American Journal of Food Technology*, 11 (1-2) : 37-43.
- Malini DR., Arief II., Nuraini H. 2016. Utilization of durian seed flour as filler ingredient of meatball. *Media Peternakan* 39 (3) : 161-167.
- Martínez, L., Ros G., Nieto G. (2018). Fe, Zn and Se bioavailability in chicken meat emulsions enriched with minerals, hydroxytyrosol and extra virgin olive oil as measured by caco-2 cell model. *Nutrients* 10(8):969.

- Marwansyah, A.J., Okarini, IA., Miwada INS. (2019) Pengaruh lama perendaman daging ayam petelur afkir dalam larutan daun kelor (*moringa oleifera* lamk.) terhadap kualitas organoleptic. *Peternakan Tropika* 7(1):738-749
- Mena, B., Zhongxiang F., Hollis A., Scott H., Minh H., Phyllis JS., Robyn DW. (2019) Influence of cooking method, fat content and food additives on physicochemical and nutritional properties of beef meatballs fortified with sugarcane fibre. *International Journal of Food Science & Technology* 55(6):2381-2390.
- Nistor, E., Bampidis VA., Păcală N., Pentea M., Tozer J., Prundeanu H. (2013) Nutrient content of rabbit meat as compared to chicken, beef and pork meat. *Journal of Animal Production Advances* 3(4): 172-176.
- Nusi, M. (2010) Penggunaan tongkol jagung dan undegraded protein dalam complete feed terhadap penambahan bobot badan, persen- tase karkas dan kualitas daging pada sapi peranakan ongole. Tesis. Universitas Gadjah Mada. In Progress. Yogyakarta.
- Patriani, P., Apsari NL. (2022) Improving the physical quality of beef meatballs using andaliman spice (*Zanthoxylum acanthopodium* DC) on shelflife. The 5th International Conference on Agriculture, Environment, and Food Security Series Earth and Environmental Science, p. 977. Indonesia : IOP Publishing
- Persson, El., Sjolom I., Skog E. (2003) Effect of high water-holding capacity on the formation of heterocyclic amines in fried beef burgers. *Journal of Agricultural and Food Chemistry* 51(15):4472- 4477.
- Pramuditya, G., Yuwono SS. (2014) Peunentuan atribut mutu tekstur bakso sebagai syarat tambahan dalam sni dan pengaruh lama pemanasan terhadap tekstur bakso. *Jurnal Pangan dan Agroindustri* 2(4): 200-209.
- Puspani, E., Bidura IGNG., Sumadi IK., Nuriyasa IM., Candrawati DPMA. (2019) Growth performance, meat cholesterol and β -carotene content in rabbit fed with carrot leaves, grass, and concentrates. *International Journal of Multidisciplinary Approach and Studies* 6(3):32-41
- Rahmah L., Nurul AC. (2021) Peningkatan nilai gizi dan sifat fisik bakso ayam dengan substitusi kulit buah naga dan jamur tiram. *Jurnal Teknologi Pertanian* 10(2):125-132
- Salazar, DM., Rodríguez MR., Valencia AF., Amancha P., Robalino DR., Mañay P., Rodríguez CA. (2018) Physicochemical, microbiological and sensory evaluation of rabbit meatballs marinated in tamarillo juice (*Solanum betaceum*). *Italian Journal of Food Science* 30:84-92
- Sallam, KI., Abd-Elghany SM., Imre K., Morar A., Herman V., Hussein MA., Mahros MA. (2021) Ensuring safety and improving keeping quality of meatballs by addition of sesame oil and sesamol as natural antimicrobial and antioxidant agents. *Food Microbiology* 99(4):1-11.
- Setyawardani T., Sumarmono J., Arief II., Rahardjo HDA., Widayaka K., Santosa SS. 2020. Improving composition and microbiological characteristics of milk kefir using colostrum. *Food Science and Technology* 40 : 699 – 707.
- Sihombing, DE., Arief II., Budiarti S. 2015. Application of antimicrobial agents produced by *Lactobacillus plantarum* IIA-1A5 as natural preservative on beef during room temperature storage. *Advance Journal of Food Science and Technology* 8 (4) : 251-255
- Skipnes, D., Østby ML., Hendrickx ME. (2007). A method for characterising cook loss and water holding capacity in heat treated cod (*Gadus morhua*) muscle. *Journal of Food Engineering* 80(4):1078–1085.
- Sulaiman, NB, Arief II, Budiman C. 2016. Characteristic of lamb sausages fermented by Indonesian meat-derived probiotic, *Lactobacillus plantarum* IIA-2C12 and *Lactobacillus acidophilus* IIA-2B4. *Media Peternakan* 39 (2): 104-111.
- Sutaryo., Jannah A., Rizqi A., Lestari D., Purnomoadi A. (2021) Produksi karkas, nilai gizi dan profil asam lemak daging serta produksi limbah kelinci new zealand white akibat penyertaan rumput laut cokelat (*Sargassum* sp.) pada ransum. *Livestock Animal Research* 19 (1): 120-129.
- Szczesniak, AS. (2002) Texture is a sensory property. *Food Quality and Preference* 13(4):215–225
- Tahtma, FR., Wibowo T., Taufik IM., Cahyadi M. (2019) Color and texture analyses of meatballs made from beef, pork, rat, dog meats, and their mixtures. International Conference on Food Science and Engineering Series Materials Science and Engineering, p. 633. Indonesia : IOP Publishing
- Uzun, I., Oz F. (2021) Effect of basil use in meatball production on heterocyclic aromatic amine formation. *Journal of Food Science and Technology* 58(8):3001–3009.

Weller, G., Caballero A., Karlsson L., Hernández F., Gutiérrez AJ., Rubio C. Revert C., Troyano JM., Hardisson A. (2014) Determination of iron, copper, zinc and manganese in sausage, poultry-rabbit meat, viscera and red meats consumed by the population in the canary islands, spain. *Journal of Toxins* 1(1):1-7

Widati AS., Mustakim., Widyastuti ES., Evanuarini H., Amertaningtyas D., Apriliyani MW. (2022). The effect of theseuse of different types and d levels of tapioca flour on the physical quality of rabbit meatballs. *Jurnal Ilmu Dan Teknologi Hasil Ternak* 17(1):27-33

Wing Morphology and Echolocation of *Rhinopoma hardwickii* (Lesser Mouse-tailed Bat, Gray, 1831)

Shaktivardhan Singh^{1a}, Vadamalai Elangovan^{2a}, Sanjay Kumar Bharti^{3a}, Pawan Kumar Misra^{4a}

Abstract: *Rhinopoma hardwickii* is currently classified as a member of the Yinpterochiroptera suborder, which includes frugivorous and some insectivorous bats. This species is the smallest in the Rhinopomatidae family and easily identified by its long tail. The wing morphology and echolocation calls of this species were studied to see if there were any changes in wing morphology between sexes, echolocation calls across different environments such as natural (roost and field) and controlled (captive), as well as different geographical areas. In this study, a total of 41 individuals (27 male and 14 female) of *R. hardwickii* were captured and their wing morphology was measured. The results show that there were no statistically significant variations in their morphometric characteristics or in wing morphology between the sexes. This species has with high wing loading and a high aspect ratio, as well as pointed wing tips. The echolocation calls consisted up to five harmonics of FM and CF-FM sweeps. Peak frequencies, start frequency, end frequency, and IPI of three separate environment parameters (roost, captive, and field recording) differed significantly ($p > 0.001$). Moreover, we compared the frequency at maximum energy with four different geographical regions such as Kerala, Gujarat, and Israel to current study, and found that the frequencies of bat calls do not vary with geographical region ($H=0.667$, $df=3$, $p=0.881$). Therefore, the current study provides accurate identification of *R. hardwickii* on the basis of echolocation call in a different environment. The echolocation call and wing morphology data clearly show that this species is a fast flyer with limited manoeuvrability that feeds on forest canopy or over water bodies.

Keywords: Echolocation, frequency, rhinopoma, morphology, multi-harmonic, wing.

1. Introduction

Members of Rhinopomatidae family are insectivorous bats native to Old-World tropics that live primarily in deserts and steppes. Rhinopomatidae is a monotypic family with a single known genus, *Rhinopoma* (Geoffroy, 1818), with five species: *Rhinopoma hardwickii* (Gray, 1831), *R. microphyllum* (Brünnich, 1782), *R. muscatellum* (Thomas, 1903), *R. cystops* (Thomas, 1903) and *R. macinnesi* (Hayman, 1937). *Rhinopoma hardwickii*, commonly known as the Lesser Mouse-Tailed Bat or Long-Tailed Bat, was named after Major General Thomas Hardwicke (1755–1835), an English soldier and naturalist who served many years in India. These bats are smallest in their family and are easily identified by their long tail. They primarily roost in natural caves, monuments, abandoned buildings, dry bushes, rocky places, and barren mountains (Prakash, 1961; Benda et al., 2004). Their colony consists of hundreds to thousands of individuals (Purohit and Senacha, 2004; Benda et al., 2004). They also share colonies with *Taphozous* spp. (Singh et al., 2021). They are distributed over a wide range of geographic areas from Morocco, Senegal, and Kenya, as well as Arabia and the Middle East, India, Thailand, and the Sudan Archipelago (Van Cakenberghe and De Vree, 1994; Hill,

1977). The Rhinopomatidae family has been classified into a new suborder, Yinpterochiroptera (Springer, 2001) along with Pteropodidae, Rhinolophidae, Hipposideridae, Megadermatidae and Craseonycteridae (Hulva and Horacek, 2002; Teeling et al., 2002; Van Den Bussche and Hofer, 2004). Simmons and Stein (1980) reported that *R. hardwickii* as a primitive echolocating bat, however, Habersetzer (1981) research revealed that *R. hardwickii* possesses a complex echolocating system that produces at least two distinct types of sounds: Frequency Modulated (FM)-sounds are produced when approaching an obstacle and during cluster outfly, while Constant Frequency (CF) sounds are generated in the open by both solitary and group flying bats.

Few studies have been conducted on the echolocation of *R. hardwickii* (Hackett et al., 2016; Srinivasulu and Srinivasulu, 2017; Shah and Srinivasulu, 2020), but none have taken into account changes in habitats such as the captive, field and roost recording. In addition to echolocation, wing morphology is a key element in determining the behavior of any bat species (Norberg and Rayner, 1987; Pennycuik 1989). Except for Norberg and Rayner (1987), no information on the wing morphology of *R. hardwickii* is currently available. There is a possibility of species misidentification due to lack of bat call data accessible for comparative purposes, particularly survey calls (Duffy et al., 2000; Gannon et al., 2004). Many factors contribute for the intraspecific call variability, including age (Jones and Kokurewicz, 1994),

Authors information:

^aDepartment of Zoology, School of Life Science, Babasaheb Bhimrao Ambedkar University Lucknow-226025, INDIA. E-mail: shaktivardhansingh7@gmail.com¹; elango17@yahoo.com²; sanjaybharti.kumar64@gmail.com³; pawanmsr17@gmail.com⁴

*Corresponding Author: pawanmsr17@gmail.com

Received: January 24, 2023

Accepted: July 5, 2023

Published: December 31, 2024

individual identity (Masters et al., 1995), foraging mode (Griffin et al., 1960), flight situation (Berger-Tal et al., 2008), acoustic clutter (Broders et al., 2004), ambient noise (Gillam and McCracken, 2007) and presence of conspecifics (Chiu et al., 2009). The problem became much more complicated when regional call comparisons were not performed (Thomas et al., 1987; Barclay et al., 1999; O'Farrell et al., 2000; Reinhold et al., 2001; Law et al., 2002).

Therefore, the following questions were arising: (1) are there any differences in wing morphology between sexes, (2) are there any difference in echolocation calls between natural (field and roost recording) and controlled (captive), and (3) are there any differences in echolocation calls between different geographical areas (frequency at maximum energy; FMaxE). FMaxE, which occurs in the outward pulse of a call, is regarded one of the most consistent and crucial echolocation call parameters (Fullard et al., 1991). The study was conducted to fill the current knowledge gap, considering the three questions listed above.

2. Materials and Methods

Field Survey and Identification of Bats

Field surveys were carried out from April 2019 to February 2020. Bats were captured for individual identification at their roosting sites using nylon mist nets (9.0 m X 2.0 m, with mesh size 38.0 mm, Avinet, Dryden, USA), and hoop net. Maps of roosting sites were prepared using Arc GIS. Morphological measurements of adult bats such as body length, forearm length, hind arm, metacarpals, tail, head length and wingspan etc. were taken using digital venire calipers (Mitutoyo, Japan), and body mass was measured with electronic balances (ACCULAB Sartorius group, EC-211). Bats were recognized using morphological criteria, as described by Bates and Harrison (1997). Bats were captured and handled in accordance with the guidelines of the American Society of Mammologists (Sikes et al., 2011) and relevant ethical permits were secured for data collection vide Letter No. 214/11/DAAS/BBAU/2011 of Babasaheb Bhimrao Ambedkar University and Archaeological Survey of India, Lucknow circle for bat survey (F. No. 10-16/23/2013-M 11535).

Wing Morphology and Call Analysis

The bat was positioned on its ventral side on a large graph paper, with their wings stretched to their leading-edge perpendicular to the body axis. The wing outlines were then traced onto the graph paper and the area of wings was assessed. Arm length, wing length (cm) and hand wing (cm), arm wing area (cm²) and hand wing area (cm²), wing span (cm) and wing area (cm²) were also measured, as reported (Norberg and Rayner 1987). The wing loading (WL), aspect ratio (AR), and tip shape index (TSI) were estimated as per the Norberg and Rayner (1987) and Pennycuik (1989) reports. Relative wing loadings (RWL) were estimated using Norberg et al. (2000).

The echolocation calls of *R. hardwickii* were recorded at four separate places (Fig. 1) in three environments: roost, field and captivity. The conditions for three separate ecosystems were as follows.

- a) Roost: bat detector was placed on unattended mode overnight to record calls under the roosts.
- b) In the field: manual recoding was performed at the moment of emergence near the roost in open ground.
- c) Captive: Individuals of this species were captured using mist and hoop nets, then released in a room (10X10 feet). Once relaxed, the recorder was set to unattended mode for at least 2 hours per recoding.

The calls were recorded using a heterodyne in an unattended mode with time expansion (10X). The fast fourier transform (FFT) size was 512 samples with Hanning window. Each 20 sec recording lasted 2 min and included a maximum of five strings at a five-minute interval. The bat calls were analyzed using Bat sound Pro analysis software (version 2.1), which yielded the following call parameters: peak frequency, start and end frequencies, call duration, inter-pulse interval, band width, maximum and minimum frequency. We also compare the echolocation call of *R. hardwickii* with previous studies (Hackett et al., 2016; Srinivasullu and Srinivasullu, 2017; Shah and Srinivasullu, 2020) and the current study in Uttar Pradesh, which are from different geographical areas (Fig. 2, Table 4).

Statistical Analysis

The data was analyzed using SPSS 21.0 (SPSS Inc, USA). The distribution of data sets was analysed using a descriptive statistic, with normality and homogeneity being considered. $P < 0.05$ was considered for normally distributed data sets. All morphological data were abnormally distributed ($p > 0.05$), so the Kruskal Wallis H-test was applied to see whether there were any statistical variations in wing morphology between sexes.

3. Results

A total of 41 *R. hardwickii* individuals (27 male and 14 female) of were captured from their day roost utilizing hoop and mist nest. Table 1 shows the morphological measurements of *R. hardwickii*. Males had little higher body mass (20.71 ± 2.95 g) then females (19.86 ± 3.38 g) but there was no significant differenc in weight ($H = 0.41$, $p=0.522$). Females had somewhat larger forearms (60.73 ± 1.62) than males (58.83 ± 2.26 mm), although the differences was not significant ($H=0.126$, $p=0.723$). There were no statistical significance differences in arm wing length, hand wing length, arm wing area, hand wing area, aspect ratio, tip length ratio, wing-loading and relative wing loading between the sexes ($p > 0.05$, Table 2). Therefore, we pooled the wing morphology data of

males and females. The average wing loading of *R. hardwickii* was 11.92 ± 1.87 (N/m²) with an aspect ratio was 7.04 ± 0.44 . The relative wing loading for *R. hardwickii* was 8.41 ± 5.57 . The tip length ratio and tip area ratios were 0.68 ± 0.04 and 0.44 ± 0.05 , respectively. The tip shape index was measured and found 1.57 ± 0.15 .

We recorded 5330 *R. hardwickii* calls throughout a 15-hour 50-minutes period at four sites, and 167 of them were selected for analysis. The calls consisted up to five harmonics of FM and CF-FM sweeps, with the fourth harmonic being the most common; the second harmonic was the most strong. The second harmonic's peak frequency is 28.8 – 38.7, the third harmonic is 37.9 – 50.6, and the fourth harmonic 42.7 – 62.7 kHz. The Frequency at maximum energy (FMaxE) ranged from 28.8 to 38.7 (33.23 ± 2.38) kHz. The start frequency ranged from 19.90 to 36.90 kHz (30.78 ± 3.04), and the end frequency ranged from 21.4 to 38.8 kHz (32.15 ± 2.84). The pulse interval was 39.92 ± 46.86 ms. When we analysed start frequency, end frequency and peak frequency along with Inter Pulse Interval (IPI) at three different sites (roost, captive and field recording), we found that there were significant differences between captive, field and roost sites ($p=0.001$, Table 3). When we compared the frequency at maximum energy of *R. hardwickii* to four different geographical regions, namely Kerala, Gujrat, and Israel, with the current study, we found that the frequency did not vary by geographical region ($H=0.667$, $df=3$, $p=0.881$) (Table 4).

4. Discussion

The current study reveals that *R. hardwickii* is a fast flyer with poor maneuverability that feeds on forest canopy or over water body, has a larger aspect ratio ($AR > 8.0$), a short wing span, high wing loading, average relative wing loading, and a small surface area. Bats with high AR and RWL are fast flyer but have poor flight maneuverability (Freeman, 1981), and they feed in open unobstructed environment such as over forest canopy or over water (Marinello and Bernard, 2014). Kingdon (1974), Smith and Starrett (1979) report rhinopomatids foraging in open ground, apart from impediments, at relatively high altitude, but Neuweiler (1984), Habersetzer (1986) describe their fly at intermediate heights in open spaces of forest around the canopy, but below the high and fast flyer Emballonuridae and Molossidae in the same habitat. *Rhinopoma hardwickii* have a series of alternating flutters and glides, with a rising and falling motion (Harrison, 1964).

Previously, only five studies on *R. hardwickii* echolocation calls were conducted, some of which were incomplete (Chaturvedi et al., 2018), and no one considered the wing morphology, despite the fact that wing morphology is directly related to echolocation and feeding behavior in all insectivorous bat species.

Rhinopoma hardwickii produces narrowband, multi harmonic signals with CF/FM, which are dominated by harmonic other than

fundamental harmonic, as supported by other authors (Habersetzer, 1981; Jones and Teeling, 2006). The narrow broadband call with low frequency is associated with high wing loading and high aspect ratio reported in fast flying, open area foraging species (Norberg and Rayner, 1987); consequently, the foraging result clearly show that *R. hardwickii* is fast flyer who forages in open space. Many authors also reported that this species generates multi harmonic calls with CF/FM (Srinivasullu and Srinivasullu, 2017; Shah and Srinivasullu, 2020), quasi constant frequency (QCF) calls (Hackett et al., 2016), second harmonics with maximal energy. The call frequency of *R. hardwickii* differs from previous findings, which ranges from 32–35 kHz (Hackett et al. (2016), 31.3 - 33.6 kHz (Srinivasulu and Srinivasulu 2017), 30.90 - 32.25 kHz (Shah and Srinivasulu 2020) while the current result shows the 28.8 – 38.7 kHz, that's is approx. 2 kHz less than minimum call frequency and 3 kHz higher call frequency in previous reports. Lower frequency calls with narrow band widths are required for long range detection of prey, which is characteristic feature of fast flyer species (Neuweiler, 1984), these assertions supports the current finding.

All of the author mentioned did not investigate the differences in *R. hardwickii* echolocation calls in different environments, such as natural (field and roost), controlled (captive), although the result of this study clearly indicated that the *R. hardwickii* has varied call frequencies at different habitats. Habersetzer (1981) also reported that *R. hardwickii* has complex echolocating system which alters the form of signals in different situation. The result of current study, which is also supported by many authors, found that individuals of bats species changes their calls in response to changing habitats as well as distance from obstacles (Kalko and Schnitzler, 1993; Bartonicka and Rehak, 2005) or proximity to other bats (Obriest, 1995; Ratcliffe et al., 2004; Ulanovsky et al., 2004; Gillam et al., 2007; Bates et al., 2008; Amichai et al., 2015).

This study found that the call frequency and structure of *R. hardwickii* did not vary by geographical regions, however, some authors reported that the populations of same species in different geographical region may have different call structures (Thomas et al., 1987 and Murray et al., 2001).

5. Conclusion

The result of current study found that there were no differences in wing morphology between the sexes. *Rhinopoma hardwickii*'s echolocation calls vary according to situation, such as natural (roost and field recording) and controlled (captive), but do not change with geographical regions. The wing morphology data clearly indicates that *R. hardwickii* is fast flyer with limited maneuverability, and this species feeds on forest canopy or over water bodies. The data provided in this study may provide to other researchers in accurately identifying of *R. hardwickii* based on echolocation calls in various habitats, whereas wing morphology indicates foraging nature.

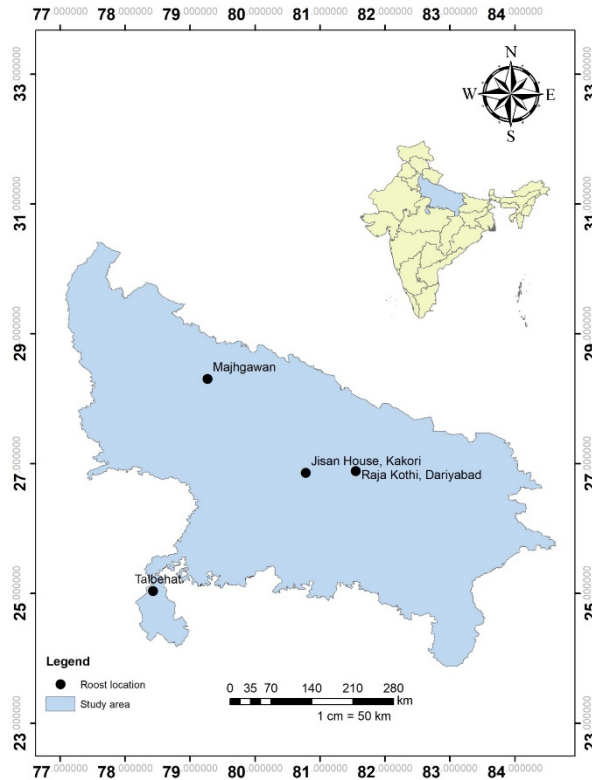


Figure 1. The roosts location of *R. hardwickii* in Uttar Pradesh, India.

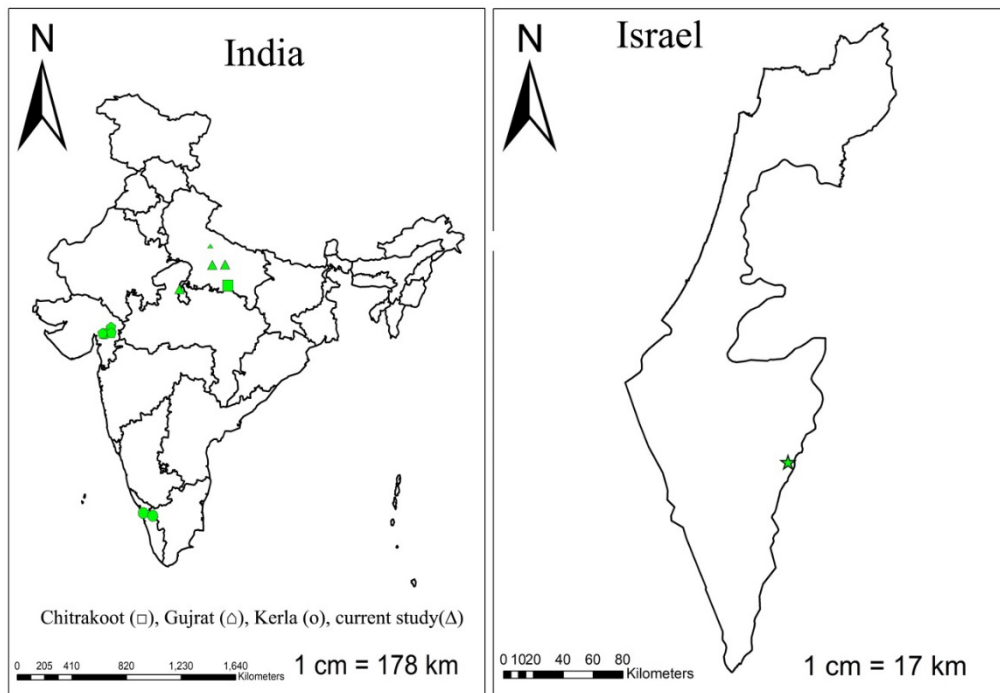


Figure 2. The echolocation calls of *R. hardwickii* recorded from various geographical regions. Right panel map shows location within India (Chitrakoot, Gujrat, Kerala) whereas, left panel indicates location in Israel.

Table 1. Morphological measurements of males and females *R. hardwickii* in millimetre (mm), unless otherwise mentioned. Values are given Mean ± SD.

Parameter	Male (n=27)	Female (n=14)	H value	P value
Body mass (g)	20.71 ± 2.95	19.86 ± 3.38	0.41	0.522
BH length	71.46 ± 3.69	71.12 ± 3.39	0.261	0.61
Head length	19.71 ± 4.33	23.05 ± 1.25	2.847	0.092
Tail length	58.37 ± 6.49	60.73 ± 6.34	1.557	0.212
Ear length	14.23 ± 1.44	13.96 ± 1.13	0.001	0.974
Ear width	8.96 ± 1.09	8.09 ± 1.11	3.031	0.082
Targus	5.90 ± 0.81	5.82 ± 0.39	0.39	0.532
Forearm length	58.83 ± 2.26	60.01 ± 1.62	0.126	0.723
5th Metacarpal	43.54 ± 1.53	42.60 ± 1.43	2.185	0.139
First phalanx	10.80 ± 0.59	10.85 ± 0.69	0.002	0.964
Second phalanx	9.52 ± 0.86	9.28 ± 0.42	1.155	0.282
4th Metacarpal	38.26 ± 1.67	36.66 ± 1.70	5.013	0.025
First phalanx	12.87 ± 0.67	13.32 ± 0.40	2.187	0.139
Second phalanx	10.55 ± 1.63	10.98 ± 0.13	0.032	0.858
3rd Metacarpal	44.05 ± 2.26	40.82 ± 1.65	5.43	0.2
First phalanx	8.76 ± 0.75	9.03 ± 1.32	0.98	0.754
Second phalanx	17.72 ± 1.06	18.10 ± 0.41	0.393	0.531
2nd Metacarpal	43.47 ± 2.26	42.08 ± 1.10	2.896	0.89
Thumb length	7.00 ± 0.49	6.46 ± 0.59	7.967	0.005
Hind arm	30.19 ± 1.75	29.76 ± 1.11	1.287	0.257
Foot	7.47 ± 3.10	8.30 ± 3.74	0.586	0.444
Body width	28.85 ± 7.93	25.83 ± 10.17	1.001	0.317
Wing span (cm)	20.51 ± 6.18	29.88 ± 0.87	3.509	0.061

Table 2. Wing morphology of male and female *Rhinopoma hardwickii*. Values are given Mean ± SD.

Wing characteristics	Male (n = 27)	Female (n = 14)	H	P
Arm Wing Length	10.23 ± 0.34	10.20 ± 0.42	0.077	0.782
Arm Wing Area	58.35 ± 6.63	58.96 ± 3.59	0.049	0.826
Hand Wing Length	6.90 ± 0.33	6.99 ± 0.34	0.292	0.589
Hand Wing Area	25.22 ± 1.84	25.80 ± 2.29	0.291	0.590
Wing Area	1.67 ± 0.14	1.70 ± 0.11	0.206	0.650
Tip Length Ratio	0.68 ± 0.04	0.69 ± 0.04	0.219	0.640
Tip Aspect Ratio	0.44 ± 0.06	0.44 ± 0.03	0.027	0.869
Tip shape index	1.56 ± 0.17	1.57 ± 0.09	0.170	0.680
Wing Loading	12.27 ± 1.83	11.23 ± 1.82	2.676	0.102
Relative Wing loading	8.83 ± 2.54	7.60 ± 2.51	2.287	0.130
Aspect Ratio	7.06 ± 0.47	6.99 ± 0.39	0.076	0.783

H= Kruskal – Wallis H test

Table 3. Echolocation calls of *R. hardwickii* in three different habitats. Values were presented in Mean ± SD.

Echolocation	Captive (n =94)	Field (n =35)	Roost (n = 38)	H*	p – value
Start Freq.	31.04 ± 2.19	26.81 ± 1.53	29.39 ± 0.97	80.165	0.001
End Freq.	34.77 ± 1.71	30.83 ± 1.21	36.12 ± 1.34	85.403	0.001
Peak Freq.	32.83 ± 2.13	30.04 ± 0.81	32.76 ± 0.87	101.791	0.001
I.P.I. (ms.)	38.75 ± 7.59	112.09 ± 49.76	24.00 ± 16.56	64.401	0.001
Bandwidth	3.73 ± 1.71	4.02 ± 1.08	6.72 ± 1.18	81.245	0.001

Freq. = Frequency, all frequency in KHz, H = Value of Kruskal Wallis H – test

Table 4. Comparison of wing morphology and Echolocation of *Rhinopoma hardwickii* bats with other studies, frequencies were given in kHz, pulse duration and pulse interval were given in millisecond (ms.). Values are given in Mean \pm SD

Parameters/ Studies	Habersetzer, 1981 (n =)	Hackett et al., 2016 (*n =257/3)	Srinivasulu & Srinivasulu, 2017 (*n=1/12)	Srinivasulu, Chaturvedi et al. 2018 (*NM)	Shah and Srinivasulu, 2020 (*n=58)	Present study (*n = /167)	
Echolocation calls	Peak Frequency	30	33.99 \pm 1.13	32.48 \pm 0.75	32	31.32 \pm 0.93	33.23 \pm 2.38
	Start frequency	32.50	35.85 \pm 1.81	37.05 \pm 0.46	-	34.52 \pm 2.40	32.15 \pm 2.84
	End frequency	35.0	32.72 \pm 1.39	26.66 \pm 0.94	-	28.32 \pm 3.58	30.78 \pm 3.04
	Pulse duration		8.57 \pm 1.28	2.21 \pm 0.44	-	3.86 \pm 1.48	
	Pulse interval		-	-	-		39.92 \pm 46.86
	Band width						4.47 \pm 1.78
Wing morphology (n= 41)	Wing span (cm)	-	-	-	-	-	34.31 \pm 0.96
	Wing area ($\times 10^{-3}$ m ²)	-	-	-	-	-	1.68 \pm 0.13
	Aspect ratio	-	-	-	-	-	7.04 \pm 0.44
	Wing loading (N/m ²)	-	-	-	-	-	11.92 \pm 1.87
	Hand-wing area ($\times 10^{-3}$ m ²)	-	-	-	-	-	25.42 \pm 1.99
	Arm-wing area ($\times 10^{-3}$ m ²)	-	-	-	-	-	58.56 \pm 5.73
	Tip length ratio	-	-	-	-	-	0.68 \pm 0.04
	Tip area ratio	-	-	-	-	-	0.44 \pm 0.05
	Tip shape index	-	-	-	-	-	1.57 \pm 0.15

6. Acknowledgements

We are greatly thankful to the Archeological survey of India (ASI) for the permitting us in the monuments to collect the samples, vide letter no. 16/23/2019/-Monuments 9970. This work was supported by Science Engineering Research Board, New Delhi [EEQ/ 2018/000104]. We thank the Dr. Rahul Shukla for proofreading the manuscript.

7. References

- Amichai E., Blumrosen G and Yovel Y. (2015) Calling louder and longer: how bats use biosonar under severe acoustic interference from other bats. *Proceedings of the Royal Society B* 282: 1-10. <https://doi.org/10.1098/rspb.2015.2064>
- Barclay R M R., Fullard J H and Jacobs D S. (1999) Variation in the echolocation calls of the hoary bat (*Lasiurus cinereus*): influence of body size, habitat structure, and geographic location. *Canadian Journal of Zoology* 77: 530–534. DOI: 10.1139/cjz-77-4-530
- Bartonicka T and Rehak Z. (2005) Variability in echolocation calls of *Pipistrellus pygmaeus* (Chiroptera: Vespertilionidae) during search flight in different habitats, *Acta Theriologica* 50 (2): 145–160. DOI: 10.1007/BF03194478
- Bates P J J and Harrison D L. (1997) Bats of the Indian subcontinent. *Harrison zoological museum, Publications, Sevenoaks* 258pp. <https://doi.org/10.2307/1383036>
- Bates P., Bumrungsri S., Francis C., Csorba G., Walston J., Molur S and Srinivasulu C. (2008) *Arielulus circumdatus*. The IUCN Red List of Threatened Species e.T41534A10493431. <https://dx.doi.org/10.2305/IUCN.UK.2008.RLTS.T41534A10493431.en>.
- Benda P., Andreas V H., Reiter M A and Uhrin M. (2004) Two new species of bats (Chiroptera) for the fauna of Libya: *Rhinopoma hardwickii* and *Pipistrellus rueppellii*, *MYOTIS* 41-42: 109-124.
- Berger-tal O., Berger-tal R., Korine C., Holderied M W and Fenton M B. (2008) Echolocation calls produced by *Kuhl's pipistrelles* in different flight situations, *Journal of Zoology* 274: 59–64. DOI: 10.1111/j.1469-7998.2007.00357.x
- Broders H G., Findlay C S and Zheng L. (2004) Effects of clutter on echolocation call structure of *Myotis septentrionalis* and *M. lucifugus*, *Journal of Mammalogy* 85: 273–281. <https://doi.org/10.1644/BWG-102>
- Brunnich M T. (1782) *Dyrenes Histoieog Dyre-Samlingenudi Universitets Natur-Theater*. Nicolaus Moller, *Copenhagen* 4: 1-76.
- Chiu C., Xian W and Moss C F. (2009) Adaptive echolocation behavior in bats for the analysis of auditory scenes, *Journal of Experimental Biology* 212: 1392–1404. DOI: 10.1242/jeb.027045
- Duffy A M., Lumsden L F., Caddle C R., Chick R R and Newell G R. (2000) The efficacy of Anabat ultrasonic detectors and harp traps for surveying microchiropterans in south-eastern Australia, *Acta Chiropterologica* 2(2): 127–144.
- Freeman P W. (1981) A multivariate study of the family (Molossidae Mammalia, Chiroptera): Morphology, ecology, evolution. *Fieldiana Zoology, New Series* 7: 1–173. <https://doi.org/10.5962/bhl.title.3128>
- Fullard J., Koehler C., Surlykke A. and McKenzie N. (1991) Echolocation ecology and flight morphology of insectivorous bats (Chiroptera) in south-Western Australia. *Australian Journal of Zoology*, 39(4): 427 – 438. <https://doi.org/10.1071/zo9910427>
- Gannon W L., O'Farrell M J., Corben C. and Bedrick E J. (2004) Call character lexicon and analysis of field recordings of bat echolocation calls. Pp. 478–484, in *Echo - location in bats and dolphins* (eds. J.A. Thomas, C.F. Moss, and M. Vater). The University of Chicago Press, Chicago, IL, USA 604 pp.
- Geoffroy Saint-Hilaire E. (1818) Description de l'Égypt. Historire naturelle. Description des mammiferes qui se trouvent en, *Egypte* 2: 99- 135.
- Gillam E H and McCracken G F. (2007) Variability in the echolocation of *Tadarida brasiliensis*: effects of geography and local acoustic environment, *Animal Behaviour* 74: 277–286. DOI:10.1016/j.anbehav.2006.12.006
- Gray J E. (1831) Description of some new genera and species of bats, *The Zoological Miscellany* 1: 37-38.
- Griffin D R., Webster F A and Michael C R. (1960) The echolocation of flying insects by bats, *Animal Behaviour* 8 (3-4): 141–154. [https://doi.org/10.1016/0003-3472\(60\)90022-1](https://doi.org/10.1016/0003-3472(60)90022-1)
- Habersetzer J. (1981) Adaptive echolocation sounds in the bat *Rhinopoma hardwicki*, *Journal of Comparative Physiology* 144: 559–566. <https://doi.org/10.1007/BF01326841>
- Habersetzer J. (1986) Vergleichende fl?gelmorphologische Untersuchungen an einer Fledermausgesellschaft in Madurai. In *Biona Reporte, Bat flight – Fledermausflug*, ed. W. Nachtigall, 75-106. Stuttgart: Gustav Fischer.
- Hackett T D., Holderied M W and Korine C. (2016) Echolocation call description of 15 species of Middle-Eastern desert dwelling insectivorous bats, *Bioacoustics* 26: 217–235. <https://doi.org/10.1080/09524622.2016.1247386>

- Harrison D L. (1964) The mammals of Arabia. Ernest Benn Ltd., London 1:1-192
- Hill J E. (1977) A review of the Rhinopomatidae (Mammalia: Chiroptera), *Bulletin of the British Museum (Natural History) Zoology* 32 (2): 29-43.
- Hulva P. and Horacek I. (2002) *Craseonycteris thonglongyai* (Chiroptera: Craseonycteridae) is a rhinolophoid: Molecular evidence from cytochrome b. *Acta Chiropterologica* 4(2):107-120. doi: 10.3161/001.004.0201
- Jones G and Kokurewicz T. (1994) Sex and age variation in echolocation calls and flight morphology of Daubenton's bats *Myotis daubentonii*, *Mammalia* 58: 41–50. <https://doi.org/10.1515/mamm.1994.58.1.41>.
- Jones G and Teeling E C. (2006) The evolution of echolocation in bats, *Trends in Ecology and Evolution* 21(3): 149–156. doi:10.1016/j.tree.2006.01.001
- Kalko E K V and Schnitzler H U. (1993) Plasticity in echolocation signals of European pipistrelle bats in search flight: implications for habitat use and prey detection. *Behavioral Ecology and Sociobiology* 33: 415–428. <https://doi.org/10.1007/BF00170257>
- Kingdon J. (1974) East African Mammals: An Atlas of Evolution in Africa vol. II, part A (Insectivores and Bats). *University of Chicago Press*.
- Law B S., Reinhold L and Pennay M. (2002) Geographic variation in the echolocation calls of *Vespadelus* spp. (Vespertilionidae) from New South Wales and Queensland, Australia. *Acta Chiropterologica* 4: 201–215. <https://doi.org/10.3161/001.004.0208>
- Marinello M M and Bernard E. (2014) Wing morphology of Neotropical bats: a quantitative and qualitative analysis with implications for habitat use, *Canadian Journal of Zoology* 92 (2): 141–147. <https://doi.org/10.1139/cjz-2013-0127>
- Masters W M., Raver K A S and Kazial K A. (1995) Sonar signals of big brown bats, *Eptesicus fuscus*, contain information about individual identity, age and family affiliation, *Animal Behaviour* 50 (5): 1243–1260. [https://doi.org/10.1016/0003-3472\(95\)80041-7](https://doi.org/10.1016/0003-3472(95)80041-7)
- Murray K L., Britzke E R and Robinsons L W. (2001) Variation in search phase call of bats, *Journal of Mammalogy* 82(3): 728 – 737. <https://doi.org/10.1644/1545-1542>
- Neuweiler G. (1984) Foraging, echolocation and audition in bats, *Naturwissenschaften* 71: 446-455. <https://doi.org/10.1007/BF00455897>
- Norberg U M and Rayner J M V. (1987) Ecological morphology and Flight in bats (Mammalia; Chiroptera): wing adaptations, Flight performance, foraging strategy and echolocation, *Philosophical Transactions of the Royal Society B: Biological Sciences* 316 (1179): 335-427. DOI: 10.1098/rstb.1987.0030
- Norberg U M L., Brooke A P And Trehwella W J. (2000) Soaring and non-soaring bats of the family Pteropodidae (flying foxes, *Pteropus* spp.): wing morphology and flight performance, *The Journal of Experimental Biology* 203 (3): 651–664. <https://doi.org/10.1242/jeb.203.3.651>
- O'farrell M J., Corben C and Gannon W L. (2000) Geographic variation in the echolocation calls of the hoary bat (*Lasiurus cinereus*), *Acta Chiropterologica* 2 (2): 185–195.
- Obrist M K. (1995) Flexible bat echolocation: the influence of individual, habitat and conspecifics on sonar signal design, *Behavioral Ecology and Sociobiology* 36 (3): 207–219. DOI: 10.1007/BF00177798
- Pennycuik C J. (1989) Bird Flight Performance: a Practical Calculation Manual. Oxford: *Oxford University Press* 153pp.
- Prakash I. (1961) Die Säugetiere der Rajasthan—Wüste in Indien. *Nature* 91:443-448.
- Purohit A K and Senacha K R. (2004) Distribution of bats in and around Jaisalmer of the Great Indian Desert, India, *Vespertilio* 8: 99-104.
- Ratcliffe J M., Hofstede H M T., Avila-Flores R., Fenton M B., McCracken G F., Biscardi S., Blasko J., Gillam E., Orprecio J and Spanjer G. (2004) Conspecifics influence call design in the Brazilian free-tailed bat, *Tadarida brasiliensis*, *Canadian Journal of Zoology* 82(6):966–971. <https://doi.org/10.1139/cjz-2017-0284>
- Reinhold L., Herr A., Lumsden L., Reardon T., Corben C., Law B., Prevett P., Ford G., Conole L., Kutt A., Milne D and Hoye G. (2001) Geographic variation in the echolocation calls of Gould's wattled bat *Chalinolobus gouldii*, *Australian Zoologist* 31 (4): 618–624. <https://doi.org/10.7882/AZ.2001.008>
- Shah T A and Srinivasulu C. (2020) Echolocation calls of some bats of Gujarat, India, *Mammalia* 84 (5): 1-10. <https://doi.org/10.1515/mammalia-2019-0015>
- Sikes R S., William L G and the Animal Care and Use Committee of the American Society of Mammalogists. (2011) Guidelines of the American Society of Mammalogists for the use of wild mammals in research, *Journal of Mammalogy* 92(1): 235-253. DOI: 10.1644/10-MAMM-F-355.1

- Simmons J A and Stein R A. (1980) Acoustic imaging in bat sonar: echolocation signals and the evolution of echolocation, *Journal of Comparative Physiology* 135:61-84. <https://doi.org/10.1007/BF00660182>
- Singh S., Misra P K and Elangovan V. (2021) Distribution of Sheath-Tailed bats (Emballonuridae) in Bundelkhand region of Uttar Pradesh, *Journal of Advanced Zoology* 42 (2): 176–185. <https://doi.org/10.17762/jaz.v42i02.52>
- Smith J D and Starrett A. (1979) Morphometric analysis of chiropteran wings. In *Biology of bats of the New World family Phyllostomidae*, ed. R. J. Baker, J. K. Jones, Jr., and D. C. Carter. 427-437. Special Publication Museum Texas Tech University.
- Springer M S., Teeling E C., Madsen O., Stanhope M J., and de Jong, W W. (2001) Integrated fossil and molecular data reconstruct bat echolocation. *Proceedings of National Academy of Science U. S. A.* 98: 6241–6246. doi:10.1073/pnas.111551998
- Srinivasulu B and Srinivasulu C. (2017) A first record of three hitherto unreported species of bats from Kerala, India with a note on *Myotis peytoni* (Mammalia: Chiroptera: Vespertilionidae), *Journal of Threatened Taxa* 9 (5): 10216–10222. DOI: 10.11609/jott.3324.9.5.10216-10222
- Teeling E C., Madsen O., Van Den Bussche R A., de Jong W W., Stanhope M J. and Springer, M S. (2002) Microbat paraphyly and the convergent evolution of a key innovation in Old World rhinolophid microbats. *Proceedings of National Academy of Science U. S. A.* 99: 1431 – 1436. doi.org/10.1073/pnas.02247719
- Thomas D W., Bell G P and Fenton M B. (1987) Variation in echolocation call frequencies recorded from North American vespertilionid bats: a cautionary note, *Journal of Mammalogy* 68 (4): 842–847. <https://doi.org/10.2307/1381562>
- Thomas O. (1903) On the species of the genus *Rhinopoma*, *Annals and Magazine of Natural History* 11(7): 496-499.
- Ulanovsky N., Fenton M B., Tsoar A and Korine C. (2004) Dynamics of jamming avoidance in echolocating bats, *Proceedings of the Royal Society B: Biological Sciences* 271 (1547): 1467–1475. doi:10.1098/rspb.2004.2750
- Van Cakenberghe V., De Vree F. (1994) A revision of the Rhinopomatidae Dobson 1872 with the description of a new subspecies (Mammalia: Chiroptera), *Senckenbergiana Biologica* 73 (1-2):1-24.
- Van Den Bussche R A. and Hooper S R. (2004) Phylogenetic relationships among recent chiropteran families and the importance of choosing appropriate out-group taxa. *J. Mammal.* 85: 321 – 330. doi.org/10.1644/1545-1542(2004)085<0321:PRARCF>2.0.CO;2

Photocatalytic Degradation of Ethylene Bis-Dithiocarbamate Fungicide from Wastewater Using Cerium Oxide Nanoparticles under Natural Solar Irradiation

Mahadi Danjuma Sani^{1ac*}, Abbaraju V.D.N. Kumar^{2a} and Venugopal N.V.S.^{3b}

Abstract: This study developed a suitable method for the degradation of ethylene bis-dithiocarbamate pesticide mancozeb in wastewater and agricultural runoff using nanoceria as photocatalysts. The nanoceria or cerium oxide nanoparticles were synthesized using a simple coprecipitation method with cerium nitrate hexahydrate ($\text{Ce}(\text{NO}_3)_3 \cdot 6\text{H}_2\text{O}$) and Potassium carbonate (K_2CO_3) as a precursor and precipitating agent respectively. The synthesized powder particle was further ascertained through characterization using Scanning Electron Microscopy SEM for surface morphology, Fourier Transform Infrared Spectroscopy FTIR for the determination of the functional groups, Powder X-ray diffraction PXRD for crystal structure, phase and crystallite size and Energy Dispersive X-ray Spectroscopy EDAX for elemental composition of the synthesized nanoceria. It was revealed that the nanoparticle was successfully synthesized with a crystallite size of 27 nm. Photocatalytic degradation of mancozeb pesticide using the synthesized NPs was determined in batches with optimization of certain parameters including; the initial concentration of pesticide, quantity of the photocatalyst, irradiation time, calcination temperature and UV index. Nanoceria was found to degrade more than 62% of the initial concentration of mancozeb in 2 hours. Nanoceria usually acts as an active sorbent in the destruction of pesticides in wastewater and as such, its application on the degradation of mancozeb is crucial and significant. This method can be suitable for agricultural runoff and synthetic chemical pesticides effluent with proper optimisation.

Keywords: Synthesis, Nanoceria, mancozeb, wastewater, and photocatalytic degradation.

1. Introduction

Pesticides are part of the major water pollutants or contaminants throughout the globe. Synthetic pesticides are playing a critical role in food production and global sustainability. These chemicals have a broad range of applications, including controlling weeds and insect infestations in agricultural fields, and managing pests and diseases-carrying organisms like mosquitoes, ticks, rats, and mice in both residential, commercial and public areas (Kim et al., 2016). However, because pesticides do not target a specific species, there are concerns about the potential environmental hazard associated with exposure, through different routes, such as the presence of pesticide residues in water and food (Kim, et al. 2016; Chang 2018; Vijgen et al. 2018). Moreover, studies have revealed that pesticide residues were found to be present in the blood and living system (Bonvoisin et al., 2020; Chang, 2018; El-Alfy et al., 2019; Nicolopoulou-Stamati & , Sotirios Maipas, Chrysanthi Kotampasi, 2016; Walker et al., 2022; Zhao et al., 2020).

Mancozeb MCZ pesticide is one of the most widely used

fungicides to protect fruits, crops and vegetables (Bao et al., 2022). The cost and effectiveness of this fungicide made it accessible to farmers all over the world. Studies have shown that mancozeb accounts for about 20% of the global fungicide market (Bao et al., 2022). In terms of its chemical composition, mancozeb is a combination of polymerized complexes of ethylene-bis-dithiocarbamate with both Manganese and Zinc in a 1:1 ratio. When consumed, mancozeb is metabolized in the body and produces a primary urine metabolite called ethylene-bis-thiourea (ETU) in a ratio of approximately 1:2 (Mandić-Rajčević et al., 2020; Quds et al., 2022; Saraiva et al., 2021). Furthermore, mancozeb has been associated with various health hazards due to its continued widespread use among farmers and its chemical nature.

In a research conducted by (Morales-Ovalles et al., 2018), examinations of tissue and cell structures of a particular organism revealed that there was a rise in cell death, inflammation in the nervous system, and loss of the protective coating around nerve cells (demyelination) as a result of the pesticide. These findings indicate that mancozeb caused harmful effects on cells responsible for producing hormones in the hypothalamus through induced cytotoxicity in a male mouse. Analysis of the tissue structure of mice exposed to MCZ by (Bao et al., 2022) indicated that there was harm done to the structure of their ovaries and that there was an increase in the process of cell death known as apoptosis. These findings suggest that MCZ can

Authors information:

^aDepartment of Environmental Science, GITAM School of Science, GITAM (Deemed to be University), Visakhapatnam, A.P. INDIA. Email: mahdi.d@fur.edu.ng¹; vabbaraj@gitam.edu²

^bDepartment of Chemistry, GITAM School of Science, GITAM (Deemed to be University), Visakhapatnam, A.P. INDIA. Email: vnutulap@gitam.edu³

^cDepartment of Environmental Science, Federal University Dutse, Jigawa State, NIGERIA. Email: mahdi.d@fur.edu.ng¹

*Corresponding Author: mahdi.d@fur.edu.ng

Received: July 26, 2023

Accepted: November 29, 2023

Published: December 31, 2024

interfere with the normal functioning of the mitochondrial respiratory chain, leading to a decoupling of oxidative phosphorylation and the production of oxidative stress, ultimately resulting in injury to the ovaries and cell death in mice

As such, it is crucial to come up with means to deter this menace of water pollution by pesticides. Researchers and scientists took several measures throughout the globe to come up with suitable alternatives to pesticides, suitable, effective and cheap clean-up or treatment methods and awareness. Several conventional measures for wastewater treatment that include; physical and chemical methods have been in use with issues at one point or another. The realization and validation of particle size as one of the major factors that influence the physicochemical properties of a material (Keerthana et al. 2022; Singh et al. 2022), nanomaterials have recently gotten more attention from researchers and industries to harness their capabilities in today's world.

A semiconductor cerium oxide is getting the attention of scientists and researchers due to its unique nature, properties and abundance. Cerium oxide CeO_2 nanoparticles are becoming significant in our societies and are in use at different levels of civilization. Studies have shown that CeO_2 nanoparticles (NPs) have gained significant consideration from researchers in recent times due to their distinctive structure and attractive properties, making them a highly promising material for a variety of applications (Muduli and Ranjan 2022; Muthuvel et al. 2020). It possesses distinctive chemical and thermal stability, high conductivity, reliable oxygen storage capacity, the ability to absorb UV light, catalytic activity and a broad energy band gap of around 3.19 eV (Eka Putri et al., 2021). These nanoparticles can be utilized in various industrial products such as photocatalysts, sunscreens, polishing agents, and sensor applications, among others (Muduli and Ranjan 2022; Pradeepa and Nayaka 2022; Muthuvel et al. 2020).

Cerium oxide (CeO_2) is a type of semiconductor material that exhibits n-type conductivity. This material possesses unique characteristics, such as the ability to catalyze both metal oxidation and reduction reactions through electronic transitions between Ce^{3+} and Ce^{4+} (Kumaraguru et al., 2022). It also has high ionic mobility and the capability to store and release oxygen (Kumaraguru et al. 2022; Shetty et al. 2022; Muduli and Ranjan 2022). Studies involving applications of cerium oxide nanoparticles are reported in recent literature which include; (Lin et al., 2021) for anti-oxidative and anti-reduction regarding ROS, (Mohamed, 2021) involving acute oral administration of the particle for suppressing lead acetate genotoxicity, (Samai & Bhattacharya, 2018) enhanced photocatalytic activity in wastewater treatment for dye degradation, (Pradeepa & Nayaka, 2022) electrochemical investigation of pantoprazole, (Eka Putri et al., 2021) high anti-microbial activity, (Muthuvel et al., 2020) photocatalytic degradation of methyl orange dye and anti-microbial activity, (Miri et al., 2021) for photocatalytic degradation of organic pollutants and (Kashyap et al., 2022) for effective removal of uranium from aqueous solution.

Nanoceria or cerium oxide nanoparticle is a great sorbent or

catalyst for the degradation and destruction of persistent environmental pollutants. Despite its wide range of applications, the particles' utilisation for different chemical pesticides in wastewater is still lagging. More focus is given to its photocatalytic activity in the degradation of dye and organophosphate pesticides, especially parathion. As such, in this study, we aim to explore the intrinsic capacity of nanoceria synthesized via the coprecipitation method for the degradation of a carbamate pesticide Mancozeb.

2. Materials and Methods

Chemicals

The chemicals used were of analytical reagent grade and were used with no further purification. Cerium nitrate hexahydrate ($\text{Ce}(\text{NO}_3)_3 \cdot 6\text{H}_2\text{O}$), Potassium carbonate (K_2CO_3), acetonitrile HPLC grade and ethanol were all purchased from Merck company (India), Mumbai. Dithiocarbamate pesticide/Mancozeb 75 % wp was obtained from the farmer's market in Visakhapatnam, Andhra Pradesh state of India. Millipore water/Deionized water was used throughout the experiments.

Synthesis of Cerium Oxide NPs

Cerium oxide NPs were synthesized using a simple coprecipitation method as adopted from the work of (Farahmandjou et al., 2016) and reported in our previous work (Sani et al., 2023). Specifically, two separate solutions of 0.02 M cerium III nitrate and 0.03 M potassium carbonate were carefully prepared by dissolving 2.17 g and 1.036 g respectively in 2 separate 250 ml volumetric flasks. 50 ml of cerium III nitrate was weighed in a conical flask and placed under a burette containing 20 ml of potassium carbonate on a magnetic stirrer. Drops of potassium carbonate were added into the conical flask on the magnetic stirrer through the wall of the container with constant stirring. The pH of the system was maintained at 6 by adding millipore water into the solution. After constant stirring for 3 hours, a white precipitate of cerium III carbonate was formed which was further dried in a hot air oven at 65 °C for 2 hours. The particles were later dried to room temperature and aged at 220 °C for 2.5 hours which gives brownish particles of nanoceria. The particles were later calcinated at 600 °C in a muffle furnace for 3 hours to obtain the pure cerium oxide nanoparticles.

The whole procedure was repeated multiple times until the required quantity of the nanoparticles were obtained for further analysis.

Characterization

The structural characterization processes were conducted to ascertain the formation of cerium oxide nanoparticles through the above-mentioned method. Scanning Electron Microscopy SEM was employed for surface analysis/morphology analysis using SEM-EDAX Jeol 6390 LA/OXFORD XMXN with accelerating voltage of 0.5 to 30 kv, magnification of 300,000 times and tungsten filament. Elemental analysis was conducted by Energy Dispersive X-Ray Spectroscopy EDAX using the same facility with

an EDAX resolution of 136 eV and detector area of 30 mm².

The particles' crystal structure and crystallite size were determined by powder X-Ray Diffraction PXRD Brucker D8 advance. The scan type and mode are coupled two theta/theta and continuous scan respectively. The scanning begins at 10.000° and ends at 79.994° at an interval of 0.020° and a temperature of 25 °C/room temperature. Fourier transform Infrared spectroscopy was employed for spectral analysis of the functional groups present. It was achieved using FTIR spectrophotometer Nicolet iS50 with IR source, DTGS KBr detector and KBr beam splitter. A total number of 32 sample scans were conducted at the collection length of 47.3 seconds with a resolution of 4.000. The FTIR range for the analysis was 500-4000 cm⁻¹ wavenumber.

Preparation of Different Concentrations of Pesticides

Three standard concentrations of the mancozeb 75% wp were prepared by dissolving certain weights of the powder mancozeb in millipore water to produce 3 different concentrations of 100 ppm, 50 ppm and 10 ppm. The standards were prepared by dissolving 25 mg, 12.5 mg and 2.5 mg of the 75% wp mancozeb for 100 ppm, 50 ppm and 10 ppm respectively into 250 ml volumetric flasks. Each prepared pesticide solution was immediately used for sample preparation and control.

2.5 Degradation Experiments

The photocatalytic degradation and removal of mancozeb pesticide from wastewater was carefully conducted from 13th December 2022 to 10th March 2023 at GITAM University, Visakhapatnam, Andhra Pradesh, India. For each batch of the experiment, temperature, UV index, Humidity and atmospheric pressure were noted and recorded to understand the suitable atmospheric conditions for better degradation.

100 ml of each of the concentrations of the pesticides were exposed to 2 quantities of nanoceria 50 mg and 10 mg which were carefully mixed using a magnetic stirrer under dark conditions and a control setup with no nanoceria. Before exposure to natural solar irradiation, the samples were kept in the dark for 30 minutes to achieve adsorption-desorption equilibrium. Table 1 below shows the different compositions of the samples.

Table 1. Sample composition

Sample name	Pesticide concentration (ppm)	initial	Quantity of nanoparticle Cerium oxide (mg)	of NPs
MCE-1	100		50	
MCE-2	100		10	
MCE-3	50		50	
MCE-4	50		10	
MCE-5	10		50	
MCE-6	10		10	

After exposure to natural solar irradiation, a certain amount of the sample was withdrawn after every 30 minutes from each of the samples which were wrapped in foil paper to avoid light penetration for further analysis. Subsequently, the samples were

collected/withdrawn for six consecutive rounds until 3 hours (0.5 hour, 1 hour, 1.5 hours, 2 hours, 2.5 hours and 3 hours), wrapped in foil paper and kept in the dark after recording the pH at each point. Furthermore, all the samples were centrifuged at 3500 rpm for 10 minutes and the supernatant liquids were separately collected for further analysis. The settled nanoparticles were collected and washed thrice with millipore water and ethanol and used for other rounds of the degradation experiment. The same procedure was applied for the control with no photocatalyst.

Shimadzu 1800 UV spectrophotometer was used to determine the absorbance and concentration of each of the samples and control. The absorbance was recorded at the range of 200-400 nm wavelength whereas the initial and final concentrations of the pesticide were determined at λ_{max} wavelength of 240 nm. For each round of the concentration determination, a set of standards were carefully prepared using the serial dilution method to form a linear graph of the concentration and absorbance.

Moreover, three optimization parameters considered for this research were; the initial concentration of the pesticide, the amount of the photocatalyst/nanoparticle, and irradiation time. However, the calcination temperature of the nanoceria and environmental conditions of each experimental period were considered. Moreover, the environmental/atmospheric conditions were not controlled but only recorded, and additional runs of the experiment were conducted whenever there was a reasonable change in the temperature and UV index (three scales of UV index; 7 as high, 8, 9, and 10 as very high and 11, 12 as extreme). The reason for these choices is for feasibility in field application and other parameters may be difficult to control in the field.

The degradation efficiency was determined using the following formula;

$$\% \text{ degradation/degradation efficiency} = \frac{C_0 - C_f}{C_0} \times 100 \quad (1)$$

Where C₀ is the initial concentration of mancozeb pesticide and C_f is the final concentration of mancozeb pesticide.

3. Results and Discussion

Synthesized nanoceria

Cerium oxide nanoparticles were successfully synthesized using the above-mentioned method and the result of the synthesis is presented below.

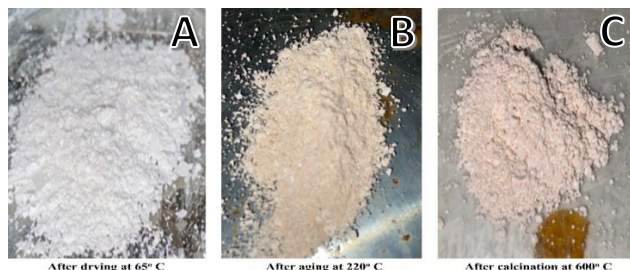


Figure 1. Synthesized nanoparticles at various points of synthesis

Figure 1 captioned A, B, and C shows the different stages of the nanoceria synthesis with A showing the drying of the cerium carbonate at 65 °C to B showing the ageing of the product at 220°C and C revealing the calcination at 600 °C to form the cerium oxide nanoparticles. The physical nature and colour of the synthesized NPs are in agreement with the findings of (Miri et al., 2020) where a brownish-yellow powder particle is formed.

Characterization

Scanning Electron Microscopy SEM

Scanning electron microscopy SEM which is a morphology analysis method was employed for the determination of the surface morphology of the NPs.

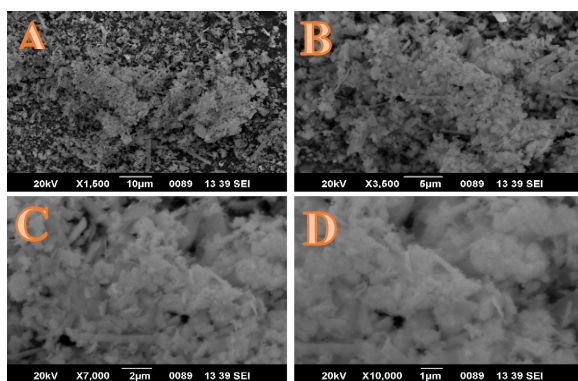


Figure 2. Scanning electron microscopy showing the morphology of the particles

From the images obtained from SEM Fig. 2, it can be observed that there exists some agglomeration at various points which may be due to various factors including temperature and solvents employed for washing the NPs. As revealed in C and D images with 1 and 2 µm resolution images, the morphology of the particles is somehow spherical with clusters of thin plate shapes of irregular sizes which may be a result of the agglomeration and annihilation process. Similar findings for the spherical surface morphology was reported by (Farahmandjou et al., 2016) and the thin plate shapes of irregular sizes were revealed by the work of (Janos et al., 2014).

Energy Dispersive X-Ray Spectroscopy EDAX

The elemental composition of the synthesized NPs was determined by the SEM-EDAX facility where the peaks for cerium and oxygen are obtained on the spectrum.

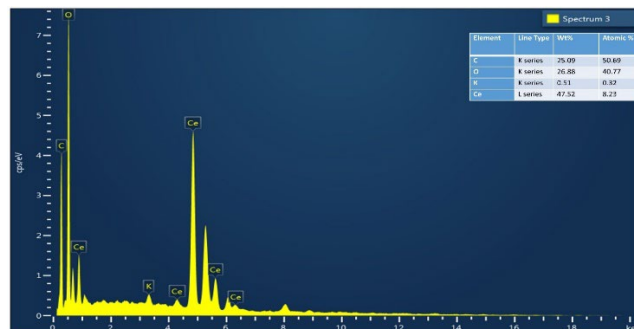


Figure 3. EDAX spectrum showing the elemental composition of the particles

The EDAX spectrum in Fig. 3 above revealed the elemental composition of the NPs with peaks for cerium, oxygen, carbon and potassium which confirms the existence of the elements in the synthesized NPs. The weight of cerium was found to be 47.52 % and that of oxygen found to be 26.88 %

3.2.3 Powder X-Ray Diffraction PXR

The crystal structure, phase and crystal size of the synthesized nanoceria were determined by PXR analysis which involves analyzing the diffraction pattern of scattered X-rays by the planes of CeO₂ NPs.

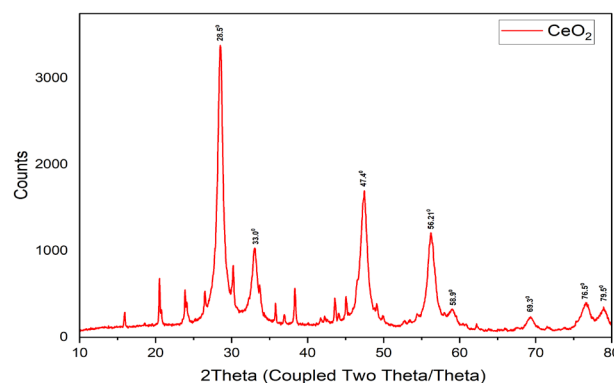


Figure 4. PXR spectrum showing the crystallography and particle size under the diffraction peaks

Figure 4 presents the XRD peaks of the annealed/calcined NPs at various points. The peaks exhibited at 28.507 °, 33.032 °, 47.446 °, 56.214 °, 58.994 °, 69.327 °, 76.598 ° and 79.5° correspond to (111), (200), (220), (311), (222), (400), (311) and (420) planes of cubic fluorite structure of nanoceria. The planes and diffracted angles are in agreement with the results of JCPDS (Farahmandjou et al., 2016; Janoš et al., 2022; Keerthana et al., 2022).

The crystallite size was computed from the XRD data using the Debye-Scherrer equation,

$$d = \frac{0.9 \lambda}{\beta \cos \theta} \quad (2)$$

where; d is the crystallite size

λ is the wavelength of Cu $K\alpha$ radiation

β is the full-width at half maximum (FWHM) of the diffraction peak

θ is the diffraction angle

The crystallite size of the synthesized particle was found to be 27nm.

Fourier Transform Infrared Spectroscopy FTIR

Fourier transform Infrared spectroscopy FTIR was employed for the identification of the functional groups present which involves the detection of vibration bands of organic and inorganic species.

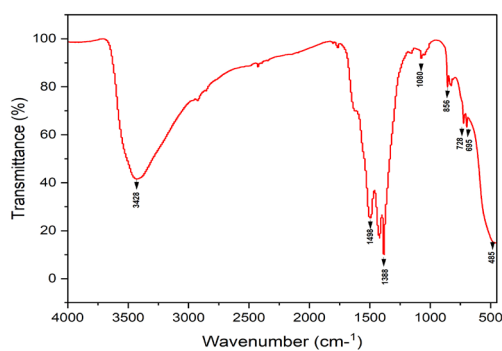


Figure 5. FTIR spectrum showing the functional groups present

The peaks as presented in Fig. 5 spectrum revealed the functional groups present in the sample, reagents and solvents used for the synthesis. The broad peak at 3428.19 cm^{-1} may be attributed to the $-\text{OH}$ stretching of water molecules used as a solvent for the synthesis process. The H-O-H bending vibration of water molecules may be responsible for the transmittance band

at 1498.06 cm^{-1} which is somewhat similar to the band reported by (Raees et al., 2022). However, the transmittance band below 500 cm^{-1} wavenumbers may be a result of the stretching vibration band of Ce-O (Janoš et al., 2022; Raees et al., 2022). However, in other studies, the vibration band of Ce-O was reported to be at exactly 500 cm^{-1} wavenumber (Farahmandjou et al., 2016).

Photocatalytic Degradation of Mancozeb

This experiment was conducted in batches under natural environmental conditions. For each sample setup, 3 different concentrations of the mancozeb pesticide were exposed to 2 quantities of the photocatalyst.

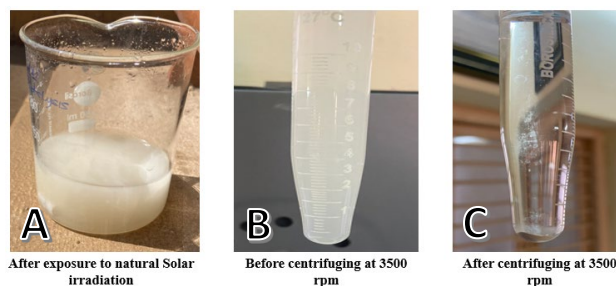


Figure 6. Photocatalytic degradation process

Figure 6 A, B, and C above shows some of the stages of the degradation experiment ranging from A, exposure of the sample and control to natural solar irradiation to B, collection/withdrawal of 10 ml of the sample at the 30-minute interval for centrifuging and C showing sample and settled nanocatalyst after centrifugation.

Uv Absorbance of The Samples at Different Time Intervals

All the samples have shown a great decrease in absorbance over time with little variation between 2-3 hours. By Beer's law which relates the concentration of a particular solution with light absorbance, the initial and final mancozeb residue and the reaction kinetics were determined.

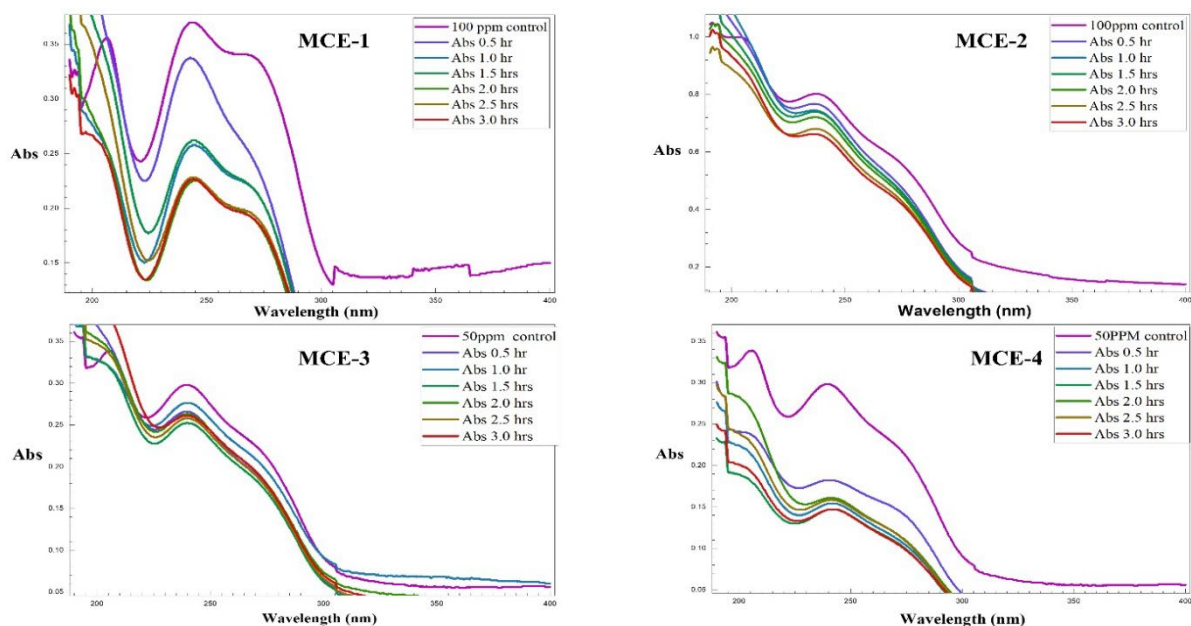


Figure 7. UV Absorbance spectrum for MCE-1, MCE-2, MCE-3 and MCE-4

From Figure 7, it can be observed that MCE-1 shows a sharp change in the absorbance of the solution which can be considered a strong indication of a decrease in the concentration of the pesticide. From the spectrum, it can also be observed that the control setup with no photocatalyst has the highest absorbance. Although, after 2 hours of the experiment, there was not much change in the UV absorbance with a few rounds showing a slight increase in the absorbance over time.

A similar scenario as MCE-1 above was observed in MCE-3 with a slight increase in absorbance at 2.5 and 3.0 hours. Although, the decrease in the absorbance for MCE-3 is quite lower when compared with MCE-1. A similar amount of the catalyst was used

for the samples.

However, MCE-4 with 10 mg photocatalyst has shown the best decrease in absorbance after several runs under natural environmental conditions. In this sample setup, there was a slight difference between 2 and 3 hours with 2.5 hours having greater absorbance as compared to the former. In general, there was a great decrease in the absorbance regarding this setup after several runs. Moreover, a lower amount of the NPs has shown greater action against the pesticide residue in comparison with the standard which may be attributed to the high light penetration.

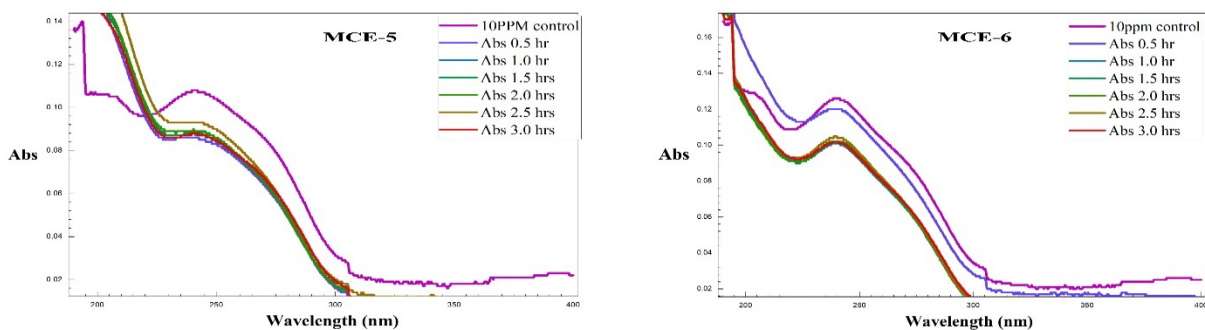


Figure 8. UV Absorbance spectrum for MCE-5 and MCE-6

Decreasing the concentration of mancozeb to 10 ppm shows yet another decrease in the absorbance with a similar pattern as compared to the setups with 50 mg photocatalyst as shown in Fig. 8. A similar scenario that happens to all the samples with 10 mg photocatalyst occurs in MCE-6. The absorbance pattern at 2.0, 2.5 and 3.0 hours of exposure to natural solar irradiation and 10 mg photocatalyst shows a close absorbance peak. This can be considered as an indication that the photocatalysis process may have reached a saturation level at between 2-3 hours of

irradiation time.

Determination of the Concentrations and Degradation Efficiency

The concentrations at time t of the MCZ residue were determined at a maximum wavelength absorbance of 240 nm λ_{max} using Shimadzu UV spectroscopy which was computed from the UV absorbance spectrum.

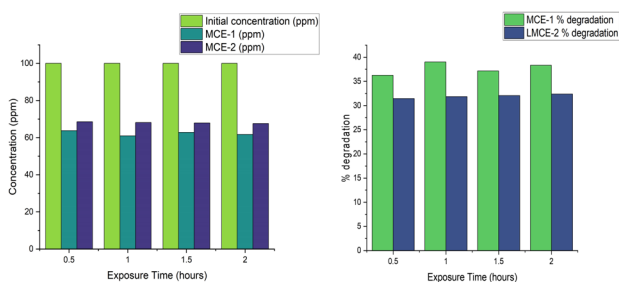


Figure 9. Initial and final concentration and percentage degradation of MCE-1 and MCE-2 over time

Concerning the first 2 sample setups; MCE-1 and MCE-2 containing 100 ppm mancozeb pesticide and 2 quantities of 50 mg and 10 mg NPs respectively, the initial and final concentrations were determined including that of control at different time intervals. From Fig. 9, it was observed that the initial concentration of each of the samples continued to decrease with an increase in the irradiation time. However, after 2 hours of exposure, no significant change was observed for the samples signifying that the process may have slowed down. For MCE-1, the initial concentration decreased by 36% at 0.5 hours exposure time to about 39.0% after an hour and stabilized at 38.3% degradation at 2 hours and above. However, there was a lower degradation or percentage degradation in regards to MCE-2 with 10 mg NPs quantity where only 31.5% degradation was observed at 0.5 hour irradiation time with a gradual increase in the degradation to about 32.4%. A similar scenario occurs here where the decrease in the concentration was slow after 2 hours. The activation of the photocatalytic reaction or process begins only when the surface of the photocatalyst is exposed to illumination. Consequently, the reaction zone, which corresponds to the top layer of the solution experiencing the highest intensity, becomes the most active area for pollutant degradation. However, when the initial pesticide concentration is high, it tends to excessively adhere to the surface of nanocatalysts thereby obstructing the necessary light energy penetration on the surface (Sraw et al., 2022). Moreover, the initial degradation efficiency was revealed to show a faster rate which subsequently stabilized with time and resulted in a small change in the concentration after 0.5 hour of irradiation.

Generally, for MCE-1 and MCE-2 samples setup, the percentage degradation was higher in the former which may be attributed to many factors including the quantity of the photocatalyst. When compared at each time interval, MCE-1 with 50 mg NPs was found to possess higher catalytic action than MCE-2 with 10 mg NPs. As can be observed in the figure, a 50 mg nanocatalyst was found to be more efficient towards the degradation of 100 ppm MCZ than a 10 mg nanocatalyst with the same MCZ concentration.

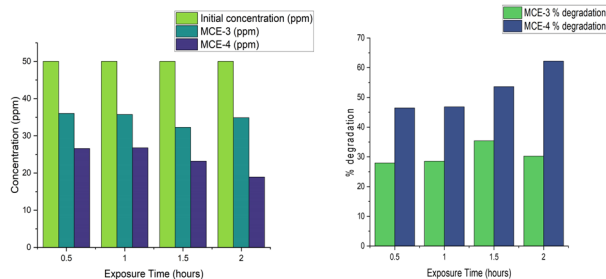


Figure 10. Initial and final concentration and percentage degradation of MCE-3 and MCE-4 over time

However, MCE-3 and MCE-4 samples setup were found to exhibit an entirely different pattern from MCE-1 and MCE-2. From Fig. 10, it can be observed that the initial 50 ppm concentration of the pesticide has shown more degradation in MCE-4 with 10 mg NPs than in MCE-3 with 50 mg NPs. However, a similar pattern regarding exposure time applies to all. At 0.5 hour exposure time, only 27.9% was degraded which was further increased to about 35% at 1.5 hours and stabilized at 30.3% at 3 hours and above. It is crucial to note the broad difference in the degradation between MCE-3 and MCE-4. About 46.5% degradation occurs at 0.5 hour exposure which is greater than the 2 hours and above for MCE-3. Additionally, the degradation continues like this for all the experiments with regards to MCE-4 with a mean percentage degradation of about 62.2% at 2 hours exposure time.

MCE-4 with 10 mg NPs was found to possess a higher degradation capacity than the 50 mg in MCE-3. Therefore, the higher quantity of the NPs/photocatalyst may not be crucial at this concentration of 50 ppm mancozeb. It may also be inferred that lower concentrations like 50 ppm of this setup as compared to 100 ppm of the previous setup may have given more room for catalytic degradation.

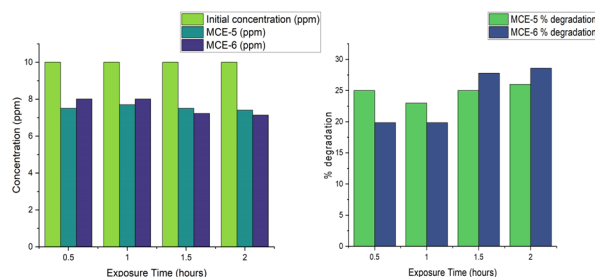


Figure 11. Initial and final concentration and percentage degradation of MCE-5 and MCE-6 over time

MCE-5 and MCE-6 sample setups follow similar patterns to MCE-3 and MCE-4. Although the degradation was found to be low after several runs as compared to the setup of the previous sample. The degradation pattern obtained may be used to infer that lower concentrations of MCZ do not require a higher quantity of the NPs/photocatalysts. Although, at 0.5 and 1-hour exposure, the degradation efficiency was higher for MCE-5 than MCE-6, after 1 hour the efficiency of the MCE-6 was higher with about 28.6%

degradation as can be observed in Fig 11.

The above table shows the percentage degradation between the 2 samples at various time intervals. MCE-6 with 10 ppm mancozeb pesticide and 10 mg NPs/photocatalyst was found to possess a lower initial degradation capacity as compared to MCE-5. However, from 1.5 hours, the degradation efficiency was higher for MCE-6 than that MCE-5.

Optimization

(Ederer et al., 2019) revealed that pesticides like other organic pollutants can degrade on the surface of the nanoceria with a reaction mechanism similar to a hydrolysis reaction happening in the solvent/water. Additionally, (Janoš et al., 2022) reported that hydroxyls play an important role in the degradation of organophosphate pesticides in the presence of nanoceria. Therefore, the solvent involved in these processes also plays a crucial role in the activity. Nanoceria was revealed to be a reactive sorbent in the destruction of parathion methyl together with other organophosphate but, the process was found to be greatly affected by the solvent involved (Janos et al., 2014). In this study, our focus was on the field application of the particle where wastewater will be the solvent during the degradation process.

Throughout the experiment, MCE-1 and MCE-2 were exposed to

the same experimental condition with only the quantity of the NPs different. The same applied to MCE-3 and MCE-4, and MCE-5 and MCE-6. The initial and final concentrations of the pesticide were determined at each level of the experiment after considering all the stated conditions. From the findings of this research, it was observed that the initial concentration of the pesticide, the exposure/irradiation time, the quantity of the nanoparticles/photocatalyst, calcination temperature, and atmospheric conditions that include temperature and UV index UVI play a significant role in the degradation process. Each of the aforementioned conditions was tested during the study.

There was a little change in the absorbance in the dark before exposure to natural solar irradiation, possibly due to adsorptions and desorption equilibrium. Also, the reuse of the NPs was tested after 3 rounds with little change in its activity. The light sensitivity of nanoceria was also tested during the experiment when comparing the dark reaction before exposure to solar irradiation and the light reaction after exposure. The photocatalytic activity of nanoceria was reported by multiple researchers (Janoš et al. 2022; Keerthana et al. 2022; El Desouky, Saadeldin, and El Zawawi 2022; Samai and Bhattacharya 2018; Muthuvel et al. 2020)

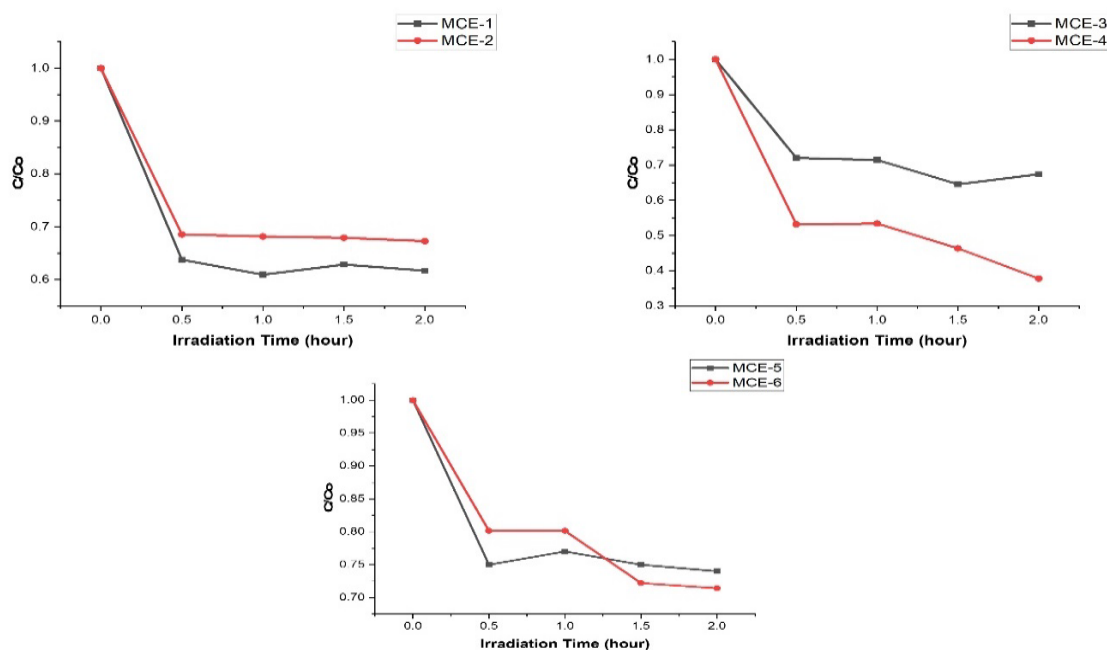


Figure 12. Photocatalytic degradation rate for 3 different concentrations of 100 ppm, 50 ppm and 10 ppm with 50 mg and 10 mg of the photocatalyst

Figure 12 revealed the degradation rate of the samples with all the setups showing very fast initial degradation activity followed by a subsequent slower activity to stabilization at a certain point. As shown in the degradation figures, the initial concentration of the pesticide may be said to affect the degradation process with 100 ppm concentration showing more affinity to degradation with 50 mg NPs while lower concentrations of 50 ppm and 10 ppm show a different trend with 10 mg NPs giving best results. As such, it may be inferred that with increasing the quantity of the NPs, only higher concentrations like 100ppm mancozeb show more

degradation which may be due to adsorption as a result of more NPs with more surface area-to-volume ratio and/or photocatalysis due to high concentration of the pesticide. However, lower concentrations like 50 ppm and 10 ppm show a different trend with more degradation with 10 mg NPs. This may be a result of many factors including more room for light penetration and photocatalysis that involves the split of holes and electrons between the valance and conduction band which attacks the pesticide from different angles in the reaction.

Throughout the experiment, the exposure time was found to be

an important factor where the more the exposure time the higher the degradation until 2 hours after which the process stabilized with few exceptions. Other studies with nanoceria have also revealed similar results regarding irradiation time (Keerthana et al. 2022; Samai and Bhattacharya 2018; Miri et al. 2021; Janos et al. 2014; Keerthana et al. 2021; Janoš et al. 2022). The calcination temperature was tested between the aged and calcinated products. It was observed that the calcinated product at 600 °C was found to be more active than the others which is in agreement with the findings of (Ederer et al., 2019; Janos et al., 2014) with calcination or annealed temperature of between 500 °C and 700 °C. For the atmospheric conditions, temperature and UV index considered were found to play an important role in the entire process. This was determined during the period of the experimentation. In the experiments conducted during the month of December when the temperature was moderate 26-28 °C in Visakhapatnam, Andhra Pradesh with a moderate to high UV index of 5-7, the rate of degradation was found to be low as compared to experiments in the month of February-march with a temperature of about 29-32 °C and very high UV index 8-10. As such, the degradation efficiency was higher with high UVI which may be a result of the UV portion light's capability to initiate the process of photocatalysis using semiconductor nanoparticles.

Overall, at optimal conditions considered for this research, 50 ppm mancozeb concentration, 10mg quantity of the nanoceria, 2 hours and a very high UV index of 8 to above, nanoceria was able to degrade about 62% of the pesticide under natural solar irradiation. However, with appropriate optimization and doping to reduce the band gap energy of the photocatalyst and improve light absorbance, more degradation may be achieved in a speculated time. The findings of this research are compatible with the photocatalysis of mancozeb nanoformulation using titanium oxide nanoparticles under natural solar irradiation reported by (Daqa et al., 2022). The sharp initial degradation rate followed by subsequent slow degradation rate over time was also reported.

4. Conclusion

The abundance of cerium as compared to other rare earth elements REE and lanthanides and the adsorptive reactivity of cerium oxide has made nanoceria to be significant particles for the destruction of contaminants like pesticides in wastewater and agricultural runoff. Nanoceria was successfully synthesized by a simple coprecipitation method which was further confirmed and ascertained by characterization through SEM, EDAX, XRD and FTIR. The XRD pattern has shown the crystallite shape and size of the synthesized to be cubic structure and 27 nm respectively. Although the SEM images were observed to contain agglomeration at various points, the clusters of thin plate shapes of the NPs were observed on the images. The FTIR analysis revealed a peak at around 500 cm⁻¹ wavenumber for cerium oxide functional with other peaks depicting the -OH group in the water molecule and other solvents. EDAX spectra of the synthesized nanoceria have revealed the elemental composition of the particles with high purity. The photocatalytic degradation of the mancozeb pesticide was conducted using the synthesized

nanoceria as a photocatalyst which was found to show great activity and efficiency towards the degradation of the mancozeb pesticide. It was observed that the degradation activity of nanoceria was affected by the initial concentration of the pesticide, quantity of photocatalyst, time, calcination temperature and UV index. Nanoceria usually acts as an active sorbent in the destruction of pesticides in wastewater. At optimal conditions considered during this study, nanoceria was found to degrade more than 62% of the initial concentration of the pesticide in 2 hours. Although, only the intrinsic capacity of the particle/nanoceria to act as a photocatalyst was considered with no doping or hole scavenger, the photocatalytic activity of the particle towards mancozeb pesticide is quite significant.

Moreover, it is crucial to note that further studies need to focus more on optimizing the conditions necessary for the photocatalytic activity of nanoceria which include but are not limited to, anneal/calcination temperature, the intensity of UV or source of energy, initial concentration of the contaminant, and nature and amount of dopant for better photocatalysis.

5. Acknowledgement

The authors acknowledge GITAM University, STIC Coaching Institute and Federal University Dutse. Also, the authors are thankful to the anonymous reviewers for their incredible work. Appreciation is extended to the DST analytical chemistry laboratory at GITAM University.

6. Declaration

The authors declare no known competing interests including financial and personal interests.

7. References

- Bao, J., Zhang, Y., Wen, R., Zhang, L., & Wang, X. (2022). Low level of mancozeb exposure affects ovary in mice. *Ecotoxicology and Environmental Safety*, 239, 113670. <https://doi.org/10.1016/J.ECOENV.2022.113670>
- Bonvoisin, T., Utyasheva, L., Knipe, D., Gunnell, D., & Eddleston, M. (2020). *Suicide by pesticide poisoning in India : a review of pesticide regulations and their impact on suicide trends*. 1–16.
- Chang, G. R. (2018). Persistent organochlorine pesticides in aquatic environments and fishes in Taiwan and their risk assessment. *Environmental Science and Pollution Research*, 25(8), 7699–7708. <https://doi.org/10.1007/S11356-017-1110-Z/TABLES/3>
- Daqa, W. M., Alshoabi, A., Ahmed, F., & Rao, T. N. (2022). Synthesis and Characterization of Nanoformulation of the Broad-Spectrum Enzyme Inhibitor Mancozeb by Polyethylene Glycol Capping and Its Dissipation Kinetics in Water Using TiO₂ Nanoparticles. *Processes*, 10(12). <https://doi.org/10.3390/pr10122733>
- Ederer, J., Štastn, M., DošekDošek, M., Henych ab, J., &

- JanošJanoš, P. (2019). *Mesoporous cerium oxide for fast degradation of aryl organophosphate flame retardant triphenyl phosphate*. <https://doi.org/10.1039/c9ra06575j>
- Eka Putri, G., Rilda, Y., Syukri, S., Labanni, A., & Arief, S. (2021). Highly antimicrobial activity of cerium oxide nanoparticles synthesized using *Moringa oleifera* leaf extract by a rapid green precipitation method. *Journal of Materials Research and Technology*, 15, 2355–2364. <https://doi.org/10.1016/J.JMRT.2021.09.075>
- El-Alfy, M. A., Hasballah, A. F., Abd El-Hamid, H. T., & El-Zeiny, A. M. (2019). Toxicity assessment of heavy metals and organochlorine pesticides in freshwater and marine environments, Rosetta area, Egypt using multiple approaches. *Sustainable Environment Research*, 29(1), 1–12. <https://doi.org/10.1186/S42834-019-0020-9/TABLES/6>
- El Desouky, F. G., Saadeldin, M. M., & El Zawawi, I. K. (2022). Synthesis and tuning the structure, morphological, optical, and photoluminescence properties of heterostructure cerium oxide and tin oxide nanocomposites. *Journal of Luminescence*, 241, 118450. <https://doi.org/10.1016/J.JLUMIN.2021.118450>
- Farahmandjou, M., Farahmandjou, M., Zarinkamar, M., & Firoozabadi, T. P. (2016). Synthesis of Cerium Oxide (CeO₂) nanoparticles using simple CO-precipitation method Article in Revista Mexicana de Fisica · Synthesis of Cerium Oxide (CeO₂) nanoparticles using simple CO-precipitation method. *Revista Mexicana de Física*, 62(October), 496–499. <https://www.researchgate.net/publication/308742876>
- Janoš, P., Ederer, J., Štastný, M., Tolasz, J., & Henych, J. (2022). Degradation of parathion methyl by reactive sorption on the cerium oxide surface: The effect of solvent on the degradation efficiency. *Arabian Journal of Chemistry*, 15(6). <https://doi.org/10.1016/j.arabjc.2022.103852>
- Janos, P., Kuran, P., Kormunda, M., Stengl, V., Grygar, T. M., Dosek, M., Stastny, M., Ederer, J., Pilarova, V., & Vrtoch, L. (2014). Cerium dioxide as a new reactive sorbent for fast degradation of parathion methyl and some other organophosphates. *Journal of Rare Earths*, 32(4), 360–370. [https://doi.org/10.1016/S1002-0721\(14\)60079-X](https://doi.org/10.1016/S1002-0721(14)60079-X)
- Kashyap, K., Khan, F., Verma, D. K., & Agrawal, S. (2022). Effective removal of uranium from aqueous solution by using cerium oxide nanoparticles derived from citrus limon peel extract. *Journal of Radioanalytical and Nuclear Chemistry*, 1–11. <https://doi.org/10.1007/S10967-021-08138-4/TABLES/3>
- Keerthana, M., Malini, T. P., & Sangavi, R. (2021). Efficiency of cerium oxide (CeO₂) nano-catalyst in degrading the toxic and persistent 4-nitrophenol in aqueous solution. *Materials Today: Proceedings*, 50, 375–379. <https://doi.org/10.1016/j.matpr.2021.10.082>
- Keerthana, M., Malini, T. P., & Sangavi, R. (2022). Efficiency of cerium oxide (CeO₂) nano-catalyst in degrading the toxic and persistent 4-nitrophenol in aqueous solution. *Materials Today: Proceedings*, 50, 375–379. <https://doi.org/10.1016/J.MATPR.2021.10.082>
- Kim, K., Kabir, E., & Ara, S. (2016). Science of the Total Environment Exposure to pesticides and the associated human health effects. *Science of the Total Environment*. <https://doi.org/10.1016/j.scitotenv.2016.09.009>
- Kumaraguru, S., Nivetha, R., Gopinath, K., Sundaravadivel, E., Almutairi, B. O., Almutairi, M. H., Mahboob, S., Kavipriya, M. R., Nicoletti, M., & Govindarajan, M. (2022). Synthesis of Cu-MOF/CeO₂ nanocomposite and their evaluation of hydrogen production and cytotoxic activity. *Journal of Materials Research and Technology*, 18, 1732–1745. <https://doi.org/10.1016/J.JMRT.2022.03.028>
- Lin, Y. H., Shen, L. J., Chou, T. H., & Shih, Y. hsin. (2021). Synthesis, Stability, and Cytotoxicity of Novel Cerium Oxide Nanoparticles for Biomedical Applications. *Journal of Cluster Science*, 32(2), 405–413. <https://doi.org/10.1007/S10876-020-01798-4/FIGURES/6>
- Mandić-Rajčević, S., Rubino, F. M., & Colosio, C. (2020). Establishing health-based biological exposure limits for pesticides: A proof of principle study using mancozeb. *Regulatory Toxicology and Pharmacology*, 115, 104689. <https://doi.org/10.1016/J.YRTPH.2020.104689>
- Miri, A., Beiki, H., Najafidoust, A., Khatami, M., & Sarani, M. (2021). Cerium oxide nanoparticles: green synthesis using Banana peel, cytotoxic effect, UV protection and their photocatalytic activity. *Bioprocess and Biosystems Engineering*, 44(9), 1891–1899. <https://doi.org/10.1007/S00449-021-02569-9/FIGURES/10>
- Miri, A., Sarani, M., & Khatami, M. (2020). *Nickel-doped cerium oxide nanoparticles: biosynthesis, cytotoxicity and UV protection studies*. <https://doi.org/10.1039/c9ra09076b>
- Mohamed, H. R. H. (2021). Acute Oral Administration of Cerium Oxide Nanoparticles Suppresses Lead Acetate–Induced Genotoxicity, Inflammation, and ROS Generation in Mice Renal and Cardiac Tissues. *Biological Trace Element Research*, 200(7), 3284–3293. <https://doi.org/10.1007/S12011-021-02914-9/FIGURES/7>
- Morales-Ovalles, Y., Miranda-Contreras, L., Peña-Contreras, Z., Dávila-Vera, D., Balza-Quintero, A., Sánchez-Gil, B., & Mendoza-Briceño, R. V. (2018). Developmental exposure to mancozeb induced neurochemical and morphological alterations in adult

- male mouse hypothalamus. *Environmental Toxicology and Pharmacology*, **64**, 139–146. <https://doi.org/10.1016/J.ETAP.2018.10.004>
- Muduli, S., & Ranjan Sahoo, T. (2022). Green synthesis of cerium oxide, Co-doped cerium oxide nanoparticles and its dielectric properties. *Materials Today: Proceedings*. <https://doi.org/10.1016/J.MATPR.2022.07.308>
- Muthuvel, A., Jothibas, M., Mohana, V., & Manoharan, C. (2020). Green synthesis of cerium oxide nanoparticles using Calotropis procera flower extract and their photocatalytic degradation and antibacterial activity. *Inorganic Chemistry Communications*, **119**, 108086. <https://doi.org/10.1016/J.INOCHE.2020.108086>
- Nicolopoulou-Stamati, P., & Sotirios Maipas, Chrysanthi Kotampasi, P. S. and L. H. (2016). *Chemical Pesticides and Human Health: The Urgent Need for a New Concept in Agriculture*. **4**(July), 1–8. <https://doi.org/10.3389/fpubh.2016.00148>
- Pradeepa, E., & Nayaka, Y. A. (2022). Cerium oxide nanoparticles via gel-combustion for electrochemical investigation of pantoprazole in the presence of epinephrine. *Journal of Materials Science: Materials in Electronics*, **33**(23), 18374–18388. <https://doi.org/10.1007/S10854-022-08692-X/TABLES/2>
- Quds, R., Amiruddin Hashmi, M., Iqbal, Z., & Mahmood, R. (2022). Interaction of mancozeb with human hemoglobin: Spectroscopic, molecular docking and molecular dynamic simulation studies. *Spectrochimica Acta Part A: Molecular and Biomolecular Spectroscopy*, **280**, 121503. <https://doi.org/10.1016/J.SAA.2022.121503>
- Raees, A., Jamal, M. A., Ahmad, A., Ahmad, I., Saeed, M., Habila, M. A., AlMasoud, N., & Alomar, T. S. (2022). Synthesis and characterization of Ceria incorporated Nickel oxide nanocomposite for promising degradation of methylene blue via photocatalysis. *International Journal of Environmental Science and Technology*, **19**(7), 6445–6452. <https://doi.org/10.1007/S13762-021-03584-9/FIGURES/6>
- Samai, B., & Bhattacharya, S. C. (2018). Conducting polymer supported cerium oxide nanoparticle: Enhanced photocatalytic activity for waste water treatment. *Materials Chemistry and Physics*, **220**, 171–181. <https://doi.org/10.1016/J.MATCHEMPHYS.2018.08.050>
- Sani, M. D., Abbaraju, V. D. N. K., & Venugopal, N. V. S. (2023). Photocatalytic degradation and removal of type II pyrethroid pesticide (lambda - cyhalothrin) residue from wastewater using nanoceria for agricultural runoff application. *Journal of Applied and Natural Science*, **9411**, 1219–1229.
- Saraiva, M. A., de Carvalho, N. R., Martins, I. K., Macedo, G. E., Rodrigues, N. R., de Brum Vieira, P., Prigol, M., Gomes, K. K., Ziech, C. C., Franco, J. L., & Posser, T. (2021). Mancozeb impairs mitochondrial and bioenergetic activity in *Drosophila melanogaster*. *Heliyon*, **7**(1), e06007. <https://doi.org/10.1016/J.HELIVON.2021.E06007>
- Shetty, A. N., Kaveri, , Kiran, , Desai, K., Somanathreddy, , & Patil, C. (2022). Green Combustion Synthesis of CeO₂ Nanostructure Using Aloe vera (L.) Burm f. Leaf Gel and Their Structural, Optical and Antimicrobial Applications. *BioNanoScience* **2022**, **1**, 1–9. <https://doi.org/10.1007/S12668-022-01001-0>
- Singh, P., Mohan, B., Madaan, V., Ranga, R., Kumari, P., Kumar, S., Bhankar, V., Kumar, P., & Kumar, K. (2022). Nanomaterials photocatalytic activities for waste water treatment: a review. *Environmental Science and Pollution Research* **2022** **29**(46), 69294–69326. <https://doi.org/10.1007/S11356-022-22550-7>
- Sraw, A., Kaur, T., Thakur, I., Verma, A., Wanchoo, R. K., & Toor, A. P. (2022). Photocatalytic degradation of pesticide monocrotophos in water using W-TiO₂ in slurry and fixed bed recirculating reactor. *Journal of Molecular Structure*, **1265**, 133392. <https://doi.org/10.1016/J.MOLSTRUC.2022.133392>
- Vijgen, J., Weber, R., Lichtensteiger, W., & Schlumpf, M. (2018). The legacy of pesticides and POPs stockpiles—a threat to health and the environment. *Environmental Science and Pollution Research* **2018** **25**:32, **25**(32), 31793–31798. <https://doi.org/10.1007/S11356-018-3188-3>
- Walker, E. K., Brock, G. N., Arvidson, R. S., & Johnson, R. M. (2022). Acute Toxicity of Fungicide–Insecticide–Adjuvant Combinations Applied to Almonds During Bloom on Adult Honey Bees. *Environmental Toxicology and Chemistry*, **41**(4), 1042–1053. <https://doi.org/10.1002/ETC.5297>
- Zhao, G. P., Yang, F. W., Li, J. W., Xing, H. Z., Ren, F. Z., Pang, G. F., & Li, Y. X. (2020). Toxicities of Neonicotinoid-Containing Pesticide Mixtures on Nontarget Organisms. *Environmental Toxicology and Chemistry*, **39**(10), 1884–1893. <https://doi.org/10.1002/ETC.4842>

A Spatial Tropical Island Database of Northern Borneo, Malaysia using Google Earth

Mohd Harun Abdullah^{1a}, Zulherry Isnain^{2a}, Kam-Cheng Yeong^{3b}, Thor-Seng Liew^{4ab}, Mohd. Talha Anees^{5c}, Chin Yik Lin^{6c*}

Abstract: The state of Sabah in Northern Borneo, Malaysia is surrounded by numerous small tropical islands. However, the recent surge in tourist activities has significantly impacted the biological diversity and natural resources of these islands. This study aims to develop a systematic database for the region to prioritize and preserve the conservation and integrity of these tropical islands. The database was compiled using topographic maps and Google Earth data. Variables such as island size, distance, distribution, and isolation from the Sabah coastline were analysed through maps and scatter plots generated in a GIS environment. The significance of the islands was evaluated across various aspects based on the compiled data. The database identifies a total of 510 islands along Sabah's coastline with 82 located on the west coast and the remaining 428 on the east coast. Approximately 80% of these islands are small with an area of less than 1 km². Only five islands exceed 100 km², while smaller islands are predominantly located closer to the coast. The findings indicate that the significance of the islands varies based on factors such as tourist attractions, flora and fauna, marine ecosystems, and national security. The methodology adopted in this study is robust and offers potential for examining island distribution in other regions.

Keywords: Islands, geographical information system (GIS), database, maps, Northern Borneo

1. Introduction

The Malay Archipelago, located between mainland Indochina and Australia, is densely populated with numerous small tropical islands. An island is defined as a contiguous area of land surrounded by water and smaller than a continent. Countries such as Indonesia, Thailand, the Philippines, and Malaysia collectively host 25,000 islands (Persoon & van Weerd, 2006). Specifically, Malaysia is home to 878 islands and 510 offshore geographical features (JUPEM, 2005; The Star, 2011). These small tropical islands are fragile and more vulnerable to environmental degradation compared to the mainland due to its limited surface area and close proximity to the coast. Despite their small size, these islands support a significant proportion of biodiversity and cultural richness (Tershy et al., 2015). Previous studies have highlighted that the rapid loss of biological and cultural diversity is primarily driven by anthropogenic activities (Keitt et al., 2011; Sodhi et al., 2010a, 2010b). To address these challenges, integrating key information into a comprehensive database system provides scientists, policymakers, and decision-makers with an efficient tool for storing, retrieving, and analysing data, ultimately facilitating informed decision-making. However, given

the difficulty of conserving and managing all islands in island-dense regions such as Northern Borneo, conservation efforts should be prioritized and focus on the most ecologically and culturally significant islands.

Global studies on invasive species have often overlooked the islands of Southeast Asia compared to other regions of the world (Keitt et al., 2011; Medina et al., 2011). Malaysia, located in Southeast Asia, hosts more than 800 islands, with over half situated in the waters of Sabah, northern Borneo (Figure 1). Sabah features a rugged topography, particularly along its west coast, and is primarily composed of very thick, folded marine sedimentary rocks from the Upper Cretaceous to Tertiary periods. In addition to sedimentary formation, Sabah also contains volcanic and plutonic rocks, as well as subordinate Mesozoic metamorphic rocks. The oldest sedimentary rocks are Early Cretaceous radiolarian cherts, limestones, and conglomerates. The igneous rocks in Sabah display diverse compositions, including serpentinites, basalts/spilites, agglomerates, gabbros, dolerites, andesites, granodiorites, and adamellites formed during the Miocene-Pliocene period. Metamorphic rocks, such as hornblende schists and gneisses, are also prevalent (Tongkul, 1990). The oldest rocks in the region include the crystalline basement of Eastern and central Sabah, which comprises a metamorphic complex (including amphibolites and gneisses) intruded by, or in tectonic contact with granite, gabbro, and ultramafic rocks (Moores & Fairbridge, 1997). Tectonically, Sabah lies near dynamic plate boundaries in Southeast Asia. It is influenced by intermittent expansion of the South China Sea Basin and the counterclockwise rotation of the island of Borneo (Tongkul, 1990). While Sabah is not seismically active, it exhibits a

Authors information:

^aSmall Islands Research Centre (SIRC), Universiti Malaysia Sabah, 88400 Kota Kinabalu, Sabah, MALAYSIA. E-mail: harunabd@ums.edu.my¹; zulherry@gmail.com²

^bInstitute for Tropical Biology and Conservation, Universiti Malaysia Sabah, 88400 Kota Kinabalu, Sabah, MALAYSIA. E-mail: kamchengyeong@gmail.com³; thorsengliew@gmail.com⁴

^cDepartment of Geology, Faculty of Science, Universiti Malaya, 50603 Kuala Lumpur, MALAYSIA. talhaanees_alg@yahoo.in⁵; chinyik@um.edu.my⁶

*Corresponding Author: chinyik@um.edu.my

Received: July 27, 2023

Accepted: January 4, 2024

Published: December 31, 2024

complex geological history, as highlighted by recent studies (Greenfield et al., 2022).

Bazliah et al. (2021) investigated the tectonic geomorphology of Northern Borneo using remote sensing data. Their findings reveal that the active faulting in northwest Borneo results from oblique crustal extension, forming normal and strike-slip faults. Notable evidence includes the Pamol fault zone, which is part of a broader fault network associated with ongoing extension. This suggests that tectonic forces primarily drive Borneo's deformation, with gravity-induced processes playing a supplementary role.

In Sabah, islands hold significance not only for their rich natural resources and aesthetic appeal for tourism and economic activities but also for their critical roles in national sovereignty, territorial integrity, and security. However, the state has faced recurrent challenges from terrorist incursions, particularly from neighbouring regions around the Sulu Sea, which have posed severe problems and garnered widespread attention.



Figure 1. Sabah is a region in Malaysia situated in the northern region of Borneo Island. The red box indicates the location of Kota Kinabalu, the capital of Sabah.

Information about most islands in Sabah, particularly regarding their environment, boundaries, social and economic, history, geology, and biodiversity, is scarce and fragmented in the existing literature (Phung et al., 2017). There is currently no comprehensive or easily accessible database for these islands, and their geographical properties remain largely unexplored. Traditional field-based approaches, such as ecological censuses, are labour-intensive and costly, underscoring the urgent need for effective management strategies to conserve biological and cultural diversity. The objectives of this study are (i) to establish a functional GIS database containing fundamental geographical properties of all islands in Sabah, and (ii) to evaluate the islands based on their size, distribution, and degree of isolation for various aspects. Additionally, this study outlines a clear methodology for creating an island database, which could serve as a model for similar efforts in other regions with numerous islands.

To the best of our knowledge, this is the first study to analyse the distribution, size, and isolation of islands in Malaysia providing a comprehensive overview of the island's states and characteristics. It offers critical insights into related issues and highlights the unique strengths of each island based on factors such as flora and fauna, marine ecosystems, geological

significance, tourist attractions, and national security considerations. The resulting database, accessible via Google Earth, is intended for use by various stakeholders, including state authorities and research institute, as a baseline for future studies and conservation effects.

2. Materials and Methods

Islands Mapping

In the initial stage, the island's locations were cross-reference using Google Earth and topographic maps obtained from the Department of Survey and Mapping Malaysia (JUPEM) to validate their existence. Subsequently, island digitization was conducted directly in Google Earth by tracing the outline of each island as a polygon (Figure 2). The polygon titles were labelled with the islands' gazetted names where available. For islands without gazetted names on the JUPEM maps, the prefix "Pulau" was assigned, followed by a numerical code starting with 001. Most islands were easily distinguishable from the surrounding marine environment, except for smaller "sand bar"-sized island. To locate these smaller islands, approximate coordinates from the report "Maklumat Keluasan & Perimeter Negeri, Daerah, Pulau-Pulau di Malaysia" were used as a guide (JUPEM, 2005). Islands currently fused with the Sabah mainland were excluded from the study. The digitized outline and names of each island were saved in a single Keyhole Markup Language (KML) file for further analysis and modification. This systematic approach ensures the comprehensive documentation of island locations and attributes for subsequent research and management.

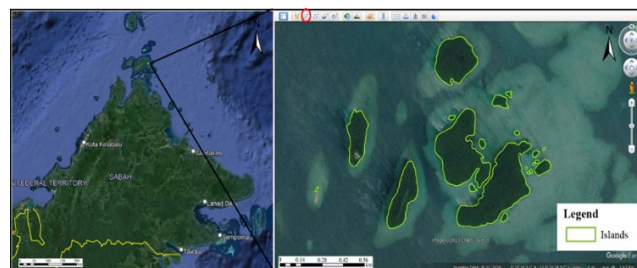


Figure 2. Digitization of islands in Google Earth using polygon tool (Red circle).

Quantifying Island Physical Parameters

The KML files consisting 510 island polygons were converted into a polygon shapefile (*.shp) with a Universal Transverse Mercator (UTM) coordinate system. Island size, isolation, and distribution patterns were analyzed using R (R Core Team, 2016) and QGIS version 2.18.2 (QGIS Development Team, 2017). Specifically, the "rgdal" (Bivand et al., 2015) and "rgeos" (Bivand & Rundel, 2015), packages were used in R for processing, while QGIS facilitated spatial analysis. To quantify the size of each island (i.e., area; km²), the polygon shapefile was processed in R using a custom script (Supplementary File 1). Histograms with varying bin sizes were generated to visualize the size distribution of islands in Sabah.

The degree of isolation of each island was determined by

converting the polygon shapefile into a point shapefile, where each island was represented by its centroid using the “polygon centroid” function. An island density raster layer with a 100-meter cell size was created using the “Heat map analysis” with a 10 km search radius. The density values from the 10 km raster layer were extracted for each island centroid using the “Add grid values to points” function in SAGA GIS version 3.0.0 (Conrad et al., 2015). For instance, an island with a raster value of 5 in the 10 km heat map indicates that there are four other islands within a 10 km radius of that island. This analysis provided valuable insights into the spatial relationships and isolation patterns among the islands in Sabah.

Create Island GIS Database in the form of KMZ file

To develop a user-friendly island GIS database, the digitized map, references, and physical parameters of the islands were integrated into a single KMZ file accessible via the Google Earth interface. The same KML file used for digitizing the islands’ outline was adopted as a template for this integration. Each island’s physical parameters and characteristics were summarized in a single graph, which consists of the location, shape, and degree of isolation. The overall methodology for creating the database is shown in Figure 3.

3. Results and Discussion

Distribution and Size of Islands Along the Coastlines

Sabah consists of 26 districts, 19 of which have coastlines. The inland districts without islands are Beaufort, Keningau, Pensiangan, Ranau, Sipitang, Tambunan, Tenom. The names of the remaining coastal districts are listed in Table 1.

Table 1. The number of Islands per district*.

District	Number of Islands
Beluran	40
Kinabatangan	6
Kota Belud	10
Kota Kinabalu	12
Kota Marudu	20
Kuala Penyu	7
Kudat	103
Kunak	8
Labuan	8
Lahad Datu	46
Papar	5
Penampang	1
Pitas	6
Sandakan	56
Semporna	130
Tawau	36
Tuaran	15

* Labuan is a Federal Territorial

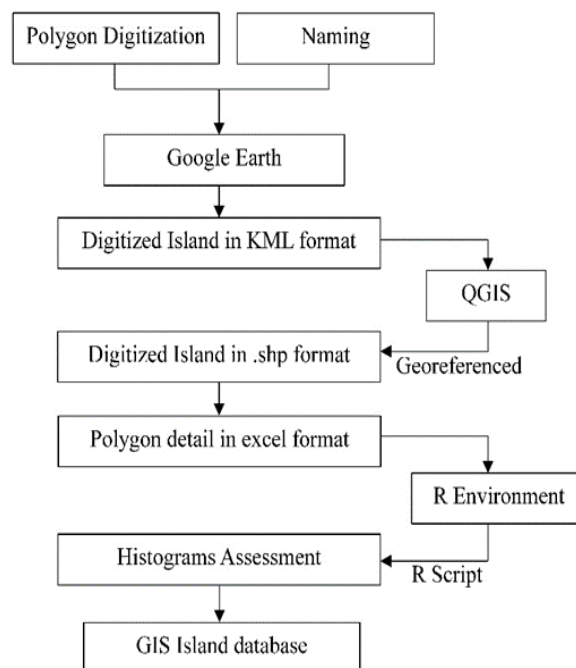


Figure 3. Overall methodology flow chart.

It is important to note that Labuan, a Federal Territory, is included among the 19 districts, but Pulau Layang-Layang is excluded from this study due to its significant distance from Sabah’s coastline (272 km) and its small size. As illustrated in Figure 4, Sabah’s coastline extends from the west to the south-eastern part of the state. Our findings reveal a total of 510 islands along the coast of Sabah, with 82 located along the west coast and the remaining 428 along the east coast. The majority of the islands are concentrated in the northern region of Sabah. Two districts, namely, Kudat (103) and Semporna (130) host over 100 islands each, followed by Sandakan (56), Lahad Datu (46), and Beluran (40).

In terms of size, more than 80% of the islands are smaller than 1 km², with two-thirds of these being smaller than 0.2 km². Larger islands such as Pulau Banggi and Pulau Sebatik exceed 400 km², while intermediate-sized islands, including Pulau Balambangan, Pulau Timbun Mata, and Pulau Jambungan, range between 100 to 200 km². Figure 4 depicts the frequency distribution of the sizes of Sabah’s islands.

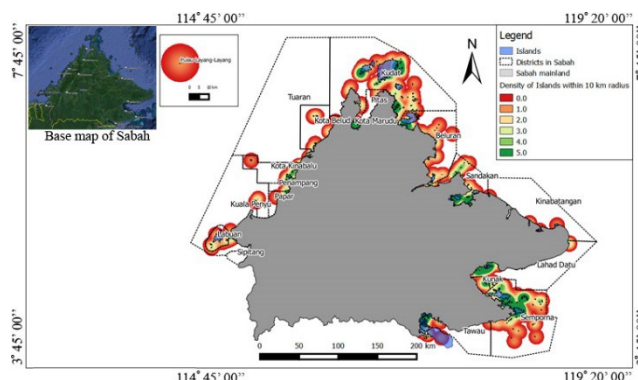


Figure 4. Distribution and density of islands around Sabah.

The Distance of Islands from Sabah’s Coastline and Their Isolation

Figure 5A shows the spatial distribution of islands based on their distances from both the nearest neighbouring island (ordinate) and the Sabah coastline (abscissa). The plot reveals that the majority of islands are located within a 50 km radius of the coastline. However, Pulau Layang-Layang and Pulau Mengalum are two notable outliers, being situated at greater distances of 272 km and 50 km from the coastline, respectively. Excluding these outliers, the maximum inter-island distance is approximately 21 km, indicating that most islands are relatively close to both the Sabah coastline, and neighboring islands.

Figure 5B illustrates the distribution of islands with respect to their proximity of the shoreline. Most islands exhibit inter-island distances of around 7.5 km, forming a dense cluster along the abscissa. However, some islands are more isolated, with inter-island distances of approximately 20 km. Among these, Pulau 200, Pulau Ligitan, Pulau Straggler, and Pulau Sipadan stand out as the most isolated islands in this analysis.

In summary, Figure 5B emphasizes that a significant number of islands are closely spaced, creating a dense distribution pattern. Despite this, certain islands including Pulau 200, Pulau Ligitan, Pulau Straggler, and Pulau Sipadan are more secluded, with larger inter-island distances distinguishing them from the majority.

Significances of Islands Based on the Island Database

Island size, distance from the coastline, and inter-island distances are key parameters influencing aspects such as biodiversity (flora and fauna), marine life, geological significance, tourism potential, and national security (Weigelt and Kreft, 2013; Gjerde et al., 2015). While small islands with an area of less than 0.2 km² are generally considered insignificant, their importance can increase in cases where inter-island distances are minimal.

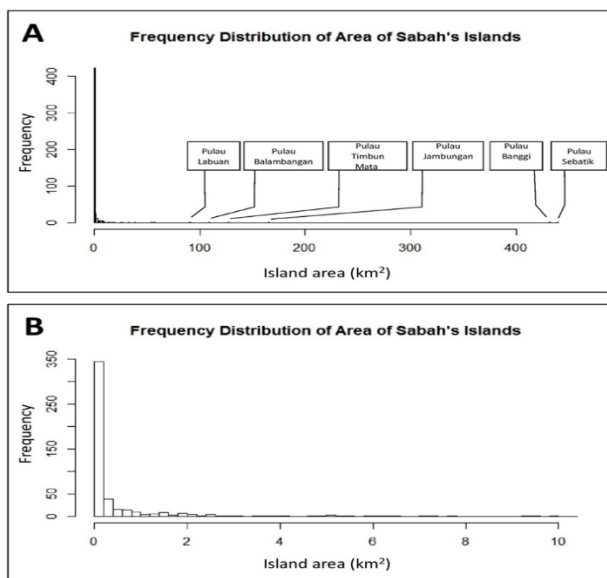


Figure 5. Histograms showing the size distribution of Sabah’s 510 islands. (A) Histogram showing all 510 islands, with a bin size of 1 km². (B) Histogram depicts the number of islands smaller than 10 km², with bin's size of 0.2 km².

Figure 6B illustrates a high density of islands within 10 km of the coastline, with inter-island distances averaging around 5km. This suggests that most small islands in Sabah are relatively clustered and situated close to the coastline (< 10 km), making them significant in the aforementioned aspects. In contrast, isolated islands situated more than 20 km from the coastline tend to be small and insignificant. Additionally, most large islands (as depicted in Figure 5A) are located within 10 km of the coastline, highlighting their greater significance compared to smaller, more distant islands.

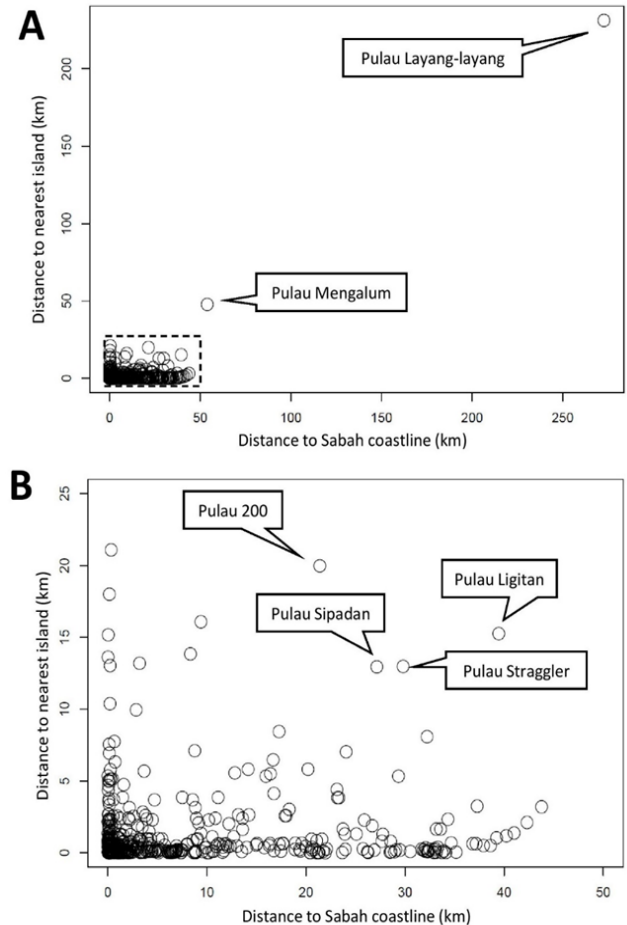


Figure 6. Scatterplot showing the degree of isolation for Sabah’s 510 islands. (A) The two most isolated islands, while the dash-line box highlights a portion of the plot shown in greater detail in B. (B) the enlarged displays other notable isolated islands.

Tourism, Frontline Safety and Other Aspects of Island Significance

According to Sabah tourism's official website, approximately 4.2 million tourists visited Sabah in 2019, reflecting an 8.2% increase from the previous year. Given the substantial influx of visitors, the islands database developed in this study can assist policymakers in identifying suitable and sustainable sites for resorts and hotel development. Islands that are well-clustered (inter-island distance < 5km) and located near the coastline are considered to have greater potential compared to more isolated islands. Larger islands which hold more natural resources (e.g., groundwater) and provide greater space for infrastructure development are

particularly significant as tourists destination. For instance, islands closer to the mainland and with larger surface areas are ideal for activities such as jungle trekking, scuba diving, paragliding, and island hopping. Their proximity to the coastline also makes them more economically viable for attracting tourists and promoting sustainable tourism.

In addition to tourism, national security and sovereignty are critical priorities for any country. Identifying and establishing strategic military sites is essential for combat piracy and terrorist activities, especially along the borders of the Sulu Sea. The island database derived from this study provide valuable insights for the government in managing and securing frontline safety. Strategically isolated islands with adequate coverage and sufficient size for structures such as observation posts and airstrips are highly significant. Results indicate that Pulau Layang-Layang, Pulau Mengalum, and the other isolated islands are among the most suitable sites for such purposes. The database will be made available to local authorities and the government upon request to aid in security planning.

Tropical islands are widely recognized for its sensitive, fragile, and highly vulnerable ecology (Glaser, 1983; Dahl, 1980). Preserving flora and fauna, especially endemic species is crucial for in-situ wildlife conservation (McGinley et al., 2017). Islands not designated for military or tourism purposes can serve as optimal locations for the establishing of marine and national parks. Even islands developed for tourism can be significant for marine life preservation, as marine park status often attracts researchers, marine enthusiasts, and eco-tourists, thereby promoting eco-tourism and conservation in Sabah. Finally, the compiled database facilitates marine spatial planning and coastal zone management, enabling the sustainable development of state resources. Sharing this data with the public would further enhance its utility and impact, ensuring direct benefits are maximized for the sustainable future of Sabah.

The Direct Impact of the Developed Islands Database in Different Fields

Tourism Promotion Through Unique Selling Points: The database offers a detailed overview of the islands in Sabah, categorizing them by size, location, and ecological significance. Tourism authorities can utilize this information to promote unique and less-crowded islands, effectively distributing tourist activities across the region. Highlighting the scenic and ecological value of these islands can attract visitors seeking authentic and less-explored destinations.

Preservation of Fragile Ecosystems: Understanding the ecological importance of each island enables the implementation of targeted conservation measures. Biodiverse islands or those with critical marine habitats can be designated as protected areas, limiting tourist access and activities to preserve their fragile ecosystems. This ensures a balance between tourism and environmental sustainability.

Mitigating Overcrowding and Environmental Impact: The database can guide tourism policies to prevent overcrowding on popular islands by promoting lesser-known yet ecologically

valuable ones. This reduces pressure on heavily visited areas, minimizing pollution and the over-harvesting of marine resources associated with overcrowding.

Educational Initiatives for Sustainable Tourism: The database supports the launch of educational campaigns to raise awareness about the ecological significance of these islands. These initiatives can encourage tourists to adopt eco-friendly practices and respect the natural environment, fostering responsible tourism.

Frontline Safety and Security: Analyzing islands based on frontline safety allows authorities to enhance security measures in strategic areas. This ensures tourism activities contribute to the local economy without compromising national security.

Adaptability for Other Regions: The study's robust methodology can serve as a model for other regions. Its approach to island cataloguing can be adapted globally, helping assess island distribution and informing decision-making in environmental and tourism management.

Pros and Cons of the Developed Islands' Database

Advantages of the developed islands database includes (i) comprehensive information which provides detailed data on islands size, distribution, proximity to the coast, and other variables; (ii) systematic approach incorporating topographic maps and Google Earth data, ensuring reliability and organized, accessible information; (iii) sophisticated GIS tools for mapping and analysing the data, adding precision and depth to the study, (iv) relevance to multiple parameters as addresses diverse factors including biodiversity, marine life, and national security; and (v) applicability to other regions facing similar challenges to increase the scalability and usefulness of the approach.

Disadvantages of the developed islands includes (i) data limitations like incomplete or outdated information on certain islands may affect the accuracy and comprehensiveness of the analysis; (ii) dynamic nature of islands where the database does not fully capture changes caused by natural processes (e.g., erosion) or human activities (e.g., development), (iii) challenges in development where creating database of this magnitude requires advanced technology, GIS expertise, and continuous efforts for data collection and validation; (iv) interconnected factors like tourism's impact on biodiversity and other interdependent factors complicates decision-making; and (v) assumptions and generalizations which causes uncertainties in the outcomes.

4. Conclusion and Recommendation

In conclusion, we developed a comprehensive database of Sabah's using Google Earth data and Geographic Information System (GIS) tools, addressing diverse aspects such as tourism, frontline safety, and wildlife/marine ecological preservation. Our analysis revealed that most islands are located within 10 km of the Sabah coastline, with inter-island distances typically less than 5 km, forming a dense network of islands the coastline. We found that island's size, distribution, and isolation significantly influence tourism, security, and conservation efforts in the region.

Our findings suggest that the significances of the islands varies depending on their characteristics and roles. For instance, aspects such as tourist attractions, biodiversity (flora and fauna), marine life, and national security are strongly influenced by the spatial attributes of the islands. Larger islands tend to attract diverse ecotourism opportunities, while smaller, closer islands are more prone to overcrowding. Isolated islands, on the other hand, hold strategic importance for security and contribute significantly to ecosystem resilience. These findings align with previous studies that explore the relationships between island size and isolation in terms of biodiversity, demographic assessments on inhabited island, and the sustainability of island tourism development (Tye et al., 2002; National Records of Scotland, 2015; Chi and Liu, 2023). Furthermore, the research highlights critical connections between island features and their impacts on tourism, security, and conservation. Key insights include (1) larger islands offering enhanced opportunities for biodiversity and ecotourism, (2) risks of overcrowding on smaller islands, more accessible islands, (3) strategic significance of isolated islands for security and military considerations, (4) the role of island distribution in shaping conservation priorities and ecosystem resilience, and (5) reinforcement of findings through statistical correlations and scenario-based analyses. Finally, the proposed methodology and results provide a valuable tool for government and policymakers, both locally and internationally, enabling informed decision-making for sustainable island management. We recommend prioritizing identified islands for further assessment, including geographical, autecological, synecological parameters, to enhance conservation efforts. This balanced approach will not only safeguard biological and cultural diversity but also generate additional income for the country through sustainable tourism and resource management.

5. Acknowledgement

It is acknowledged that this project was financially supported by Small Islands Research Centre (SIRC) of Universiti Malaysia Sabah.

6. References

- Bazliah, B., Sahari, S., Shah, A. A., Navakanesh, B., Syafiqah, N. (2021). Tectonic Geomorphology of NW Borneo, Malaysia. In 5th International Young Earth Scientists (YES) Congress "Rocking Earth's Future" (pp. 15-19). German YES Chapter, GFZ German Research Centre for Geosciences.
- Bivand R., Rundel C. (2015). Rgeos: interface to geometry engine - open source (GEOS). R package version 0.3-15. <http://CRAN.R-project.org/package=rgeos>.
- Bivand R., Keitt T., Rowlingson B. (2015). Rgdal: bindings for the geospatial data. Abstraction Library. R package version 1.1-3. <http://CRAN.R-project.org/package=rgdal>.
- Chi, Y., Liu, D. (2023). Measuring the island tourism development sustainability at dual spatial scales using a four-dimensional model: A case study of Shengsi archipelago, China. *Journal of Cleaner Production*, 388: 135775.
- Conrad, O., Bechtel, B., Bock, M., Dietrich, H., Fischer, E., Gerlitz, L., Wehberg, J., Wichmann, V., Böhner, J. (2015). System for automated geoscientific analyses (SAGA) v. 2.1.4. *Geoscientific Model Development*, 8(7):1991-2007.
- Dahl, A. L. (1980). Conservation planning and environmental monitoring for tourism development. *New Zealand Man and the Biosphere Report*, Department of Geography, University of Canterbury, (6):125-129.
- Donlan, C. J., Tershy, B. R., Keitt, B. S., Wood, B., Sánchez, J. Á., Weinstein, A., Alguilar, J. L., (2000). Island conservation action in northwest Mexico. In *Proceedings of the Fifth California Islands Symposium*, 29 March to 1 April 1999, pp. 330-338.
- Donlan, C. J., Wilcox, C. (2008). Diversity, invasive species and extinctions in insular ecosystems. *Journal of Applied Ecology*, 45(4):1114-1123.
- Gjerde, I., Blom, H. H., Heegaard, E., Saetersdal, M. (2015). Lichen colonization patterns show minor effects of dispersal distance at landscape scale. *Ecography*, 38:939 – 948.
- Glaser, G. (1983). Unstable and vulnerable ecosystems: A comment based on MAB research in island ecosystems. *Mountain Research and Development*, 3(2):121 – 123.
- Greenfield, T., Gilligan, A., Pilia, S., Cornwell, D. G., Tongkul, F., Widiyantoro, S., Rawlinson, N. (2022). Post-subduction tectonics of Sabah, northern Borneo, inferred from surface wave tomography. *Geophysical Research Letters*, 49(3), e2021GL096117.
- Moores, E. M., Fairbridge, R. W. (Eds.). (1997). *Encyclopedia of European and Asian regional geology*. London: Chapman & Hall. Springer, Dordrecht.
- JUPEM (2005). *Maklumat keluasan dan perimeter negeri-negeri, daerah-daerah, dan pulau-pulau di Malaysia*, Jabatan Ukur dan Pemetaan Malaysia, 1 atlas, Kuala Lumpur, 43 – 75.
- Keitt, B., Campbell, K., Saunders, A., Clout, M., Wang, Y., Heinz, R., Newton, K., Tershy B., (2011). The global islands invasive vertebrate eradication database: a tool to improve and facilitate restoration of island ecosystems. *Island invasives: eradication and management*. IUCN, Gland, Switzerland, 74-77.

- McGinley, K. A., Robertson, G. C., Friday, K. S., Carpenter, C. A. (2017). Assessing forest sustainability in the tropical islands of the United States. USDA, General Technical Report, IITF-GTR-48.
- Medina, F. M., Bonnaud, E., Vidal, E., Tershy, B. R., Zavaleta, E. S., Josh Donlan, C., Nogales, M. (2011). A global review of the impacts of invasive cats on island endangered vertebrates. *Global Change Biology*, 17(11):3503-3510.
- Persoon, G. A., van Weerd, M. (2006). Biodiversity and natural resource management in insular Southeast Asia. *Island Studies Journal*, 1(1):81-108.
- Phung, C-C., Yu, F.T.Y., Liew, T-S. (2017). A checklist of land snails from the west coast islands of Sabah, Borneo (Mollusca, Gastropoda). *Zookeys*. 673:49 – 104.
- QGIS Development Team. (2017). QGIS Geographic Information System. Open-Source Geospatial Foundation Project. <http://qgis.osgeo.org>
- R Core Team. (2016). R: a language and environment for statistical computing. R Foundation for Statistical Computing, Vienna, Austria. Available at <http://www.R-project.org/>
- National Records of Scotland (2015). Scotland's Census 2011, Inhabited islands report, published on 24th September 2015. https://www.scotlandscensus.gov.uk/media/ybpbfnfbp/inhabited_islands_report.pdf (Last access on 30th December 2023)
- Sodhi, N. S., Wilcove, D. S., Subaraj, R., Yong, D. L., Lee, T. M., Bernard, H., Lim, S. L. (2010a). Insect extinctions on a small denuded Bornean Island. *Biodiversity and conservation*, 19(2):485-490.
- Sodhi, N. S., Wilcove, D. S., Lee, T. M., Sekercioglu, C. H., Subaraj, R., Bernard, H., Yong, D. L., Lim, S. L. H., Prawiradilaga D. M. Brook, B. W. (2010b). Deforestation and avian extinction on tropical landbridge islands. *Conservation Biology*, 24(5):1290-1298.
- Tershy, B. R., Shen, K. W., Newton, K. M., Holmes, N. D., Croll, D. A. (2015). The importance of islands for the protection of biological and linguistic diversity. *Bioscience*, 65(6):592-597.
- The Star (2011). Retrieved from <https://www.thestar.com.my/news/nation/2011/02/21/m-sia-must-assert-sovereignty-over-236-islands-without-names-kurup/> on 1/11/2021
- Tongkul, F. (1990). Structural style and tectonics of Western and Northern Sabah.
- Tye, A., Snell, H. L., Peck, S. B., Adersen, H. (2002). Outstanding terrestrial features of the Galapagos archipelago. A biodiversity vision for the Galapagos Islands, 25-35.
- Weigelt, P., Kreft, H. (2013). Quantifying island isolation – insights from global patterns of insular plant species richness. *Ecography*, 36:417 – 429.

Mapping Earthquake Vulnerable Areas Based on Microtremor Measurements Near Kebumen City

Danang Widyawarman^{1a*}, Sismanto^{2b}, Aditya Yoga Purnama^{3c}

Abstract: Kebumen, a district in Central Java, is regarded as a risky location because of the possibility of earthquakes. The risk level of earthquake hazard was assessed using a microtremor experiment in 10 subdistricts surrounding Kebumen, Java Tengah, using the characteristic soil dynamic parameters. A total of 82 points were collected using a single station seismometer, which has three components. An HVSR analysis was performed on the data. This vulnerability map also considers social, infrastructure, and economic vulnerabilities. According to the results of the microtremor analysis, the dominating frequency range is between 0.62 and 5.26 Hz. The amplification values ranged from 1,16 to 10,61. The thickness of the sediment layer ranged from 0.56 to 83.46 m. The seismic map was merged with maps of social vulnerability, infrastructure, and economics. The risk of earthquakes in the Kebumen area can be classified into three categories. The Pejagoan and Klirong sub-districts had the lowest earthquake risk. The second category area has a medium earthquake risk and predominates the experimental area, whereas the third category area has a high earthquake risk and predominates the Sruweng subdistrict.

Keywords: Kebumen City, microtremor, HVSR

1. Introduction

The Indonesian archipelago is situated in an active tectonic zone where three major tectonic plates—the Eurasian, Indo-Australian, and Pacific plates—meet. Indonesia is a region with high tectonic activity and forms a triple-junction due to the movement of these three plates. The Indo-Australian plate generally moves northward at 6–7 cm per year, subducting below the Eurasian plate, and the two plates meet in the Indonesian region between the southern tip of Sumatra and the Maluku Islands, as shown in Figure 1. (Sili, 2013).

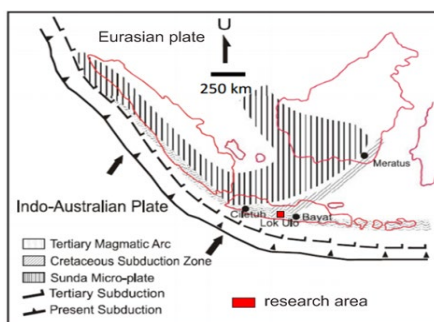


Figure 1. Regional tectonic framework (modified after Kartanegara, et al., 1987)

Because of the interaction between the Indo-Australian and Eurasian plates, the southern region of Java is one of Indonesia's highest seismically active regions. Local onshore faults, such as the Kebumen-Muria-Meratus major fault and the Cilacap-Pamanukan-Lematan major fault systems, cause earthquakes on shear faults, as shown in Figure 2. The southern region of Java is seismically active because of several tectonic factors (Tanjung et al., 2021).

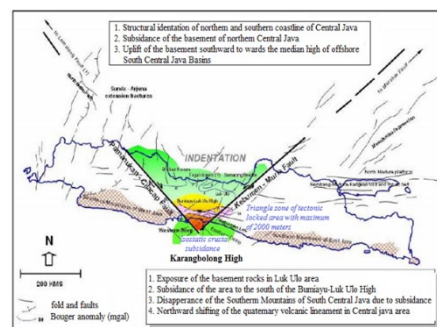


Figure 2. Two paired shear faults, the Kebumen-Muria Fault and the Pamanukan-Cilacap Fault (after Satyana, 2007)

Map of seismicity from 1900 to 2017 showing focal depths between 0–300 m and earthquake magnitudes of 5–10 on the Richter scale. In the historical record of earthquake events in Java, in the Kebumen area, an earthquake occurred on July 23, 1943. The earthquake was centered at 8.6 LS - 109.9 BT at a depth of 90 km with a magnitude of 8.1 on the Richter scale, or with an intensity of VII - VIII on the MMI scale, which caused damage in the area from West to East Java (Ashadi & Kaka, 2019; Griffin et

Authors information:

^aUniversitas PGRI Yogyakarta, Program Sarjana Teknologi Rekayasa Elektro-medis, Fakultas Sains dan Teknologi, Universitas PGRI Yogyakarta, Indonesia. E-mail: danangwidyawarman@upy.ac.id¹

^bUniversitas Gadjah Mada Yogyakarta, INDONESIA. E-mail: sismanto@ugm.ac.id²

^cUniversitas Sarjanawiyata Tamansiswa, INDONESIA. E-mail: adityayoga@ustjogja.ac.id³

*Corresponding Author: danangwidyawarman@upy.ac.id

Received: July 13, 2023

Accepted: December 22, 2023

Published: December 31, 2024

al., 2019).

In the Kebumen area, the two ends of a significant fault system came together in opposition in the regional geological context. The major Kebumen-Muria-Meratus and Cilacap-Pamanukan-Lematan major fault systems merged to form a fault junction, as shown in Figure 2. The extensive Kebumen-Muria-Meratus fault system extends from the Meratus Mountains in South Kalimantan in the northeast to the Kebumen coast. From Kebumen's shore, the extensive Cilacap-Pamanukan-Lematan fault system runs northwest towards Lematang, in South Sumatra (Harun, 2018). The Kebumen–Muria and Cilacap–Pamanukan faults caused the appearance of a depressed morphology on the Central Java coastline.

The two major fault systems are now inactive, except for a small segment of the large Cilacap-Pamanukan-Lematang Fault, including the Kroya, Bumiayu, and Baribis faults. Even though they were dead, the activities of the two in the past made the Kebumen area "locked" so that it was uplifted to the extreme, which made the Luk Ulo melange complex rise to the surface. This lifting also formed the South Gombang Mountains or Karangbolong, which have a height of more than 2,000 m; however, erosion has reduced these mountains to a height of approximately 600 m (Ansori & A Wardhani, 2019). The mainland of Kebumen has an old Kedungkramat fault, often known as the Kedungbener fault, as shown in Figure 3.

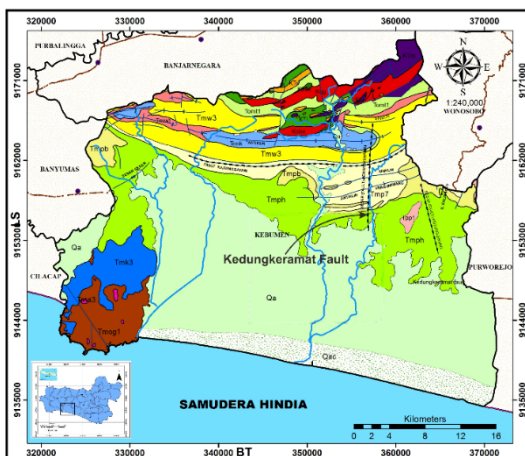


Figure 3. Regional Geologic Map of Kebumen Regency and Kedungkeramat Fault

The Kedungbener Valley is a relatively straight north-south trending valley that stretches for about 8 kilometers from the eastern side of the city of Kebumen to the hilly areas of Karanggulung. This valley is an expression of a fault on the Earth's surface currently called the Kedung Bener Fault or the Kedungkramat Fault. This fault is suspected of being responsible for the emergence of hot springs and the Alian geothermal reservoir system.

In the historical record of earthquake events in Java in the Kebumen region, an earthquake occurred on July 23, 1943. The earthquake was centered at 8.6 South Latitude - 109.9 East

Longitude or more precisely the Bantul area at a depth of 90 km with a magnitude of 8.1 on the Richter scale and an intensity of VII - VIII on the MMI scale; it caused damage in the West to East Java regions (Devi Riskianingrum, 2013). Every earthquake incident produces ground shaking, which can be identified by the value of the ground vibration acceleration at a certain location. The greater the value of ground vibration acceleration at a place, the greater the danger of an earthquake occurring at that place. The value of the ground vibration acceleration is one of the factors that can indicate the level of earthquake risk. The map of earthquake-prone areas was made based on the weighting of four parameters: geology (rock, morphology, and geological structure), intensity of earthquakes that have occurred, seismicity, and earthquake wave acceleration. Based on these parameters, earthquake disaster zones were created as very low, low, medium, and high earthquake hazard zones.

Microtremor measurements were performed because in the Kebumen Regency, there is a confluence of the two ends of a large fault system, which makes this area a zone of high earthquake shocks. From the microtremor measurements, the dominant frequency and amplification values were obtained, which were used to map the level of earthquake hazards using the vulnerability index parameter. A high vulnerability index indicates a high potential hazard caused by an earthquake.

2. Research Method

This study was conducted in Kebumen Regency, Central Java Province. Kebumen Regency is geographically located between 7°27' and 7°50' South latitude and 109°33' and 109°50' East longitude as shown in Figure 4.

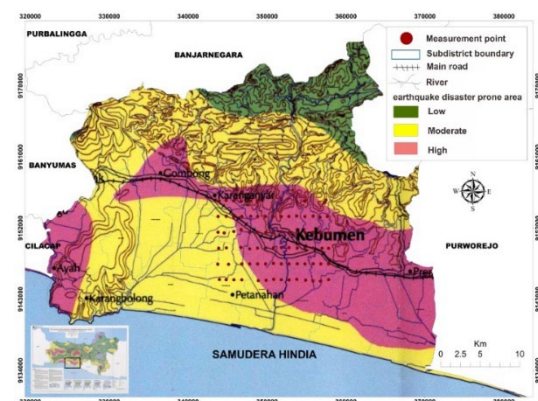


Figure 4. Map of the study area

The Purworejo Regency and Wonosobo Regency border the Kebumen Regency to the east, Banjarnegara Regency to the north, Banyumas Regency and Cilacap Regency to the west, and the Indonesian Ocean to the south. The 82 points of microtremor measurements for this investigation were obtained between September 15 and 24, 2017. Area measures are implemented in places vulnerable to disasters. Figure 5 shows the location map

and measurement sites.

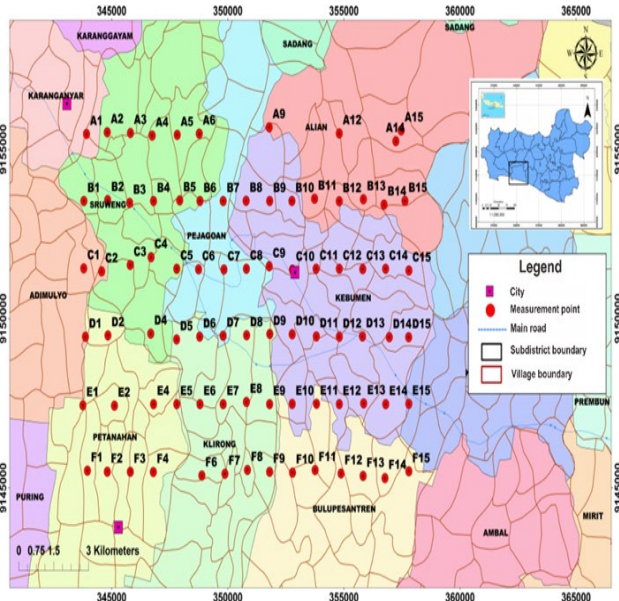


Figure 5. Map of locations and microtremor measurement points

The measurement area includes the ten districts of Karanganyar, Sruweng, Kebumen Kota, Pejagoan, Adimulyo, Petanahan, Klirong, Buluspesantren, Alian, and Kutowinangun, which surround Kebumen City's central business district. A single-station microtremor was used to collect measurement data. The locations were spaced 1000 m apart in a west-east direction and 2000 m apart in the north-south direction. A sample frequency of 100 Hz was used during the 35-minute measurement at each point.

The microtremor data sample locations in the research area were chosen after considering several criteria related to the norms established by the SESAME European Research Project (Alamri et al., 2020). A general layout of the study flowchart is shown in Figure 6. The acquired single-station microtremor data were represented by signals with three components: north-south (N-S), east-west (E-W), and vertical (Z). Figure 7 depicts the input signals for the three parts of the microtremor measurement results. The measurement data remain in the time domain because the data derived from the measurements are time series data. The output signal consists of a stationary signal and a transient signal. A steady signal, or one with the same amplitude, and no time-dependent variations, is required for microtremors.

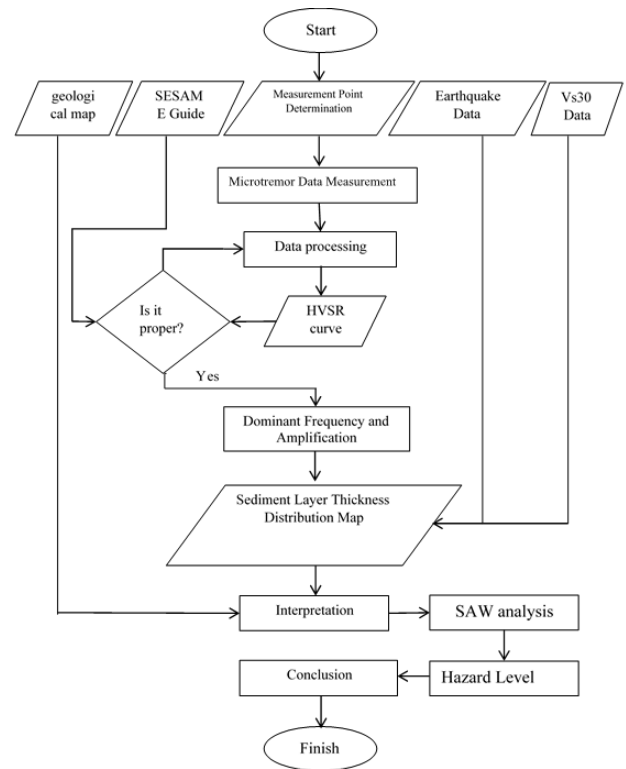


Figure 6. Research flowchart in general

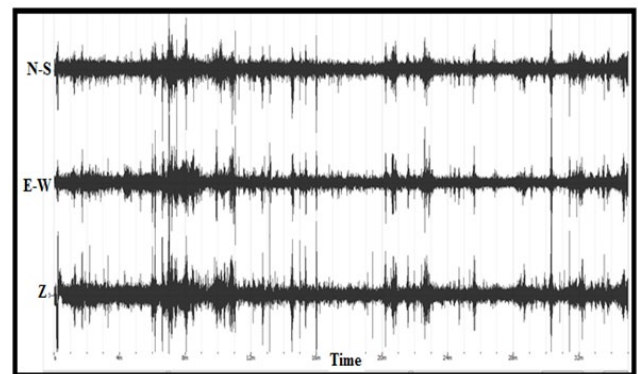


Figure 7. Raw 3-component single-station microtremor data in the time domain at point B-10

Figure 7 shows that processing in Geopsy software begins by displaying 3-component single station microtremor data in the time domain. Next, windowing was performed, which is a technique used to cut the signal to a limited number of sample points. The data in the window of each component were Fourier-transformed to obtain the average spectrum of each component. The resultant horizontal component, consisting of the north-south component and the east-west components, was divided by the vertical component to obtain the HVSr curve, as shown in Figure 8.

The HVSR (Horizontal to Vertical Spectral Ratio) curve is used to determine the natural frequency (f_0) and amplification (A_0) values, which are then used to compute the maximum ground vibration acceleration (PGA), seismic vulnerability index (K_g), sediment layer thickness value (h), and ground shear strain (γ) values. The two HVSR curve criteria suggested by SESAME were used to analyze the HVSR curve after processing using GEOPSY Software (Abdel-Rahman et al., 2012). The analysis was based on trustworthy HVSR curve criteria and SESAME's proposed HVSR curve criteria with distinct peaks (Abdel-Rahman et al., 2012). Eighty-two measurement points were obtained and an accurate HVSR curve was constructed by analyzing the HVSR curve. Twenty-four measurement points were obtained from the HVSR curve analysis results, in accordance with the requirements for a clear HVSR curve (clear peak).

3. Research Results

The results obtained from this research are natural frequency (f_0) and amplification (A_0) values at 82 measurement points in the Kebumen Regency, which are located in 10 subdistricts: Karanganyar, Sruweng, Kebumen Kota, Pejagoan, Adimulyo, Petanahan, Klirong, Buluspesantren, Alian, and Kutowinangun. The HVSR curves of the measurement results are shown in Figure 8.

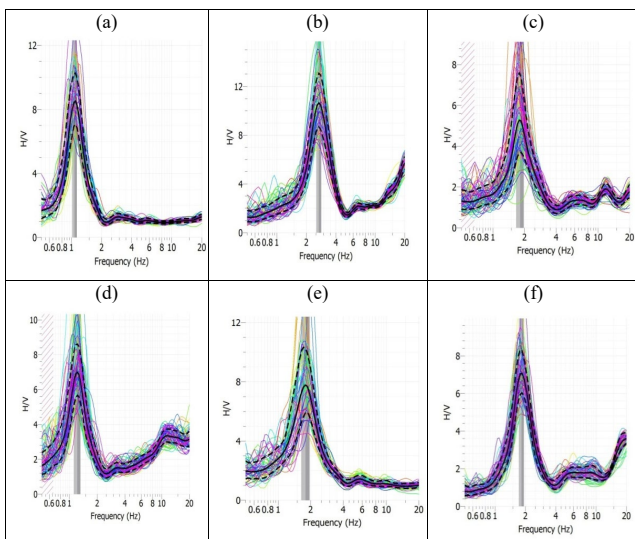


Figure 8. HVSR spectrum at points (a) B-10, (b) B-15, (c) C-06, (d) C-09, (e) D-08, and (f) E-15.

The HVSR curve results were used to determine the dominant frequency value, which was subsequently used to create a contour map of the dominant frequency distribution in Kebumen City and its surroundings, as shown in Figure 9. Between 0.62 and 5.26 Hz is the dominating frequency in the study area. Low dominant frequency values, which span the frequency range of 0.62 to 1.51 Hz, predominate in the frequency distribution of Kebumen City District. Adimulyo District, Alian District, Bulus Pesantren District, Klirong District, and Sruweng District; these districts were also scattered with low dominant frequencies, as shown in green in Figure 9.

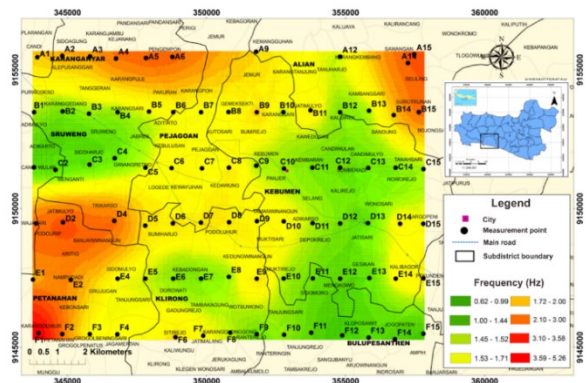


Figure 9. Distribution map of dominant frequency (f_0) overlaid with administrative map of Kebumen Regency

Low dominant frequency values are found at measurement points A12, B01, B02, B03, B04, B05, B10, B12, B13, C01, C02, C03, C04, C05, C09, C10, C11, C12, C13, C14, C15, D11, D12, D13, E05, E06, E07, E08, E09, E10, E11, E12, E13, F08, F10, F11, F12, F13, F14, and F15. Areas with moderate frequency values of 1.52 Hz to 1.74 Hz are spread across Kota Kebumen District, Alian District, Kutowinangun District, Klirong District, Pejagoan District, and Petanahan District which are shown in yellow in Figure 9.

Moderate frequency values are at measurement points B06, B07, B08, C06, C07, C08, B11, D05, D06, D07, D08, D09, D10, D14, D15, E01, E04, E09, E14, E15, F03, F04, and F06. Areas with moderate frequency were mostly found in the alluvial formation in the central part of the study area, with some entering the Halang Formation in the northern and eastern parts of the study area. Areas with high frequency values of 1.75 Hz to 5.26 Hz are scattered in Kota Kebumen District, Alian District, Karanganyar District, Sruweng District, and Petanahan District as shown in red in Figure 9. High-frequency values were observed at measurement points A01, A02, A03, A04, A05, A06, A14, A15, B09, B14, B15, D01, D02, E02, F01, and F02. The Halang Formation, composed of andesitic sandstones, tuffaceous conglomerates, and marl mixed with sandstones, has the majority of prominent high-frequency values. Due to the thinner sediment layer in the southwest of the study area than in the south, high frequencies were also discovered in the alluvial formations. If the dominant frequency value is adapted to the topography of the study area based on the processing results, it is appropriate. Low dominant frequency values were found in regions with low altitudes compared with other measurement locations.

The amplification value is the strengthening of shaking during an earthquake, which was obtained from the results of the HVSR analysis and was then used to create a contour map of the distribution of amplification values in Kebumen City and its surroundings, as shown in Figure 10. This amplification is caused by the impedance contrast, that is a considerable change in rock compactness between the sedimentary and bedrock layers (Kyaw et al., 2015). The amplification value is related to the rock density level; a lower rock density can increase the amplification value. A low dominant frequency value results in a high amplification value (amplification) for earthquake waves, and vice versa. If an earthquake occurs in an area, there will be amplification (strengthening) according to the amplification value for that area. This can lead to an even greater potential earthquake risk.

The amplification value in the study area ranged from 1.16 to 10.61 shown in Figure 10. Based on Figure 10 the low amplification value are shown in green with a range of values from 1.16 to 4.30 which are spread across Sruweng District, Kecamatan Pejagoan, the northern part of Kebumen City District, Petanahan District, Klirong District, Buluspesantren District, and Alian District. Low amplification value are at measurement points A12, A14, B04, B05, B06, B07, B08, C06, C07, C13, C15, D01, D02, E05, E06, E07, E08, E09, E10, F01, F02, F03, F04, F06, F07, F08, F09, F10, F11, F12, F13, F14, and F15. Low amplification values were observed in the alluvial formation to the south of the study area and Halang Formation to the north of the study area. Moderate amplification values with a range from 4.31 to 5.50, are shown in yellow and spread over Alian, Klirong, Pejagoan, and Petanahan sub-districts. Moderate amplification values were obtained at the measurement points A01, A03, A09, A15, C14, D05, D06, D07, E02, E04, E11, F13, F14, and F15.

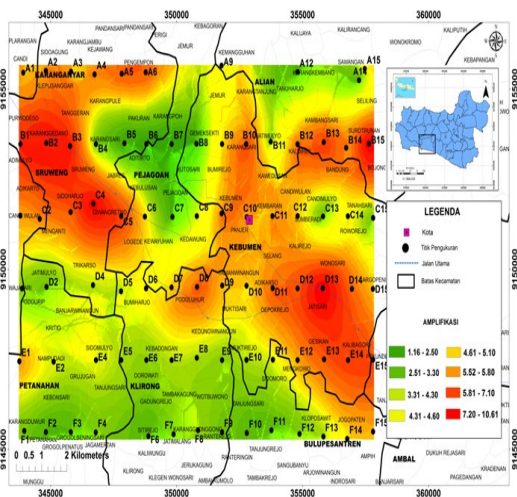


Figure 10. Map of the amplification value (A0) distribution overlaid with the administrative map of Kebumen Regency

The dominant frequency and shear wave velocity at a depth of 30 m (V_{s30}) were used to calculate the sediment layer thickness. Equation 1 can be used to express the sediment layer thickness and dominant frequency (Wulandari et al., 2018). A contour map of the distribution of the sediment layer thickness values was then created, as shown in Figure 11. The sediment layer thickness

values were interconnected with the dominant frequency values in the area.

Very low dominant frequency values affect long-period vibration hazards and low dominant frequency values produce thick layers of sediment (Thamarux et al., 2019). An area with a thick layer of sediment over a long period can threaten high-rise buildings if earthquakes occur in the area. Areas with high dominant period values have thick layers of sediment (Edison, 2022). A thick layer of sediment causes sufficiently high damage when an earthquake occurs because the value of the dominant period is directly proportional to the amplification value (Edison, 2022). A thick layer of sediment causes significant damage when an earthquake occurs.

$$h = \frac{V_s}{4f_0} \tag{1}$$

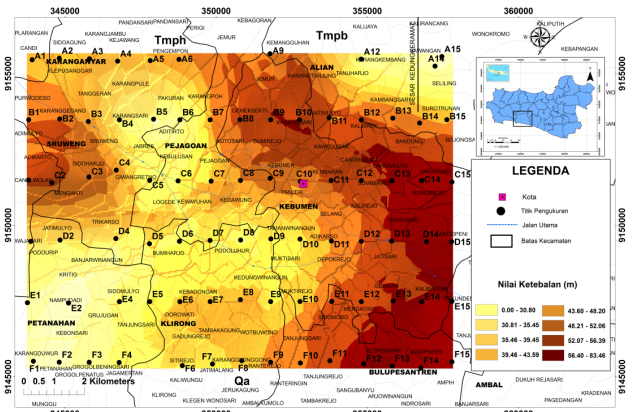


Figure 11. Distribution map of sediment layer thickness values (h) overlaid with the administrative map of Kebumen Regency

From Figure 11, the distribution of moderate sediment thickness values was found to be at measurement points A01, A02, A03, A04, A05, A06, A15, B01, B02, B03, B04, B05, B06, B09, B11, B14, B15, C01, C02, C03, C04, C05, C06, C07, C08, C09, C10, C11, C12, C14, D04, D05, D06, D07, D08, D09, D10, D11, D12, D13, E04, E05, E06, E07, E08, E09, E10, E11, E12, E13, E14, E15, F03, F04, F06, F07, F08, F09, F10, F13, and F11. Areas that have thick sediment layer with thickness between 60 and 120 m are shown in dark brown, which are spread in the eastern part of Kota Kebumen District, Alian District, and Buluspesantren District. These sediment thickness values were distributed at measurement points A09, A12, A14, B10, B12, C15, D14, F12, F14, and F15.

4. Conclusion

Microtremor readings taken in Kebumen and its vicinity were used to produce the findings of this study. Eighty-two measurement points were obtained and an accurate HVSR curve was constructed by analyzing the HVSR curve. Twenty-four measurement points were obtained from the HVSR curve analysis results, in accordance with the requirements for a clear HVSR curve (clear peak). The amplification value (Ao) ranged from 1.16 to 10.61, and the dominating frequency (fo) ranged from 0.62 to 5.26 Hz based on the processing of microtremor data. The seismic map was merged with maps of social vulnerability, infrastructure, and economics. The risk of earthquakes in the Kebumen area can be classified into three categories. A few places in Petanahan District, Klirong District, Bulus Pesantren District, and Pejagoan District have low levels of seismic danger. There are a few places in Pejagoan District, Sruweng District, Petanahan District, Kebumen City District, Buluspesantren District, and Alian District that are moderately dangerous. Sruweng, Adimulyo, Kota Kebumen, Alian, and Buluspesantren Districts contain several high-risk zones.

5. References

- Abdel-Rahman, K., Abd El-Aal, A. K., El-Hady, S. M., Mohamed, A. A., & Abdel-Moniem, E. (2012). Fundamental site frequency estimation at new domiat city, Egypt. *Arabian Journal of Geosciences*, 5(4), 653–661. <https://doi.org/10.1007/s12517-010-0222-2>
- Alamri, A. M., Bankher, A., Abdelrahman, K., El-Hadidy, M., & Zahran, H. (2020). Soil site characterization of Rabigh city, western Saudi Arabia coastal plain, using HVSR and HVSR inversion techniques. *Arabian Journal of Geosciences*, 13(2). <https://doi.org/10.1007/s12517-019-5027-3>
- Ansori, C., & A Wardhani, F. (2019). Tipe Magmatik Batuan Beku Formasi Gabon di Tinggian Karangbolong, Kebumen. *Jurnal Geologi Dan Sumberdaya Mineral*, 20(2), 63. <https://doi.org/10.33332/jgsm.v20i2.406>
- Ashadi, A. L., & Kaka, S. L. I. (2019). Ground-Motion Relations for Subduction-Zone Earthquakes in Java Island, Indonesia. *Arabian Journal for Science and Engineering*, 44(1), 449–465. <https://doi.org/10.1007/s13369-018-3563-x>
- Devi Riskianingrum. (2013). Penanganan Bencana Dan Transformasi Pengetahuan Tentang Kegempaan Di Masa Kolonial. *Paramita: Historical Studies Journal*, 23(1), 1–13. <https://journal.unnes.ac.id/nju/index.php/paramita/article/view/2492/2545>
- Edison, R. (2022). Pemetaan Vs30 Dengan Menggunakan Korelasi Zhao Di Pesisir Cilacap. *Jurnal Geosaintek*, 8(1), 181. <https://doi.org/10.12962/j25023659.v8i1.12601>
- Griffin, J., Nguyen, N., Cummins, P., & Cipta, A. (2019). Historical earthquakes of the eastern sunda arc: Source mechanisms and intensity-based testing of Indonesia's national seismic hazard assessment. *Bulletin of the Seismological Society of America*, 109(1), 43–65. <https://doi.org/10.1785/0120180085>
- Harun, A. (2018). Subvolcanic Hydrocarbon Prospectivity of Java: Opportunities and Challenges. October, 13–16. <https://doi.org/10.29118/ipa.0.15.g.105>
- Kyaw, Z. L., Pramumijoyo, S., Husein, S., Fathani, T. F., & Kiyono, J. (2015). Seismic Behaviors Estimation of the Shallow and Deep Soil Layers Using Microtremor Recording and EGF Technique in Yogyakarta City, Central Java Island. *Procedia Earth and Planetary Science*, 12, 31–46. <https://doi.org/10.1016/j.proeps.2015.03.024>
- Sili, P. D. (2013). Penentuan Seismisitas dan Tingkat Risiko Gempa Bumi. In *Gempa Bumi*. Universitas Brawijaya Press.
- Tanjung, N. A. F., Permatasari, I., & Yuniarto, A. H. P. (2021). Mapping of weathered layer thickness and Seismic Vulnerability in Tegal using HVSR method. *Journal of Physics: Conference Series*, 1951(1). <https://doi.org/10.1088/1742-6596/1951/1/012053>
- Thamarux, P., Matsuoka, M., Poovarodom, N., & Iwahashi, J. (2019). VS30 seismic microzoning based on a geomorphology map: Experimental case study of Chiang mai, Chiang rai, and Lamphun, Thailand. *ISPRS International Journal of Geo-Information*, 8(7), 1–18. <https://doi.org/10.3390/ijgi8070309>
- Wulandari, A., Suharno, Rustadi, & Robiana, R. (2018). Pemetaan Mikrozonasi Daerah Rawan Gempabumi Menggunakan Metode HVSR Daerah Painan Sumatera Barat. *Jurnal Geofisika Eksplorasi Vol.*, 4(1).

A Spatial Epidemiological Investigation of COVID-19 in the MENA Region: Modeling Incidence and Impact Factors

Mustafa Shebani Aboalyem^{1ab*}, Mohd Tahir Ismail^{2a}

Abstract: The COVID-19 pandemic has negatively impacted the global economy and society. World Health Organization (WHO) reported that as of early July 2023, the virus has infected more than 690 million individuals and has resulted in more than 6.9 million deaths worldwide. This study aims to investigate spatial epidemiological factors of COVID-19 in the Middle East and North Africa (MENA) region. By employing various spatial modeling techniques, this study establishes that multiscale geographically weighted regression (MGWR) is the best-fitted model, with the lowest residual sum of squares (11.22) and the lowest Akaike's Information Criteria (AIC) value (58.41), explaining 84.3% of the variance ($R^2=0.843$). Our study finds that population density, total vaccination doses, unemployment, and GDP per capita are critical factors associated with COVID-19 in the MENA region. These valuable insights provide policymakers and public healthcare experts with the information needed to develop targeted interventions that can mitigate risk factors related to the COVID-19 pandemic.

Keywords: COVID-19, GIS modelling, global models, MENA Region, MGWR, spatial modeling.

1. Introduction

SARS-CoV-2, also known as COVID-19, is a virus that causes severe acute respiratory syndrome. This highly contagious and novel pathogen first emerged in Wuhan, China, in late 2019. It quickly became a global pandemic, posing major challenges to public health systems and negative impacts on the global economy and society. While many COVID-19 studies examined the impacts of epidemic outbreaks, they tend to focus on specific countries. One gap in existing research is the limited use of geospatial data for a comprehensive understanding of the disease's incidence and impact. For example, (Daniel & Adejumo, 2021) found no clear relationship between COVID-19 and population density in Nigeria using a binomial regression model. However, when (Bayode et al., 2022) expanded their analysis in spatial regression, they uncovered the significance of population density. Similarly, (Iyyanki et al., 2020) applied spatial modeling to identify a sudden surge in COVID-19 cases during social isolation or quarantine periods.

In a broader context, the likelihood of COVID-19 cases significantly increased due to urbanization and population density (Dutta et al., 2021). Their study utilized spatial models, along with geographically weighted models, to reach this conclusion. Spatial regression has also contributed during vaccination response (Ahasan et al., 2020; Franch-Pardo et al., 2020), providing valuable insights into the course of COVID-19 and helping identify factors contributing to the disease's spread. Consequently, it has

become essential to implement effective strategies for social isolation and mobility restrictions (Jaber, 2022). Thus, geospatial data analysis remains critical for an epidemiological investigation across various spatial and spatiotemporal scales (Mollalo et al., 2020).

Several authors have employed spatial analysis to examine the geographical determinants of COVID-19 (Aboalyem et al., 2024; Abolfazl Mollalo et al., 2021; Dutta et al., 2021; Mansour et al., 2021). They have used methods like GWR, MGWR, spatial lag model (SLM), and spatial error model (SEM). As mentioned earlier, geospatial data analysis provides valuable insights into the course of COVID-19 and helps identify regional factors contributing to the disease's spread. However, prior studies primarily focused on the national level, with no regional analysis conducted in the Middle East and North Africa (MENA) region. This present study represents the first of its kind in utilizing spatial analysis of five distinct models to examine the primary causes of the COVID-19 outbreak and assess the presence of geographical dependence in the MENA region.

Globalization has intensified travel, communication, and socioeconomic participation, of which indirectly amplified the speed, frequency, and geographic reach of diseases (Mansour et al., 2021). There is, for example, a geographical link between the Middle East and North Africa, indicating that the disease's possible effects cannot be overlooked. The aim of this research is to investigate the spatial relationship between 13 independent variables and the incidence of COVID-19 in MENA countries (Table 1). The study utilized five statistical models, namely ordinary least square (OLS), SLM, SEM GWR, and MGWR.

This present study found that GDP per capita, unemployment, total vaccination, and population density are the main factors that

Authors information:

^aSchool of Mathematical Sciences, Universiti Sains Malaysia, 11800 USM Penang, MALAYSIA. E-mail: m.aboalyem@misuratau.edu.ly¹; m.tahir@usm.my²

^bDepartment of Statistics, Faculty of Sciences, Misurata University, Misrata, LIBYA. E-mail: m.aboalyem@misuratau.edu.ly¹

*Corresponding Author: m.aboalyem@misuratau.edu.ly

Received: September 15, 2023

Accepted: December 21, 2023

Published: December 31, 2024

determine the speed of COVID-19 transmission. The findings of this study can help develop effective strategies to reduce the impact of COVID-19 on people and the global economy. These findings may also contribute to evidence-based decision-making in public health programs to design interventions to reduce transmission and risk causes related to the COVID-19 epidemic in the MENA region. The remainder of the paper is organized as follows: Section 2 presents the study region and database, Section 3 describes OLS and spatial analysis, Section 4 presents results, and Section 4 discusses OLS and spatial regression results. Conclusions are drawn in Section 6.

2. Study Region and Database

Study Region

The MENA region consists of many countries, from rich oil-exporting Gulf countries to low- and middle-income countries. However, different organizations classify the region differently, and the terms (Arab World) and (Greater Middle East) are used interchangeably (Seyfi & Hall, 2020). According to the World Bank, the region covers 19 countries and accounts for 6.03% of the world's population (Wang & Wang, 2021). This includes countries like Algeria, Bahrain, Djibouti, Egypt, Iran, Iraq, Israel, Jordan, Kuwait, Lebanon, Libya, Morocco, Oman, Palestine, Qatar, Saudi Arabia, Somalia, Syria, the United Arab Emirates, and Yemen. However, Turkey, Sudan, and Cyprus are occasionally included in the MENA region (Gollin et al., 2016; Karim et al., 2022). This study is based on the World Bank and the United Nations Statistics Division, which listed Algeria, Bahrain, Djibouti, Egypt, Iran, Iraq, Sudan, Israel, Jordan, Kuwait, Lebanon, Libya, Morocco, Oman, Tunisia, Palestine, Qatar, Saudi Arabia, Syria, Somalia, Turkey, Cyprus, United Arab Emirates and Yemen as part of the MENA region (Fig. 1) (Aminova et al., 2020; Davoodi & Abed, 2003).

Database

In this analysis, we collected data from Our World in Data, International Labor Organization (ILO), and PEMANDU Associates, the responsible body for monitoring COVID-19 across the MENA region. Our data collection began with the initial reported cases in each nation and continued until December 2022. We computed the incidence rate at the regional level (Fig. 2). To achieve this, we established a geodatabase using GIS software, which includes GeoDa 1.20.0.20, QGIS 3.30.2, and ArcMap 10.8.2. Additionally, RStudio 2023.06.0 was deployed to link demographic, healthcare, and socioeconomic variables into geopolitical boundary shapefile (Table 1).

3. Methodology and Methods

Ordinary Least Squares (OLS)

Multicollinearity diagnostics and forward stepwise regression with multiple OLS are used to determine the linear relationship between COVID-19 incidence (dependent variable) and demography, behavioral, medical, and socioeconomic variable groups as follows (Ward & Gleditsch, 2018):

$$y_i = \beta_0 + x_i\beta + \varepsilon_i \quad (1)$$

x_i is the explanatory variables, y_i is the dependent variable, ε_i is the error term, β_0 is the intercept, and β is the coefficients (Anselin & Arribas-Bel, 2013; Ward & Gleditsch, 2018). In OLS, observations must be independent from each other and constant with independent error components (Aboalyem & Ismail, 2023). OLS implies that the observation at the county level is independent and that spatial dependence does not occur (M Rahman et al., 2020).

Spatial Lag Model (SLM)

SLM regression incorporates spatial lagged dependent variables into the OLS equation. According to (Sannigrahi et al., 2020), spatial lag accounts for the influence or impact of neighbor countries or regions (M Rahman et al., 2020). The weight matrix of the SLM takes autocorrelation into account. SLM can be illustrated as below:

$$y_i = \beta_0 + x_i\beta + \rho W_i y_i + \varepsilon_i \quad (2)$$

W_i is the spatial weights vector; ρ is the parameter of spatial autoregressive; and $x_i, \beta_0, \beta, \varepsilon_i$ are same as in Equation 1. The weight matrix (W_i) relates one independent variable to the other independent variable and describes how the both independent variables interact (Anselin & Arribas-Bel, 2013; Ward & Gleditsch, 2018).

Spatial Error Model (SEM)

This model implies that error terms are spatially dependent. Consequently, residuals are dissected into error terms and the model's overall structure (Abolfazl Mollalo et al., 2021):

$$y_i = \beta_0 + x_i\beta + \lambda W_i \xi_i + \varepsilon_i \quad (3)$$

The spatial component of the error term is denoted by ξ_i , while lambda (λ) represents the strength of correlation between the elements. The uncorrelated standard error is represented by ε_i . W_i is the spatial of weight matrices, $W_i \xi_i$ is the strength of the correlation between the spatial component of the error term. The rest, x_i, β_0 , and β are as same as in Equation 1 (Ward & Gleditsch, 2018). The SEM model compensates spatial error autocorrelation through the spatially weight matrices (Dutta et al., 2021).

Geographically Weighted Regression (GWR)

The GWR builds spatial modelling between an y and x_i variables (Comber et al., 2022). As explained below, GWR is a technique that establishes the spatial association among variables (Abolfazl Mollalo et al., 2021):

$$y_i = \beta_{i0} + \sum_{j=1}^m \beta_{ij} X_{ij} + \varepsilon_i, \quad i = 1, 2, 3, \dots, n \quad (4)$$

where at country i , y_i is the the dependent variable, and β_{i0} is the intercept, β_{ij} is the j th regression parameter, X_{ij} is the value

of the j th explanatory parameter, and ε_i is an error term (Abolfazl Mollalo et al., 2021). Traditional global models cannot consider a non-stationary spatial problem (Sannigrahi et al., 2020). Consequently, these models estimate average throughout the entire area of interest (Deilami & Kamruzzaman, 2017; Hamad et al., 2023). The GWR model, in contrast, overrides this restriction because of its cumulative local efficiency, which incorporates a geographic context from which parameters are estimated individually (Oshan et al., 2019).

Multiscale Geographically Weighted Regression (MGWR)

The Multiscale-GWR is an extension of GWR model that allows analysis at multiple scales and bandwidths (Dai et al., 2022). Therefore, it relaxes the GWR assumption. The ideal bandwidth vector must be derived, with every component representing the spatial scale upon which a certain function occurs (Hamad et al., 2023). Theoretically, MGWR is close to Bayesian framework and may offer a more adaptable and scalable framework for analyzing multiscale phenomena (Abolfazl Mollalo et al., 2021):

$$y_i = \sum_{j=1}^m \beta_{bwj} X_{ij} + \varepsilon_i, \quad i = 1, 2, \dots, n \quad (5)$$

At area i , β_{bwj} is the bandwidth utilized, X_{ij} is the value of the j th iv parameter (Abolfazl Mollalo et al., 2021; Fotheringham et al., 2017). Its advantages over MGWR include its ability to accurately capture regional heterogeneity, reduce collinearity, and biasedness in the estimates (Oshan et al., 2019). The MGWR is often regarded as the generalized additive model (GAM), for allowing a back-fitting technique in calibrating MGWR models (Buja et al., 1989; Hastie & Tibshirani, 1990).

4. Results

Table 1 presents the description of the response and explanatory variables. At the same time, the statistical summary of the global OLS model is shown in Table 2. The best-fitted model will be chosen after using the forward stepwise regression technique. We found that GDP per capita, unemployment, and the total vaccination are essential explanatory variables and significant at a 5% level, but the population density is significant at a 10% level. Moreover, the significant variables show variance inflation factors (VIF) below 10, indicating the absence of serious multicollinearity issue (Thompson et al., 2017).

However, a moderate level of collinearity is evident between the total vaccination and GDP per capita variables, as indicated by the higher standard errors in the model. Consequently, the OLS regression model produced the lowest R-squared value ($R^2=0.743$) in comparison to the spatial dependence models. Nevertheless, this finding underscores that approximately 26% of the incidence rate across MENA countries can be attributed to country-level differences, presenting a challenge for OLS in estimating the model. To address this challenge, the SEM and SLM models were added to the OLS. As improvements, all variables became statistically significant at the 5% level, thereby enhancing the OLS

model. However, due to the previous underestimation of the spatial process, the SEM and SLM models may exhibit lower standard errors than the OLS estimation (Table 3), indicating limited ability to estimate accurately in modeling.

However, we use GWR and MGWR to solve this issue by exploring any local spatial differences. The results demonstrate that the value of R^2 grew from 80.4% in the SLM model, the model with the greatest R^2 globally to 84.3% in the MGWR model, while the AIC reduced from 70.06 in the SLM model to 58.41 in the MGWR model. Therefore, given that MGWR's coefficient of determination was the highest, the model may account for 84.3% of all variations in COVID-19 incidence rates. With a higher AIC of 58.82 compared to MGWR's with an AIC of 58.41, regular GWR had a slightly poorer goodness-of-fit score of 0.840 (Table 4). With a higher RSS of 11.38 than MGWR's RSS of 11.22, the residual sum of squares behaves similarly to AIC, slightly different across the local models.

Figure 1 shows how the y_i incidence rate of COVID-19 variable is distributed across subnational borders. Five models (global and local) were to be implemented to understand the linear and spatial relationship of independent variables to the incidence of COVID-19 in MENA countries. By enabling the computation of local levels rather than stationary parameter values, the local-level modelling procedure was a powerful method that improves conventional global regression. Population density and GDP per capita significantly impact the explanation of disease incidence rates in different MENA countries (Fig. 1).

Figures 2 and 3 present the results of GWR and MGWR models. As shown in Figure 3, while the effect of population density is seen at the country level, the COVID-19 infection situation follows a similar trend at the regional level for local models. Population density is crucial in determining COVID-19 infection rates across North African nations, particularly in Morocco, Sudan, Somalia, and Djibouti. However, the impact of GDP per capita on COVID-19 incidences was found to be inconsistent between the models.

Figure 4 shows that the unemployment indices in the GWR and MGWR models are the same and significantly impact the disease incidence rates in parts of Asia (Iran, Jordan, and Palestine) and northern Africa like Algeria, Egypt, Libya, Morocco, and Tunisia. Conversely, both models performed poorly in the countries of the southern MENA, namely Djibouti and Somalia. Furthermore, both models concluded that the geographical distribution of COVID-19 incidence rates in Iran, Djibouti, and Somalia could be significantly explained by the total vaccine doses coefficient.

Finally, the spatial distributions of local R^2 values in the GWR and MGWR models are shown in Figure 5. The darker shade shows higher values, while the lighter shades show lower values. All countries are found to have acceptable local R^2 values, and the model was most suitable for Somalia and Djibouti. Furthermore, the independent variables in both models account for at least 80% of the variation in Egypt and Palestine; the highest explanation percentage comes from Yemen, Somalia, and Djibouti, at 88%.

5. Discussion

In this study, we analyzed 19 variables, divided into four

categories (demographic, behavioral, medical, and socioeconomic) that describe the geographic distribution of the COVID-19 situation in the MENA countries. We estimated the regional distribution of COVID-19 cases using a spatial regression and autoregressive model. Our analysis suggests that a combination of population density, GDP per capita, unemployment rate, and total vaccination response may be responsible for differences in the disease incidence rates across MENA countries.

Findings from the GWR and MGWR models show a strong relationship between the incidence of diseases in this region and population density, GDP per capita, unemployment, and vaccination. As the virus continued to spread, healthcare systems faced vulnerabilities, the economy declined, and unemployment rates rose. Our findings are also consistent with the importance of vaccination during the epidemic.

According to the positive GDP per capita coefficient, increasing population density in areas with high GDP per capita will increase the probability of contracting COVID-19. The emergence of new or different strains can positively impact overall immunity. This suggests that outbreaks are more severe in areas with higher immunity.

6. Conclusions

Understanding factors that affect incidence of diseases is important, especially for diseases such as COVID-19, which has a global impact. The aim of this study is to identify variables that may affect the incidence of COVID-19 in MENA countries. We investigated the incidence patterns and impact factors of COVID-19 in the MENA region, using spatial models. Among these models, MGWR showed the highest level of fit, strengthening and extending previous findings. Regional differences observed in MGWR may indicate variations in COVID-19 incidence based on the identified independent variables. This study is important for future understanding as, to our knowledge, there have been no previous studies using spatial trends of COVID-19 incidence in the MENA region

7. References

- Shebani Aboalyem, M., & Ismail, M. T. (2023). *Mapping the pandemic: A review of GIS-based spatial modeling of COVID-19*. *Journal of Public Health in Africa*, *14*(11). <https://doi.org/10.4081/jphia.2023.2767>.
- Aboalyem, M. S., Ismail, M. T., & Abdul Karim, S. A. (2024). Understanding COVID-19 Recovery Dynamics in the MENA Region: A Geospatial Analysis of Key Determinants and Implications. In S. A. Abdul Karim (Ed.), *Intelligent Systems Modeling and Simulation III: Artificial Intelligent, Machine Learning, Intelligent Functions and Cyber Security* (pp. 235-253). Springer Nature Switzerland. https://doi.org/10.1007/978-3-031-67317-7_15
- Abolfazl Mollalo, Kiara M. Rivera, & Nasim Vahabi. (2021). Spatial statistical analysis of pre-existing mortalities of 20 diseases with COVID-19 mortalities in the continental United States. *Sustainable Cities and Society*, *67*, 102738.
- Ahasan, R., Alam, M. S., Chakraborty, T., & Hossain, M. M. (2020). Applications of GIS and geospatial analyses in COVID-19 research: A systematic review. *F1000Research*, *9*.
- Aminova, M., Mareef, S., & Machado, C. (2020). Entrepreneurship Ecosystem in Arab World: the status quo, impediments and the ways forward. *International Journal of Business Ethics and Governance*, *3*(3), 1-13.
- Anselin, L., & Arribas-Bel, D. (2013). Spatial fixed effects and spatial dependence in a single cross-section. *Papers in Regional Science*, *92*(1), 3-17.
- Bayode, T., Popoola, A., Akogun, O., Siegmund, A., Magidimisha-Chipungu, H., & Ipingbemi, O. (2022). Spatial variability of COVID-19 and its risk factors in Nigeria: A spatial regression method. *Applied Geography*, *138*, 102621.
- Buja, A., Hastie, T., & Tibshirani, R. (1989). Linear smoothers and additive models. *The Annals of Statistics*, 453-510.
- Comber, A., Brunsdon, C., Charlton, M., Dong, G., Harris, R., Lu, B., ., & Wang, Y. (2022). A route map for successful applications of geographically weighted regression. *Geographical Analysis*, 2022.
- Dai, Z., Wu, S., Wang, Y., Zhou, H., Zhang, F., Huang, B., & Du, Z. (2022). Geographically convolutional neural network weighted regression: a method for modeling spatially non-stationary relationships based on a global spatial proximity grid. *International journal of Geographical Information Science*, 1-22.
- Daniel, O., & Adejumo, O. (2021). Spatial Distribution of COVID-19 in Nigeria. *West African Journal of Medicine*, *38*(8), 732-737.
- Davoodi, M. H. R., & Abed, M. G. T. (2003). *Challenges of growth and globalization in the Middle East and North Africa*. International Monetary Fund.
- Deilami, K., & Kamruzzaman, M. (2017). Modelling the urban heat island effect of smart growth policy scenarios in Brisbane. *Land use policy*. *The International Journal Covering All Aspects of Land Use*, *64*, 38-55.
- Dutta, I., Basu, T., & Das, A. (2021). Spatial analysis of COVID-19 incidence and its determinants using spatial modeling: A study on India. *Environmental Challenges*, *4*, 100096.
- Fotheringham, A., S, Yang, W., & Kang, W. (2017). Multiscale geographically weighted regression (MGWR). *Annals of the American Association of Geographers*, *107*(6), 1247-1265.

- Franch-Pardo, I., Napoletano, B. M., Rosete-Verges, F., & Billa, L. (2020). Spatial analysis and GIS in the study of COVID-19. A review. *Science of the Total Environment*, 739, 140033.
- Gollin, D., Jedwab, R., & Vollrath, D. (2016). Urbanization with and without industrialization. *Journal of Economic Growth*, 21(1), 35-70.
- Hamad, F., Younus, N., Muftah, M. M., & Jaber, M. (2023). Viability of Transplanted Organs Based on Donor's Age. *Sch J Phys Math Stat*, 4, 97-104.
- Hastie, T. J., & Tibshirani, R. J. (1990). *Generalized additive models* (Vol. 43). CRC press.
- Iyyanki, M., Prisilla, J., & Kandle, S. (2020). Spatial modeling for COVID-19 analysis: An Indian case study. *J Med Sci Res*, 8(S1), 19-32.
- Jaber, M. (2022). A Spatiotemporal Bayesian Model for Population Analysis.
- Karim, M. S., Ambrosetti, E., & Ouadah-Bedidi, Z. (2022). Demographic Features in West Asian and North African Countries: The Impact of Population Policies. In *International Handbook of Population Policies* (pp. 229-254). Springer.
- Mansour, S., Al Kindi, A., Al-Said, A., Al-Said, A., & Atkinson, P. (2021). Sociodemographic determinants of COVID-19 incidence rates in Oman: Geospatial modelling using multiscale geographically weighted regression (MGWR). *Sustainable Cities and Society*, 65, 102627.
- Mollalo, A., Vahedi, B., Bhattarai, S., Hopkins, L. C., Banik, S., & Vahedi, B. (2020). Predicting the hotspots of age-adjusted mortality rates of lower respiratory infection across the continental United States: Integration of GIS, spatial statistics and machine learning algorithms. *International Journal of Medical Informatics*, 142, 104248.
- Oshan, T., M, Li, Z., Kang, W., Wolf, L., J, & Fotheringham, A. (2019). mgwr: A Python implementation of multiscale geographically weighted regression for investigating process spatial heterogeneity and scale. *ISPRS International Journal of Geo-Information*, 8(6), 269.
- Rahman, M., Zafri, N., M, Ashik, F., R, & Waliullah, M. (2020). GIS-based spatial modeling to identify factors affecting COVID-19 incidence rates in Bangladesh. *MedRxiv*, 1202.
- Rahman, M., Zaman, N., Asyhari, A., T, Al-Turjman, F., Bhuiyan, M., Z, A, & Zolkipli, M. (2020). Data-driven dynamic clustering framework for mitigating the adverse economic impact of Covid-19 lockdown practices. *Sustainable Cities and Society*, 62, 102372.
- Sannigrahi, S., Pilla, F., Basu, B., Basu, A., S, & Molter, A. (2020). Examining the association between socio-demographic composition and COVID-19 fatalities in the European region using spatial regression approach. *Sustainable Cities and Society*, 62, 102418.
- Seyfi, S., & Hall, C. M. (2020). Cultural heritage tourism in the MENA: Introduction and background. In *Cultural and heritage tourism in the Middle East and North Africa* (pp. 1-33). Routledge.
- Thompson, C. G., Kim, R. S., Aloe, A. M., & Becker, B. J. (2017). Extracting the variance inflation factor and other multicollinearity diagnostics from typical regression results. *Basic and Applied Social Psychology*, 39(2), 81-90.
- Wang, Q., & Wang, L. (2021). The nonlinear effects of population aging, industrial structure, and urbanization on carbon emissions: A panel threshold regression analysis of 137 countries. *Journal of cleaner production*, 287, 125381.
- Ward, & Gleditsch. (2018). *Spatial regression models* (Vol. 115). Sage Publications.

Table 1: Description of response and explanatory variables and data sources.

Parameters	Description	Measurement unit	Source
Incidence rate (response variable)	Cumulative Daily confirmed COVID-19 cases in the period (Jan 4, 2020, To Dec 31, 2022)	No. of cases	' https://ourworldindata.org/coronavirus '
Population density (explanatory variable)	The number of people per MENA country is calculated by dividing the total number of people by the total land area	people per sq. km of land area	https://data.worldbank.org/indicator/
GDP per capita (explanatory variable)	GDP per capita is gross domestic product divided by midyear population. It is calculated without making deductions for depreciation of fabricated assets or for depletion and degradation of natural resources	Most Recent Value in US\$	https://data.worldbank.org/indicator/
Total vaccine doses (explanatory variable)	All COVID-19 vaccine doses, including boosters, are counted individually till Dec 31, 2022	No. of cases	' https://ourworldindata.org/coronavirus '
Unemployment (explanatory variable)	Unemployment refers to the share of the labor force that is without work but available for and seeking employment in MENA countries in 2022	Index	https://ilostat.ilo.org/data/
People fully vaccinated (explanatory variable)	Total number of people who received all doses prescribed by the initial COVID-19 vaccination protocol till Dec 31, 2022	No. of cases	' https://ourworldindata.org/coronavirus '
GDP Gross Domestic Product (current US\$) (explanatory variable)	The total monetary or market value of all the finished goods and services produced within a country's borders in 2021	Most Recent Value (Millions)	https://data.worldbank.org/indicator/
Population (explanatory variable)	The last population count of MENA countries in 2022	Total number	https://data.worldbank.org/indicator/
Population aged 65+ (explanatory variable)	Total population 65 years of age or older in each MENA country in 2022	Total number	https://data.worldbank.org/indicator/
Inflation (explanatory variable)	Inflation as measured by the consumer price index reflects the annual percentage change in the cost to the average consumer of acquiring a basket of goods and services that may be fixed or changed at specified intervals	Index	https://data.worldbank.org/indicator/
Severity index (explanatory variable)	The Severity Index factors information on proportionate death rates due to COVID-19 and confirmed cases as a	Index	https://covid19.pemandu.org/

Recovery index (explanatory variable)	factor of the country's population The Recovery Index considers recovery rates, active cases per population, testing levels, and countries' ability to detect, respond, and treat epidemics based on the Global Health Security Index.	Index	https://covid19.pemandu.org/
Hospital beds (per 1,000 people) (explanatory variable)	The total number of beds available in public, private, general, and specialized hospitals, and rehabilitation centers in each MENA country in 2022	Index	https://data.worldbank.org/indicator/
Nurses and midwives (per 1,000 people) (explanatory variable)	Nurses and midwives include professional nurses, professional midwives, auxiliary nurses, auxiliary midwives, enrolled nurses, enrolled midwives, and other associated personnel in each MENA country in 2022	Index	https://data.worldbank.org/indicator/

Table 2. Summary statistics of the global OLS model.

Variable	Coefficient	St. Error	t-Statistic	Probability	VIF
Intercept	-11.6942	3.7859	-3.09	0.0060	-
Population density	0.0011	0.0005	2.04	0.0551	1.195
GDP per capita	0.8735	0.2166	4.03	0.0007	2.141
Unemployment	0.1160	0.0424	2.73	0.0131	2.419
Total vaccine doses	0.9623	0.1536	6.26	0.0000	1.306

Table 3. Summary statistics of SLM and SEM models.

Variable	Coefficient		St. Error		Z-score		P-value	
	SLM	SEM	SLM	SEM	SLM	SEM	SLM	SEM
Intercept	-13.9003	8.9763	3.1607	3.0262	4.3979	2.9662	0.0000	0.0030
Pop-density	0.0009	0.0012	0.0004	0.0004	2.2372	2.8864	0.0252	0.0038
GDP per capita	0.8201	0.8114	0.1693	0.1509	4.8436	5.3756	0.0000	0.0000
Unemployment	0.1261	0.1173	0.0333	0.0320	3.7811	3.6603	0.0001	0.0002
Total vaccine doses	0.8446	0.8338	0.1244	0.1267	6.7854	6.5770	0.0000	0.0000
Rho	0.3442	-	0.1379	-	2.496	-	0.0125	-
Lambda	-	0.4692	-	0.1815	-	2.585	-	0.0097

Table 4. Measures of goodness-of-fit for OLS, SEM, SLM, GWR, and MGWR in modeling COVID-19 incidence rate.

Criterion	OLS	SEM	SLM	GWR	MGWR
R2	0.743	0.794	0.804	0.840	0.843
AIC	73.54	72.14	70.06	58.82	58.41
RSS	18.26	14.63	13.95	11.38	11.22

RSS= Residual sum of squares

Fig. 1. Location of the study area.

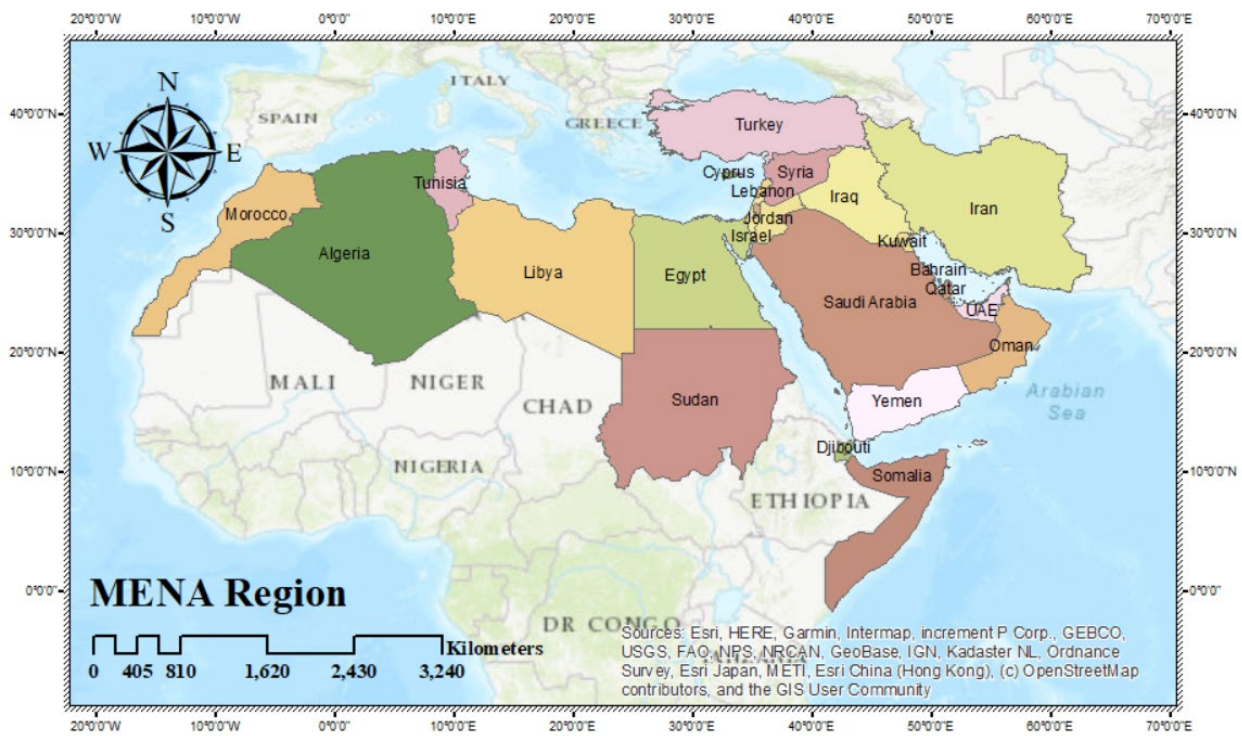


Fig. 2. Distribution of the dependent variable (COVID-19 incidence rate) across subnational boundaries

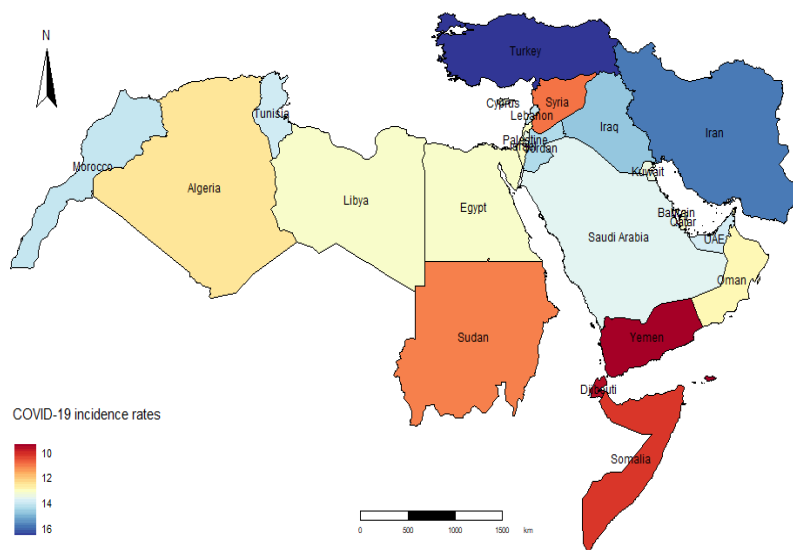


Fig. 3. The effects of %Population density (above) and GDP per capita (below) in describing COVID-19 incidence rates using GWR (right) and MGWR (left) models across the MENA region.

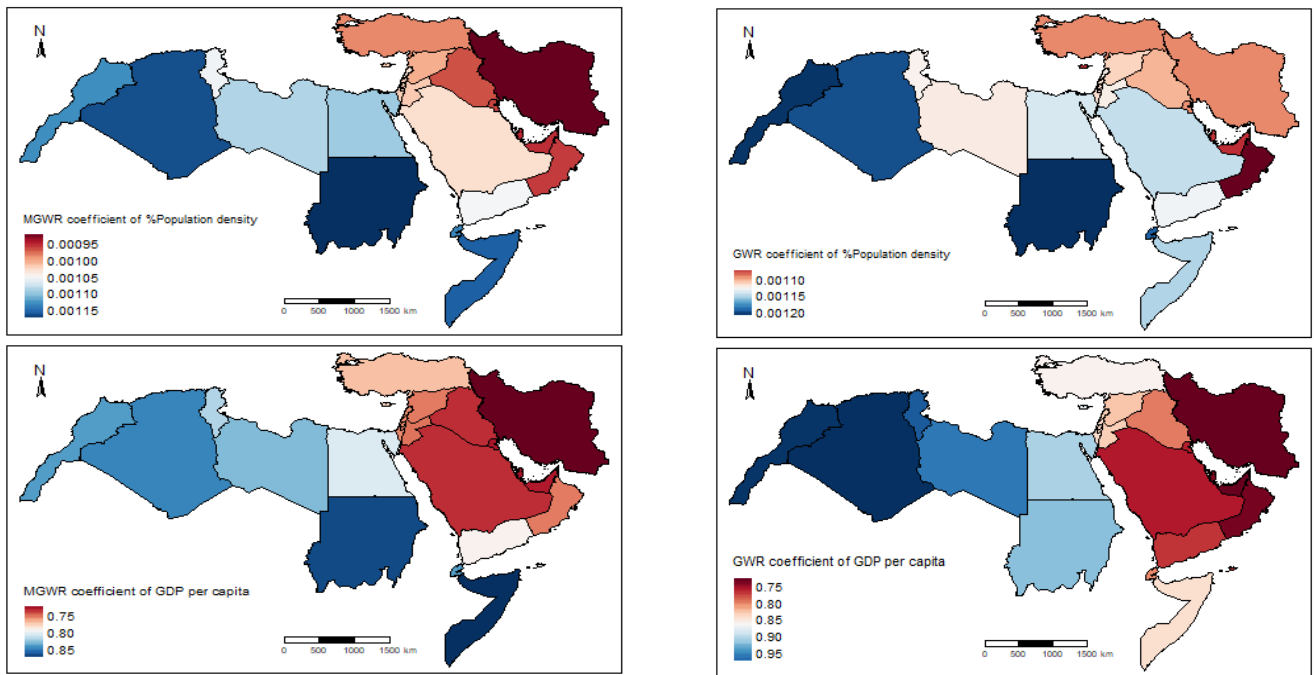


Fig. 4. The effects of % Unemployment (above) and Total vaccine doses (below) in describing COVID-19 incidence rates using GWR (right) and MGWR (left) models across the MENA region.

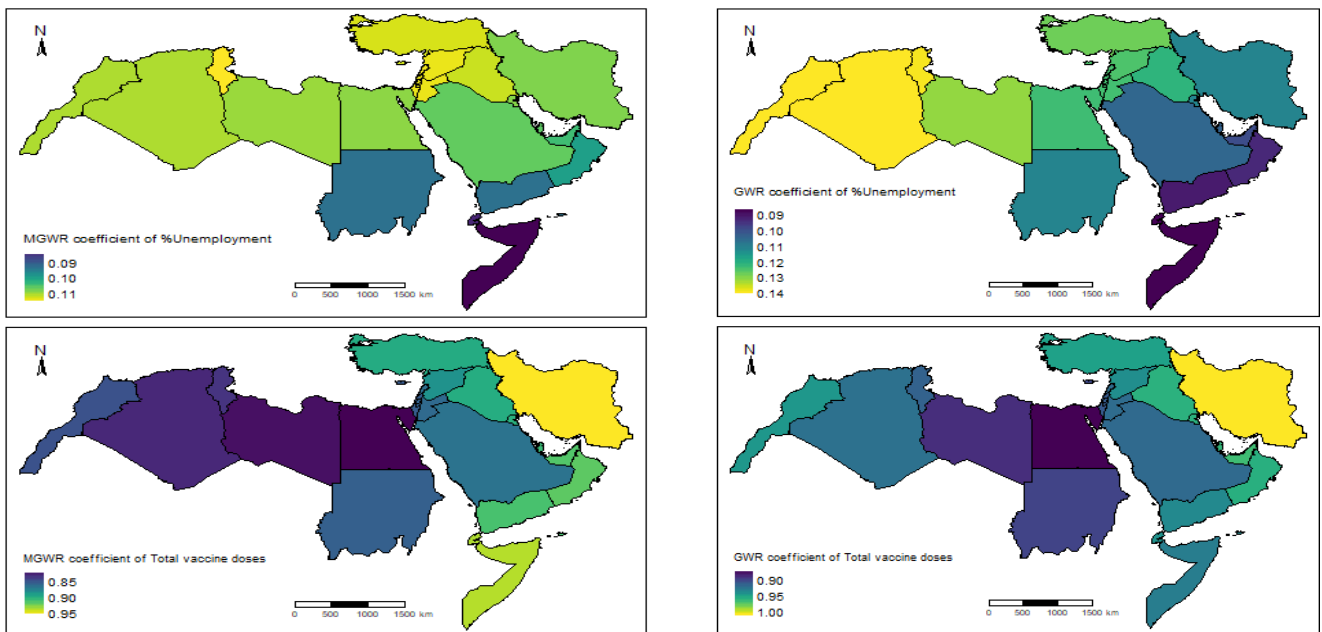
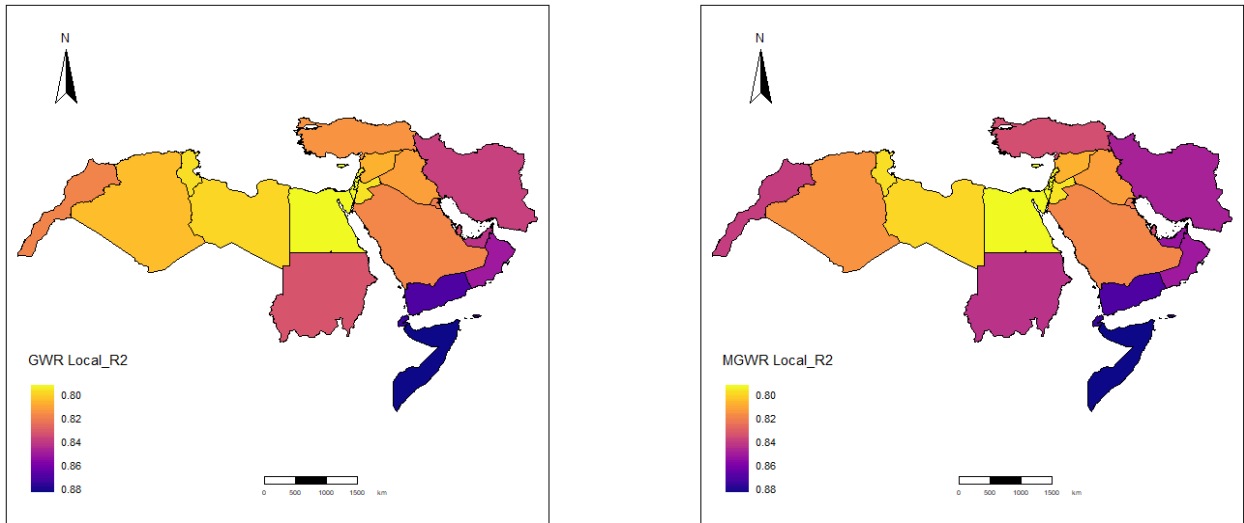


Fig. 5. Spatial distribution of local R2 of GWR and MGWR models for COVID-19 incidence rate associated with the significant covariates across the MENA region.



Spatial Analysis of Tropical Cyclone Yaas using Satellite Data

N. Umakanth^{1a}, Rajesh Gogineni^{2b}, K. Madan Mohan Rao^{3c}, B. Revanth Reddy^{4c}, Sk. Hasane Ahammad^{5d} and M.C. Rao^{6e}

Abstract: Tropical cyclones are the major natural disasters in India. They cause high death toll and property destruction, that lead to a negative socioeconomic impact. For early warning alerts, real-time monitoring, impact and damage pre-assessment, and relief operations, remote sensing and geographic information systems (GIS) are helpful. Tropical cyclone warning bulletins detail the cyclone intensity, direction and position of occurrence of cyclonic event, velocity of the winds across the coastal areas, expected landfall site. During the period of May 23rd to May 28th, 2021, an attempt was made to examine Yaas cyclone over Bay of Bengal Sea (BOBS). Rainfall (RF), Convective available potential energy (CAPE), cloud top temperature (CTT), total precipitable water (TPW), lifted index (LI), convective inhibition (CIN), sea level pressure (SLP), divergence and sea surface temperature (SST) are used to analyze cyclonic activity. Cold dry air from high latitudes meet with warm moist air in low latitudes leading to instability. This instability is responsible for the conducive feature in convection occurrence. The weather research forecasting (WRF) model forecast results matched well with MERRA2 reanalysis results. The model performed well in prior occurrence of convection activity.

Keywords: Convective inhibition, sea level pressure, cloud top temperature, sea surface temperature.

1. Introduction

Tropical cyclones originating in the Indian Ocean pose the greatest threat to countries in South Asia, particularly those located near the Bay of Bengal (BOBS). More than 80% of major cyclonic activities took place in BOBS of North Indian Ocean. In the BOBS, 5–6 tropical cyclones form each year, with roughly two of them becoming severe. The majority of BOBS severe cyclones form in the post-monsoon season, between October and November. In May month, high intensity cyclones were observed but the most damaging cyclonic activities were observed in post-monsoon season. We usually observe high formation of low pressure systems during post-monsoon season over South Asia (Singh, 2007). Most cyclones formed in BOBS made their landfall on Bangladesh's coast since the BOBS funnel shape terminates here.

In cyclone-prone areas, the influence of powerful winds, torrential rains and storm surges (abnormally high sea levels) are seen that lead to high death rate and damage to public life. Winds

over 117 kilometers per hour often damage delicate structures (Hossain & Mullick, 2020). Heavy rain can cause catastrophic floods and considerable crop damage in a short period of time. In few occasions, nearly 50 cms of rainfall will be recorded in 3-7 days time period (Dasgupta et al. 2010). Several cyclones have blasted on the BOBS in the last 35 years, inflicting massive disruptions, damages and a staggering number of deaths (Hossain et al. 2008; Islam et al. 2011). Few are, in 1970 Bhola cyclone, in 1991 Hurricane, in 1997 BOB 07, in 2002 06B, in 2007 Sidr cyclone, in 2008 Rashmi cyclone, in 2009 Aila cyclone, in 2013 Mahasen cyclone, in 2015 Komen cyclone, in 2016 Rohanu cyclone, in 2017 Mora cyclone and in 2019 Fani cyclone. The 1970 Bhola cyclone was a powerful hurricane that hit India on November 12th, 1970, killing an estimated 250,000 people and making it one of the deadliest natural catastrophes in modern history (Islam & Peterson, 2009). In 1985, Urir Char and Sandwip cyclones occurred and they were researched to understand the factors that contributed to high cyclone related fatality rates. In Sandwip cyclone, eight cyclone shelters were arranged whereas in Urir Char cyclone, 40% of people along the cyclone hit area were dead due to lack of cyclone shelters (Siddique & Eusof, 1987). On April 29th, 1991, at 19:00 UTC, a hurricane hit the Chittagong shoreline, located northeast of the BOBS, with winds of 240 km/h, killing approximately one and half lakh people over Bangladesh region (Chowdhury et al. 1993). The people most vulnerable to cyclones around the coastal places are those with little economic resources, outmoded technology, poor knowledge on cyclones mitigation aspects and poor infrastructure. Such communities are failing to execute perfect rescue plans to defend the people against the cyclones (O'Hare, 2001). As a result of climate change,

Authors information:

^aIndian Institute of Tropical Meteorology (IITM), Dr. Homi Bhabha Road, Pashan, Pune, Maharashtra 411008, INDIA. E-mail: numakanth23@gmail.com¹

^bDepartment of ECE, Dhanekula Institute of Engineering and Technology, Vijayawada-521139, INDIA. E-mail: rgogineni9@gmail.com²

^cIndian Institute of Tropical Meteorology (IITM), Dr. Homi Bhabha Road, Pashan, Pune, Maharashtra 411008, INDIA. E-mail: kmadan.rao@tropmet.res.in³; revanthreddy93.b@gmail.com⁴

^dDepartment of ECE, Koneru Lakshmaiah Education Foundation, Vaddeswaram-522502, INDIA. E-mail: ahammadklu@gmail.com⁵

^eDepartment of Physics, Andhra Loyola College, Vijayawada-520008, INDIA. E-mail: raomc72@gmail.com⁶

*Corresponding Author: raomc72@gmail.com

Received: June 12, 2023

Accepted: January 18, 2024

Published: December 31, 2024

cyclonic events may occur at any time (Karim & Mimura, 2008).

The cyclones that pass through BOBS have both beneficial and harmful consequences. From a meteorological standpoint, these cyclones are linked to a lot of rain and these rains affect the hydrological cycle with raising groundwater levels by filling rivers that increase the water flows at dams. Despite recent advances in weather prediction, predicting cyclone intensity is still challenging. For a better prediction, it is also essential to comprehend the characteristics of cyclogenesis and the mechanisms that lead to their intensification over BOBS (Webster, 2008; McPhaden et al. 2009; Wu et al. 2012; Sreenivas et al. 2012a; Sreenivas et al. 2012b; Sreenivas and Gnanaseelan 2014; DeMaria, 1996; Balaguru et al. 2012; Zehr 2003).

A week after Cyclone Tauktae wreaked devastation on India's west coast, Cyclone Yaas made landfall in Odisha and West Bengal on the east coast, leaving a trail of death and destruction in its wake. India is the sixth-most severely impacted nation in the world in 2019 according to the Global Climate Risk Index 2021. The main obstacles for researchers studying tropical cyclogenesis include a lack of information about large tropical basins, a lack of data on tropical cyclone formation despite the existence of long-term large-scale conditions that favor cyclone occurrence, variations in atmospheric patterns, and ocean currents of various ocean basins (Mazzarella et al. 2014). Investigations are still ongoing to understand the crucial factors that affect whether cloud clusters develop into tropical storms. Karyampudi and Pierce (2002) looked into how different mesoscale elements interacted during the early stages of tropical storm formation. Venkatesh (2006) noted the mesoscale interaction that took place during the development and intensification of the 1999 superstorm in Orissa. In order to distinguish between developing and non-developing cloud clusters, Mazzarella et al. (2014) employed lightning data as a proxy for convective activity. According to descriptions by Zehnder and Gall (1991) and Velasco and Fritsch (1987), tropical Storm Priscilla began life as a mesoscale convective system (MSCSM) over a land area in 1989. Hurricane season was established in 1989 because of the increased number of hurricanes that year. Prior to the development of the MSCSM, the influence of moisture and vertical wind profiles during that season set the path for cyclone formation (Smith and Gall, 1989; Siewert et al. 2010, König, 2002).

In operational meteorology, the so-called instability indices are often used to identify the optimal conditions for the development of deep wet convection and severe weather. They are computed using profiles of atmospheric temperature and humidity. Thanks to the arrival of meteorological satellites, atmospheric instability is operationally determined using data that is worldwide and frequent (5–15 minutes). Compared to traditional radio-sounding metrics, the use of satellite data to develop instability indices results in significant gains in both temporal and spatial coverage (Purdum, 1976). As a result, Conte et al. (2011) looked into cyclones associated with various stability indices. They concluded

that the KI, LI, CAPE, and TPW variables significantly contribute to the establishment of deep convection. They also showed a direct relationship between indices and the frontal system of the storm. Since massive thunderstorms effectively encircle the cyclone's eye, the onset of the intense cyclonic rainfall is correlated with an increase in the CAPE value.

Furthermore, the region of thermodynamic disequilibrium that follows the route of the cyclone—that is, the warm, humid air at low altitudes and the cold, dry air at higher altitudes—is associated with the LI minimum. According to Conte et al. (2011), there is evidence of an impending explosive development of the cyclone due to the overlap of convection-friendly zones east of the Calabria region. This study provided us with the necessary motivation for this scientific endeavour. We have also investigated the relationship between these indicators and cyclones, drawing on the study work of Conte et al. (2011). Numerous research initiatives have centered on the creation of satellite-based sensors over the past 20 years (König and de Coning, 2009; Roberts and Rutledge, 2003; Seemann et al. 2003). The indices developed for the convective investigation based on satellite implementations are used in the current analysis. It is possible to track the progress of a cyclone using instability indicators. This was brought up by Moscatello et al. (2008) as yet another successful method for cyclone evolution. In a few instances, he examined the usefulness of such signs to the diagnosis of severe convection.

At the moment, the regular and thorough data gathered by geostationary satellite sensors, such as the onboard imager and sounder products, can be helpful for the quick identification of potentially severe weather characteristics. The most comprehensive depiction of historical weather and climate currently available is based on reanalysis data. They are based on a combination of recent short-term weather forecasts that have been revised and observations as well. The dynamical core, parameterizations and resolution of the reanalysis model all influence the output of severe events in reanalysis data. For example, newer generations of reanalyses produce better resolutions and use modern data assimilation methodologies. Many recent research, for example, have employed reanalysis data sets to construct tropical cyclone climatology, explore the impact of large-scale mechanisms on tropical storm evolution (Maloney & Hartmann, 2000; Maloney et al. 2000) and estimate tropical cyclone power dissipation (Sriner & Huber, 2006). As a result, greater representation of tropical cyclones in the reanalysis data set is critical for better understanding tropical storm inner core dynamics and interactions with the climate system (Scoccimarro et al. 2012). So, utilizing satellite data from May 23rd through May 28th, 2021, we tried to explore in this research the relationship between stability-related indicators and tropical cyclone Yaas over the Bay of Bengal Sea. The following is the paper's structure: The data and methodology utilized in the study are described in Section 2. Section 3 examines the findings and Section 4 summarizes the most important conclusions.

2. Data and Methodology

Data

This study investigates the tropical cyclone Yaas. The Catastrophic Cyclone Yaas, which has a six-day duration (23rd to 28th, May 2021), first appeared in BOBS on May 23rd as a low-pressure system. By May 24th, the low pressure system had migrated westward and formed a deep depression. The storm quickly shifted north-eastward, steadily intensifying due to warm waters along the shore and the system was upgraded to a cyclonic storm and called Yaas later that day. Yaas intensified further on May 25th, becoming a severe cyclonic storm later that day. On May 26th, Yaas made a landfall near Odisha coast.

Global Precipitation Measurement (GPM) is a new generation of satellite precipitation products. Its objective is to develop the following-generation of a space measuring system that can perform routine and accurate measurements of global precipitation. The Tropical Rainfall Measuring Mission (TRMM) has been replaced by this. On the website <https://gpm.nasa.gov/data/directory> the GPM IMERG (Integrated Multi-satellite Retrievals for Global Precipitation Measurement) half-hourly rainfall data of 0.1°x0.1° have been downloaded (Huffman GJ et al., 2019). The most recent (5th generation) reanalysis data product from the European Centre for Medium-Range Weather Forecasts (ECMWF) has been put on a data server under the title of environmental services by the Copernicus Climate Change Service (C3S) (Hersbach et al., 2020). It is crucial to have access to these global data in order to comprehend the microphysical and dynamical aspects of earlier events. We used reanalysis data of the temperature and relative humidity in the study region with a spatial resolution of 0.250x0.250 for the current experiment. The data for the research region can be downloaded by users through the C3S data server (<https://cds.climate.copernicus.eu/cdsapp#!/home>). We computed the CAPE, CIN, TPW, and LI parameters using the temperature and relative humidity reanalysis data. All other parameters were taken from the MERRA2 dataset. Modern Era Retrospective Analysis for Research and Application (MERRA) data with a resolution of 0.25° was obtained from the website <https://disc.gsfc.nasa.gov/datasets?project=MERRA-2> from 23rd to 28th of May, 2021 (Gelaro et al. 2017). The FNL data has been downloaded from the website <https://rda.ucar.edu/datasets/ds083.2/>

Methodology

The formulas used in this study's attempt to calculate the different indexes are listed below.

(i) Convective available potential energy (CAPE)

Moncrieff and Miller's (1976) formula is used to determine CAPE.

$$CAPE = \int_x^y g \left[\frac{TV_{parcel} - TV_{env}}{TV_{env}} \right] dz \text{ ----- (1)}$$

Where TV_{parcel} represents the virtual temperature of an air parcel and TV_{env} represents the virtual temperature of an

environment respectively. The levels of free convection and neutral buoyancy are represented by x and y.

(ii) Lifted Index (LI)

This index is used to evaluate the troposphere's lowest levels. The LI threshold values are listed below (Galway, 1956).

$$\text{Lifted Index (LI)} = a_{500} - a_{parcel} \text{ ----- (2)}$$

Where a is the air temperature and a_{parcel} is the parcel temperature elevated from the ground to a pressure level of 500 hpa.

(iii) Total precipitable water (TPW)

In TPW, the amount of water vapour present in the air is expressed. The formula for calculating TPW is as follows:

$$TPW = \frac{1}{g} \int_{P_1}^{P_2} W dP \text{ ----- (3)}$$

Where P_1 and P_2 indicate the levels related to pressure, W denotes mixing ratio (Carlson TN et al.1990)

(iv) Convective Inhibition (CIN):

The Parker (2002) formula is used to calculate CIN.

$$CIN = \int_{Z_l}^{Z_f} g \left[\frac{T_{v,parcel} - T_{v,env}}{T_{v,env}} \right] dz \text{ ----- (4)}$$

Where $T_{v,parcel}$ indicates parcel's virtual temperature and $T_{v,env}$ represents the environment's virtual temperature respectively. Z_f demonstrates the level of free convection and Z_l denotes the surface level.

(v) Storm Relative Helicity (SRLH):

The computation of SRLH is done to understand the updraft rotation of winds in cyclonic activity. This estimation is mainly done by considering the lower atmospheric level data such as from ground surface to one kilometer (Parker 2002).

SRLH is defined as

$$SRLH = \int_0^h \left(\frac{\vec{v}}{V} - \frac{\vec{c}}{C} \right) X \frac{d\vec{v}}{dz} dz \text{ ----- (5)}$$

Where V represents the environment's wind vector, C represents the storm's translation velocity, $k \times dV/dz$ represents the horizontal vorticity and k represents the vertical unit vector, h is set to 3 kilometers in SCAN, as it is in other studies. The V(z) is the wind profile.

These metrics can indicate weather conditions that are conducive to the occurrence of severe weather if their values surpass specific thresholds, which are typically determined empirically and may change depending on the season and the location.

Table 1. Model Details

Model features	Specifications
Horizontal resolution	9 km
Vertical levels	42 levels
Radiation	RRTMG scheme
Cu_physics	Grell-Devenyi ensemble scheme
Planetary boundary layer	Yonsei University Scheme
Mp_physics	Morrison scheme
Surface layer physics	Revised MM5 Monin-Obukhov Scheme
Land surface physics	Noah Land Surface Model

Weather Research Forecasting Model (WRF)

On May 26th, 2021, a cyclone associated with convection was predicted using WRF. For this study, the model is setup for 9Km resolution domain.

The WRF model is a next generation numerical weather prediction (NWP) model that is fully compressible and offers a range of features for enhanced comprehension of atmospheric processes and applications related to weather forecasting (Skamarock et al., 2019). The National Centre for Atmospheric Research (NCAR) in the United States developed it, and it was made available in 2000. Its scales vary from tens of meters to thousands of kilometres, making it suitable for a broad spectrum of meteorological applications. In WRF (version 3.9.1), the vertical momentum equation can be solved without the need for a hydrostatic approximation. Its two dynamical cores for solving the atmospheric governing equations are the Non-hydrostatic Mesoscale Model (NMM) and the Advanced Research WRF (ARW). Cloud-resolving simulations of the thunderclouds in this work are carried out using the ARW core. In order to improve the starting and boundary conditions, it offers a sophisticated data assimilation mechanism and strong multiple nesting capabilities.

A double-moment approach for the four hydrometeor classes—droplets, cloud ice, rain, and snow—is the Morrison scheme (Morrison et al., 2005). It is projected what the mass mixing ratios will be for five different types of hydrometeors: raindrops, pristine ice crystals, cloud liquid droplets, snow (big crystals or aggregates), and graupel or hail. Predictions are also made

regarding the overall concentrations of ice, snow, rain, and glaciers. Morrison approach considers new physically based parameterizations for simulating homogeneous and heterogeneous ice nucleation. A semi-analytic approach to the three phase (vapour, ice, and liquid) supersaturation equation is used to forecast the tendency rates of condensation/deposition and supersaturation field.

The National Center for Atmospheric Research (NCAR) created this model in collaboration with the National Center for Environmental Prediction (NCEP) of the National Oceanic and Atmospheric Administration (NOAA). We have utilized hybrid sigma vertical coordinate system. Following Rajeevan et al. (2010) for radiation schemes, the Rapid Radiative Transfer Model (RRTM) (Mlawer et al., 1997) was utilized for long wave radiation in all of the simulations, while the Dudhia short wave scheme (Dudhia, 1989) was employed for short wave radiation. The Rapid Radiative Transfer Model (RRTM) (Mlawer et al., 1997) long wave scheme is used to treat radiation in all simulations, which were inspired by Rajeevan et al. (2010). It takes into consideration various bands, trace gases, and species of microphysics. Short wave radiation has been addressed by the Dudhia Shortwave system (Dudhia, 1989). This short wave radiation strategy allows for clouds and clear-sky absorption and scattering due to its simple downward integration. Using the FNL (Final) Operational Global Analysis data from the NCEP, the model's fundamental initial conditions were gathered with a spatial resolution of 1 degree. The BOBS region employed in this study for WRF model prediction is situated between latitudes 0° and 30°N and longitudes 45° and 105°E. In this investigation, the 3.9.1 Model version was employed (Skamarock et al. 2008). Table 1 lists the model's most important characteristics. Thus, the WRF simulation began at 0000 UTC on May 22nd and ran for entire cyclonic event, while the storm made landfall at 0330 UTC on May 26th. The WRF model requires six hours to spin up. The model result displayed in this study was used for a 24-hour period, starting at 0000UTC on May 26th, 2021 and ending at 0000UTC on May 27th, 2021.

3.1 Results and discussion

Tropical cyclone Yaas travelled across the BOBS from May 23rd to May 28th, 2021 and this study looked into it. RF, CTT, CIN, SST, CAPE, SLP, LI, TPW and divergence are all used to assess cyclonic activity.

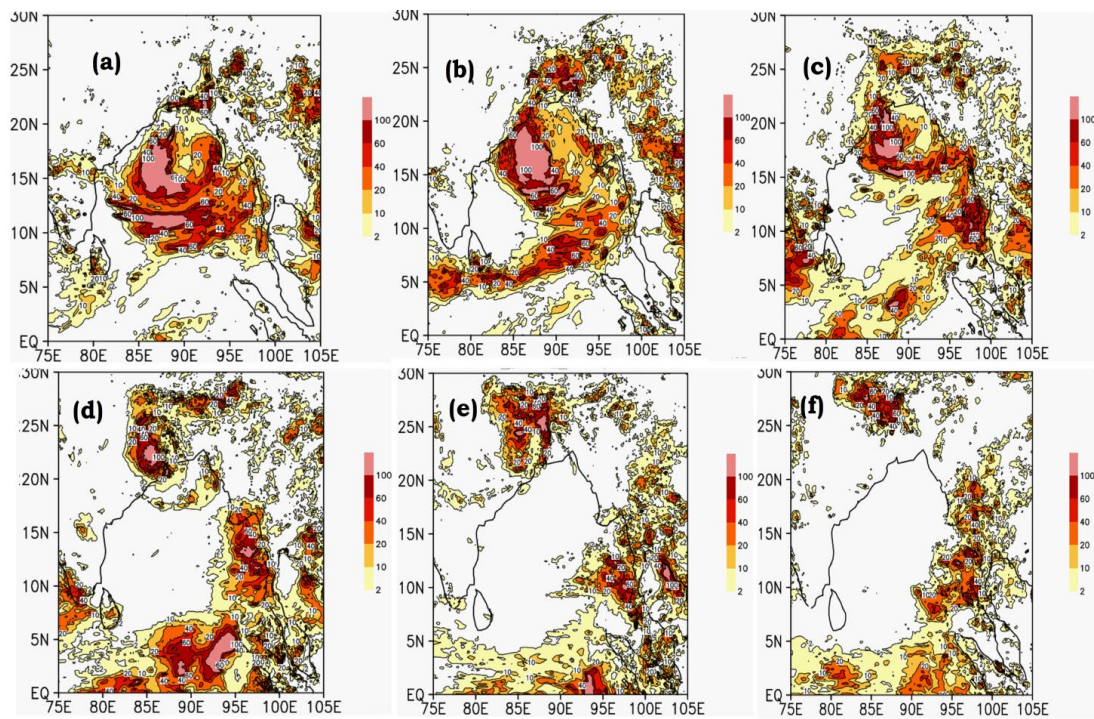


Figure 1. Spatial distribution of daily rainfall during (a) May 23rd, 2021, (b) May 24th, 2021, (c) May 25th, 2021, (d) May 26th, 2021, (e) May 27th, 2021, (f) May 28th, 2021.

We've drawn rainfall maps across the BOBS region in Figure 1 from May 23rd to May 28th, 2021. High rainfall is expected near the Northern Tamilnadu and Southern Andhra Pradesh coasts on May 23rd, 2021. The rainfall values range between 20 and 100 mm over BOBS (Figure 1 (a)). On 24th May, 2021, high rainfall is seen near Northern Andhra Pradesh and Southern Odisha coastal areas. The rainfall values range between 40 and 100 mm over BOBS (Figure 1 (b)). On 25th May, 2021, high rainfall is seen near Odisha coastal areas. The rainfall values range between 60 and 100 mm over BOBS (Figure 1 (c)). On 26th May, 2021, high rainfall is seen near Odisha coastal area Bahanaga. The rainfall values range between 60 and 100 mm over Dhamra port and Bahanaga area (Figure 1 (d)). On 27th May, 2021, the rainfall activity has been decreased near Odisha. The rainfall values range between 10 and 20 mm over BOBS (Figure 1 (e)). On 28th May, 2021, no rainfall is seen near Odisha and entire east coastal areas over BOBS (Figure 1 (f)).

We have plotted spatial maps of CTT over the BOBS region in Figure 2 from May 23rd to May 28th, 2021. On 23rd May, 2021 low CTT is seen near Northern Tamilnadu and Southern Andhra Pradesh coastal areas. The CTT values range between 180 and 200 K over BOBS (Figure 2(a)). On 24th May, 2021 low CTT is seen near Northern Andhra Pradesh coastal areas. The CTT values range between 180 and 200 K over BOBS (Figure 2(b)). On 25th May,

2021 low CTT is seen near Northern Andhra Pradesh coastal areas. The CTT values range between 180 and 190 K over BOBS (Figure 2(c)). On 26th May, 2021 very low CTT is seen near Odisha Coastal area Bahanaga. The CTT values range between 180 and 200 K over BOBS (Figure 2(d)). On 27th May, 2021 the CTT are higher near Odisha. The CTT values range between 200 and 210 K over BOBS (Figure 2(e)). On 28th May, 2021 the CTT values are seen increased near Odisha and Andhra Pradesh coastal areas over BOBS (Figure 2(f)). We have produced SST spatial maps across the BOBS region from May 23rd to May 28th, 2021 in Figure 3. SST readings in the BOBS region range from 30.5 to 31 degrees celsius on May 23rd, 2021 (Figure 3(a)). SST readings in the BOBS region on the 24th of May, 2021 vary from 30.3 to 31.2°C (Figure 3(b)). On 25th May, 2021, the high SST is seen near Northern Andhra Pradesh and Southern Odisha coastal areas. The SST values range between 29 and 30.9°C over BOBS (Figure 3(c)). On 26th May, 2021, high SST values are seen near Odisha coastal areas. Over BOBS, the SST values range from 30.5 to 31.10c (Figure 3(d)). The SST is comparatively lower near Odisha on May 27, 2021. Over BOBS, the SST values vary between 29.5 and 30°C (Figure 3(e)). The SST values are shown to be decreasing over BOBS on May 28, 2021, towards the coastal regions of Northern Andhra Pradesh and Southern Odisha (Figure 3(f)).

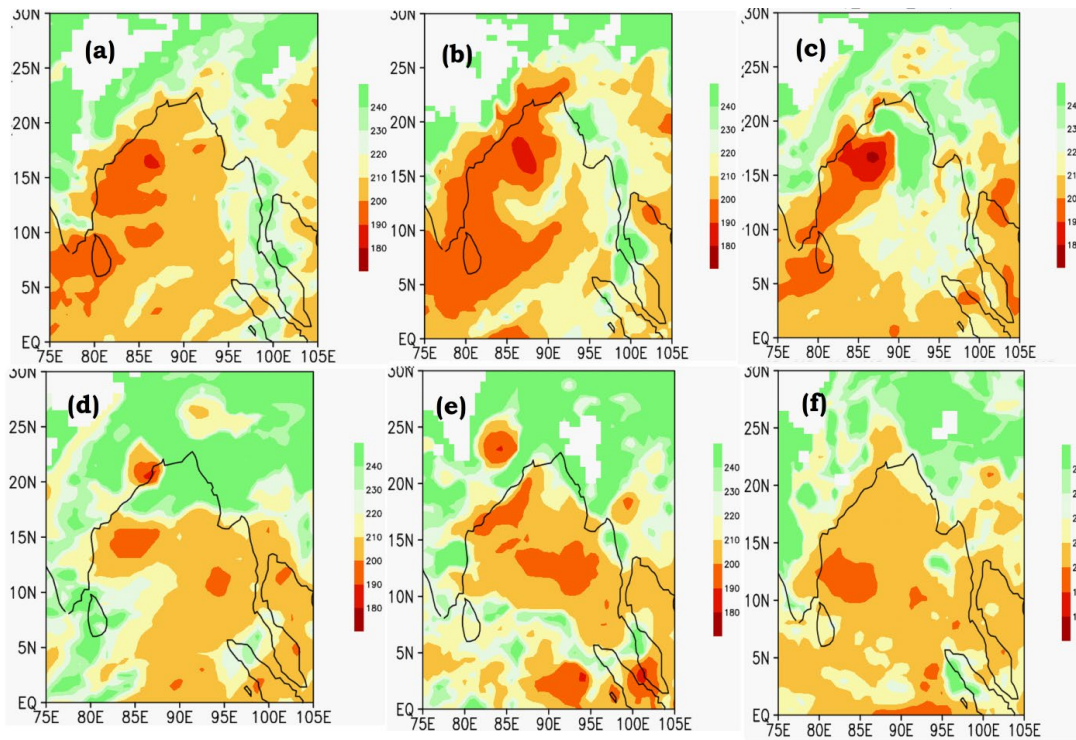


Figure 2. Spatial distribution of daily cloud top temperature during (a) May 23rd, 2021, (b) May 24th, 2021, (c) May 25th, 2021, (d) May 26th, 2021, (e) May 27th, 2021, (f) May 28th, 2021.

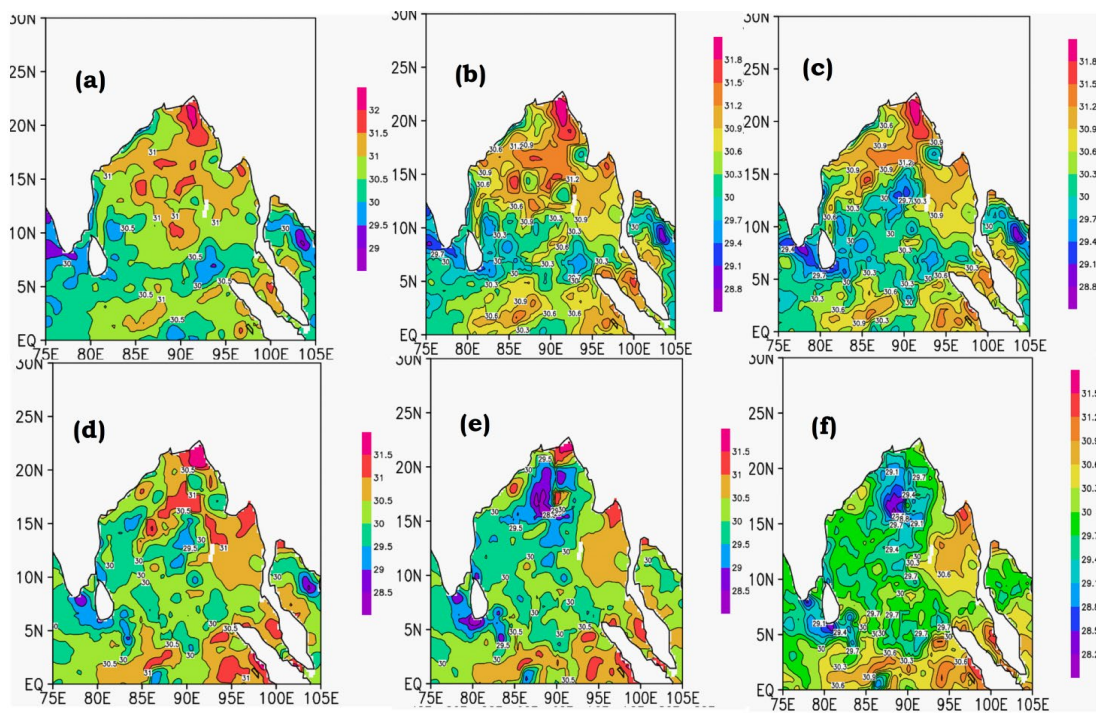


Figure 3. Spatial distribution of daily sea surface temperature during (a) May 23rd, 2021, (b) May 24th, 2021, (c) May 25th, 2021, (d) May 26th, 2021, (e) May 27th, 2021, (f) May 28th, 2021.

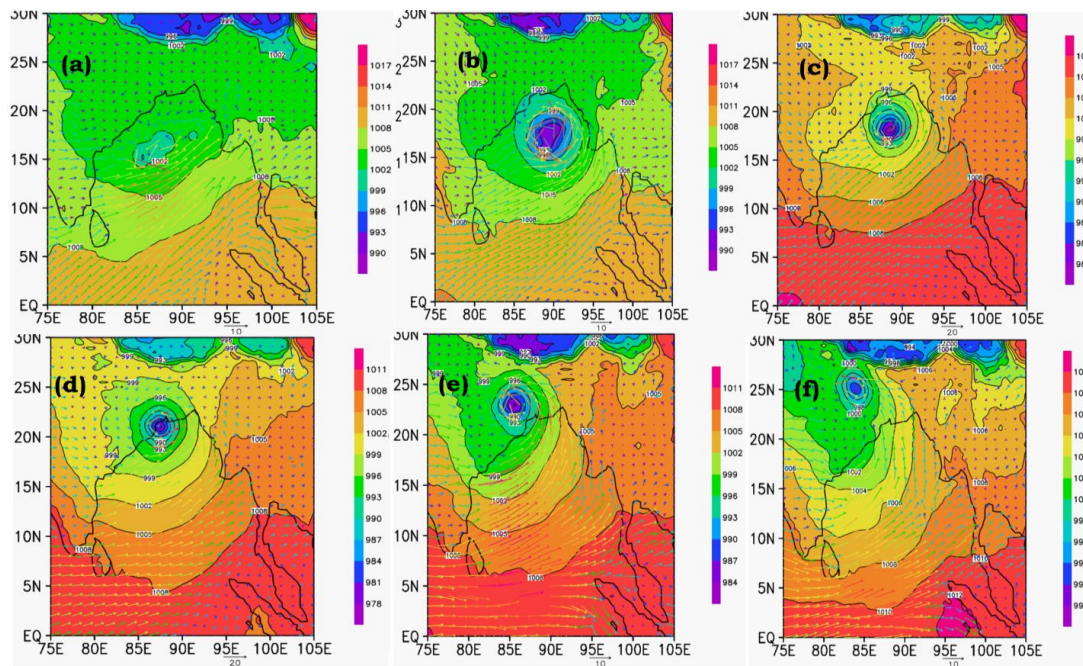


Figure 4. Daily sea level pressure distribution (in shaded areas) and wind vectors for the dates of (a) May 23, (b) May 24, (c) May 25, (d) May 26, (e) May 27, and (f) May 28 in 2021.

We have produced SLP (Shaded) and winds (Vectors) spatial maps across the BOBS region from May 23rd to May 28th, 2021 in Figure 4. On 23rd May, 2021, the SLP values are low near Central Andhra Pradesh coastal area in BOBS. The SLP values drops from 1002hpa to 999hpa over BOBS region. The wind vectors represent that the westerly winds are accumulated around the low pressure area and they move with a speed of nearly 10 m/s (Figure 4(a)). On 24th May, 2021, the SLP values are low near Northern Andhra Pradesh and Southern Odisha coastal area in BOBS. The SLP values drops from 1002hpa to 990hpa over BOBS region. Strong winds (10 m/s) have been seen close to the low pressure area, according to the wind vectors (Figure 4(b)). The SLP values are low near the beaches of Odisha in BOBS on May 25, 2021. Over the BOBS region, the SLP values decrease from 993 hpa to 981 hpa. According to the wind vectors (Figure 4(c)), strong wind gusts (20 m/s) have been seen near low pressure area. The SLP values are low around the Bahanaga coastal region of Odisha on May 26, 2021, according to BOBS. Over the BOBS region, the SLP values decrease from 990 hpa to 978 hpa. According to the wind vectors (Figure 4(d)), 20 m/s-per-second strong winds have been seen in the area surrounding the low pressure. The SLP values are low on May 27, 2021, around the coast of Odisha and in the BOBS land area. On May 26, the cyclone made landfall. Over the BOBS region, the SLP values decrease from 996 hpa to 984 hpa. According to the wind vectors (Figure 4(e)), 10 m/s-per-second gusty winds are seen in the area surrounding the low pressure. The SLP values are rising around the states of Odisha and Andhra Pradesh on May 28, 2021. On the 26th, the cyclone made landfall. As a result, over the BOBS region, the SLP values start rising on the 28th, from 1000hpa to 1008hpa. According to the wind vectors (Figure 4(f)), the wind speed has fallen to 10 m/s.

In Figure 5, we've presented TPW (Shaded) and divergence (Contour) spatial maps over the BOBS region from May 23rd to May 28th, 2021. The TPW values are high near the Central Andhra Pradesh coast in BOBS on May 23, 2021. Over the BOBS region, 50 to 70 mm is the range of the TPW values. The divergence values are in the range of -0.5 to -0.2, favoring the accumulation of moisture across the BOBS (Figure 5(a)). On 24th May, 2021, the TPW values are high near Northern Andhra Pradesh and Southern Odisha coastal areas in BOBS. Over the BOBS region, the TPW values range from 60 to 70 mm. The divergence values in BOBS (Figure 5(b)) range from -0.5 to -1.0, favouring moisture accumulation along the Odisha coast. The TPW values near the southern Odisha coast in BOBS are high on May 25, 2021. Over the BOBS region, TPW values range from 60 to 80 mm. The divergence values in BOBS (Figure 5(c)) ranges from -0.5 to -1.0, favouring moisture accumulation across the Odisha coastal areas. On 26th May, 2021, the TPW values are high near Bahanaga coast area near Odisha cast in BOBS. Over the BOBS region, the TPW values range from 60 to 80 mm. The divergence values in BOBS (Figure 5(d)) ranges from -0.1 to -0.3, favouring moisture accumulation along the Odisha beaches. On 27th May, 2021, the TPW values are high near Odisha coast and land area in BOBS. The TPW values lies between 55 and 65 mm over BOBS region. The divergence values range between -0.5 and -1.0 favouring the moisture accumulation across the Odisha coast (Figure 5(e)). On 28th May, 2021, the TPW values are high near Odisha area over land. The cyclone made landfall on 26th. So on 27th, the TPW values starts decreasing from 80 to 50 mm over Odisha region. The divergence values range between -0.1 and -0.3 across the BOBS (Figure 5(f)).

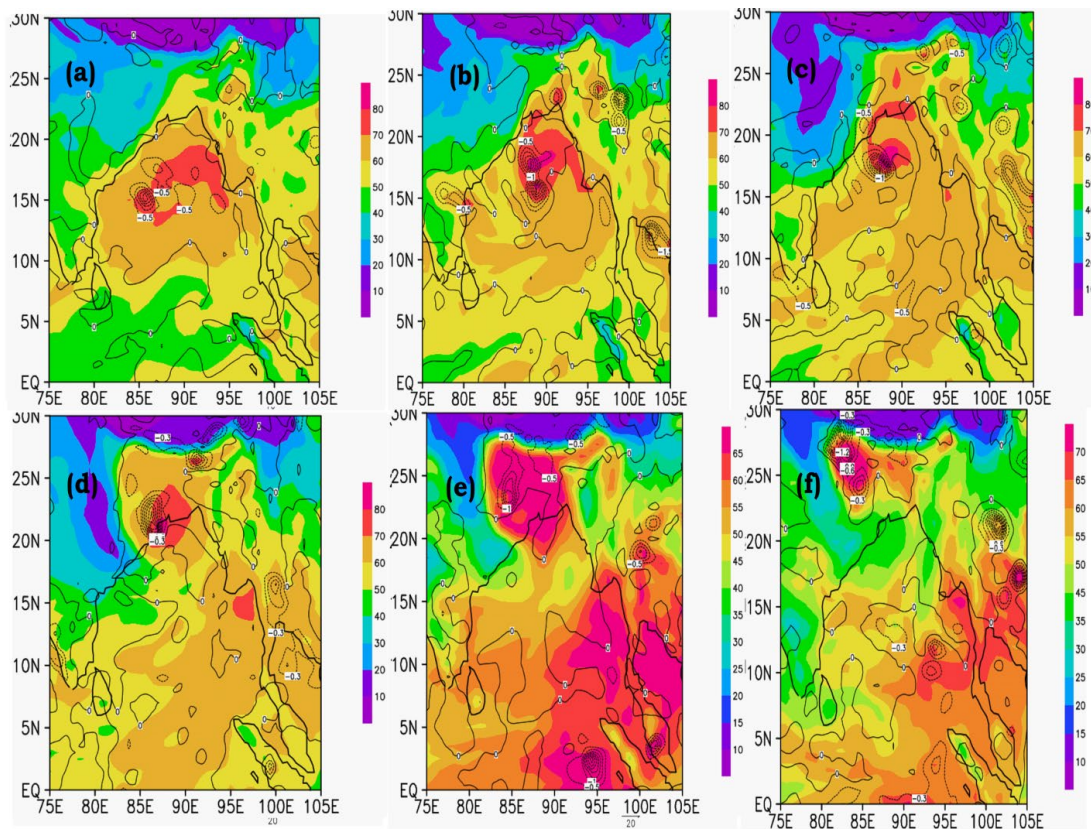


Figure 5. Spatial distribution of daily TPW (shaded) and divergence (contour) during (a) May 23rd, 2021, (b) May 24th, 2021, (c) May 25th, 2021, (d) May 26th, 2021, (e) May 27th, 2021, (f) May 28th, 2021.

We plotted CAPE spatial maps of the area surrounding the Bay of Bengal Sea between May 23 and May 28, 2021 (Figure 6). On May 23rd, 2021, CAPE levels in the BOBS region range from 1000 to 2000 J/kg (Figure 6(a)). On May 24th, 2021, CAPE levels in the BOBS region range from 1200 to 2100 J/kg (Figure 6(b)). The high CAPE is observed near Andhra Pradesh coastal areas on May 25th, 2021. Over BOBS, CAPE values range from 1500 to 2400 J/kg (Figure 6(c)). High CAPE values were observed around Odisha coastal areas on May 26th, 2021. Over BOBS, CAPE values vary from 1500 to 2700 J/kg (Figure 6(d)). The CAPE is greater near Odisha on May 27th, 2021. CAPE values over BOBS range from 1000 to 2500 J/kg (Figure 6(e)). On May 28, 2021, CAPE values along the coast of Odisha decreased over BOBS (Figure 6(f)). We produced spatial maps of LI over the Bay of Bengal Sea region from May 23 to May 28 of 2021 (Figure 7). On May 23rd, 2021, the LI values in the BOBS region range from -4 to -2 K (Figure 7(a)). On

the 24th of May, 2021, the LI values in the BOBS region vary from -4 to -2 K (Figure 7(b)). The low LI is visible near Andhra Pradesh coastal areas on May 25th, 2021. Over BOBS, LI values range from -6 to -4 K (Figure 7(c)). The LI values are seen around Northern Andhra Pradesh and Southern Odisha coastal areas on May 26th, 2021. Over BOBS, LI values vary from -6 to -4 K (Figure 7(d)). The LI values near Odisha ranged between -4 and -2 K on May 27th, 2021. Over BOBS, LI values vary from -2 to 0 K (Figure 7(e)). On the 28th of May, 2021, the LI values near the Odisha and Andhra Pradesh coasts plummeted over BOBS (Figure 7(f)). We have displayed geographical maps of CIN over the Bay of Bengal Sea region from May 23rd to May 28th, 2021 in Figure 8. CIN values in the BOBS region range between 100 and 300 J/kg from May 23rd to May 28th, 2021 (Figure 8(a-f)). This is a strong indicator of severe atmospheric instability.

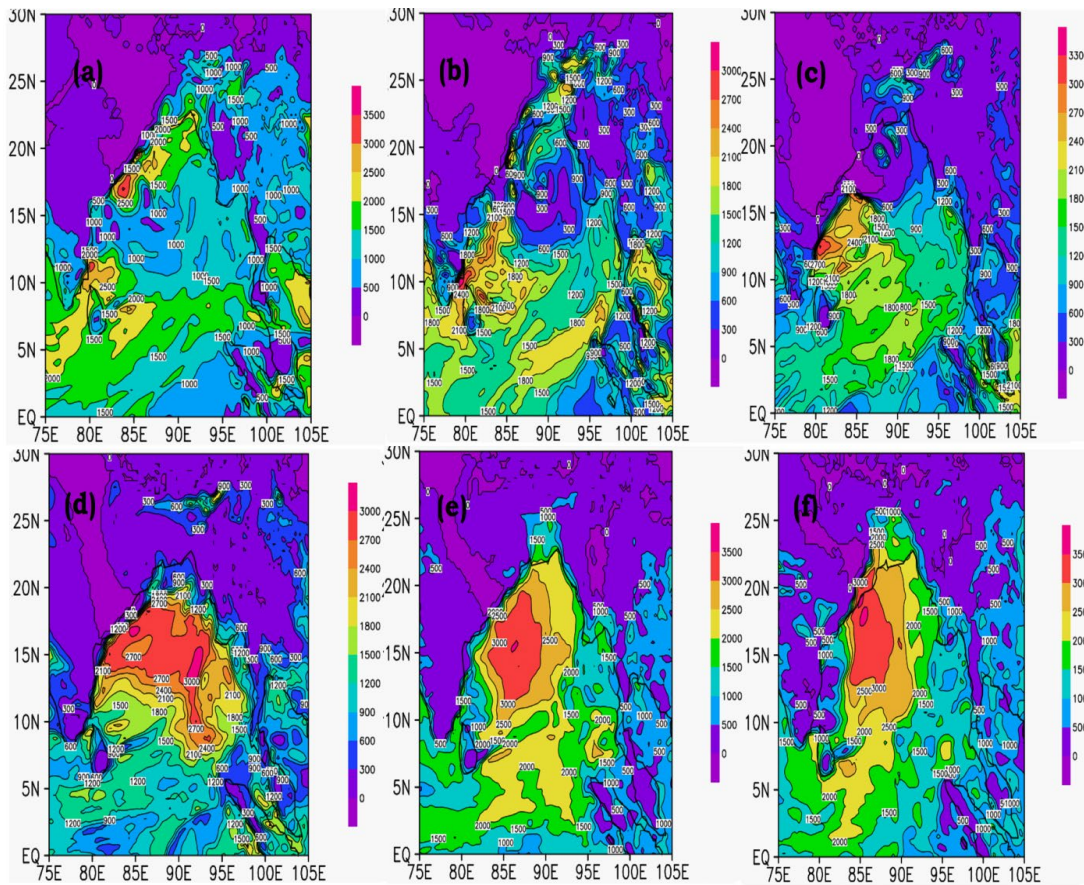


Figure 6. Spatial distribution of daily CAPE during (a) May 23rd, 2021, (b) May 24th, 2021, (c) May 25th, 2021, (d) May 26th, 2021, (e) May 27th, 2021, (f) May 28th, 2021.

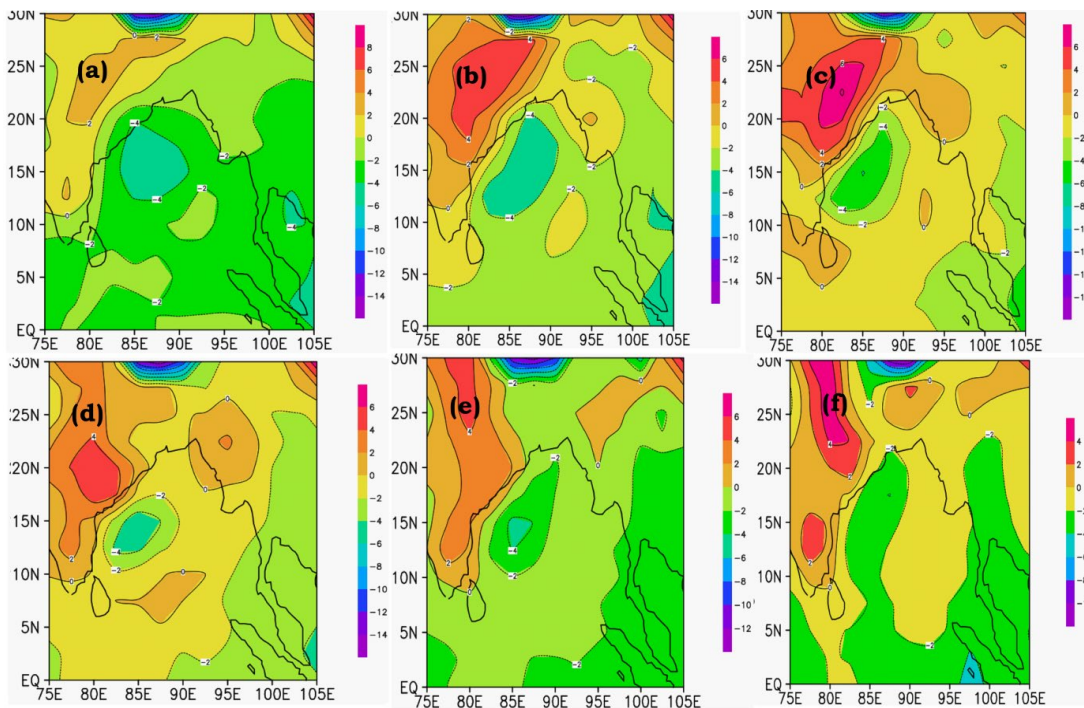


Figure 7. Spatial distribution of daily LI during (a) May 23rd, 2021, (b) May 24th, 2021, (c) May 25th, 2021, (d) May 26th, 2021, (e) May 27th, 2021, (f) May 28th, 2021.

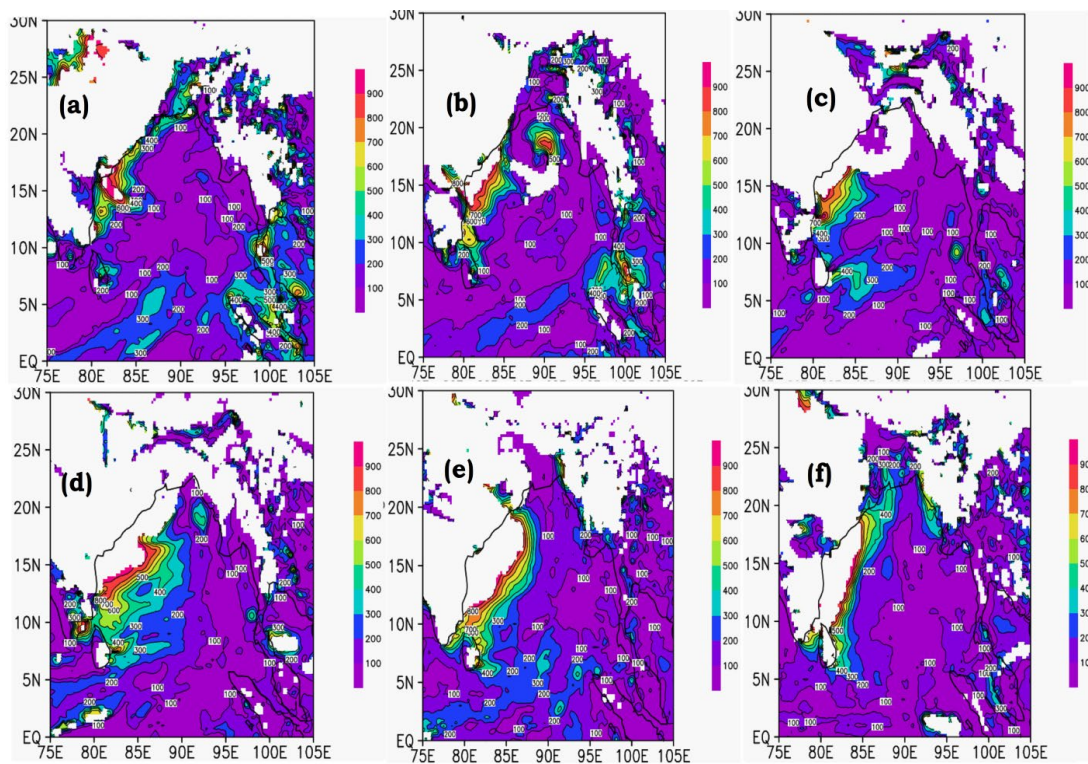


Figure 8. Spatial distribution of daily CIN during (a) May 23rd, 2021, (b) May 24th, 2021, (c) May 25th, 2021, (d) May 26th, 2021, (e) May 27th, 2021, (f) May 28th, 2021.

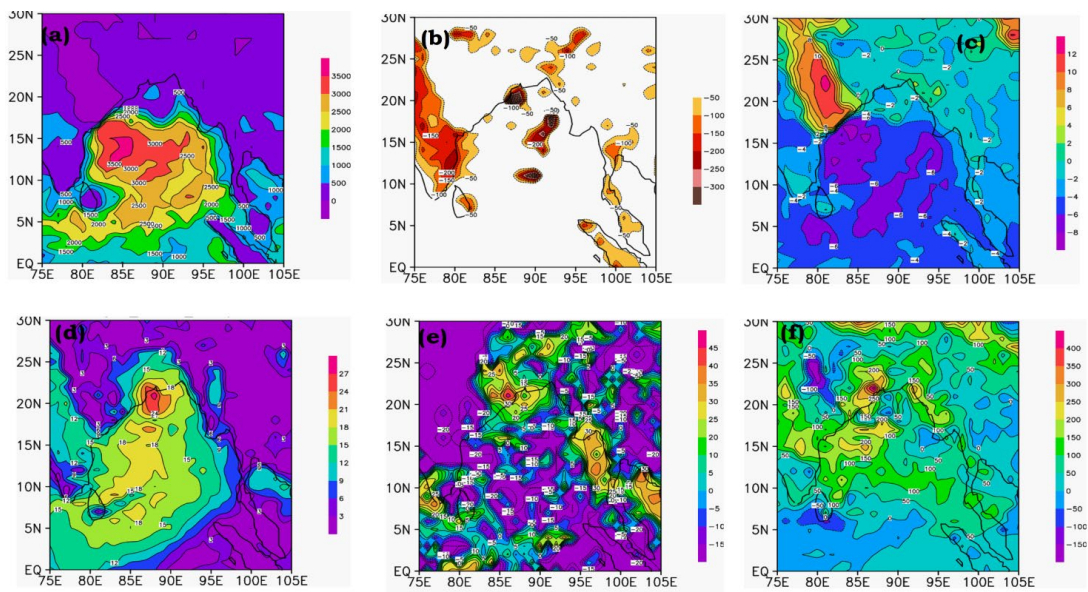


Figure 9. Spatial distribution of WRF calculated (a). CAPE parameter, (b). CIN parameter, (c). LI parameter, (d). wind gust parameter, (e). composite reflectivity parameter, (f). SRLH parameter, for May 26th, 2021.

For Cyclone Yaas, the WRF Model Anticipated the Following Outcomes

According to the IMD report, the cyclone made landfall on May 26, 2021, early in the morning (0330UTC). We have made an effort to forecast the cyclone Yaas prior using the WRF model. Since the storm reached landfall at 0330 UTC on May 26th, the WRF simulation started at 0000 UTC on May 22nd and ran throughout the full cyclonic event. The WRF model runs require six hours to spin up. High CAPE values were reported nearer the

North Andhra Pradesh coast and Southern Odisha coast on May 26th, 2021. The CAPE values nearly approached 3500 J/kg, indicating the seriousness of the situation (Figure 9). The CAPE anticipated by the WRF model was higher than the MERRA2 data. The WRF predicted CIN values also showed the convection severity of the cyclone. The values ranged between -50 and -200 which indicate severity near Dhamra port (Figure 10). The WRF predicted LI values ranged between -6 to -4 K at Orissa coast as seen in Figure 11. We have also tried to look at the wind gust in

WRF model. High wind gust is seen near north coast of Dhamra Port and south coastal area of Bahanaga. Wind gust values almost lie between 18 and 24 m/s indicating the severity of cyclone (Figure 12). The complex reflectivity values (~ 20 to 30) showed the severity of the cyclone occurrence prior (Figure 13). The SRLH values (~ 150 to 250) showed the severity of the cyclone occurrence prior (Figure 14). We can see that from Figure 9(a-f) the WRF predicted parameters almost indicated the severity of cyclone prior when compared to MERRA over BOBS.

4. Summary and Conclusion

Between May 23 and May 28, 2021, a tropical cyclone named Yaas swept over the Bay of Bengal Sea. This study tries to better understand it. The discussion of the cyclone evolution tracked by instability indices provides a distinct perspective on the subject. It also makes it possible to analyze if these indices may be used to diagnose severe convection in situations of this nature. High rainfall was recorded along Odisha's coastal areas on May 26th, 2021. Over BOBS, rainfall ranges from 60 to 100 mm. CTT are significant because of their tight relationship to cloud top height (CTH). The lower is the CTT, the higher the cloud. As a result, the coldest IR pixels usually depict the highest tops of clouds, such as convective storm "overshooting tops." CTT is quite low around Odisha coastal area Bahanaga on May 26th, 2021. Over BOBS, CTT values range from 180 to 200K. A high rate of evaporation and moisture pumping into the cyclone can occur when the weather is sufficiently warm. Storms are made violent by the condensation of this vast volume of water vapor, which can result in massive amounts of rain when they impact land. High SST values were seen around Odisha coastal areas on May 26th, 2021. Over BOBS, SST values vary from 30.5 to 31.1°C. Intense tropical cyclones produce the lowest air pressure on the planet, when water vapor condenses to form clouds and rain, releasing heat that warms the air column in the storm's eye. The air rises around the low pressure, cools and condenses into clouds and precipitation as it does so. SLP values near the Odisha coastal area in BOBS are low on May 26th, 2021. Over the BOBS region, the SLP values drop from 990hpa to 978hpa. High winds of 20 m/s have been detected near the low pressure, according to the wind vectors. Divergence in the top layers of the atmosphere is required to keep the rising air currents within the cyclone pumped out and the cyclone's core pressure low. There is a region of divergence aloft above the developing low-pressure centre if the upper levels are conducive for cyclone development. This will aid in the upward movement of air that is converging at the surface and the development of the surface cyclone. The TPW values around Bahanaga coastal area of Odisha coast in BOBS are high on the 26th of May, 2021. Over the BOBS region, the TPW values vary from 60 to 80 mm. The divergence values in BOBS range from -0.1 to -0.3, favoring moisture accumulation along the coastal areas of Odisha. High CAPE values were observed around Odisha coastal areas on May 26th, 2021. CAPE values across BOBS range from 1000 to 3500 J/kg. A stability metric that can be used to gauge the atmosphere's buoyancy is the lifted index. As one increases altitude, the temperature of the atmosphere decreases. Air cools as it ascends

to the surface. Occasionally, nevertheless, it does cool more slowly than its surroundings.) On May 26, 2021, coastal parts of Odisha have extremely low LI values. LI values over BOBS range from -4 to -2 K. When compared to MERRA over BOBS, WRF predicted metrics almost indicated the strength of the cyclone previously.

5. Acknowledgements

Authors thank the European Centre for Medium Range Weather Forecasting (ECMWF) for providing a free accessible dataset of Copernicus Climate Change Service (C3S) for our study. We also thank National Aeronautics and Space Administration (NASA) for providing free available datasets of MERRA and GPM IMERG for this analysis.

6. References

- Balaguru, K., Chang, P., Saravanan, R., Leung, L. R., Xu, Z., Li, M., & Hsieh, J. S (2012) Ocean barrier layers' effect on tropical cyclone intensification. *Proceedings of the National Academy of Sciences*, 109(36), 14343-14347.
- Das Someshwar., Ashrit, R., Moncrieff, M.W (2006a) Simulation of a Himalayan Cloudburst Event. *Journal of Earth System Science*, 115(3), 299-313.
- Carlson, T. N., Perry, E. M., & Schmutge, T. J (1990) Remote estimation of soil moisture availability and fractional vegetation cover for agricultural fields. *Agricultural and Forest Meteorology*, 52(1-2), 45-69.
- Chowdhury, A. M. R., Bhuyia, A. U., Choudhury, A. Y., & Sen, R (1993) The Bangladesh cyclone of 1991: why so many people died. *Disasters*, 17(4), 291-304.
- Conte, D., Miglietta, M. M., and Levizzani, V (2011) Analysis of instability indices during the development of a Mediterranean tropical-like cyclone using MSG-SEVIRI products and the LAPS model. *Atmospheric research*, 101(1-2), pp. 264-279.
- Dasgupta, S., Huq, M., Khan, Z. H., Ahmed, M. M. Z., Mukherjee, N., Khan, M., & Pandey, K. D (2010) Vulnerability of Bangladesh to cyclones in a changing climate: Potential damages and adaptation cost. *World Bank Policy Research Working Paper*, (5280).
- DeMaria, M (1996) The effect of vertical shear on tropical cyclone intensity change. *Journal of Atmospheric Sciences*, 53(14), 2076-2088.
- Dudhia, J (1989) Numerical study of convection observed during the winter monsoon experiment using a mesoscale two dimensional model. *J. Atmos. Sci.* 46, 3077-3107, doi: 10.1175/1520-0469(1989)046<3077: NSOCOD>2.0.CO; 2.

- Galway, J. G (1956) The lifted index as a predictor of latent instability. *Bulletin of the American Meteorological Society*, 37(10), 528-529.
- Gelaro, R., McCarty, W., Suárez, M. J., Todling, R., Molod, A., Takacs, L., & Zhao, B (2017) The modern-era retrospective analysis for research and applications, version 2 (MERRA-2). *Journal of climate*, 30(14), 5419-5454.
- Gray, W. M (1968) Global view of the origin of tropical disturbances and storms. *Monthly Weather Review*, 96(10), 669-700.
- Gray, W. M (1975) Tropical cyclone genesis (Doctoral dissertation, Colorado State University. Libraries).
- Gray, W. M (1998) The formation of tropical cyclones. *Meteorology and atmospheric physics*, 67(1), 37-69.
- Hersbach, H., Bell, B., Berrisford, P., Hirahara, S., Horányi, A., Muñoz-Sabater, J., & Thépaut, J. N (2020) The ERA5 global reanalysis. *Quarterly Journal of the Royal Meteorological Society*, 146(730), 1999-2049.
- Hossain, I., & Mullick, A. R (2020) Cyclone and Bangladesh: A historical and environmental overview from 1582 to 2020. *International Medical Journal*, 25(6), 2595-2614.
- Hossain, M. Z., Islam, M. T., Sakai, T., & Ishida, M (2008) Impact of tropical cyclones on rural infrastructures in Bangladesh. *Agricultural Engineering International: CIGR Journal*.
- Huffman, G. J., Stocker, E. F., Bolvin, D. T., Nelkin, E. J., Jackson, Tan (2019) GPM IMERG Early Precipitation L3 Half Hourly 0.1 degree x 0.1 degree V06, Greenbelt, MD, Goddard Earth Sciences Data and Information Services Center (GES DISC), Accessed: [Data Access Date], 10.5067/GPM/IMERG/3B-HH-E/06
- Islam, M. T., Hossain, M. Z., & Ishida, M (2011) Trends analyses for several factors affected by tropical cyclones. *American Journal of Environmental Sciences*, 7(3), 200-206.
- Islam, T., & Peterson, R. E (2009) Climatology of landfalling tropical cyclones in Bangladesh 1877–2003. *Natural Hazards*, 48(1), 115-135.
- Karim, M. F., & Mimura, N (2008) Impacts of climate change and sea-level rise on cyclonic storm surge floods in Bangladesh. *Global environmental change*, 18(3), 490-500.
- Karyampudi, V. M., & Pierce, H. F (2002) Synoptic-scale influence of the Saharan air layer on tropical cyclogenesis over the eastern Atlantic. *Monthly weather review*, 130(12), 3100-3128.
- Koenig, M., & De Coning, E (2009) The MSG global instability indices product and its use as a nowcasting tool. *Weather and forecasting*, 24(1), 272-285.
- König, M., Tjemkes, S., & Kerkmann, J (2002) Atmospheric instability parameters derived from MSG SEVIRI observations. Darmstadt, Germany: EUMETSAT.
- Le Marshall, J. F., & Riley, P (1994) Real-time assimilation and synoptic application of local TOVS raw radiance observations. *Australian Meteorological Magazine*, 43(3), 153-166.
- Ma, X. L., Schmit, T. J., & Smith, W. L (1999) A nonlinear physical retrieval algorithm—its application to the GOES-8/9 sounder. *Journal of Applied Meteorology*, 38(5), 501-513.
- Maloney, E. D., Gettelman, A., Ming, Y., Neelin, J. D., Barrie, D., Mariotti, A., & Zhao, M (2019) Process-oriented evaluation of climate and weather forecasting models. *Bulletin of the American Meteorological Society*, 100(9), 1665-1686.
- Maloney, E. D., & Hartmann, D. L (2000) Modulation of eastern North Pacific hurricanes by the Madden-Julian oscillation. *Journal of climate*, 13(9), 1451-1460.
- Maloney, E. D., & Hartmann, D. L (2000) Modulation of hurricane activity in the Gulf of Mexico by the Madden-Julian oscillation. *Science*, 287(5460), 2002-2004.
- Mazzarella, L. A., Ritchie, E. A., & Wood, K. M (2014) 2C. 7 EASTERN NORTH PACIFIC TROPICAL CYCLOGENESIS USING SATELLITE-BASED OBSERVATIONS.
- Mcphaden, M. J., Foltz, G. R., Lee, T., Murty, V. S. N., Ravichandran, M., Vecchi, G. A., & Yu, L (2009) Ocean-atmosphere interactions during cyclone nargis. *EOS, Transactions American Geophysical Union*, 90(7), 53-54.
- Mecikalski, J. R., Mackenzie Jr, W. M., & Bedka, K. M (2008) Algorithm for convective initiation for GOES-R. NOAA NESDIS Algorithm Theoretical Basis Document, 30pp.
- Mecikalski, J. R., Feltz, W. F., Murray, J. J., Johnson, D. B., Bedka, K. M., Bedka, S. T., & Williams, E (2007) Aviation applications for satellite-based observations of cloud properties, convection initiation, in-flight icing, turbulence, and volcanic ash. *Bulletin of the American Meteorological Society*, 88(10), 1589-1607.
- Menzel, W. P., Holt, F. C., Schmit, T. J., Aune, R. M., Schreiner, A. J., Wade, G. S., & Gray, D. G (1998) Application of GOES-8/9 soundings to weather forecasting and nowcasting. *Bulletin of the American Meteorological Society*, 79(10), 2059-2078.
- Mlawer, E. J., Taubman, S. J., Brown, P. D., Iacono, M. J., Clough, S. A (1997) Radiative transfer for inhomogeneous atmosphere:

- RRTM, a validated correlated-k model for the long-wave. *J. Geophys. Res.* 102, 16663–16682, doi: 10.1029/97JD00237.
- Moncrieff, M. W., & Miller, M. J (1976) The dynamics and simulation of tropical cumulonimbus and squall lines. *Quarterly Journal of the Royal Meteorological Society*, 102(432), 373-394.
- Morrison, H., Curry, J. A., Shupe, M. D., Zuidema, P (2005) A new double-moment microphysics parameterization for application in cloud and climate models. Part II: Single-column modeling of arctic clouds. *J. Atmos. Sci.* 62, 1678–1693.
- Moscattello, A., Marcello Miglietta, M., & Rotunno, R (2008) Observational analysis of a Mediterranean hurricane over south-eastern Italy. *Weather*, 63(10), 306.
- Parker, D. J (2002) The response of CAPE and CIN to tropospheric thermal variations. *Quarterly Journal of the Royal Meteorological Society: A journal of the atmospheric sciences, applied meteorology and physical oceanography*, 128(579), 119-130.
- O'Hare, G (2001) Hurricane 07B in the Godavari Delta, Andhra Pradesh, India: vulnerability, mitigation and the spatial impact. *Geographical Journal*, 167(1), 23-38.
- Purdum, J. F (1976) Some uses of high-resolution GOES imagery in the mesoscale forecasting of convection and its behavior. *Monthly Weather Review*, 104(12), 1474-1483.
- Rajeevan, M., Kesarkar, A., Thampi, S.B., Rao, T. N., Radhakrishna, B., Rajasekhar, M (2010) Sensitivity of WRF cloud microphysics to simulations of a severe thunderstorm event over Southeast India. *Ann. Geophysic.*, 28, 603–619.
- Roberts, R. D., & Rutledge, S (2003) Nowcasting storm initiation and growth using GOES-8 and WSR-88D data. *Weather and Forecasting*, 18(4), 562-584.
- Scoccimarro, E., Fogli, P. G., Reed, K. A., Gualdi, S., Masina, S., & Navarra, A (2017) Tropical cyclone interaction with the ocean: The role of high-frequency (subdaily) coupled processes. *Journal of Climate*, 30(1), 145-162.
- Seemann, S. W., Li, J., Menzel, W. P., & Gumley, L. E (2003) Operational retrieval of atmospheric temperature, moisture, and ozone from MODIS infrared radiances. *Journal of Applied Meteorology and Climatology*, 42(8), 1072-1091.
- Siddique, A. K., & Eusof, A (1987) Cyclone deaths in Bangladesh, May 1985: who was at risk. *Tropical and geographical medicine*, 39(1), 3-8.
- Siewert, C. W., Koenig, M., & Mecikalski, J. R (2010) Application of Meteosat second generation data towards improving the nowcasting of convective initiation. *Meteorological Applications*, 17(4), 442-451.
- Singh, O. P (2007) Long-term trends in the frequency of severe cyclones of Bay of Bengal: observations and simulations. *Mausam*, 58(1), 59-66.
- Skamarock WC, Klemp J, Dudhia J, Gill DO, Barker DM, Wang W and Powers JG 2005 A Description of the Advanced Research WRF Version 2. NCAR Technical Note; NCAR/TN-468+STR. Mesoscale and Microscale Meteorology Division, National Center for Atmospheric Research, Boulder, Colorado, USA.
- Skamarock, W. C., Klemp, J. B., Dudhia, J., Gill, D. O., Zhiquan, L., Berner, J., Wang, W., Powers, J.G., Duda, M.G., Barker, D.M., Huang, X. Y (2019) A Description of the Advanced Research WRF Model Version 4. NCAR Tech. Note NCAR/TN-475+STR 145. <https://doi.org/10.5065/1dfh-6p97>.
- Smith, W. P., & Gall, R. L (1989) Tropical squall lines of the Arizona monsoon. *Monthly weather review*, 117(7), 1553-1569.
- Sriver, R., & Huber, M (2006) Low frequency variability in globally integrated tropical cyclone power dissipation. *Geophysical Research Letters*, 33(11).
- Sreenivas, P., & Gnanaseelan, C (2013) Impact of oceanic processes on the life cycle of severe cyclonic storm "Jal". *IEEE Geoscience and Remote Sensing Letters*, 11(2), 519-523.
- Sreenivas, P., Gnanaseelan, C., & Prasad, K. V. S. R (2012a) Influence of El Niño and Indian Ocean Dipole on sea level variability in the Bay of Bengal. *Global and Planetary Change*, 80, 215-225.
- Sreenivas, P., Chowdary, J. S., & Gnanaseelan, C (2012b) Impact of tropical cyclones on the intensity and phase propagation of fall Wyrтки jets. *Geophysical research letters*, 39(22).
- Sun, D., Kafatos, M., Cervone, G., Boybeyi, Z., & Yang, R (2007) Satellite microwave detected SST anomalies and hurricane intensification. *Natural Hazards*, 43(2), 273-284.
- Velasco, I., Fritsch, J.M (1987) Mesoscale convective complexes in the Americas; *Geophys Res* 92 9591–9613.
- Venkatesh, T. N (2006) Mesoscale interactions during the genesis and intensification of October 1999 Orissa super cyclone. *Mausam*, 57(1), 31-36.
- Webster, P. J (2008) Myanmar's deadly daffodil. *Nature Geoscience*, 1(8), 488-490.
- Wu, L., Su, H., Fovell, R. G., Wang, B., Shen, J. T., Kahn, B. H., & Jiang, J. H (2012) Relationship of environmental relative

humidity with North Atlantic tropical cyclone intensity and intensification rate. *Geophysical research letters*, 39(20).

Zehnder, J. A., & Gall, R. L (1991) Alternative mechanisms of tropical cyclone formation in the Eastern North Pacific. *Atmósfera*, 4(1), 37-51.

Zehr, R. M (2003) Environmental vertical wind shear with Hurricane Bertha (1996). *Weather and forecasting*, 18(2), 345-356.

Preliminary Study of Tsunami Impact on Soil Salinity for Agriculture Based on Geophysical Data, a Case Study of Aceh Besar, Indonesia

Muhammad Syukri^{1a}, Sabrian Tri Anda^{2b*}, Rini Safitri^{3a}, Zul Fadhl^{4c} and Fiqa Miftahunnisa Hs^{5c}

Abstract: The Tsunami, (natural phenomenon) that occurred in Aceh Province in 2004, not only caused severe damage to the infrastructure and human casualties but also altered the conditions of the soil. The change in soil condition led to economic loss (productivity and activity) in certain areas that were affected by the Tsunami. Studies show that the land inundated with Tsunami flood and sedimentation caused the land to become unproductive since the salinity level increased. The geophysical method was used to delineate the level of soil salinity in areas affected by Tsunami. A total of four measurement lines ranging in length from 160 to 210 meters were constructed specifically in Aceh Besar region. In the Blang Krueng District, three measuring lines (K1, K2, and K3) were positioned slightly away from the shoreline and one measurement line was conducted in the Blang Bintang (B1) region to validate the difference between the conductivity values of land polluted with tsunami sediment and seawater intrusion. Results show that the areas affected by Tsunami sedimentation had a greater conductivity value than unaffected areas classified by the conductivity value of 0.06 – 2 S/m and 0 – 0.05 S/m for Blang Krueng and Blang Bintang areas respectively.

Keywords: *Tsunami, soil salinity, geophysical method, conductivity*

1. Introduction

Aceh Province is located in the northernmost and westernmost parts of Indonesia and it is renowned as a province with a high level of natural disasters. Based on geological conditions, Aceh lies on the confluence of two tectonic plates; Eurasian and Indo-Australian. Therefore, geologically induced conditions of plate activities are quite frequent (Syukri et al., 2019; 2020), such as the Tsunami phenomenon. The impact of the 2004 Tsunami not only caused severe damage to the economy, infrastructure, and human casualties (Rusydy et al., 2020; Suppasri et al., 2019; Azmeri et al., 2017) but also affected the change in soil conditions. This change in soil conditions could lead to decreased economic activity and production, especially in agriculture. Due to changes in soil structure and qualities produced by the deposition of Tsunami sediments, the area once used as agricultural land is thought to be unproductive because Tsunami sediments covered the subgrade surface (Niino, 2008; Tinning G., 2011; Marohn et al., 2012). 92.81% of Aceh's economic activities rely on agriculture (farming, forestry, and fishing). In order to assess the level of efficacy of land usage for agricultural purposes, particularly in the Aceh Besar region, a comprehensive study of post-tsunami soil conditions is necessary. Using observations on a limited scale,

such as in the laboratory, soil structure can be determined by incorporating more sophisticated imaging capabilities. (Helliwell et al., 2013; Schlüter et al., 2014). Nevertheless, Romero et al; (2018) state that there is presently large-scale method of measuring the whole soil structure using the geophysical method. Therefore, this study aims at using the geophysical method capacity to determine soil salinity for agricultural purposes by mapping the soil conditions. In addition, the geophysical approach can describe the subsurface structure across a vast area. Moreover, the implementation of the 2-D geoelectric approach is regarded as the most appropriate technique because it can explain various elements crucial for plant development (Johnson et al., 2001; Kravchenko et al., 2002)

Tsunami Impact on Soil Characteristics

The magnitude 9.1 Sumatra-Andaman earthquake, which occurred on December 26, 2004, produced the most catastrophic Tsunami in recorded history (Lay et al., 2005). The Tsunami submerged up to 29,000 hectares of agriculture in Aceh Province, causing damage to the farms. The agricultural area is contaminated due to seawater's entrance and mud deposition. The entrance of seawater and mud accumulation increased the inundated farmland's salinity. As the salinity level rises, the osmotic potential of the soil falls, and it is anticipated that saltwater and debris-inundated fields could limit plant growth. As a result, the plant's roots would have trouble absorbing the water, as it is strongly bound to the soil particles, resulting in physiological dryness. Hereinafter, the high level of salinity could also lead the protoplast to be wrinkled as a result of cell damage

Authors information:

^aDepartment of Physics, Faculty of Mathematics and Sciences, Universitas Syiah Kuala, Banda Aceh, Indonesia. E-mail: m.syukri@usk.ac.id¹; rsafitri@usk.ac.id³

^bGeophysics Study Program, Faculty of Science and Technology, Universitas Samudra, Indonesia. E-mail: sabriantrianda@unsam.ac.id²

^cDepartment of Engineering Geophysics, Engineering Faculty, Universitas Syiah Kuala, Indonesia. E-mail: zulfadhli@usk.ac.id⁴; Fiqa.miftahunnisa@gmail.com⁵

*Corresponding Author: sabriantrianda@unsam.ac.id

Received: December 12, 2022

Accepted: December 3, 2023

Published: December 31, 2024

and sodium poisoning. The decrease in plant growth activity is caused not only by the inability of plant roots to obtain water but also by the tendency of the plant's water content to discharge the surrounding high salt concentration. Hereinafter, the high level of salinity could also lead the protoplast to be wrinkled as a result of cell damage.

Soil Salinity and pH

The presence of the primary inorganic solutes dissolved in water constitutes soil salinity. The salt concentration of the soil is considered detrimental to plant growth. The salt content in the soil alters a soil's ability to absorb water. As the salt content of the soil rises, the fluctuation of ions within plants impedes the natural passage of water from the soil to the plant roots. This also causes the water absorbed by plant roots to be sucked back into the soil, leaving plants dehydrated. In addition, an increase in the concentration of dissolved salts in the soil will increase the osmotic pressure; thus, inhibiting the absorption of nutrients and water absorption, resulting in a decrease in the amount of water entering the roots and a depletion of the water supply in plants (Muliawan et al., 2016).

According to Aizat et al; (2014), soil pH is related to soil electrical conductivity (EC). Soil pH is one of the most informative characteristics of soil about its state. The measured properties are the concentration of hydrogen ions in the soil. Additionally, it defines the presence of fertilizers and soil solubility. Since it determines the soil's toxicity and nutrient deficiency, pH at a certain level can be harmful to plants. Aizat et al (2014b), also stated that the amount of soluble salt in alkaline soil makes it to drop. It indicates that soil with a high salt level can be detected by its high EC and low pH levels. Table 1 present the tier of soil salinity level based on soil electrical conductivity.

Table 1. Classification of Soil Salinity and Soil EC (Rhoades et al., 1989).

No.	Salinity Level	Soil EC (S/m)	Class of Salinity
1	Non-Saline	0 – 0.2	0
2	Low	0.2 – 0.4	1
3	Moderate	0.4 – 0.8	2
4	High	0.8 – 1.6	3
5	Very High	>1.6	4

2. Study Area

Aceh Besar Regency is an administrative city surrounding the provincial capital of Aceh. Physio- graphically, Aceh Besar consists of an undulating alluvium that stretches from northwest to southeast. This area's alluvium is predominantly composed of gravelly sand, gravel, sandy clay, sandy silt, clayey silt, silty clay, and sediment originating from a wetland (Syukri et al., 2020b). The Aceh Besar Regency is divided into two distinct regions based on geological and geomorphological features. A mountainous region dominates the first section with modest hills and undulating terrain. Plain lands dominate the second section of Aceh Besar, and the majority of the suburbs are situated near the coast (Figure 1).

The research areas are situated in two distinct Aceh Besar districts. The first research area is located in the district of Blang Krueng and comprises a total of three measuring lines (Figure 2). Based on geological setting, this area is dominated by alluvium which has a type of sand, gravel, and mud (Bennet, et al., 1981). The selection of the study region is because the 2004 tsunami severely damaged Blang Krueng due to its proximity to the coast. Despite its proximity to the coast, most of the inhabitants of Blang Krueng are farmers. This issue prompted the author to study whether land contaminated with tsunami sedimentation is still efficient for agriculture.

The second study area is subsequently separated from the first study region (Figure 3). The research area is determined based on its morphology and topography, which classify it as a hilly region. Geologically, this area is formed by breccia, Agglomerate, Andesite, Dacite, Tuff, dan volcanic ash from Lam Teuba Volcano (Bennet, et al., 1981b). Two measured lines were undertaken to determine the difference in conductivity values between Tsunami sediment-contaminated and uncontaminated ground.

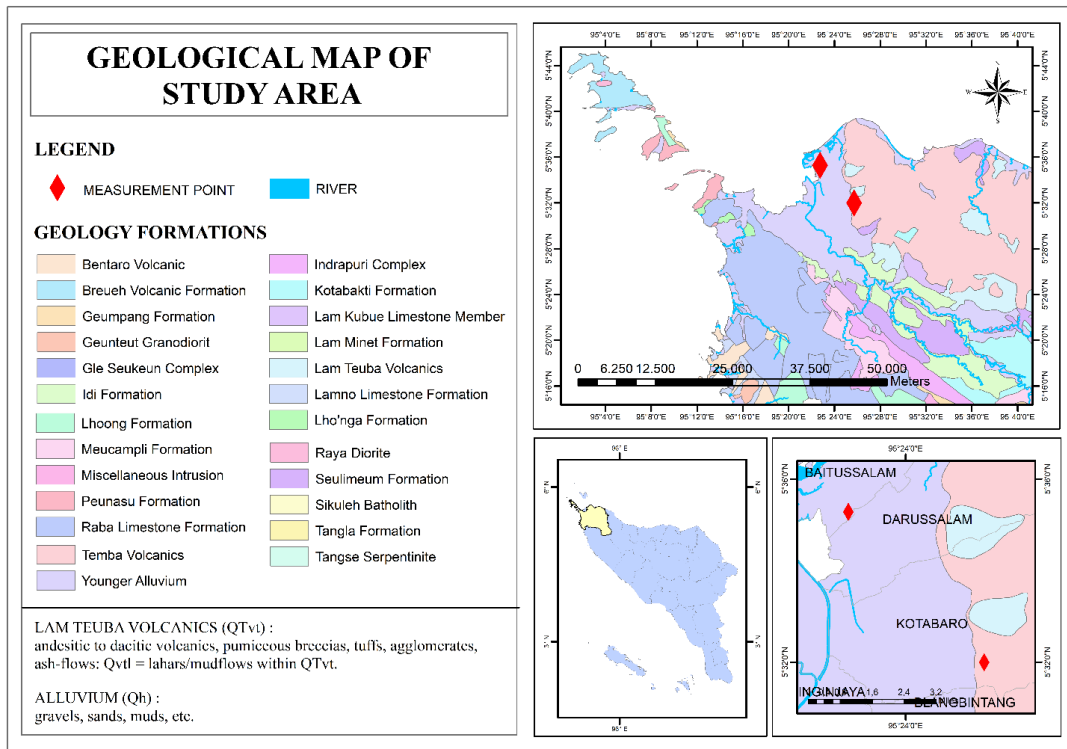


Figure 1. Geological Map of Aceh Besar Regency (Bennett et al., 1981c)

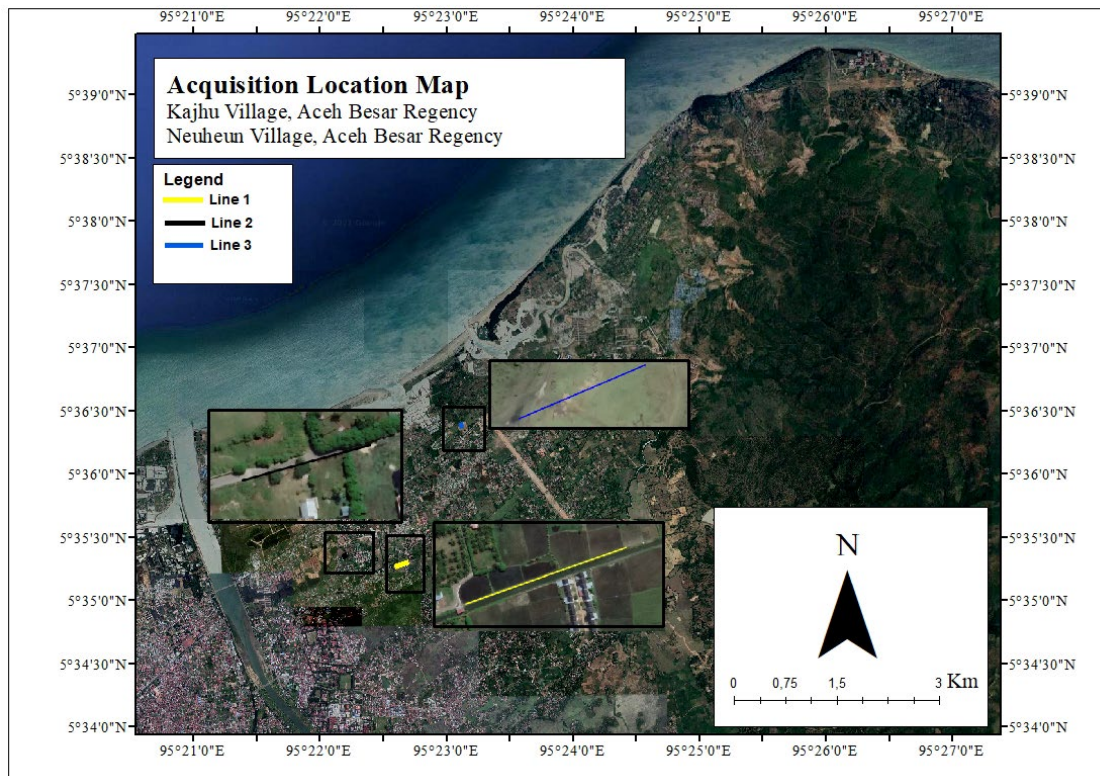


Figure 2. Study area of Blang Krueng District with three 2-D geoelectric measurement lines

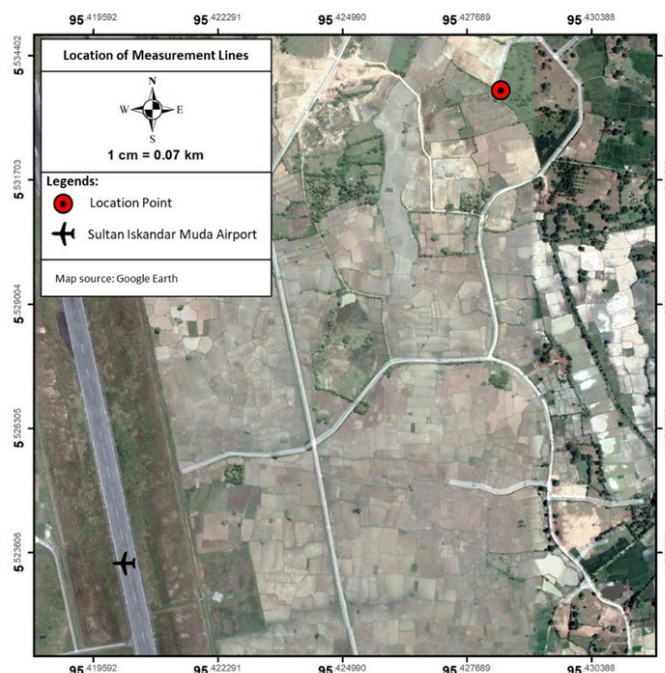


Figure 3. Study area of Blang Bintang District with 2-D geoelectric measurement lines

3. Methodology

2-D geoelectric approach and field measurements were conducted at two separate sites. The 2-D Geoelectric approach was utilized due to the correlation between soil salinity and electrical current propagation below the surface. According to (Raja et al., 2009), anthropogenic activities, such as the inefficient management of land and water resources and the weathering of parent materials, have resulted in the pervasive salinization of soils. Nonetheless, large-scale tsunamis also contribute to the salinization of soil conditions. The 2-D geoelectrical method is an active geophysical technique that involves delivering a regulated direct current (dc) into the subsurface via an iron electrode rod. Subsurface information is classified by calculating the apparent resistivity (ρ_a) from the recorded resultant electrical potential at a certain point/depth. Since the conductivity data are the inversion of the resistivity data, they were obtained automatically. Using software inversion, the tomography/pseudo-section approach is also used to depict the detail of the subsurface via tomography/pseudo-section model yield (Pierce et al., 2012).

In order to determine the amount of soil salinity in Aceh Besar, a total of four measurement lines ranging in length from 160 to 210 meters were constructed. In the Blang Krueng District, three measuring lines (K1, K2, and K3) were positioned slightly away from the shoreline, as illustrated in Figure 2. In addition to observing the variation of soil electrical conductivity in relation to soil salinity induced by tsunami sedimentation, the objective of line geometry was to explain

the soil salinity level based on saltwater intrusion. In addition, one measurement line was conducted in the Blang Bintang (B1) region to validate the difference between the conductivity values of land polluted with tsunami sediment and seawater intrusion and without intrusion.

4. Result and Discussion

The result of measuring the geoelectric field in two dimensions along the lines K1, K2, K3, and B4 is represented in Figures 4, 5, 6, and 7. The pseudo-sections have revealed conductivity values ranging from 0 to 15 S/m at depths ranging from 20 to 40 meters. In general, the pseudo-section is divided into two primary zones based on the depth of plant roots. Based on observation and field data, the author concludes that the initial zone of lines K1, K2, and K3 in the Blang Krueng district, which has a thickness of < 5 m, is interpreted as a tsunami sediment-contaminated layer.

Figure 4 depicts the result of the Blang Krueng district's lines K1, K2, and K3. The results indicate that the area is categorized as conductive. It is demonstrated by the conductivity of up to 10 S/m. The first zone of lines K1, K2, and K3 have a conductivity value of between 0.06 and 2 S/m. The zones are regarded as a sandy clay-dominated alluvium layer with a thickness of ± 5 m. The second zone of lines K1, K2, and K3 is then characterized as having a conductivity value between 2 and 10 S/m and a depth of > 5 m. The high conductivity value of the second zone is thought to be the result of sea-derived sedimentation.

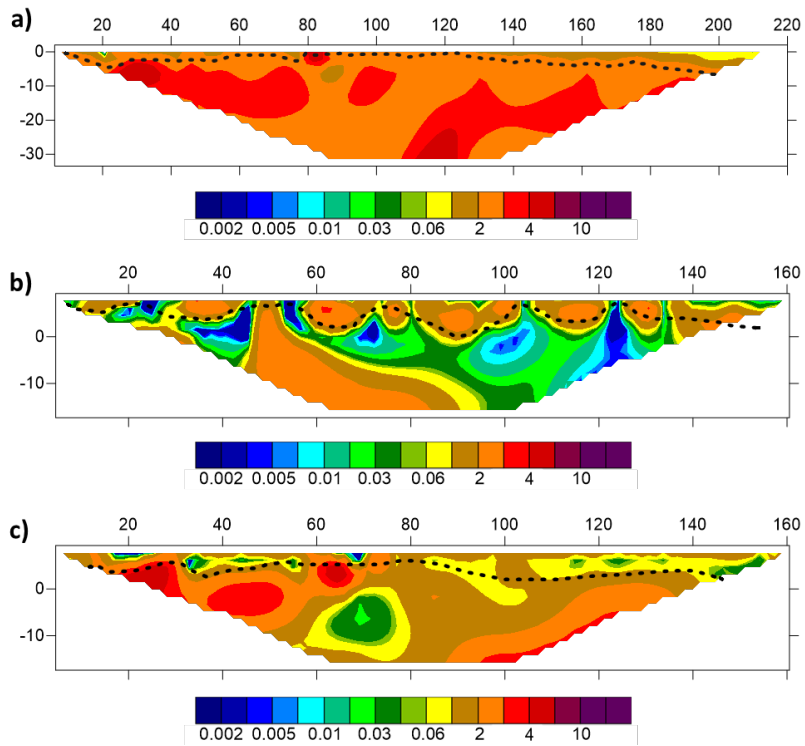


Figure 4. Conductivity inversion models of Blang Krueng district; a) K1, b) K2, c), and K3

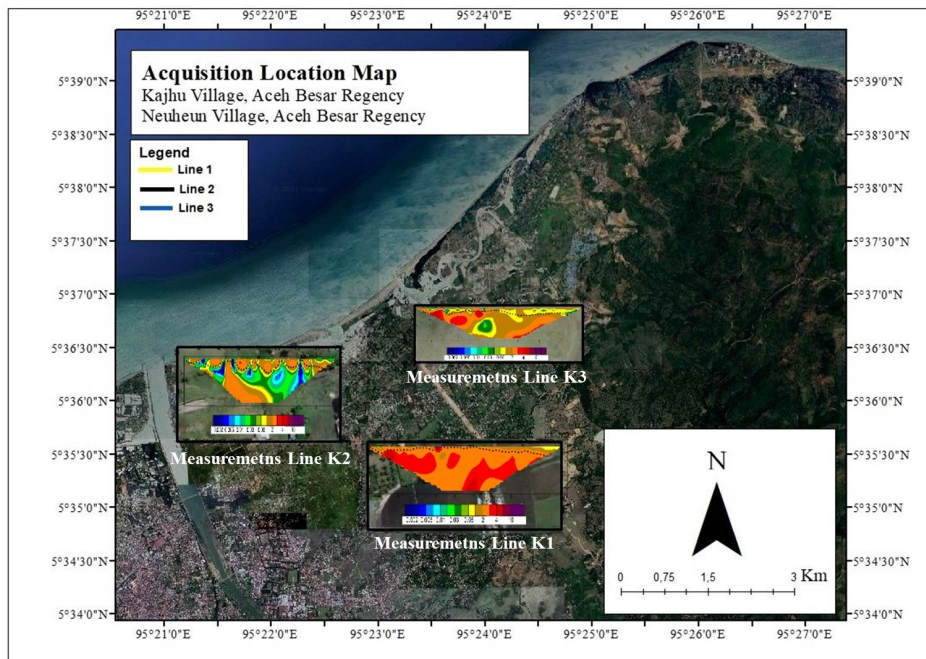


Figure 5. Conductivity inversion model based on location of measurement lines at Blang Krueng district.

Figure 6 shows the pseudo-section of line B1 in the Blang Bintang region. The observed value of conductivity is less than 1 S/m. With a depth of 40 meters, the distribution of conductivity values is typically between 0 and 0.08 S/m. The pseudo-section is also divided into two major zones, with the first zone having conductivity values of between 0 and 0.005

S/m understood to be the first layer, which is dominated by clay and has a thickness of < 5 m. In contrast, the second zone is understood as a layer of tuff and andesite. The zone is characterized by a conductivity value of > 0.05 S/m and a depth of > 5 meters.

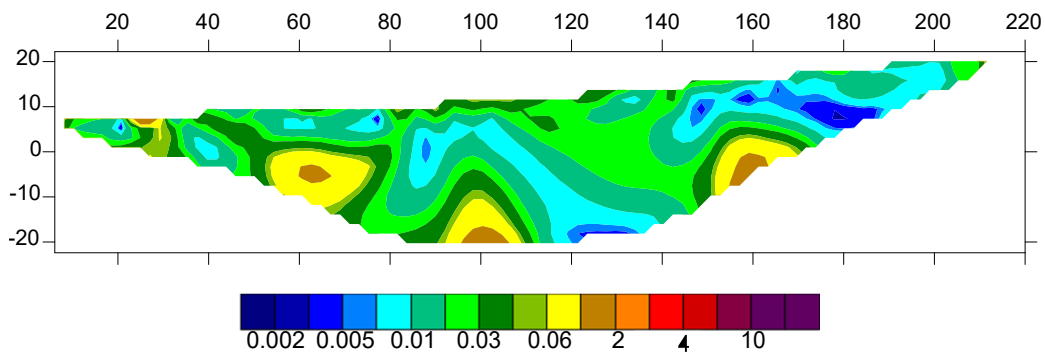


Figure 6. Conductivity inversion models of Blang Bintang district; measurement line of B1

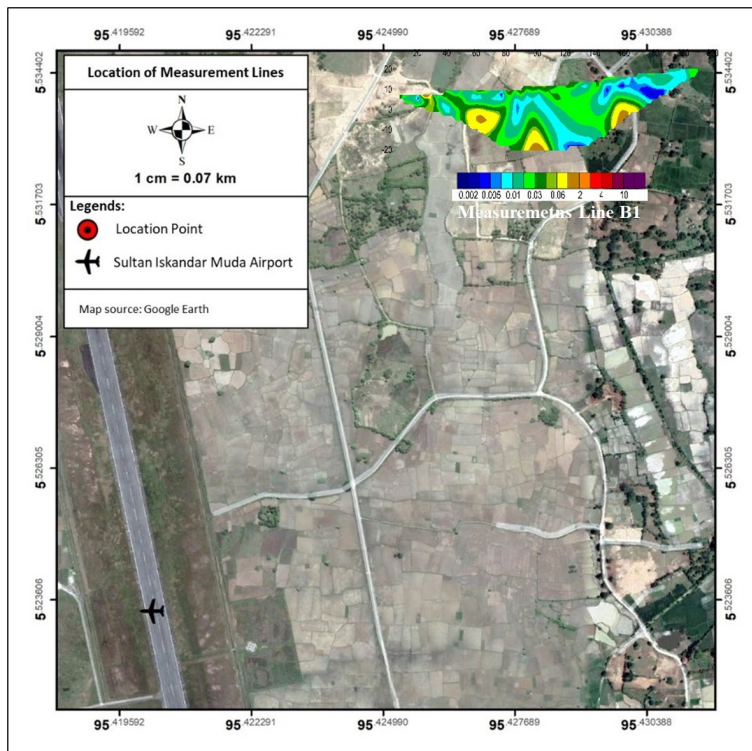


Figure 7. Conductivity inversion model based on location of measurement lines at Blang Bintang district

In addition, the result of soil pH reveals that the area covered by Tsunami sediment deposition (Blang Krueng) has a lower pH range than the Blang Bintang region. In the Blang Krueng region, the measured pH ranges from 5.0 to 6.4; however, in the Blang Bintang region, the pH range is significantly greater, ranging from 6.7 to 7.2.

Based on observation and interpretation of field measurements, it was determined that the soil condition of the region contaminated with depositional tsunami sediment in 2004 (Blang Krueng) differs significantly from that of the unaffected area. With a thickness of 5 m, it has a wide range of conductivity values between two regions, 0.06 – 2 S/m and 0 – 0.05 S/m respectively. The obtained result indicates that the salinity level in the tsunami-contaminated Blang Krueng region is significantly greater than in the Blang Bintang region. It is also corroborated by the fact that

the Blang Bintang region is located far from the shoreline; hence the 2004 tsunami did not touch the region.

In addition, it was discovered that the Blang Krueng the studied area, which was a tsunami-affected location in 2004, had undertaken a mitigation effort in the form of land reclamation (Yusya’ et al., 2008). This suggests that even though the Agency for the Rehabilitation and Reconstruction of Aceh and Nias, United Nations, and Non-Governmental Organizations have completed the mitigation stage of sediment removal from severely damaged land, the sustainability effects produced by the tsunami sediment still affects the soil in the region. According to Roy et al (2014), although the rehabilitation of agricultural land productivity has been conducted, it has not been fully accomplished due to different phenomena stemming from the physicochemical and biological status of topsoil under long-term natural conditions.

5. Conclusion

Based on the research findings, it can be stated that locations damaged by tsunami sedimentation in 2004 had a greater conductivity value than unaffected areas. The measurement findings showed a conductivity value of > 2 S/m at a depth of 5 m in the category of extremely high salinity. In addition, the measurement results suggest that the measurement of land salinity for agricultural purposes may be described in detail with a broad range of geophysical measures, particularly the 2-D geoelectric method used in this study.

6. Acknowledgement

The authors would like to thank the Directorate General of Higher Education, Research and Technology Directorate of Resources, Indonesia, Indonesia Endowment Fund for Education, Rispro with contract number 011/E4.1/AK.04.RA/2021 for fully supporting the research through the research grant of Riset Keilmuan, Hibah Riset Kemanusiaan. Furthermore, special gratitude also given to staff and students of Physics and Engineering Geophysics Department of Syiah Kuala University, and staff of Geophysics Study Program, Universitas Samudra for the efforts during data acquisition and analysis.

7. References

- Aizat, A. M., Roslan, M. K., Sulaiman, W. N. A., & Karam, D. S. (2014). The relationship between soil pH and selected soil properties in 48 years logged-over forest. *International journal of environmental sciences*, 4(6), 1129-1140.
- Azmeri, A., Mutiawati, C., Al-Huda, N., & Mufiaty, H. (2017). Disaster Recovery Indicators of Housing Reconstruction: The Story of Post Tsunami Aceh, Indonesia. *International Journal of Disaster Management*, 1(1), 35-45.
- Bennett, J.D., Bridge, D.McC., Cameron, N.R., Djunuddin, A., Ghazali, S.A., Jeffery, D.H., Kartawa, W., Keats, W., Rock, NMS & Thompson, S.J. (1981). *Geologic Map of the Calang Quadrangle, Sumatra*. Geological Research and Development Centre, Bandung.
- Helliwell, J. R., Sturrock, C. J., Grayling, K. M., Tracy, S. R., Flavel, R. J., Young, I. M., ... & Mooney, S. J. (2013). Applications of X-ray computed tomography for examining biophysical interactions and structural development in soil systems: a review. *European Journal of Soil Science*, 64(3), 279-297.
- Johnson, C. K., Doran, J. W., Duke, H. R., Wienhold, B. J., Eskridge, K. M., & Shanahan, J. F. (2001). Field-scale electrical conductivity mapping for delineating soil condition. *Soil Science Society of America Journal*, 65(6), 1829-1837.
- Kravchenko, A. N., Bollero, G. A., Omonode, R. A., & Bullock, D. G. (2002). Quantitative mapping of soil drainage classes using topographical data and soil electrical conductivity. *Soil Science Society of America Journal*, 66(1), 235-243.
- Lay, T., Kanamori, H., Ammon, C. J., Nettles, M., Ward, S. N., Aster, R. C., ... & Sipkin, S. (2005). The great Sumatra-Andaman earthquake of 26 december 2004. *Science*, 308(5725), 1127-1133.
- Marohn, C., Distel, A., Dercon, G., Tomlinson, R., Noordwijk, M. V., & Cadisch, G. (2012). Impacts of soil and groundwater salinization on tree crop performance in post-tsunami Aceh Barat, Indonesia. *Natural Hazards and Earth System Sciences*, 12(9), 2879-2891.
- Muliawan, N. R., Sampurno, J., & Jumarang, M. I. (2016). Identification of salinity value in agricultural land in Jungkat Area based on the electrical conductivity (EC) method. *Jurnal Prisma Fisika*, 4(2), 69-72.
- Niino, Y. (2008). Agricultural Impacts in Tsunami-Affected Areas: Regional Perspectives. In *International Workshop on Post-tsunami Soil Management (Vol. 1, p. 21)*.
- Pierce, S. K., Liechty, D. C., & Rittgers, J. B. (2012). Geophysical Investigations, Electrical Resistivity Surveys, Santee Basin Aquifer Recharge Study. US Department of the Interior Bureau of Reclamation Technical Service Center Seismotectonics and Geophysics Group, Lower Colorado Region, Southern California Area Office, Santee, California, USA, Phase, 2, 1-71.
- Raja, R., Chaudhuri, S. G., Ravisankar, N., Swarnam, T. P., Jayakumar, V., & Srivastava, R. C. (2009). Salinity status of tsunami-affected soil and water resources of South Andaman, India. *Current Science*, 152-156.
- Rhoades, J. D., Manteghi, N. A., Shouse, P. J., & Alves, W. J. (1989). Soil electrical conductivity and soil salinity: New formulations and calibrations. *Soil Science Society of America Journal*, 53(2), 433-439.
- Romero-Ruiz, A., Linde, N., Keller, T., & Or, D. (2018). A review of geophysical methods for soil structure characterization. *Reviews of Geophysics*, 56(4), 672-697.
- Roy, K., Sasada, K., & Kohno, E. (2014). Salinity status of the 2011 Tohoku-oki tsunami affected agricultural lands in northeast Japan. *International Soil and Water Conservation Research*, 2(2), 40-50.
- Rusydy, I., Idris, Y., Muksin, U., Cummins, P., & Akram, M. N. (2020). Shallow crustal earthquake models, damage, and loss predictions in Banda Aceh, Indonesia. *Geoenvironmental Disasters*, 7(1), 1-16.
- Saad, R., Syukri, M., Anda, S. T., & Fadhli, Z. (2019). Resistivity and Chargeability Signatures of Tsunami Deposits at Aceh Besar and Banda Aceh Coastal Area, Indonesia. *GEOMATE Journal*, 17(59), 133-143.

- Schlüter, S., Sheppard, A., Brown, K., & Wildenschild, D. (2014). Image processing of multiphase images obtained via X-ray microtomography: a review. *Water Resources Research*, 50(4), 3615-3639.
- Suppasri, A., Al'Ala, M., Luthfi, M., & Comfort, L. K. (2019). Assessing the tsunami mitigation effectiveness of the planned Banda Aceh Outer Ring Road (BORR), Indonesia. *Natural hazards and earth system sciences*, 19(1), 299-312.
- Syukri, M., Anda, S. T., Safitri, R., Fadhli, Z., & Saad, R. (2020). Prediction of Soil Liquefaction Phenomenon in Banda Aceh and Aceh Besar, Indonesia using Electrical Resistivity Tomography (ERT). *GEOMATE Journal*, 18(70), 123-129.
- Tinning, G. (2011). The role of agriculture in recovery following natural disasters: a focus on post-tsunami recovery in Aceh, Indonesia. *Asian Journal of Agriculture and Development*, 8(1362-2016-107702), 19-38.
- Yusya' A. and Hairul B. (2008) Rehabilitation of Tsunami-Affected Agricultural Areas in Aceh and Nias. In *Proceedings International Workshop on Post-tsunami Soil Management: 1-2 July 2008*. Cisarua, Bogor, Indonesia (pp. 33-41)

Crafting a Specific Deep Network for Real-Time Identification of Ayurvedic Plants

Meghana Shetty^{1a}, Harshitha Rai^{2a}, Namyashetty^{3a}, Roopa B Hegde^{4a*}, Narendra K C^{5c}, Guruprasad Shetty^{6b}

Abstract: Plants play a vital role in the existence of living beings, especially, humans, as we rely on plants for our food, medicine, and many other needs. Plant-based medicine is an age-old science practiced in many countries. It is considered safer than chemical-based medicine for humans because of its natural ingredients. Planet Earth is home to numerous plant species with medicinal properties. However, the current generation lacks knowledge of these medicinal plants. Hence, there is a need for automated identification of medicinal plants to facilitate their use as medicine. In this work, an automated classification system for identifying medicinal leaves was designed using a deep learning approach. Furthermore, for real-time usage of the developed classification system, an Android-based smartphone app was developed. The medicinal values of the identified leaves are also displayed on the smartphone screen. The dataset required for training the deep network was acquired in the southern part of Karnataka, India. The system identifies eight types of medicinal leaves with an average accuracy of 99%. Such an automated system will help people associated with Ayurvedic medicine, botanists, and common people to use herbs as medicine.

Keywords: Medicinal leaves, automated identification, deep learning, smartphone app, real-time system

1. Introduction

A point cloud can be described as a collection of data points arranged in space. A three-dimensional (3D) structure or object might be represented by points, each with its Cartesian coordinate, which illustrates each point position (Wang & Kim, 2019). The source of point clouds can be from a 3D scanner or a photogrammetry software, and other devices.

Plants with medicinal properties have been highly important as remedies for various ailments since ancient times. This practice of utilizing plant-based remedies was widespread across diverse ancient medicinal traditions, including Ayurveda. Medicinal preparations often involved different plant components, such as roots, leaves, stems, fruits, and seeds. The method of preparation varied based on the targeted ailment and the desired shelf life of the resulting medicines. While plant-based ingredients were commonly used in these remedies, identifying the specific plants posed a formidable challenge. Practitioners like herbalists had to retain a comprehensive understanding of each plant's distinctive characteristics. Visual appearance was as a primary means of plant identification. This encompassed factors such as the plant

size, leaf shape, stem structure, and fruit characteristics (Abdollahi, 2022). The coloration of different plant parts also played a role in such identification (Picek et al., 2022).

In recent years, machine learning (ML) and deep learning (DL) have been increasingly used for accurate medicinal leaf identification (Ariful Hassan et al., 2022). By analyzing vast botanical databases and matching leaf characteristics with known properties, they have the potential to expedite the discovery of new medicinal plants. Moreover, these technologies facilitate real-time and portable leaf identification through smartphone apps or handheld devices, empowering individuals with instant access to valuable botanical knowledge. However, automatic identification of plants based on some of these visual characteristics is challenging due to data diversity and quality, intra and inter-species variability, and complexity of visual features. Thus, many methods have been proposed to identify medicinal plants based on their leaf characteristics, such as their leaves' shape, colour, and texture. Attempts to automate the task of plant identification include the use of conventional ML and DL methods (Ali et al., 2018; Pearline et al., 2019; Begue et al., 2017; Hedjazi et al., 2017; Kartikeyan & Shrivastava, 2021; Lee et al., 2023; Kumar & Pearline et al., 2023; SkandaH et al., 2019; Tan et al., 2020; Wagle et al., 2022). In addition, Oppong et al. (2021) described the use of several ML techniques to identify medicinal plants. Specifically, the multilayer perceptron method was used to identify six types of medicinal leaves based on their texture features (Naem et al., 2021) and achieved 98%–99% success. A recent study explored the use of partial least squares discriminant analysis, support vector machine, and DL methods to identify medicinal plants (Yue et al., 2021) and concluded that DL models

Authors information:

^aDepartment of Electronics and Communication Engineering, NMAM Institute of Technology, Nitte (Deemed to be University), Karkala, Udupi, Karnataka, INDIA. E-mail: shettymeghana32@gmail.com¹; harshitharai012@gmail.com²; namyashetty2001@gmail.com³; roopabhegde@nitte.edu.in⁴

^bDepartment of Panchakarma, Muniyal Institute of Ayurveda Medical Sciences, Manipal, Udupi, Karnataka, INDIA. E-mail: shettydrguruprasad@yahoo.co.in⁶

^cDept. of ECE, East West Institute of Technology, BEL layout, Bengaluru, Karnataka, INDIA 560091. E-mail: narendra@nitte.edu.in⁵

*Corresponding Author: roopabhegde@nitte.edu.in

Received: August 23, 2023

Accepted: January 9, 2024

Published: December 31, 2024

could be efficiently used to classify such plants. Geerthana et al. (2021) also used a deep network to classify four types of medicinal leaves and achieved an accuracy of around 97%. Abdollahi (2022) employed transfer learning approach of DL using MobileNetV2 to identify 30 classes of medicinal plants in Ardabil and achieved 98% accuracy. Haryono and Saleh (2020) used a combination of a convolutional neural network (CNN) and long short-term memory (LSTM) to identify and authenticate herbal leaves and achieved an accuracy of around 95%. Manoharan (2021) proposed deep knowledge-based herbal leaf identification by combining the edge detection method and DL and achieved an average accuracy of around 92%. Although many researchers are developing automated systems for recognizing medicinal plants, an optimized system for identifying leaves and their medicinal values is needed. Pudaruth et al. (2021) used the mobile app ‘MedicPlant’ to identify 70 types of medicinal leaves using CNN and achieved 90% overall accuracy. Additionally, Azadnia et al. (2022), Malik et al. (2022), and Oppong et al. (2022) developed deep CNN from scratch for the identification of medicinal plants.

In this study, a CNN was developed for the automatic identification of medicinal plants. A CNN is a class of DL artificial neural network that is extensively used for vision-related tasks. In this study, it was developed to identify the plant species based on the shape, color, and texture of its leaves. To increase the usability of the system, an Android app was also developed that would make the identification possible in the wild through a smartphone. This app would help reduce the ambiguity in the identification of the species when in a dilemma. The expected contributions of the proposed system are as follows:

- A deep neural network architecture specifically designed to identify plant species based on leaf images;
- A validated database of leaf images to help advance research in this field;
- An Android app for plant recognition by taking a picture of the leaf from a smartphone camera; and
- Pre-processing techniques for handling real-time issues, such as brightness variations and motion blur.

2. Methodology




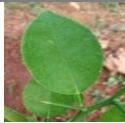




The objective is to develop a practically usable app, and hence, the system is trained to handle brightness variations and motion blur that are commonly faced issues in real-time scenarios. This requires a large dataset for training a CNN. The details of the dataset and methodology are provided in the subsequent sections.

Data Collection

The dataset required to train the CNN model was acquired from various regions of Udupi and Dakshina Kannada Districts in Karnataka, India using a smartphone camera with a 2,160×2,160 resolution. The dataset consisted of 5,160 images, including of the following eight species of medicinal leaves: *Tinospora cordifolia* (amrutha balli), *Trachyspermum ammi* (ajwain), *Hibiscus rosasinensis* (hibiscus), *Citrus limon* (lemon), *Bacopa monnieri*

(brahmi), *Ocimum sanctum* (tulsi), *Calotropis procera* (ekkamale or arka), and *Carica papaya* (papaya). The sample images in the dataset and the number of images in each category are given in Table 1.

Table 1. Dataset Details

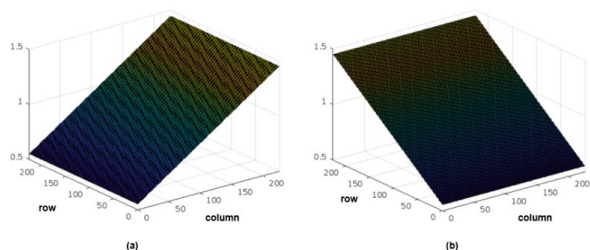
Plant name & total no. of images	Sample of image	Plant name & total no. of images	Sample of image
<i>Tinospora cordifolia</i> , 734 images		<i>Hibiscus rosasinensis</i> 500 images	
<i>Trachyspermum ammi</i> , 607 images		<i>Citrus limon</i> , 709 images	
<i>Bacopa monnieri</i> , 554 images		<i>Carica papaya</i> , 644 images	
<i>Calotropis procera</i> , 695 images		<i>Ocimum sanctum</i> , 717 images	

To meet the data requirement of the data-hungry CNN model, data augmentation was performed on the images. Data augmentation is a process of increasing the size of a dataset without loss of the original features of the images (Samuel, 2021). The augmented dataset consisted of 10,000 images. Because images in real-time apps commonly show nonuniform brightness, we introduced brightness variations onto the images (see Algorithm 1). The algorithm created row and column vectors with sizes equal to those of the rows and columns of the images. Hence, 227 values between 0.55 and 1.45 were created to form row and column vectors. These values were transformed into two 227×227-sized grids, as shown in Figure 1. The two grids corresponded to variations in the intensity values along the columns (Figure 1a) and rows (Figure 1b). As a result, two grayscale images with varying intensities were created. Intensity variations were observed on the original leaf images when these grayscale images were multiplied with the original images.

Algorithm 1. Introduction of Nonuniform Brightness on the Images

1. Input the RGB image.
2. Split the image into R, G, and B representations.
3. Determine the number of rows and columns.
4. Set $\alpha = 0.45$.
5. Create a column vector with values between $1-\alpha$ and $1+\alpha$.
6. Create a row vector with values between $1-\alpha$ and $1+\alpha$.
7. Transform the column and row vectors to a grid with a size equal to the image size.

Figure 1. Grids of Size 227×227 with Brightness Intensity Variation



(a) Brightness variation along the column. (b) Brightness variation along the row.

To expand the dataset, brightness variation was considered for the design of a robust system that could be used in real time. When a user captures a leaf image in a real-time scenario, the image may suffer from nonuniform brightness variations. Samples of brightness-varied images are shown in Figure 2 (bottom row). Both darker and brighter shades can be observed in the augmented images.

Image processing and analysis is a valuable tool for differentiating medicinal leaves based on their visual features, starting from image acquisition to classification and recognition. The efficiency and robustness of the classifier model depend on the data quality and the data diversity, respectively. Hence, ensuring that the data are well focused and positioned against a contrasting background is necessary during data acquisition. Moreover, image enhancement, colour correction, and filtering can be applied to improve the image quality and to standardize the colour. These will further improve the performance of the classifier. To design a robust architecture for the proposed classifier model, nonuniform brightness variations were introduced onto the original images.

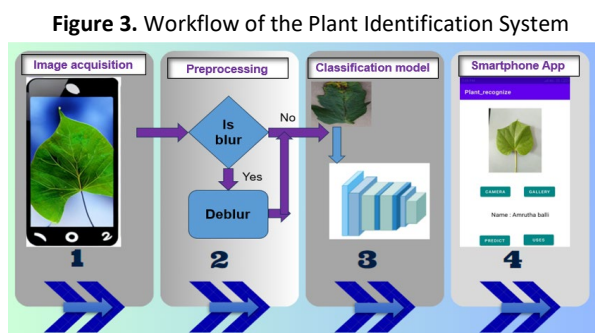
Figure 2. Sample Images of the Training Data



Top row: original images. Bottom row: augmented images.

The Plant Identification Model

A DL approach using CNN was employed to identify medicinal leaves. The overall flow diagram of the proposed system is shown in Figure 3. The image acquisition module in the proposed system is a smartphone camera. To avoid unnecessary waste of plant sources, the leaves were not plucked from the trees while their images were being captured. Hence, their movement was unavoidable. To address this challenge, the computed variance value of the Laplacian was used. In the blur estimation method, the green component of the original image was convolved with a 3×3-sized Laplacian kernel, and the variance of the output was determined. This generated a single value based on the quality of the input image. A thresh-old value of 105 was set empirically to estimate the quality of the image. A computed variance value that was less than the threshold value indicated that the image was blurred. Blurred images were deblurred. This approach reduces the computation time and complexity and allows users to capture images while they are moving or traveling, even when there is a moderate breeze, albeit at a nominal speed. Furthermore, blurred images were deblurred using the Richardson–Lucy deconvolution method. This iterative algorithm gradually refines the estimate of the original image by considering the blurred image and the degradation process. It repeatedly estimates the error and updates the image estimate to reverse the effects of blurring. The pseudocode for the Richardson–Lucy deconvolution method is given in Algorithm 2.



Algorithm 2. Richardson–Lucy Deconvolution Method

1. Input the blurred RGB image (I_m), point spread function (PSF), and number of iterations (n).
2. Convert the blurred image to double the precision and to initialize the deblurred image (D_e).
3. For iteration = 1 to n .
 - a. Estimate the error image (E_{I_m}) using the relation $E_{I_m} = I_m / D_e * PSF$.
 - b. Update D_e using the relation $D_e = D_e * (E_{I_m} * PSF)$.
4. Output the deblurred image D_e .

To sharpen the leaf images, a Laplacian filter was used. Furthermore, the images were resized to $227 \times 227 \times 3$ before they were fed to the input layer of the CNN model. The architectural details of the model are presented in Table 2. The proposed network consists of five convolution layers, followed by a Rectified Linear Unit (ReLU), three max-pooling layers, two fully connected layers, and three dropout layers with a dropout rate of 0.25. The network was trained at a learning rate of $1e-4$ and with batch sizes of 32 and 200 epochs. The model was trained with 200 epochs. An Adam optimizer was used to train the model with cross-entropy as a loss function.

Table 2. Architectural Details of the Classification System Layer Details

Layer	Details
Input	$227 \times 227 \times 3$
Convolution	Filter mask: 3×3 , depth: 32, stride: 1, padding: 1, ReLU
Max-pooling	3×3 , stride: 1
Dropout	Rate: 0.25
Convolution	Filter mask: 3×3 , depth: 64, stride: 1, padding: 1, ReLU
Convolution	Filter mask: 3×3 , depth: 64, stride: 1, padding: 1, ReLU
Max-pooling	2×2 , stride: 1
Dropout	Rate: 0.25
Convolution	Filter mask: 3×3 , depth: 128, stride: 1, padding: 1, ReLU
Convolution	Filter mask: 3×3 , depth: 128, stride: 1, padding: 1, ReLU
Max-pooling	2×2 , stride: 1

pooling	
Fully connected	1,024
Dropout	Rate: 0.25
Fully connected	8

The model was tested with real-time images, and an app was developed using An-droid Studio at the front end and Java at the backend. The developed app can be download-ed to any Android-based smartphone and can be used in real-time scenarios.

3. Results and Discussion

To design a robust architecture for the proposed classifier model, nonuniform brightness variations were introduced onto the original images. Furthermore, to address the blurred images to improve the quality of the images, the deblurring method was applied, as detailed in Algorithm 2, but only on the blurred images. Finally, Laplacian filtering was used to sharpen the edges of the leaves. These image pro-cessing methods substantially improved the quality of the images supplied as inputs to the classifier model. To design an accurate classification model, several experiments were carried out during the training by changing the number of epochs, the learning rate, and the batch size. Table 3 presents the experiment observations for different model learning rates, numbers of epochs, and batch sizes.

Table 3. Performance of the Classification System Under Different Parameters

Learning rate	No. of epoch, n	Batch size, n	Test accuracy, %	Training accuracy, %
1e-1	100	32	88.503	76.03
1e-2	100	32	50.23	72.45
1e-3	100	32	98.61	99.30
1e-3	150	32	98.76	99.21
1e-3	200	32	99.03	99.26
1e-3	100	16	98.92	90.22
1e-3	100	64	97.00	99.63
1e-4	100	32	91.97	98.82
1e-4	150	32	95.62	99.63
1e-4	200	32	98.45	99.88
1e-5	100	32	85.53	90.43

Fonts in bold represent selected training parameters for obtaining highest accuracy

Table 3 shows that better training and test accuracy were achieved at the learning rate of $1e-4$, with 200 epochs and a batch size of 32. Hence, the model with these values was used for the app development. Since for a multi-class problem, it is important to compute the categorical performance of the network, the proposed model was tested with a test dataset that was unseen by the network. The test dataset included images of eight types of leaves. The results of the use of the classifier model are shown

in Figure 4. Furthermore, evaluation metrics, such as the precision rate, recall rate, and F1 score, for each leaf type were computed and are shown in Figure 5. In this study, precision was measured by the number of correct positive predictions made, and recall, by

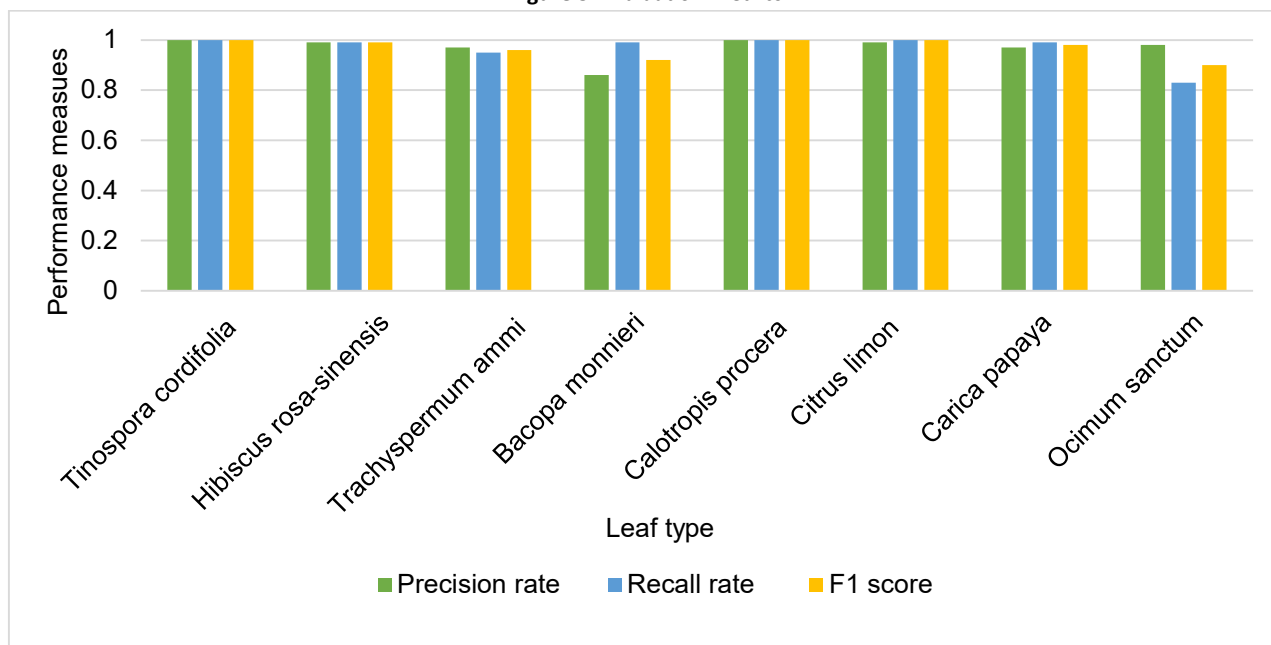
the number of correct positive predictions made from all positive predictions that could have been made. Figure 5 shows that the misclassification rate is higher in the case of *Bacopa monnieri*. This could be due to the acquisition of bunches of leaves of this plant class, which might have overlapped in appearance.

Figure 4. Confusion Matrix

	1	2	3	4	5	6	7	8
1	151	0	0	0	0	0	0	0
2	0	110	0	0	0	1	0	0
3	0	1	102	4	0	0	0	0
4	0	0	0	119	0	0	0	1
5	0	0	0	0	136	0	0	0
6	0	0	0	0	0	139	0	0
7	0	0	1	0	0	0	135	1
8	0	0	2	16	0	0	4	110

1. *Tinospora cordifolia*. 2. *Hibiscus rosa-sinensis*. 3. *Trachyspermum ammi*. 4. *Bacopa monnieri*. 5. *Calotropis procera*. 6. *Citrus limon*. 7. *Carica papaya*. 8. *Ocimum sanctum*.

Figure 5. Evaluation Metrics



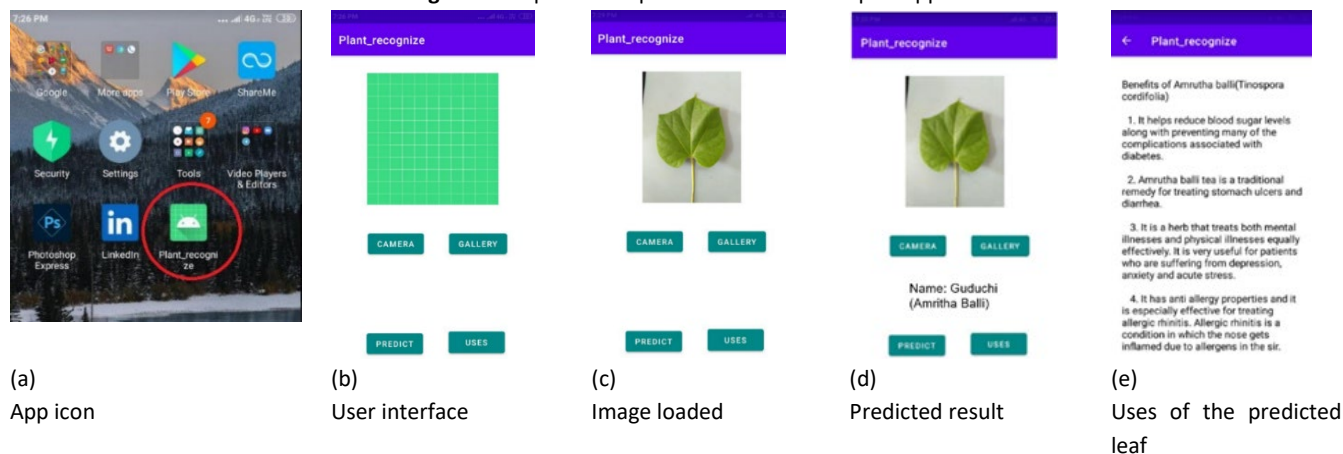
The designed network serves as the classification system in the developed app. To develop the app, Android Studio software was used, and it was programmed using Java. The steps in the app's operation are shown in Figure 6. First, the app icon is circled in Figure 6a. Clicking on this icon opens the user interface (Figure 6b). On the user interface, the user is given an option to either

capture an image using the smartphone camera or access an image from the phone's image gallery. If the "Camera" button is clicked, the user will be asked for permission for the app to access the phone's camera. Once permission is given, the user can capture the image. If the "Gallery" button is clicked, images can be accessed from the phone's image gallery (Figure 6c). If the

“Predict” button is clicked, the plant in the image is identified by the classification system, and the plant’s common name and its name in Ayurvedic science are displayed on the screen, as shown in Figure 6d. To know the medicinal values of the predicted leaf, the user can click on the “Uses” button, and the benefits will be

displayed on the screen, as shown in Figure 6e. Since this app allows the user to know the type of medicinal leaf and its benefits in real time, it could be used for teaching purposes. In addition, its user-friendliness enables common people to use it easily.

Figure 6. Steps in the Operation of the Developed App



The proposed model is compared with existing models in Table 4. The table shows that the proposed model is more accurate than the other models but identifies fewer plant classes. However, earlier studies proposed only the model, but in the present study, a real-time app was designed as well. For example, the app that Pudaruth et al. (2021) developed for medicinal leaf classification considers 70 types of leaves, but the accuracy of the Inception-v3 model that it used as its classification system was only around 90%. Moreover, while it also operates in real time, the proposed classification system identifies the medicinal leaves in a brighter shade, a darker shade, nonuniform bright-ness variations, and uniform brightness variations, which are common real-time scenarios. This functionality is made possible by CNN, which we designed from scratch and trained using images with different lighting conditions. after the transfer learning approach that we initially employed for the classification performed poorly. To enhance the performance of our proposed classification system, we will consider increasing the number of plant classes that it can process.

Table 4. Comparison of Related Studies

Study	No. of plant classes <i>n</i>	Size of dataset (no. of images) <i>n</i>	Accuracy %	Real time
Geerthana et al. (2021)	30	58,280	96.67%	No
Jafar (2022)	30	3,000	98.05%	No
Haryono & Saleh (2020)	9	-	94.96%	-
Manoharan (2021)	6	500	92.00%	No
Pudaruth et al. (2021)	70	70,000	90.00%	Yes
Malik et al. (2022)	6	23,708	87.00%	Yes
Azadnia et al. (2022)	5	750	99.00%	No
Oppong et al. (2022)	49	2,450	98.00%	No
Current study	8	10,000	99.00%	Yes

4. Conclusion

This paper presents the development of a real-time automated system for identifying medicinal plants based on their distinctive leaf characteristics. The system utilizes a specific CNN architecture tailored to accurately classify different plant species. After extensive experimentation, the CNN achieved an impressive accuracy of 99.8% when tested on a carefully validated dataset, underscoring its effectiveness in identifying medicinal plants. Optimal hyperparameters were determined after thorough testing, resulting in a learning rate of 0.0001 and a batch size of 32. These training parameters played a crucial role in achieving the high accuracy of the system. To enable the system's practical use, an Android app was developed and rigorously tested to ensure its effective performance in real-time scenarios like brightness variations and blurring effects. Hence, the proposed model was trained with nonuniform brightness images. In addition, the app was trained to deblur blurred images and to capture moving images. These features bring the system one step closer to practical application.

This automated medicinal plant identification system holds great promise in various fields. It can support education by providing a valuable tool for plant species recognition in the teaching-learning process. Additionally, it can assist in the preparation of herbal medicines, ensuring the selection of the correct plant species for medicinal purposes. Future enhancements will focus on expanding the system's capabilities to cover a broader range of plant classes. This will make the system even more useful, and applicable to a wider array of plant identification scenarios.

Oryza sativa aqueous extracts with potassium alum as mordant can be used for staining semen to allow researchers to observe the morphology of sperms. Aqueous extract of *Papaver rhoeas* with added chemicals like acetified ethylene glycol, sodium iodide, aluminium chloride, beta-cyclodextrin, and potassium alum can act as a good alternative stain to haematoxylin, as they both share the same staining principle. Besides that, *Hibiscus sabdariffa* and *Rosa hybrida* aqueous extracts with the presence of iron or alum as mordant can also be used for histopathological staining. Further studies are needed to investigate the effectiveness of *Morus nigra*, *Clitoria ternatea*, *Allium cepa*, *Syzygium cumini*, and *Punica granatum* by using different solvents to increase their staining potentials when used on various histological tissues. There is a lack of studies that analyze the stability of slides stained with natural stains, which is a very important requirement for histopathology. These lacunae presents a space for the discovery and invention of new natural stains.

5. Declaration of Interests

The authors declare that they have no known competing financial interests or personal relationships that could have influenced the work reported in this paper.

The authors declare that they did not use generative AI and AI-assisted technologies during the preparation of this work.

6. References

- Abdollahi, J. (2022). Identification of medicinal plants in Ardabil using deep learning: Identification of medicinal plants using deep learning. In 27th International Computer Conference (pp. 1–6). Computer Society of Iran. <https://doi.org/10.1109/CSICC55295.2022.9780493>
- Ali, R., Hardie, R., & Essa, A. (2018). A leaf recognition approach to plant classification using machine learning. In NAECON 2018 – IEEE National Aerospace and Electronics Conference, Dayton, OH, USA (pp. 431–434). IEEE. doi: 10.1109/NAECON.2018.8556785
- Ariful Hassan, M., Sydul Islam, M., Mehedi Hasan, M., Shorif, S. B., Tarek Habib, M., & Uddin, M. S. (2022). Medicinal plant recognition from leaf images using deep learning. In M. S. Uddin, & J. C. Bansal (Eds.), *Computer vision and machine learning in agriculture 2. Algorithms for intelligent systems* (pp. 137–154). Springer. https://doi.org/10.1007/978-981-16-9991-7_9
- Azadnia, R., Al-Amidi, M. M., Mohammadi, H., Cifci, M. A., Daryab, A., & Cavallo, E. (2022). An AI based approach for medicinal plant identification using deep CNN based on global average pooling. *Agronomy*, 12(11), 2723. <https://doi.org/10.3390/agronomy12112723>
- Begue, A., Kowlessur, V., Singh, U., Mahomoodally, F., & Pudaruth, S. (2017). Automatic recognition of medicinal plants using machine learning techniques. *International Journal of Advanced Computer Science and Applications*, 8(4), 166–175.
- Geerthana, R., Nandhini, P., & Suriyakala, R. (2021). Medicinal plant identification using deep learning. *International Research Journal on Advanced Science Hub*, 3(05S), 48–53. <https://doi.org/10.47392/irjash.2021.139>
- Haryono, K. A., & Saleh, A. (2020). A novel herbal leaf identification and authentication using deep learning neural network. In *International Conference on Computer Engineering, Network, and Intelligent Multimedia (CENIM)*, Surabaya, Indonesia, (pp. 338–342). IEEE. <https://doi.org/10.1109/CENIM51130.2020.9297952>
- Hedjazi, M. A., Kourbane, I., & Genc, Y. (2017). On identifying leaves: A comparison of CNN with classical ML methods. In 2017 25th Signal Processing and Communications Applications Conference (SIU), Antalya, Turkey, (pp. 1–4). IEEE. doi: 10.1109/SIU.2017.7960257
- Kartikayan, P., & Shrivastava, G. (2021). Review on emerging trends in detection of plant diseases using image processing with machine learning. *International Journal of Computer Applications*, 174, 39–48. doi: 10.5120/ijca2021920990

- Kumar, S., & Pearline, A. (2023). Real-Time Plant Species Recognition Using Non-averaged DenseNet-169 Deep Learning Paradigm. In: Gupta, D., Bhurchandi, K., Murala, S., Raman, B., Kumar, S. (eds) Computer Vision and Image Processing. CVIP 2022. Communications in Computer and Information Science, vol. 1777 (pp. 58-72) Springer. https://doi.org/10.1007/978-3-031-31417-9_5
- Lee, C. P., Lim, K. M., Song, Y. X., & Alqahtani, A. (2023). Plant-CNN-ViT: Plant classification with ensemble of convolutional neural networks and vision transformer. *Plants*, 12(14), 2642. <https://doi.org/10.3390/plants12142642>
- Malik, O. A., Ismail, N., Hussein, B. R., & Yahya, U. (2022). Automated real-time identification of medicinal plants species in natural environment using deep learning models – A case study from Borneo region. *Plants*, 11(15), 1952. <https://doi.org/10.3390/plants11151952>
- Manoharan, J. S. (2021). Flawless detection of herbal plant leaf by machine learning classifier through two stage authentication procedure. *Journal of Artificial Intelligence and Capsule Networks*, 3(2), 125–139. doi: 10.36548/jaicn.2021.2.005
- Naeem, S., Ali, A., Chesneau, C., Tahir, M. H., Jamal, F., Sherwani, R. A. K., & Ul Hassan, M. (2021). The classification of medicinal plant leaves based on multispectral and texture feature using machine learning approach. *Agronomy*, 11(2), 263. <https://doi.org/10.3390/agronomy11020263>
- Oppong, S. O., Twum, F., Hayfron-Acquah, J. B., & Missah, Y. M. (2021). Medicinal plant identification using Gabor filters and deep learning techniques: A paper review. *Journal of Computer Science*, 17(12), 1210–1221. <https://doi.org/10.3844/jcssp.2021.1210.1221>
- Oppong, S. O., Twum, F., Hayfron-Acquah, J. B., & Missah, Y. M. (2022). A novel computer vision model for medicinal plant identification using Log-Gabor filters and deep learning algorithms. *Computational Intelligence and Neuroscience*, article ID 1189509. <https://doi.org/10.1155/2022/1189509>
- Pearline, S. A, Vajravelu, S. K., & Harini, S. (2019). A study on plant recognition using con-ventional image processing and deep learning approaches. *Journal of Intelligent & Fuzzy Systems*, 36(3), 1997–2004. doi: 10.3233/JIFS-169911
- Picek, L., Šulc, M., Patel, Y., & Matas, J. (2022). Plant recognition by AI: Deep neural nets, trans-formers, and kNN in deep embeddings. *Frontiers of Plant Science*, 13, 787527. <https://doi.org/10.3389/fpls.2022.787527>
- Pudaruth, S., Mahomoodally, M. F., Kisson, N., & Chady, F. (2021). MedicPlant: A mobile application for the recognition of medicinal plants from the Republic of Mauritius using deep learning in real-time. *International Journal of Artificial Intelligence*, 10(4), 938–947. doi:10.11591/ijai.v10.i4.pp938-947
- SkandaH, N., Karanth, S. S., Suvijith, S., & SwathiK., S. (2019). Plant identification meth-odologies usingmachine learning algorithms. *International Journal of Engineering Research and Technology*, 8, 187–190. <https://api.semanticscholar.org/CorpusID:150158706>
- Tan, J. w., Chang, S.-W., Abdul-Kareem, S., Yap, H. J., & Yong, K.-T. (2020). Deep learning for plant species classification using leaf vein morphometric. *IEEE/ACM Transactions on Computational Biology and Bioinformatics*, 17(1), 82–90. doi: 10.1109/TCBB.2018.2848653
- Wagle, S. A., Harikrishnan, R., Ali, S. H. M., & Faseehuddin, M. (2022). Classification of plant leaves using new compact convolutional neural network models. *Plants*, 11(1), 24. <https://doi.org/10.3390/plants11010024>
- Yue, J., Li, W., & Wang, Y. (2021). Superiority verification of deep learning in the identification of medicinal plants: Taking Paris polyphylla var. yunnanensis as an example. *Frontiers in Plant Science*, 12. <https://doi.org/10.3389/fpls.2021.752863>

Biofilm Technology in the Production of *Macrobrachium rosenbergii*: an Appraisal of Feasibility - a Short Review

Sow Cyn Shieng^{1a}, Fatimah Md Yusoff^{2ab}, Norulhuda Ramli^{3c}, Keng Chin Lim^{4b}, Murni Karim^{5ab*}

Abstract: This review examines biofilm formation, composition, and its impact on prawn culture. It investigates the factors that influence the development of biofilms and their interactions with the giant freshwater prawn, *Macrobrachium rosenbergii* within the context of nutrient-rich biofilms. This review also explores the concept of biofilm production and its application in giant freshwater prawn cultivation, including the incorporation of probiotics. This study investigates the effects of biofilms on vital water quality parameters, including pH, ammonia level, and dissolved oxygen. It also examines the effects on the health and growth of crustaceans. Aquaculture's rapid growth has impacted the environment in several countries. The *M. rosenbergii* prawn holds significant importance as an aquaculture species in Malaysia, demonstrating the ability to enhance the income of farmers experiencing economic difficulties. However, large amounts of water are used, high-nutrient effluents are released, large areas are occupied, natural habitats are changed, and exotic species escape from their habitats. Several studies have demonstrated the application of biofilm technology in enhancing the production, safety, and economic sustainability of *M. rosenbergii* farmers. Biofilms are microbial consortiums embedded in extracellular polymeric substances (EPS) that adhere to submerged surfaces. This microbial cell consortium reduces ammonium and phosphate concentrations in aquaculture systems, providing a food source for the cultured species. Many studies have focused on the alternative microbial species with promising results. Therefore, the benefits of biofilm technology in the production of *M. rosenbergii* are reviewed to facilitate future research, development, and applications in aquaculture.

Keywords: Giant freshwater prawn, *Macrobrachium rosenbergii*, biofilm, water quality.

1. Introduction

Giant freshwater prawns (*Macrobrachium rosenbergii*) are dominant crustaceans identified for their size and culinary appeal. Found in freshwater environments spreading Asia, Africa, and the Americas, these prawns may grow up to an outstanding size, with some individuals reaching lengths of over a foot (Wowor et al., 2007). Due to their high market demand and fast growth, massive freshwater prawns which are distinguished by their striking blue-green tone and outstanding claws are a popular choice in aquaculture. They play a vital role in the global seafood industry due to their tolerance for various conditions and their adaptability in aquaculture systems (Ezekiel et al., 2018).

Aquaculture is a key to sustainable protein production that provides sufficient opportunity to reduce poverty and hunger while promoting the efficient use of natural resources. The aquaculture sector is expanding rapidly in most countries while

contributing immensely to global food production. In 2019, the aquaculture sector in Malaysia has achieved significant growth, with a presentation of 411,782 metric tonnes valued at RM3.304 billion. This accounts for 22% of the overall national fisheries production. Compared to 2018, the sector has demonstrated positive performance, with a notable increase of 5.19% in quantity and 8.10% in value (DOFM, 2019). Aquaculture is a rapidly expanding food production sector recognized for its ability to provide a sustainable solution for attaining global food security (Subasinghe et al., 2009).

The aquaculture industry has expanded due to the advancement of modern aquaculture technologies including hybridization, genetic engineering, and biofloc technology, applied in various culture systems, along with the introduction of new aquatic species (Ogello et al., 2014). Apparently, brackish water culture plays a significant role in the aquaculture production, contributing around 75% of the total output. Amongst the brackish water species, seaweed production represented 46% with a quantity of 188,111 metric tonnes and a value of RM65.86 million. Other species, such as shrimp, fish, and shellfish, accounted for 29% to the sector's production, yielding 119,069 metric tonnes worth RM2.46 billion. Meanwhile, freshwater aquaculture commodities made up the remaining 25% of the total production, amounting to 104,602 metric tonnes valued at RM780 million (DOFM, 2019).

Authors information:

^aSchool of Mathematical Sciences, Universiti Sains Malaysia, 11800 USM Penang, MALAYSIA. E-mail: gs61365@student.upm.edu.my¹; fatimahyus@gmail.com²; murnimarlina@upm.edu.my⁵

^bDepartment of Aquaculture, Faculty of Agriculture, Universiti Putra Malaysia, 43400 UPM Serdang, Selangor, MALAYSIA. E-mail: kengchin.lim@upm.edu.my⁴; murnimarlina@upm.edu.my⁵

^cDepartment of Biological and Agriculture Engineering, Universiti Putra Malaysia, 43400 UPM Serdang, Selangor, MALAYSIA. E-mail: m_norulhuda@upm.edu.my³

*Corresponding Author: murnimarlina@upm.edu.my

Received: September 15, 2023

Accepted: February 6, 2024

Published: December 31, 2024

The aquaculture industry plays a central role in improving fish supply. An increase in aquaculture productivity is required to fulfil the present demand for aquatic food (Boyd et al., 2022). Thus, sustainable technologies, such as biofilm and periphyton, have become relevant. These technologies are cost-effective, ecologically friendly, and contribute to the long-term viability of aquaculture.

2. The Production of *M. rosenbergii*

The giant freshwater prawn, *Macrobrachium rosenbergii* (de Man, 1879), is native to the tropical and subtropical regions of the Indo-West Pacific, spanning from India through Southeast Asia to Papua New Guinea (Jee, 1998; De Grave et al., 2013a). In 1961, Shao-Wen Ling made a significant discovery by demonstrating the ability of *M. rosenbergii* larvae to survive in brackish environments (Banu et al., 2016). Meanwhile, Takuji Fujimura and his team successfully innovated the mass breeding techniques for commercial-scale hatchery production of *M. rosenbergii* post-larvae (PL). Their findings opened up new possibilities for the advancement in freshwater prawn farming. In recognition of their remarkable contributions, the World Aquaculture Society honoured Shao-Wen Ling and Takuji Fujimura with life membership in 1974 and 1979, respectively (Banu et al., 2016). These two individuals were celebrated as the "Fathers" of giant freshwater prawn farming due to their pioneering work and significant achievements in the field.

Apart from that, Malaysia has natural environments such as lakes, streams, ponds, rivers, estuaries, and coastal areas that provide an excellent environment for aquaculture growth. Freshwater prawns hold a crucial ecological significance within river ecosystems, as emphasized by Murphy and Austin (2005). Being omnivorous scavengers, they actively feed on algae, decaying organisms, and other detritus present in the river ecosystem. The giant freshwater prawn stands out as a highly valuable aquaculture commodity. Its significant economic worth is attributed to its high protein content, alluring taste, and attractive appearance, making it sought-after and esteemed in the industry (Funari & Shen, 2022). This may be observed in the global prawn production record of 551 farms producing 233,989 tonnes in 2016 which valued at RM 2.4 billion (Banu et al., 2016). Consequently, the aquaculture sector offers Malaysia an alternative strategy to enhance local food security while simultaneously boosting export revenue (Banu et al., 2016).

The production of giant freshwater prawns through pond extension requires a lot of significant additional water and land area, both of which are minimal resources. However, by improving pond production per unit of land area, the stocking densities, water usage, feed, and fertilizer use will be increased. This also results in increased waste production, which is not a sustainable method of managing the aquaculture sector (New et al., 2002). Additionally, intensive aquaculture requires significant investment and technical expertise, which are not accessible to all aquaculture farmers. Using resources from agricultural systems and optimizing natural food are essential to increase aquaculture's total nutritional retention (Azim et al., 2007).

At present, giant freshwater prawn farming can be carried out using either the monoculture system (monoculture), also known as single farming, or the polyculture system, also known as integrated farming (New et al., 2002). There are still many unpolluted freshwater resources in our country, particularly in the states of Pahang, Negeri Sembilan, Terengganu, Sabah, and Sarawak, where these areas are strategic areas for giant freshwater prawn breeding and growth (Banu et al., 2016).

However, a few aspects should be considered before the giant freshwater larvae are introduced into the farm. Firstly, the pond's size and depth depend on the number of farmed prawns (New et al., 2002). It will result in reduced size and survival of prawns if ponds are too small. This is also due to the natural behaviour of the prawns that cannibalize each other. The second factor to consider is the timing and technique of pond drying. As the best and optimum practice, ponds should be exposed to the sun's heat to eliminate predators. In the pond's ecosystem, fish and eels are observed to be persistent predators of crustaceans if they are present. The sun plays an essential function in accelerating the decomposition of organic materials, such as human waste, leaves, and dead grass. New et al. (2002) recommended that the pond drying procedure should be longer than two weeks for optimal ecosystem health.

3. The Concept of Biofilms

Biofilm is a complex community of microorganisms that forms on various submerged surfaces in water. The complexity of aquatic biofilms is affected by variables, including the surface type and the environment (Davey et al., 2000). While all biofilms share common characteristics, their composition can differ. Typically, bacterial cells adhere to surfaces, producing multicellular biofilm structures. However, other microorganisms, such as fungi, protozoa algae, and viruses are also present in biofilms. These microorganisms interact within the biofilm, contributing to its overall complexity and enhancing its functionality (Donlan et al., 2002).

Biofilm formation is a dynamic process where bacteria initially attach to surfaces, followed by the gradual integration of other microorganisms, developing into a community. Algae can contribute nutrients to biofilm through photosynthesis, while fungi provide structural integrity (Funari & Shen, 2022). Viruses and protozoa are also members of the biofilm community and influence its dynamics. It is essential to comprehend the complexity of biofilms because they have implications in numerous disciplines, such as environmental science, medicine, and industrial processes. Biofilms can have both positive and negative impacts such as water filtration and biofouling problems. Research on biofilms enhances the understanding of their features in various environments and supports the development of effective strategies to minimize their negative impacts. Biofilms are composed of germs, extracellular enzymes, and particles that are bound with each other by a polymeric matrix (Romani et al., 2016). Most of the extracellular polymeric compounds (EPS) are consist of polysaccharides. These substances enable biofilms to

stay anchored, adhering to surfaces through a three-dimensional polymer network that temporarily stabilizes biofilm cells in place (Flemming et al., 2010).

Biofilms, consisting of microorganisms that firmly sticking to surface areas and enclosed in a polysaccharide matrix, are resistant to mild cleaning method. Furthermore, the biofilm matrix may include non-cellular elements, such as corrosion particles, mineral crystals, sediment bits, or clay, and blood components, depending on the particular environmental conditions under which the biofilm is formed (Donlan et al., 2002). Biofilms can live in various surfaces, such as living cells, medical tools, commercial pipe systems, and natural aquatic environments.

Biofilm formation is a continuous procedure affected by environmental stimuli. Initially, the cells accumulate and develop into microcolonies through division and recruitment. Eventually, they grow and envelop themselves into an extracellular matrix. Within this matrix, complex and diverse interactions occur, facilitating nutrient absorption (Hall et al., 2004). In aquatic biofilms, various trophic interactions happen including protozoa preying on bacteria and algae, rotifers consuming protozoa, bacteria and detritus, nematodes feeding on algae, and metazoans grazing on biofilm. These interactions may also result in structural modifications of the biofilm (Majdi et al., 2011).

Biofilm is an excellent source of both autotrophic and heterotrophic biomass because it is attached to various phytoplankton and zooplankton. In addition, fish and prawns can derive more energy from affixed biomass than planktonic forms. Anand et al. (2013) reported generating a wide variety of biofilm components, including 37 taxa of algae belonging to the Bacillariophyceae class (13 genera), Cyanophyceae (10 genera), Chlorophyceae (11 genera) and Euglenophyceae (3 genera), as well as five genera of zooplankton belonging to the Rotifer (3) and Crustacea (2) families.

4. Bacterial Attachment, Biofilm Formation and Growth Mechanisms

The growth of biofilms is influenced by various physical, chemical, and biological mechanisms. The adhesion process involves cells attaching to a surface, while communication refers to the interconnection of cells with each other. These attachment mechanisms determine both the adhesive and cohesive characteristics of the biofilm (Garrett et al., 2008; Zheng et al., 2021). According to Flemming et al. (2010), biofilm development usually involves 4 phases: attachment, microcolony formation, maturation with cellular differentiation, and finally, detachment or diffusion. In biofilms, microorganisms generate fimbriae, curli, flagella adhesion to healthy proteins, and capsules to firmly adhere to a surface.

Bacterial adherence is the first stage of biofilm development, which involves transporting microbes to a substrate's surface. The adsorption of macromolecules from the surface of a biomaterial, whether natural or synthetic, facilitates this procedure.

Therefore, a "conditioning layer" is formed, in which the fluid creates an inorganic or organic layer on the solid surface, modifying its physical or chemical properties (Garrett et al., 2008). Before microorganisms adhere on a surface, a conditioning layer makes it easier for bacterial cells to adhere onto that surface. Consequently, reversible connections are formed by non-specific communications at the molecular level in between surface structures of the bacteria such as flagella, fimbriae, pili, and substrate (Kreive et al., 2021). Furthermore, the conditioning layer may act as a resource of nutrients for the adhering microorganisms. Bacteria can form biofilms on surfaces that have been subjected to these preparatory fluids (Kishen & Haapasalo, 2010).

The first non-specific adhesion of microorganisms to the substrate surface makes up the second phase of biofilm development. This adhesion process is facilitated by electrostatic attraction, covalent or hydrogen bonding, and the development of bridges between bacteria and substrate (Huang et al., 2011). Initially, communications between bacteria and substrate might be weak. Nevertheless, as time passes, these interactions intensify, causing the development of permanent bacterial adhesion. Bacterial surface structures play a crucial role in forming bridges between the bacteria and the conditioning film (Zhao et al., 2023).

As demonstrated by Fathollahi and Coupe (2021), various environmental factors influence bacterial attachment to the underlying surface including pH, temperature, fluid flow rate, and nutrient availability. According to Rolfe et al. (2012), the species or strain of bacteria and the growth phase (log or stationary phase) can also influence the adherence. In addition, substrate-related factors such as substrate's physical and chemical properties, also influence bacterial adhesion (Kishen & Haapasalo, 2010).

The third stage involves the precise binding of microorganisms to the substrate, in which molecules on the surface of bacterial cells known as adhesins or ligands, connect with receptors on the substrate (Straub et al., 2019; Berne et al., 2018; Belas, 2014). This targeted bacterial adhesion is less susceptible to the effects of surrounding environmental conditions (Kreive & Reis, 2021). The process of bacterial adhesion to a substrate is dynamic and occurs over time (Dunne, 2002). The reversible and irreversible interactions that occur during the initial stage of bacterial attachment occur rapidly, typically lasting from a few seconds to a few minutes. In contrast, the observed interactions in the subsequent second and third stages are longer, spanning from several hours to multiple days. The time required for this process depends on the specific type of bacteria and the current environmental conditions (Floyd et al., 2017). Consequently, this process creates *in vitro* models that provides enough time for bacteria-substrate interaction while optimizing the environmental conditions (Guzmán-Soto et al., 2021). The formation and maturation of biofilm structure happen after the bacterial adhesion (Kishen & Haapasalo, 2010).

5. The Production *M. rosenbergii* Using Biofilm Technology

Cannibalism was observed in high-density rearing systems by (Romano & Zeng, 2017), who found high mortality levels among cultured shrimps. Cannibalism also increases among newly moulted individuals. Introducing substrates into a culture system is one of the most effective strategies for increasing survival by reducing cannibalism to a minimum level. It can provide shelter from other predators besides serving as a biofilm substrate.

Consistent findings from previous studies (Table 1) have

demonstrated an inverse relationship between stocking density and shrimp production, as noted by Wasielesky et al. (2001). Khatoon et al. (2007) observed the presence of post-larvae within PVC-coated pipes in their study, indicating the potential function of these pipes as protective shelters during moulting stages. This result led to a noteworthy increase in the survival rates (51%–60%) compared to the control group (37%). Furthermore, during the nursery phase of *Litopenaeus vannamei*, Sandifer et al. (1987) documented a notable survival rate (24%) in tanks equipped with fiberglass window screens.

Table 1. Culture organisms that use substrate to promote the growth of biofilm.

Species	Substrate type	Response	Water quality	Reference
1. Pink shrimp (<i>Farfantepenaeus paulensis</i>)	Flexible PVC tubes ranging 0.5 to 15 cm in length and 0.5 cm in diameter.	Reduced exportation of phosphorus by 33% and created higher outputs of nitrate and nitrite.	Ammonium level was stable and low, ranging from 5.94 to 16.09 mM.	Thompson et al. (2002)
2. Rohu (<i>Labeo rohita</i>)	Sugarcane (<i>Saccharum officinales</i>), palm leaf (<i>Borassus flabellifera</i>), coconut (<i>Cocos nucifera</i>), and bamboo (<i>Bambusa bambos</i>).	The specific growth rate was higher with sugarcane, palm, coconut, and bamboo (2.0%, 1.72%, 1.99%, and 1.62%, respectively), compared to without substrate (1.42%).	The level of ammonia was 52.4 mg/L in the control group compared to sugarcane, palm, coconut, and bamboo (78.2%, 88.9%, 69.9%, and 67.6%, respectively).	Keshavanath et al. (2012)
3. Common carp (<i>Cyprinus carpio</i>)	Sugarcane (<i>Saccharum officinales</i>), palm leaf (<i>Borassus flabellifera</i>), coconut (<i>Cocos nucifera</i>), and bamboo (<i>Bambusa bambos</i>).	The specific growth rate was higher with sugarcane, palm, coconut, and bamboo (2.0%, 1.9%, 2.0%, and 1.4%, respectively), compared to without substrate (1.4%).	The level of ammonia was 52.4 mg/L in the control group compared to sugarcane, palm, coconut, and bamboo (78.2%, 88.9%, 69.9%, and 67.6%, respectively).	Keshavanath et al. (2012).
4. White leg shrimp (<i>L. vannamei</i>)	Polyethylene mosquito screen (1 mm mesh size).	The final biomass and survival of shrimp in the tank with substrate reached 314%, with a survival rate of 93.9±2.4%.	There are no significant differences in ammonia and nitrite levels.	Schweitzer et al. (2013).
5. Giant freshwater prawn (<i>Macrobrachium rosenbergii</i>)	Bamboo kanchi (periphyton substrates).	The addition of substrate produced 660 kg ha ⁻¹ in 120 days compared to just 463 kg ha ⁻¹ with the same culture period without substrate.	The ammonia level was low (0.038 mg/L) in the culture pond compared to the culture tank without substrate.	Asaduzzaman et al. (2008).
6. Whiteleg shrimp (<i>Litopenaeus vannamei</i>)	Artificial substrate (Aquamats™).	No specific results on the growth.	Ammonia and nitrites remained between 0.17-0.19 mg L ⁻¹ and 0.10-0.11 mg L ⁻¹ .	Audelo- Naranjo et al. (2012).

7.	Giant freshwater prawn (<i>Macrobrachium rosenbergii</i>)	T1-no substrate (control), T2-hollow PVC pipe, T3-polyethylene, and T4-black coloured nylon netting.	Final weights of post-larvae (PLs) in treatments T3, T4, and T2 were 2.70%, 31.54%, and 21.05%, respectively, compared to T1 (without substrate). The specific growth rate of PLs were 5.04%, 5.19%, and 5.18% in treatments T2, T3, and T4, respectively, compared to T1 without substrate (4.72%).	Total ammonia was maintained between 0.01 to 0.15 mg L ⁻¹ .	Mamun et al. (2010).
8.	Giant tiger prawn (<i>Penaeus monodon</i>)	Polyvinyl chloride pipes (PVC).	The specific growth rate of post-larvae increased by 28% in the substrate.	The level of ammonia nitrogen was lowest (0.03 mg L ⁻¹) compared to other groups.	Khatoun et al. (2007).
9.	Asian stinging catfish (<i>Heteropneustes fossilis</i>)	Sugarcane bagasse.	The specific growth rate in sugarcane bagasse and supplemental feed group recorded 2.01%, followed by sugarcane bagasse alone (1.99%).	The ammonia level was maintained in the range of 6.7–6.9 mg L ⁻¹ .	Radhakrishnan & Sugumaran (2010).

6. Nutritional Quality of Biofilms

Fish meal and oil are important elements used as feed ingredients in poultry, aquaculture, and swine farming (El-Sayed, 2020). Aquaculture production heavily relies on wild-caught fish due to the essential role of fish meal and oil in the diets of numerous aquaculture species, as highlighted by Barlow (2003). Within the aquaculture sector, approximately 5–6 million tonnes of low-value or bycatch fish are directly utilized as feed, either in unprocessed form or as components of farm-made feeds. Additionally, from 1992 to 2006, there was a notable increase in the overall consumption of fish meal and fish oil in aquafeeds, with quantities more than tripling from 0.96 to 3.06 million tonnes and from 0.23 to 0.78 million tonnes, respectively (FAO, 2009).

Furthermore, in various aquaculture practices (intensive, semi-intensive, or extensive), the utilisation of fish meal requires 2 to 5 times more fish protein to nourish the farmed species adequately (Naylor et al., 2000). Consequently, recent research focused on developing feeds that require less fish meal supply, oil or expensive ingredients, including protein substitution to plant proteins. In addition, Naylor et al. (2000) mentioned that extensive and traditional aquaculture systems commonly refrain from using significant amounts of fish meal. Instead, they introduce nutrient-rich substances into the water to stimulate the growth of algae and other natural organisms that serve as food sources for the farmed fish. This condition contributes to the development of the biofilm technology, particularly for both intensive and semi-intensive aquaculture systems.

Previous studies have revealed that the nutritional composition of biofilms is generally compatible with fish's dietary requirements. The protein content of the biofilm ranged from 23%–30%, the lipid content from 2%–9%, the NFE content from 25%, and the ash content from 16%–42%. These findings suggest

biofilms with high nutritional value could be used as food supplements for fish and shrimp cultures. According to Siddhartha et al. (2015), *Penaeus monodon* juveniles require 35% to 40% protein and up to 10% lipids in their diet.

However, the recommended protein requirement for Indian significant carps is 30% of their body weight (Mahavadiya et al., 2021). Biofilms are recognized to be a high-quality source of protein (Ghosh et al., 2022). Therefore, biofilms are associated with improved growth in both fish and shrimps (Anand et al., 2013). Other than just providing macronutrients, microalgae and heterotrophic bacteria also act as immune boosters, growth enhancers, sources of bioactive compounds, and dietary stimulants (Ju et al., 2008; Kuhn et al., 2010; Xu et al., 2012), all of which can improve the growth performance of cultured shrimps.

7. Biofilm Impacts on Water Quality

Nitrification in aquaculture systems is pivotal in determining water quality by regulating nitrogen dynamics. The primary nitrogen source in aquaculture is derived from feed, which can substantially influence the natural nitrogen cycle, particularly in intensive or semi-intensive aquaculture settings (Kumar et al., 2017). Excessive nitrogen from the feed undergoes conversion into inorganic nitrogen compounds, particularly ammonia, posing a health risk to the cultured organisms. However, nitrifying bacteria within biofilm formations significantly mitigates ammonia levels by facilitating the conversion of nitrite to nitrate. Additionally, certain heterotrophic communities within the biofilm directly utilize inorganic nitrogen. Achieving a balanced carbon-to-nitrogen ratio in substrate-based treatments enhances water quality and substantially reduces ammonia nitrogen concentrations (Azim et al., 2002a; Kumar et al., 2017).

The incorporation of biofilms in the rearing of *Catla catla*

fingerlings resulted in a significant enhancement of water quality, as demonstrated by Pradeep et al. (2003). Within freshwater ponds, introducing biodegradable substrate contributes to improved water quality, thereby creating a more conducive environment for fish growth. The biofilm treatment exhibits significantly lower ammonia levels than a conventional aquaculture system (Keshavanath et al., 2012). Apparently, use of non-biodegradable substrates in brackish water ponds reduces ammonia and nitrite nitrogen levels, stimulating the growth of *L. vannamei* (Kumar et al., 2017). Nitrifying bacteria and microalgae create opportunities to attenuate detrimental nitrogen compounds in water, while nitrate generated through the nitrification process serves as a growth-promoting nutrient for microalgae (Thompson et al., 2002).

Maintaining appropriate alkalinity and pH levels is essential for ensuring the health and welfare of cultured animals as these factors significantly influence water quality. The addition of substrate to *L. vannamei* culture resulted in significant improvements in the pH and alkalinity levels of the culture system throughout the culture period. Notably, the pH was consistently maintained within the range of 7.4–8.4, while the alkalinity ranged from 88 to 230 mg/L as CaCO₃ (Zhang et al., 2015).

Incorporating photosynthetic organisms into biofilms alters the pH and alkalinity levels of the culture system, potentially increasing or decreasing the acidity and alkalinity levels (Kumar et al., 2017). Several studies have consistently shown improved water quality when employing biofilm-based systems with diverse substrate materials (Asaduzzaman et al., 2010; Anand et al., 2013). The biofilm and submerged substrate also reduce water turbidity by trapping organic matter or facilitating its accumulation (Van Dam et al., 2002). Some researchers also found lower dissolved oxygen (DO) levels in substrate-installed tanks (Anand et al., 2019).

8. Biofilms and Probiotics in The Production of *M. rosenbergii*

Probiotics are living microorganisms that improve gastrointestinal microbiota and the overall health of the receiving hosts when supplied in adequate amounts (Ringo, 1999; Hagiwara et al., 1994). Probiotics may also be components of microbial cells added to feed or culture water to benefit the host (Verschuere et al., 2000). They can be used separately or together with prebiotics or other immunostimulants. Applying probiotics is recommended as an environmentally friendly strategy for disease prevention in aquaculture (Servin, 2004). Several studies have extensively examined the utilization of probiotics in aquaculture, emphasizing their wide-ranging benefits such as improved growth performance, increased disease resistance, enhanced immune responses, better regulation of gut microbiota, water quality improvement through bioremediation, and augmentation of nutrient levels in zooplankton populations (Azad et al., 2019). In aquaculture, probiotics are introduced through water treatments or feed supplements. Enrichment of zooplankton with probiotics by encapsulation allows bacteria to remain alive and even multiply on the live feed. As a result,

enriched live feeds can efficiently provide probiotics to the hosts (Vijayan et al., 2006; Rahiman et al., 2010).

The growth effects of probiotics on fish and crustaceans have been investigated in multiple studies. Seenivasan et al. (2016) assessed the impacts of three probiotic strains (*Bacillus subtilis*, *Lactobacillus sporogenes*, and *Saccharomyces cerevisiae*) that incorporated into the diet of *M. rosenbergii* post-larvae and examined its survival and growth parameters over 60 days. The results indicated probiotics diets on *M. rosenbergii* produced higher weight gain and growth rates than the control. In a study conducted by Sumon et al. (2018) observed that the administration of probiotics (specifically *Clostridium butyricum*) resulted in substantial growth stimulation and enhanced enzyme production (including protease, amylase, and lipase) in *M. rosenbergii*. Additionally, Ghosh et al. (2016) and Azad et al. (2018) reported 30% enhancement in the growth and productivity of *M. rosenbergii* when supplemented with a mix of commercial probiotics, which were Zymetin (*Bacillus mesentericus*) and Super PS (*Rhodobacter* sp. and *Rhodococcus* sp.). The research showed that the combination is superior to the addition of each probiotic individually. On top of that, particular probiotics can develop biofilms in the digestion system, supplying an obstacle versus microorganisms. These probiotic biofilms can enhance the survival and function of probiotics in the digestive tract, thus preserving a healthy microbiota and promoting health.

Probiotics in the form of biofilms might raise survival rates and function. When probiotics develop a biofilm in the intestinal tract, it can give a protective environment that enables them to sustain the harsh conditions of the digestion tract, such as the acidic environment of the stomach. This condition suggests that more probiotics might reach the intestinal tracts in active and excellent state, thereby boosting their advantageous impacts (Amara & Shibl, 2015; Salas-Jara, 2016). Specific probiotic strains can produce substances that encourage the development of valuable biofilms by various probiotics or intestine microorganisms, cultivating a more varied and robust gut microbiota (Gao et al., 2022).

Generally, the capability of probiotics to form biofilms includes the significant improvement on the health of the farmed species. Nevertheless, the particulars of these impacts might differ depending on the particular probiotic species and the strains employed. Further research is essential to comprehensively understand these interactions. Consequently, the most effective approach for harnessing their health-promoting benefits in prawn culture, specifically associated with biofilm technology can be determined.

9. Conclusions and Recommendations for Future Research

Biofilm technology has several advantages, including controlling water quality, on-site feed production, and other possible additional properties. Biofilm technology provides a sustainable aquaculture approach in addressing its environmental, social, and economic concerns while supporting its growth.

Further research is required to comprehend the complexity of the biofilm, encompassing microbial relationships, physiology of gut health, and immune interactions in giant freshwater prawns. The management of biofilm and water quality monitoring are somewhat complex. Knowledge and skills still need to be improved and addressed to support the successful adoption of this technology on a commercial-scale production. Additionally, future research is required particularly on the disease resistance in *M. rosenbergii* with the potential positive effects of biofilm technology. This advancement shall enable the aquaculture development while promoting social responsibility and environmental concerns.

10. Declaration

Acknowledgement

This research was funded by the Ministry of Higher Education Malaysia (MOHE) under 'Grant Putra Berkumpulan' UPM/800/3/3/1/GP IPB/2020/9687902.

Authors' contribution

Sow Cyn Shieng conducted literature reviews and wrote the original manuscript. Keng Chin Lim assisted in manuscript preparation and revision. Fatimah Md Yusoff and Norulhuda Ramli contributed to the manuscript revision. Murni Karim supervised the content, revision, and proofreading of the manuscript. All authors confirmed the final draft of the manuscript.

Competing interests

The authors declare that they have no competing interests.

Ethical considerations

The authors declare and confirm that the manuscript is original, has no misconduct, has never been published in another journal, and written only to be published in this journal.

11. References

- Amara, A. A., & Shibl, A. (2015). Role of Probiotics in health improvement, infection control and disease treatment and management. *Saudi pharmaceutical journal*, 23(2), 107-114.
- Anand, P. S., Kohli, M. P. S., Roy, S. D., Sundaray, J. K., Kumar, S., Sinha, A., ... & kumar Sukham, M. (2013). Effect of dietary supplementation of periphyton on growth performance and digestive enzyme activities in *Penaeus monodon*. *Aquaculture*, 392, 59-68.
- Anand, P. S., Balasubramanian, C. P., Christina, L., Kumar, S., Biswas, G., De, D., ... & Vijayan, K. K. (2019). Substrate based black tiger shrimp, *Penaeus monodon* culture: Stocking density, aeration and their effect on growth performance, water quality and periphyton development. *Aquaculture*, 507, 411-418.
- Anand Pss, Kumar S, Panigrahi A, Ghoshal Tk, Dayal Js, Biswas G, Sundaray Jk, De D, Ananda, Raja gallic, b., (2010). Where do fishmeal and fish oil products come from? An analysis of the conversion ratios in the global fishmeal industry. *Marine policy* 34, 815–820.
- Asaduzzaman M, Wahab MA, Verdegem MCJ, Benerjee S, Akter T, Hasan MM, Azim ME (2008). Effects of addition of tilapia *Oreochromis niloticus* and substrates for periphyton developments on pond ecology and production in C/N-controlled freshwater prawn *Macrobrachium rosenbergii* farming systems. *Aquaculture* 287(3-4):371-380.
- Audelo-Naranjo, J. M., Voltolina, D., & Romero-Beltrán, E. (2012). Culture of white shrimp (*Litopenaeus vannamei* Boone, 1931) with zero water exchange and no food addition: an eco-friendly approach. *Latin american journal of aquatic research*, 40(2), 441-447.
- Avnimelech Y. (2007) Feeding with Microbial Floccs by Tilapia in Minimal Discharge Bioflocs Technology Ponds. *Aquaculture*, 264: 140-147.
- Azad, M. A. K., Islam, S. S., Sithi, I. N., Ghosh, A. K., Banu, G. R., Bir, J., & Huq, K. A. (2019). Effect of probiotics on immune competence of giant freshwater prawn *Macrobrachium rosenbergii*. *Aquaculture research*, 50(2), 644-657.
- Azim Me, Verdegem Mcj, Khatoon Hm, Wahab A, Van Dam Aa, Beveridge Mcm (2002a). A Comparison Of Fertilization, Feeding And Three Periphyton Substrates For Increasing Fish Production In Freshwater Pond Aquaculture In Bangladesh. *Aquaculture* 212:227-243
- Azim, M. E., & Little, D. C. (2007). Intensifying aquaculture production through new approaches to manipulating natural food. *CABI Reviews*, (2006), 23-pp.
- Barlow, S.M. (2003). 'Fish meal', *Encyclopedia of Food Sciences and Nutrition*, pp. 2486–2491. doi:10.1016/b0-12-227055-x/00479-x
- Banu, R., & Christianus, A. (2016). Giant freshwater prawn *Macrobrachium rosenbergii* farming: a review on its current status and prospective in Malaysia.
- Belas, R. (2014) 'Biofilms, flagella, and mechano sensing of surfaces by bacteria', *Trends in Microbiology*, 22(9), pp. 517–527. doi: 10.1016/j.tim.2014.05.002.
- Berne, C. et al. (2018) 'Bacterial adhesion at the single-cell level', *Nature Reviews Microbiology*, 16(10), pp. 616–627. doi:10.1038/s41579-018-0057-5.
- Boyd, C. E., McNevin, A. A., & Davis, R. P. (2022). The contribution of fisheries and aquaculture to the global protein supply. *Food security*, 14(3), 805-827.

- Daniels, C.L., Merrifield, D.L., Ringø, E. And Davies, S.J. (2015) Probiotic, Prebiotic and Synbiotic Applications for The Improvement of Larval European Lobster (*Homarus Gammarus*) Culture. Aquaculture (In Press).
- Davey, M. E., & O'toole, G. A. (2000). Microbial biofilms: from ecology to molecular genetics. *Microbiology and molecular biology reviews*, 64(4), 847-867.
- De Grave S (2013a) *Macrobrachium lepidactylus*. The IUCN Red List of Threatened Species 2013: e.T198341A2521772. <https://doi.org/10.2305/IUCN.UK.2013-1.RLTS.T198341A2521772.en> (accessed 02 November 2018)
- DOFM. (2018 (and earlier issues)). Annual Fisheries Statistics and earlier issues (2018). Retrieved from <https://www.dof.gov.my/index.php/pages/view/82>
- DOFM. (2018). Annual Fisheries Statistics 2018. Retrieved from <https://www.dof.gov.my/index.php/pages/view/3929>.
- DOFM (Department of Fisheries Malaysia). 2019. Annual Fisheries Statistics-2019. Department of Fisheries Malaysia, Kuala Lumpur, Malaysia.
- Donlan rm (2002). Biofilms: microbial life on surfaces. *Emerg. Infect. Diseases* 8(9):881-890. Food and agriculture organization of the United Nations fao and the sdgs. Indicators: measuring up to the 2030 agenda for sustainable development. <Http://www.fao.org/3/a-i6919e.pdf>, 2017; 39.
- Dunne, W.M. (2002) 'Bacterial adhesion: Seen any good biofilms lately?', *Clinical Microbiology Reviews*, 15(2), pp. 155–166. doi:10.1128/cmr.15.2.155-166.2002.
- El-Sayed, A.-F.M. (2020) 'Nutrition and feeding', *Tilapia Culture*, pp. 135–172. doi:10.1016/b978-0-12-816509-6.00007-0.
- Ezekiel, B.B.; Furuza, B.M.; Mohammad, L.A.; Subha, B. Analysis of factors for determining suitable site for Giant Freshwater Prawn (*Macrobrachium rosenbergii*) farming through the local knowledge in Negeri Sembilan of Peninsular Malaysia. *Pertanika J. Soc. Sci. Humanit.* 2018, 26, 2867–2882.
- FAO (Food and Agriculture Organization of the United Nations). (2009). The state of world fisheries and aquaculture 2008. Effect of aquaculture on world fish supplies. *Nature* 405, 1017–1024.
- Fathollahi, A. and Coupe, S.J. (2021) 'Effect of environmental and nutritional conditions on the formation of single and mixed-species biofilms and their efficiency in cadmium removal', *Chemosphere*, 283, p. 131152. doi: 10.1016/j.chemosphere.2021.131152.
- Flemming, H. C., & Wingender, J. (2010). The biofilm matrix. *Nature reviews microbiology*, 8(9), 623-633.
- Floyd, K.A., Eberly, A.R. and Hadjifrangiskou, M. (2017) 'Adhesion of bacteria to surfaces and biofilm formation on medical devices', *Biofilms and Implantable Medical Devices*, pp. 47–95. doi:10.1016/b978-0-08-100382-4.00003-4.
- Fruh, D., Norf, H., And Weitere, M. (2011). Response Of Biofilm-Dwelling Ciliate Communities to Enrichment With Algae. *Aquat. Microb. Ecol.* 63, 299–309.
- Funari, R., & Shen, A. Q. (2022). Detection and characterization of bacterial biofilms and biofilm-based sensors. *ACS sensors*, 7(2), 347-357.
- Garrett, T. R., Bhakoo, M., & Zhang, Z. (2008). Bacterial adhesion and biofilms on surfaces. *Progress in natural science*, 18(9), 1049-1056.
- Gao, J., Sadiq, F. A., Zheng, Y., Zhao, J., He, G., & Sang, Y. (2022). Biofilm-based delivery approaches and specific enrichment strategies of probiotics in the human gut. *Gut Microbes*, 14(1), 2126274.
- Ghosh, A.K., Bir, J., Azad, M.A.K., Hasanuzzaman, A.F.M., Islam, M.S. & Huq, K.A. (2016). Impact of commercial probiotics application on growth and production of giant freshwater prawn (*macrobrachium rosenbergii* de man, 1879). *aquaculture reports*, 4: 112-117.
- Ghosh, S. *et al.* (2022) 'Engineered Biofilm: Innovative next gen strategy for quality enhancement offermented foods', *Frontiers in Nutrition*, 9. doi:10.3389/fnut.2022. 808630.v
- Guzmán-Soto, I. *et al.* (2021) 'Mimicking biofilm formation and development: Recent progress in in vitro and in vivo biofilm models', *iScience*, 24(5), p. 102443. doi: 10.1016/j.isci.2021.102443.
- Hagiwara, A. *et al.* (1994) 'Increased sexual reproduction in *Brachionus plicatilis* (Rotifera) with the addition of bacteria and Rotifer extracts', *Journal of Experimental Marine Biology and Ecology*, 181(1), pp. 1–8. doi:10.1016/0022-0981(94)90100-7.
- Hall-Stoodley, L., Costerton, J.W., And Stoodley, P. (2004). Bacterial Biofilms: From the Natural Environment To Infectious Diseases. *Nat. Rev. Microbiol.* 2, 95–108.
- Huang, R., Li, M. and Gregory, R.L. (2011) 'Bacterial interactions in dental biofilm', *Virulence*, 2(5), pp. 435–444. doi:10.4161/viru.2.5.16140.

- Jee Ka (1998) Farming of Giant Freshwater Prawn. In Aquaculture Practices in Malaysia: Malaysian Fish, Society Occasional Publication.
- Keshavanath P, Manissery JK, Bhat AG, Gangadhara B (2012). Evaluation of four biodegradable substrates for periphyton and fish production. *J. Appl. Aquac.* 24:2012.
- Khatoon H, Yusoff Fm., Banerjee S, Shariff M, Mohamed S (2007). Use Of Periphyticcyano bacterium And Mixed Diatoms Coated Substrate for Improving Water Quality, Survival and Growth Of *Penaeus Monodon* Fabricius Post larvae. *Aquaculture* 271:196-205.
- Kishen, A., & Haapasalo, M. (2010). Biofilm models and methods of biofilm assessment. *Endodontic Topics*, 22(1), 58-78.
- Kreve, S. and Reis, A.C. (2021) 'Bacterial adhesion to biomaterials: What regulates this attachment? A Review', *Japanese Dental Science Review*, 57, pp. 85–96. doi: 10.1016/j.jdsr.2021.05.003.
- Kuhn Dd, Lawrence Al, Boardman Gd, Patnaik S, Marsh L, Flick Gj (2010). Evaluation Of Two Types Of Bioflocs Derived From Biological Treatment Of Fish Effluent As Feed Ingredients For Pacific White Shrimp, *Litopenaeus Vannamei*. *Aquaculture* 303: 303: 28-33.
- M.A.K. Azad, S.S. Islam, I.N. Sithi, A.K. Ghosh, G.R. Banu, J. Bir, K.A. Huq, (2019). Effect of probiotics on immune competence of giant freshwater prawn *Macrobrachium rosenbergii*, *Aquaculture. Res.* 50 (2) (2019) 644–657
- Mahavadiya, D., Jungi1, D. and Dharmesh, S. (2021) Feeding and Nutritional Requirements of Indian Major Carps: A Review, Feeding and Nutritional Requirements of Indian Major Carps: A Review. Available at: <https://ijasr.forexjournal.co.in/papers-pdf/7.pdf> (Accessed: 10 June 2023).
- Majdi, N., Traunspurger, W., Boyer, S., Mialet, B., Tackx, M., Fernandez, R., Gehner, S., Ten-Hage, L., And Buffan-Dubau, E. (2011). Response Of Biofilm Dwelling Nematodes to Habitat Changes in The Garonne River, France: Influence Of Hydrodynamics And Microalgal Availability. *Hydrobiologia* 673, 229–244.
- Mamun, M. A. A., Hossain, M. A., Hossain, M. S., & Ali, M. L. (2010). Effects of different types of artificial substrates on nursery production of freshwater prawn, *Macrobrachium rosenbergii* (de Man) in recirculatory system. *Journal of the Bangladesh Agricultural University*, 8(2), 333-340.
- Murphy, N. & Austin, C. (2005). Phylogenetic relationships of the globally distributed freshwater prawn genus *Macrobrachium* (Crustacea: Decapoda: Palaemonidae): biogeography, taxonomy, and the convergent evolution of abbreviated larval development. *Zoologica Scripta*, 34(2): 187-197
- New, M.B. (2002). Farming freshwater prawns: a manual for the culture of the giant river prawn (*Macrobrachium rosenbergii*).
- Ogello, e. O., musa, s. M., aura, c. M., abwao, j. O., & munguti, j. M. (2014). International journal of aquaculture science an appraisal of the feasibility of tilapia production in ponds using biofloc technology: a review. 5(1), 21–39.
- Oser bl (1959). An integrated essential amino acid index for predicting the biological value of proteins. In: albanese aa (eds) protein and amino acid nutrition. Academic press, new york, pp. 281-295.
- Radhakrishnan, M. V., & Sugumaran, E. (2010). Effect of sugarcane bagasse on growth performance of *Hereropneustes fossilis* (Bloch.) fingerlings. *Journal of Experimental Sciences*, 1(1).
- Ringo, E. (1999) 'Intestinal microflora of fish larvae and fry', *Aquaculture Research*, 30(2), p. 73. doi:10.1046/j.1365-2109.1999.00302. x.
- Rolfe, M.D. et al. (2012) 'LAG phase is a distinct growth phase that prepares bacteria for exponential growth and involves transient metal accumulation', *Journal of Bacteriology*, 194(3), pp. 686–701. doi:10.1128/jb.06112-11.
- Romano, N., & Zeng, C. (2017). Cannibalism of decapod crustaceans and implications for their aquaculture: a review of its prevalence, influencing factors, and mitigating methods. *Reviews in Fisheries Science & Aquaculture*, 25(1), 42-69.
- Romani, A. M., Guasch, H., & Balaguer, M. D. (2016). Aquatic biofilms: ecology, water quality and wastewater treatment. Caister Academic Press. Sandifer Pa, Hopkins Js, Stokes Ad (1987). Intensive Culture Potential of *Penaeus vannamei*. *J. World Aquac. Soc.* 18:94-100.
- Salas-Jara, M. J., Ilabaca, A., Vega, M., & García, A. Biofilm forming Lactobacillus: new challenges for the development of probiotics. *Microorganisms*. 2016; 4 (3).
- Schweitzer R, Arantes R, Baloi MF, Costodio PS, Arana LV, Seiffert WQ, Andreatta ER (2013). Use of artificial substrates in the culture of *Litopenaeus vannamei* (Biofloc system) at different stocking densities: Effects on microbial activity, water quality and production rates. *Aquacult. Eng.* 54:93-103

- Seenivasan, C., Radhakrishnan, S., Muralisankar, T. & Bhavan, P.S. (2016). Effects of probiotics on survival, growth, and digestive enzymes activities in freshwater prawn *Macrobrachium rosenbergii* (De Man, 1879). *Proceedings of the Zoological Society*, 69(1): 52-60.
- Servin, A.L. (2004) 'Antagonistic activities of *Lactobacilli* and *Bifidobacteria* against microbial pathogens', *FEMS Microbiology Reviews*, 28(4), pp. 405–440. doi: 10.1016/j.femsre.2004.01.003.
- Siddhartha Pati, A.C. and Dash BP (2015) 'A study on the growth of juveniles of tiger prawn, *Penaeus Monodon* (Fabricius) under different photoperiods', *Journal of Aquaculture Research & Development*, 6(12). doi:10.4172/2155-9546.1000385.
- Straub, H. *et al.* (2019) 'Bacterial adhesion on soft materials: Passive physicochemical interactions or active bacterial mechanosensing?', *Advanced Healthcare Materials*, 8(8), p. 1801323. doi:10.1002/adhm.201801323.
- Subasinghe, R., Soto, D., & Jia, J. (2009). Global Aquaculture and Its Role in Sustainable Development. *Reviews In Aquaculture*, 1(1), 2-9. Doi:10.1111/J.1753- 5131.2008.01002.X
- Sumon, M.S., Ahmed, F., Khushi, S.S., Ahmed, M.K., Rouf, M.A., Chisty, M.A.H. & Sarower, M.G. (2018). Growth performance, digestive enzyme activity, and immune response of *Macrobrachium rosenbergii* fed with probiotic *Clostridium butyricum* incorporated diets. *Journal of King Saud University-Science*, 30(1): 21-28.
- Sun, Y.-Z., Yang, H.-L., Huang, K.-P., Ye, J.-D. And Zhang, C.-X. (2013) Application of Autochthonous *Bacillus* Bioencapsulated in Copepod To Grouper *Epinephelus Coioides* Larvae. *Aquaculture* 392–395, 44–50.
- Thompson FI, Abreu PC, Wasielesky W (2002). Importance Of Biofilm for Water Quality and Nourishment in Intensive Shrimp Culture. *Aquaculture* 203:263-278.
- Tidwell JH, Coyle SD, Schulmeister G (1998). Effects of added substrate on the production and population characteristics of freshwater prawns (*Macrobrachium rosenbergii*) to increasing amounts of artificial substrate in ponds. *J. World Aquac. Soc.* 31:174-179.
- Van Dam Aa, Beveridge MCM, Azim Me, Verdegem MCJ (2002). The potential of fish production is based on periphyton. *rev. fish biol. fish.* 12:1-31.
- Verschuere, L. *et al.* (2000) 'Probiotic bacteria as biological control agents in Aquaculture', *Microbiology and Molecular Biology Reviews*, 64(4), pp. 655–671. doi:10.1128/mmbr.64.4.655-671.2000.
- Wasielesky WJ, Poersch LH, Bianchini A (2001). Effect of stocking density on pen reared pink shrimp *farfantepenaeus paulensis* (Pérez-Farfante, 1967) (Decapoda, *Penaeidae*). *Nauplius* 9:163-167.
- Wowor, D., & Ng, P. K. (2007). The giant freshwater prawns of the *Macrobrachium rosenbergii* species group (Crustacea: Decapoda: Caridea: *Palaemonidae*). *The Raffles Bulletin of Zoology*, 55(2), 321-336.
- Xu WJ, Pan LQ, Sun XH, Huang J (2012). Effects of bioflocs on water quality, growth and digestive enzyme activities of *litopenaeus vannamei* (Boone) in zero-water exchange tanks. *Aquacult. Res.* <http://dx.doi.org/10.1111/j.1365-2109.2012.03115.x>
- Zhang, K. *et al.* (2015) 'Effect of using sodium bicarbonate to adjust the pH to different levels on water quality, the growth and the immune response of shrimp *litopenaeus vannamei* reared in zero-water exchange biofloc-based culture tanks', *Aquaculture Research*, 48(3), pp. 1194–1208. doi:10.1111/are.12961.
- Zhao, A., Sun, J., & Liu, Y. (2023). Understanding bacterial biofilms: From definition to treatment strategies. *Frontiers in cellular and infection microbiology*, 13, 1137947.
- Zheng, S., Bawazir, M., Dhall, A., Kim, H. E., He, L., Heo, J., & Hwang, G. (2021). Implication of surface properties, bacterial motility, and hydrodynamic conditions on bacterial surface sensing and their initial adhesion. *Frontiers in Bioengineering and Biotechnology*, 9, 643722